DOTTORATO DI RICERCA IN

Physics and Nano Sciences

XXV CICLO
Sede Amministrativa Università degli Studi di MODENA e REGGIO EMILIA

E

Physique Polytechnique

Graduate School de l'ÉCOLE POLYTECHNIQUE - PALAISEAU

TESI PER IL CONSEGUIMENTO DEL TITOLO DI DOTTORE DI RICERCA

First principles Second-Harmonic Generation in quantum confined silicon-based systems

---

Candidato:
Matteo Bertocchi

Commissione esaminatrice:

Prof.	Erio Tosatti	Presidente della commissione
Prof.	Stefano Ossicini	Direttore di tesi
Dr.	Valérie Véniard	Direttrice di tesi
Dr.	Riccardo Rurali	Referee
Dr.	Maurizia Palummo	Referee
Dr.	Luca Perfetti	Esaminatore

Contents

Chapter 1

Introduction

1.1 Nonlinear Optics

Nonlinear optical phenomena [1, 2] includes all these physical processes originating from the interaction of light with matter, that modify the incoming electromagnetic field creating a new radiation of different frequency and wavelength. This is in contrast to linear optics, where the light-beam preserves its frequency and is only deviated, reflected, diffused or absorbed by the material and is described by the common laws of optics of Newton, Snell, Fresnel and Maxwell. Nonlinear optics takes place when a material interacts with an intense light so that its response yields fundamentally different properties than the one observed in the linear regime; actually an high photon density is required in order to allow three-body or higher order processes. As a consequence, until the development of laser in 1960, there was no way to access them, although theoretical prediction have been formulated already in 1931 [3]. The first experimental evidence of nonlinear phenomena has been observed in 1961 by Franken *et al.* [4]. They detected the frequency doubling of a radiation passing through a nonlinear crystal; the process was interpreted as the generation of second harmonic in visible light, a phenomenon previously known for radio waves only.

Since the linear and nonlinear optics involve a different number of photons, they can be distinguished with respect to the intensity of the field (i.e., the number of photons) that enters into their description. Consequently, while the linear response of the material is proportional to the amplitude of the applied field, in nonlinear optics it is related to the square or the higher powers of this field. Formally, one can expand the polarization of the material in terms of the field as [2]:

$$\mathbf{P} = \chi^{(1)}\mathbf{E} + \chi^{(2)}\mathbf{E}\mathbf{E} + \chi^{(3)}\mathbf{E}\mathbf{E}\mathbf{E} + \ldots \tag{1.1}$$

where the term $\chi^{(1)}$ determines the linear optical response and all the effects described by the other terms are referred to as nonlinear. Obviously, this concerns a variety of effects and different order processes that have their own properties. As an example, second order effects are completely absent for materials with inversion symmetry and a light source that can be described within the dipole approximation. On the contrary, third order effects (that are not dipole-forbidden) are present. As a consequence, the susceptibilities $\chi^{(i)}$ depend directly on the material and their efficiency can be very different.

Even within the same order there are processes that exhibit a completely different nature. Second order phenomena indeed, comprise the second-harmonic generation together with the sum- or difference-frequency generation (i.e., the creation of a beam from the sum/difference of two incoming beams), the optical parametric amplification (it consists in the splitting of one incoming photon into two outgoing ones that conserve the initial energy) or the optical rectification i.e., the creation of a DC field from an intense AC field [2]. Things are much more complex to higher orders, so that at third order one has the two photon absorption, the third harmonic generation, the self-focalization etc. or, through a polarization of the system that breaks the inversion symmetry, it can give rise to second order effects too as it happens in the electric field induced second harmonic (EFISH). Increasing the order of the process, the cross section is diminished and higher order effects are smaller and less intense.

The intense light induces a nonlinear response in the material on a microscopic level that in turn modifies the optical response. As a consequence, any nonlinear optical process can be described in two steps. The first step is related to the microscopic structure of the material and thus governed by the quantum mechanics, while the second step is described by Maxwell's equations in solids. The process should hence be described both at the microscopic and macroscopic level. As an example SHG has a microscopic origin but phase matching between the macroscopic fields is a necessary condition to have a detectable signal.

1.2 Second Harmonic Generation

In this thesis I will exclusively consider the second-harmonic generation (SHG) nonlinear process [1, 2, 5]. This is one of the most widely used nonlinear optical effects and one of the easiest to describe, involving only three-body interaction. The simpler picture to describe the process is to consider a three level system (see Fig.1.1). One of the two incoming photons excites an electron of the system which is promoted to an empty state. It is excited by the second photon from that level to the third one. Once it relaxes to the equilibrium ground-state (i.e., the first level), it emits an unique photon that, because of energy conservation, has twice the energy and the frequency of the original photons.

However, the steps are not independent and SHG is not a three-step process as depicted above, but a single three-body interaction that takes place in a unique step. The intermediate states can be thought as *virtual* states and they do not need to correspond to an energy level of the system. This is of course a simplification of what happens in the many-body electron system of the crystal, where all the particles are interacting and described by an unique many-body wave function. As a consequence, although it is described by the macroscopic second-order susceptibility tensor $\chi^{(2)}$, this quantity includes the many-body microscopic interactions such as the screening variations due to crystal local-fields and the electron-hole interaction. As an experimental tool, second harmonic generation has variety of applications that have developed during the last decades. The major use of the process is to double the source frequency in laser systems, obtaining an intense secondary beam at wavelength normally unavailable [6–9]. Indeed one can use existing lasers to achieve new frequencies without the design and development of new lasing media, but simply making the beam pass through a nonlinear crystal. Nowadays it is widely exploited in labo-

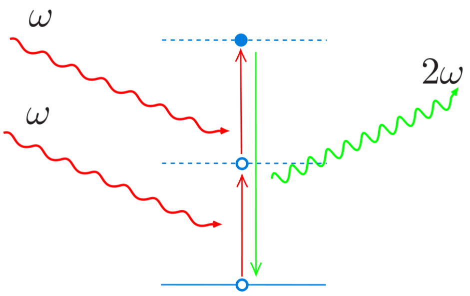

Figure 1.1: Scheme of the Second Harmonic Generation process.

ratory and there exists also the first commercial implementations of green-laser pointer. In order to have an intense outgoing signal there are some technical conditions to be fulfilled. The most important is the phase matching between the **k**-vectors of the two radiations: $\mathbf{k}(2\omega) - \mathbf{k}(\omega) = 0$. This allows to have constructive interference of the SHG beam outside the material. Moreover the medium should have a large second-order dielectric susceptibility $\chi^{(2)}$ at the desired frequency so that the signal is intense enough to be subsequently employed. These properties are material dependent and there are a lot of works devoted to the research of high-efficiency nonlinear materials [6, 10–12]. Furthermore, SHG is also interesting for the development of optoelectronic devices as frequency-doubling wave-guides [13].

The other great area of application of the SHG is its use as a probe both for spectroscopy and microscopy. Indeed, for centro-symmetric systems SHG is dipole forbidden and is consequently highly sensitive to symmetry breaking. This makes of it a selective probe for surfaces and interfaces of centro-symmetric media, where the bulk will not contribute and the frequency-doubled signal is therefore characteristic of the first few atomic layers close to the discontinuity. It allows also a time-resolved in-situ monitoring of the surface reconstruction, of its chemistry, once molecules or other adsorbates are deposited on it or can be used for measuring the surface coverage [14, 15]. Its applications range over a great variety of materials: metal surfaces, metal-electrolyte interfaces, semiconductors, oxides, insulator surfaces/interfaces etc. (see [16, 17] and Refs. therein). Also thermodynamical phase interfaces, such as liquid-liquid or liquid-air interfaces have been studied through SHG. In addition to the numerous applications of interface-SHG to the study of molecular adsorption, SHG experiments have been frequently used to determine the average orientation of molecules adsorbed at surfaces, through measurements of the polarization dependence and phase of the molecular SHG [16]. In the last decade it has affirmed as a selective non-destructive spectroscopy technique for the study of surfaces [18], superlattices [19–21] and interfaces [17, 22, 23].

Recently, second harmonic imaging microscopes (SHIM) have been employed to the study and imaging of cells and biological membranes. Light is a non-destructive probe that allows to study in-vivo biological systems in their environment [24–26]. In particular the SHG process revealed to be very efficient, in particular for collagene.

1.2.1 SHG Theoretical Description

The theoretical description of the SHG process has been addressed by scientists for several decades. It has represented indeed a difficult taks and nowadays there is a large variety of approaches that treat this nonlinear optical process at different level. In literature there are classical and semiclassical approaches or semiempirical derivations [27–34] that tries to give an accurate description of SHG, revealing useful particularly in the interpretation and analysis of experimental results. There is instead a general lack of ab initio description of the process.

Ab initio calculations, especially the ones based on Density Functional Theory (DFT), Time-Dependent Density Functional Theory (TDDFT) or Many-Body Perturbation Theory (MBPT), revealed to be useful both in the interpretation and prediction of the materials properties. In particular, a great effort has been devoted to the description of the optical response and latest results shows an excellent agreement with the experiments. Their level of accuracy and the possibility of treating from first principle (i.e., parameter free) the description of the systems, make of them a powerful spectroscopic tool with respect to semi-empirical methods. As an example, first principle calculation allows to go deep into the response of the materials, comparing the relative importance of the microscopic effects that are involved (e.g., the crystal local fields, the quasiparticle energy correction, excitonic effects, the quantum confinement etc.) with the experimental results. This permits a direct investigation of the physical nature of the system. Such a study is not always feasible in experiments where all these effects are collected and mixed in the final response. Moreover, due to the high level of accuracy obtained, nowadays ab initio calculations are used to get informations on complex systems such as DNA, proteins, superlattices, defects, nanowires, etc., or processes (from tribology to optics) that present technical difficulties for direct experimental measurements. As an example, one can study the unknown structure of the experimental sample through comparison of its measured response function with the theoretical ones obtained from a set of candidate structures (as will be shown later in chapter 6). The accuracy of ab initio calculations makes of them an ideal benchmark to predict the behavior and characteristics of new materials, guiding the design of new devices.

Due to their relevance and possibilities, it is then of great importance to improve SHG first-principle description and our knowledge of the nonlinear optical processes. The basic requirement is a comprehensive understanding of the nonlinear microscopic physical mechanisms and the corresponding macroscopic relation with physical measurable quantities. This is a formidable task and considerable difficulties have delayed accurate results for many years.

The first description of second harmonic generation based on band-structure theory was developed soon after its discovery. In 1962 Armstrong [35] and Loudon [36] gave expressions for the microscopic second harmonic susceptibility in terms of the frequency spectrum i.e., the transitions among electronic states that originate the frequency doubling. However, the theoretical results were very poor once compared with experiments. The early calculations have been restricted to the static second harmonic coefficients (i.e. at $\omega = 0$) [37, 38] and with rough approximations for the band structure evaluations. Aspnes further analyzed the formulation in 1972 [39] in terms of different gauges for the applied fields. The calculations however had to rely on empirical data. Fong and Shen [40] developed the calculations of empirical pseudopotentials showing the importance of the **k**-dependence of the matrix elements in the calculation. However, their results still underestimate the experimental value of about 2 orders of magnitude. Meanwhile, in 1987 Moss and Sipe [41] improved the technique overestimating the value by a factor of 2-4 using a semi-empirical tight-binding method, evaluating both static and frequency dependent SHG coefficients for different semiconductors. Nevertheless the spectra exhibited a lot of deficiencies. More or less in the same years appeared the first calculations on more complex systems as the Si/Ge or GaAs/AlAs superlattices [21, 42].

In the 90's, the evolution of computational methods as the Density Functional Theory allowed the first accurate ab initio calculation of second harmonic generation considering both quasi-particles effects and crystal local fields by Levine and Allan in 1991 [43–45] through the SHG description with a one-electron band theory [46]. Quasi-particle corrections were described by a scissor shift of the conduction states to better describe the quasi-particle band gap underestimated by density functional theory. Their static values were in very good agreement with the experimental results. At the same time Sipe and co-workers [41, 47] developed a formalism for the calculation of the second-order optical response of crystals in the independent particle approximations (a more recent approach has been presented by Sipe and Shkrebtii [48]), that allowed calculation of the frequency spectra [47, 49–51] and not only of the static constants. In particular Ref. [50] represents a milestone. The independent particle formulation of the SHG process they gave in the length gauge considering the optical limit is today widely used for the study of superlattices, several surface and interface systems [22, 52–60] carbon and SiC nanotubes [61–63]. They also provided the first formulation of the SHG computation including a scissor non-linear operator to recover the quasi-particle gap. An alternative formulation was given by Dal Corso *et al.* [64]. It is based on the $2n+1$ theorem. They adopted Time-Dependent Density Functional Theory and have been able to account for self-consistent local-field effects.

These calculations improve the description of the SHG, in particular because of the improvements of the DFT description of the electronic states on which the SHG derivation is based. However, the details of each approach show clearly that the second-order optical susceptibility still remains a nontrivial task, and the same accuracy obtained for linear optics has not been achieved yet.

Only few attempts tried to go beyond the independent particle picture, and quasi-particle effects have always been accounted for by the scissor operator approximation. Bechstedt and co-workers investigated the validity of this approach comparing results with the quasi-particle band structure and wave functions with the ones obtained within the scissor correction [65] Moreover, only few works exists on the inclusion of excitonic effects in $\chi^{(2)}$. Chang *et al.* [66] proposed a method where wave functions were obtained from superposition of pair excitations. Later, Leitsmann *et al.* [67] developed further this formalism using the excitonic wave functions obtained from a Bethe-Salpeter calculation to construct the many-body $\chi^{(2)}$. This approach is clearly an improvement with respect to IPA, since it includes many-body effects in the wave functions. BSE demonstrated successful for linear optics and they found a reasonable agreement with experimental data in the static limit, while in a larger energy range the comparison was not satisfactory and only a qualitative agreement was found. The question arises whether it is possible to use this approach to describe excitons for higher-energy calculations. Moreover the preliminary BSE calculation requires a great effort that demonstrates prohibitive for big-size or complex systems. Still, in this approach the crystal local field effects are only accounted for within the BSE calculation, which might be a limiting factor on the quality of the result.

These problems arise once looking to crystal structures or solid state physics, whereas accurate formalisms and schemes exist for molecular systems. There are indeed important differences between these calculations and the corresponding process in solids. In molecules, an accurate description of the DFT exchange correlation functional (e.g. going beyond LDA) gives usually accurate results. This is not the case of solids. Furthermore, whereas the ALDA TDDFT exchange-correlation kernel (the time-dependent extension of LDA) revealed to be accurate for molecules, it fails for solids optical properties already in the linear regime. It is therefore necessary to further improve the accuracy of the kernels and the ab initio description of the systems. Also the relation with the experiment is more complex in solids. Molecules indeed are microscopic and their response is usually independent and non-coherent. Consequently, a microscopic description is sufficient to model experiments. This is not the case for solids where the microscopic response (e.g. the local polarization inside the material) does not correspond directly to the macroscopic one and they should be connected via an appropriate average procedure. This is true for linear optics and much more once considering nonlinear processes. The main goal of this thesis is to advance the description of the SHG process, going beyond the standard approach for complex materials, evaluating the importance of many-body effects (crystal local fields and excitons) exploring an efficient formalism based on TDDFT[1] to make feasible large calculations normally unattainable with the methods previously presented in literature (as the BSE of [67]). This will allow me to study more in detail the origin of the SHG process and how it is related to the nature of the studied material.

The formalism, valid for any kind of classical field (longitudinal or transverse) and systems (from solids down to molecules), connect the microscopic nonlinear response to the macroscopic second-order susceptibility $\chi^{(2)}$ according to the original work of Del Sole and Fiorino [68]. I have then restricted the theory that has a general validity, to the calculation of the SHG process in the long wavelength limit $\mathbf{q} \to 0$ (see Ref [68]). In this limit, $\chi^{(2)}$ can be expressed in the TDDFT framework, but the description of the response through second-order perturbation theory allows to obtain the final response from the DFT ground state quantities accordingly to Ref. [69]. It revealed successful in a variety of systems and in particular for Si surfaces [27, 70, 71]. This IPA formalism has hence been further developed by V. Véniard [72] improving the accuracy of the response and the possibility of introducing straightforwardly many-body effects as crystal local fields and excitons in the macroscopic $\chi^{(2)}$.

Starting from previous studies on semiconductors where the formalism and the code have been successfully applied to bulk cubic materials (GaAs, AlAs, SiC [72–75]) or deformed centrosymmetric materials (strained Si [13]), I have

---

[1] For linear optics the many-body effects are considered to be well understood. Local fields in TDDFT are routinely calculated and also a connection with the MBPT Bethe-Salpeter equation, that describe excitons, has recently been established.

extended its application to the study of complex systems as the interfaces and surfaces, studying its accuracy and capabilities. This is the first time the theory and the code are applied to these kinds of systems and non-trivial problems have been encountered both of theoretical and numerical nature. Surfaces and interfaces, because of their low-dimensional structure, originate a signal that is localized in space, contrary to the bulk response. An accurate description of this transition region and its properties introduces new tasks such as the determination of its dimension and the contribution of the two materials to the total signal. Also their ratio and their thickness affects the total response as well as the interface configuration that need to be identified in according with the experimental environment [76, 77]. Moreover, simulations of interfaces and surfaces through a plane-waves DFT approach require to include vacuum into the simulation cell using a supercell method. Being the response characteristic of a small volume inside the cell, this introduces unphysical effects making the intensity dependent on the thickness of the vacuum considered. It has then been necessary to study and define an appropriate normalization procedure in order to compare different systems. Moreover, an interface system is characterized by an hard discontinuity region. Effects that demonstrated negligible in bulk materials as the crystal local fields can become relevant. Our calculations represent the first occasion to study their influence and their properties, in comparison with the independent particle response or the excitonic effects, obtaining an insight on their dependence on the nature of the system.

I have hence focused the work on the study of the Si(111)/CaF$_2$ interface. Silicon is a well known material that exhibits important optical properties. In particular the possibility of designing its electronic and optical gap through quantum confinement, makes of it a suitable material both for photovoltaic and optoelectronic devices. The combination of this material with CaF$_2$ that is a large gap insulator completely transparent in the visible and UV range has produced a complex material whose electronic and optical properties have been investigated for more than a decade [78–87].

However, these properties depends directly on the geometrical structure and in particular on the interface configuration that introduces new states into the energy gap modifying the system response. Several works have then been addressed to the study of the interface geometry [82, 88, 89], its dependency on growth conditions [76, 77, 90] and the possibilities of obtaining an epitaxial, defect free deposition. However, there was a great debate with alternative results and only the latest experiments gave an almost conclusive answer, although some discrepancies still exists. In this respect, SHG represented a great spectroscopic tool to investigate directly the interface and in 1989 Heinz *et al.* [82] studied the SHG spectra of the Si(111)/CaF$_2$ interface obtaining information about the direct transition at Γ characteristic of the interface region. This interface represents consequently a great opportunity both to test our formalism and our code and to compare the result with the experiment in which the interface structure is unknown. The eventual matching of our spectra with the experiment will also confirm the reliability of the proposed interface structure, that I have guessed in consideration of the growth conditions [76].

Si(111)/CaF$_2$ represents hence an interesting *case-study* for my purpose, allowing direct comparison with experiment, testing the accuracy of the developed theory, and permitting to go deep into the analysis of the various microscopic effects involved in the SHG process. This will allow to achieve new informations both on the microscopic nature of the SHG signal and the predictive possibilities of our description.

I will then study a new system, the Si/Ge superlattices [21, 91, 92] that demonstrated to be SHG active. These superlattices show a lot of possible applications and latest deposition techniques allow to employ these structures in more complex configurations as the multi-layers nanowires [93]. In the past some studies have been performed however, they were limited to IPA. Theoretical achievements demonstrated to fail reproducing the experiments, particularly because of differences among the experimental and theoretical configurations. The former indeed presents defects due to non-uniform molecular beam epitaxy layer deposition. For large Ge thicknesses the strain at the interface creates plane mismatch and big V-shape defects that enhance the SHG response of an order of magnitude. The analysis of this phenomenon has never been addressed before, due to the theoretical and numerical difficulties to simulate defects in materials. Thanks to the efficiency of the TDDFT formalism and the improvements of the 2light code performances, I will try to simulate these conditions. I will investigate the possibility of establishing a link between the SHG and the kind of defect present inside the structure. This work is in progress and here I will present some preliminary results.

The thesis is organized as follows: in chapter 2 I will introduce the many-body problems and the density functional theory approach to the solution and the description of the ground state properties of a system. In chapter 3 the derivation of the excitation properties of a material through TDDFT is presented, and the derivation of response function obtained within perturbation theory developed up to the second order is shown. In chapter 4 the derivation of the relation between the microscopic and macroscopic formulation of the second-order response is presented, obtaining a general expression for the macroscopic second-order susceptibility $\chi^{(2)}$ valid for any fields. This formulation is then rewritten for practical implementation for longitudinal fields in the long-wavelength limit. This allows to describe the problem using TDDFT theory. Chapter 5 briefly introduces the code 2light that implements the presented formalism, its possibilities and the different approximations that have been implemented nowadays. I will also report the major modifications that I have made in order to improve its computational efficiency and the new physical tools, as the renormalization procedure, that I introduced in order to handle the response of a cell containing vacuum. Finally, the formalism has been applied to the calculation of the SHG spectroscopy for the Si(111)/CaF$_2$ interface. The results and the detailed study of the test system are reported in chapter 6 (and detailed discussion about the renormalization problem is given in Appendix G), whereas the preliminary results of the Si/Ge superlattices are presented in chapter 7 and conclusion in chapter 8.

Chapter 2

Density Functional Theory

In the present thesis I have studied the nonlinear optical properties of solids with an *ab initio* technique. These properties are directly related to the description of the electronic states in a solid, the so-called many-body problem, that can be studied within the Density Functional Theory and the Time-Dependent Density Functional Theory formalisms. The latter, that describes the excitations of the medium, will be addressed in the following chapter. Here we focus on DFT, briefly introducing the milestones of the theory: the Hohenberg-Kohn theorems and the basic ideas to solve the problem in the Kohn-Sham scheme. Finally I will discuss some physical and numerical details.

2.1 The System of Many Interacting Electrons: the Many-Body Problem

As previously illustrated, Second Harmonic Generation and more generally the linear and nonlinear optical processes, are directly related to the electronic excitations in solids. As a consequence the knowledge of the electronic states of the system represents the key to correctly describe the physics behind these processes and determine the optical and electronic quantities of interest (e.g. the energy loss function, the optical absorption, the second harmonic generation spectrum ...). In the quantum-mechanics frame the evolution of these states is governed by the time-dependent Schrödinger equation that, for non-relativistic systems, can be written as:

$$i\hbar\frac{\partial}{\partial t}|\Psi >= \hat{H}|\Psi\rangle. \tag{2.1}$$

In solids and in a great variety of materials (in absence of any external field) $\hat{H}$ is given by the kinetic term and the Coulomb interaction of the electrons and nuclei provided that all the other interaction can be neglected:

$$\hat{H} = \sum_i -\frac{\hbar^2\nabla_i^2}{2m_e} + \sum_I -\frac{\hbar^2\nabla_I^2}{2M_I} + \frac{1}{2}\sum_{i\neq j}\frac{e^2}{|\mathbf{r}_i - \mathbf{r}_j|} - \sum_{iI}\frac{Z_I e^2}{|\mathbf{r}_i - \mathbf{R}_I|} + \frac{1}{2}\sum_{I\neq J}\frac{Z_I Z_J e^2}{|\mathbf{R}_I - \mathbf{R}_J|} \tag{2.2}$$

where the indexes (i,j) run over electrons and (I,J) run over nuclei. For the majority of the applications it is possible to reduce the complexity of this equation decoupling the electronic and nuclei motion: this is called the *Born-Oppenheimer* (BO) approximation or adiabatic approximation.

Born-Oppenheimer approximation

The Born-Oppenheimer approximation [94] is based on the observation that the nuclei have masses of 3 or more orders of magnitude larger than the electrons ($M_N \gg m_e$). This implies that their motion is slow compared with the faster electron dynamics and takes place on a different time-scale. Therefore, while solving the electronic problem, nuclear position $\mathbf{R_I}$ can be considered fixed and can be described as constant parameters. In this way the electronic problem is decoupled from the nuclear one reducing the degrees of freedom to the electronic variables only: a system of identical, indistinguishable particles. The new electronic Hamiltonian in the BO approximation is given by:

$$\hat{H}_{BO} = \sum_i -\frac{\hbar^2 \nabla_i^2}{2m_e} + \frac{1}{2}\sum_{i \neq j} \frac{e^2}{|\mathbf{r}_i - \mathbf{r}_j|} - \sum_{iI} \frac{Z_I e^2}{|\mathbf{r}_i - \mathbf{R}_I|}. \tag{2.3}$$

The first and second term are universal and independent of the system (they are respectively the kinetic energy and Coulomb interaction between the electrons), while the last one is characteristic of the studied system and contains the interaction between the electrons and the nuclei. Nevertheless, at this step the Schrödinger equation is still too complex to be solved. From now onwards we will refer to Eq. (2.3) as the Hamiltonian describing the many-body problem of Eq. (2.1), avoiding the specification of the BO label ($\hat{H} \equiv \hat{H}_{BO}$).

Approaches to the Problem

A diagonalization of the Schrödinger Eq. (2.1) would lead to a solution of the problem obtaining the energy eigenvalues and the wave functions $|\Psi\rangle$ of the system. Nevertheless, in the previous equations the wave function is contemporary functions of $3N$ variables $|\Psi(\mathbf{r}_1, ..., \mathbf{r}_N)\rangle$ that are all interconnected due to the electron-electron interaction term of Eq. (2.3). As a consequence the Schrödinger equation growths exponentially in complexity increasing N and the problem, that is not exactly solvable already for $N > 2$, cannot be handled even numerically when one deals with materials constituted of several tens of atoms. Consequently it is impossible to threat the 10^{23} particles of a macroscopic system where the degrees of freedom multiply enormously, and other paths should be explored to solve the Schrödinger equation of the system.

Several approaches exists that try to find an approximate solution of the full many-body problem: the configuration interaction and the quantum Monte-Carlo approach for example aim to describe the full many-body wave function. Nevertheless such solutions would contain informations about every single electron of the system, and such a level of detail would be hard to manage and interpret. Instead, usually one looks for the expectation values or macroscopic quantities that does not involve directly the knowledge of the exact solution of Eq. (2.1). With this consideration one can think to simplify the problem and its Hamiltonian, reducing the number of variables of the system to the ones of interest. This is in analogy with the Thermodynamic case where one describe the whole system in terms of the macroscopic average quantities, regardless of the real microscopic configuration. Between the variety of approaches that have been proposed in literature, Density Functional Theory and Time-Dependent Density Functional Theory maybe represent the prominent examples of this many-body problem simplification for treating respectively equilibrium ground-state observables or dynamical properties. Other possible approaches that will be briefly introduced later are the Many-Body Perturbation Theory and the dynamical mean-field theory.

2.2 The Density Functional Theory Approach

Density Functional Theory allows to overcome the above mentioned difficulties with the merit of being formally exact and numerically efficient for the study of the geometry and ground-state electronic properties of a great variety of materials. Thanks to this, accurate results are obtained for systems of different nature going from molecules and nanostructures, to proteins or biological matter up to solids, surfaces or interfaces.

The strength of this approach stands behind the idea of describing the entire system through the electronic density distribution, a much simpler variable with only 3 degrees of freedom with respect to the full many-body wave function. This key quantity is independent of the size of the system and therefore allows to treat structures with hundreds of atoms without increasing the amount of data to be stored in simulations as it happens in other methods based on the full many-body wave function. A possible solution of the DFT problem is then represented by the Kohn-Sham scheme. This genius approach exploits the possibility of mapping the many-body system into an easier independent-particles problem with a one-to-one correspondence that gives the same expectation value for the observables of the real ground-state system. Hence each property that depends on the ground-state configuration can be obtained solving this new simplified problem. In this section I briefly introduce DFT and the Kohn-Sham scheme that underlie all our ground-state and relaxation calculations.

2.2.1 Hohenberg-Kohn Theorems

Target of DFT is the solution of a system of N electrons in its ground-state configuration, which experiment the presence of an external, one-particle local potential v_{ext} not evolving in time. In the Born-Oppenheimer approximation this external potential is represented by the interaction with the nuclei of Eq. (2.3) that are fixed. For this stationary system Eq. (2.1) reduces to the corresponding time-independent Schrödinger equation:

$$\hat{H}|\Psi\rangle = \epsilon|\Psi\rangle \tag{2.4}$$

where $|\Psi\rangle$ represents a many-body wave function and ϵ the corresponding eigenvalue. The ground-state of the system is then identified by the particular state $|0\rangle$ of energy ϵ_0. The Hamiltonian of the N-electron system can be expressed as:

$$\hat{H} = \hat{T} + \hat{U} + \hat{V}_{ext} \quad \text{where} \quad V_{ext} = \int d\mathbf{r}\; v_{ext}(\mathbf{r})n(\mathbf{r}) \tag{2.5}$$

with T and U respectively the kinetic and the electron-electron interaction energies and V_{ext} the interaction energy with the external potential:

$$\begin{aligned} \hat{T} &= \sum_i -\frac{\hbar^2\nabla_i^2}{2m_e} \qquad \hat{U} = \frac{1}{2}\sum_{i\neq j}\frac{e^2}{|\mathbf{r}_i-\mathbf{r}_j|} \\ \hat{V}_{ext} &= -\sum_{iI}\frac{Z_I e^2}{|\mathbf{r}_i-\mathbf{R}_I|} = \int d\mathbf{r}\ v_{ext}(\mathbf{r})n(\mathbf{r}) \end{aligned} \tag{2.6}$$

As T and U have the same expression for all physical system, uniquely V_{ext} determines the particular system of interest with its Hamiltonian, wave functions, energies and all the other properties that descend from their knowledge i.e. the electron density of the system in a state $|\Psi>$:

$$n(\mathbf{r}) = N\langle\Psi(\mathbf{r}_1,...,\mathbf{r}_N)|\delta(\mathbf{r}-\mathbf{r_1})|\Psi(\mathbf{r}_1,...,\mathbf{r}_N)\rangle \tag{2.7}$$

and in particular the density $n_0(\mathbf{r})$ of the ground-state when $|\Psi\rangle = |0\rangle$. The first Hohenberg and Kohn theorem states that also the inverse assumption is valid:

Theorem 2.1. *(Hohenberg and Kohn I, 1964, Ref [95]). The ground-state density $n(\mathbf{r})$ of a system of interacting electrons subject to an external potential $v_{ext}(\mathbf{r})$ uniquely determines this potential and hence the entire physical system.*

Hence, for non-degenerate systems the Hamiltonian $H_{v_0} = T[n] + U[n] + V_0[n]$ (corresponding to the system with $v_{ext} = v_0$), its expectation value (the electronic total energy) $E_{v_0}[n] = \langle 0, [n]|H_{v_0}|0, [n]\rangle$, and any observable become unique functionals of the electron density n. This one-to-one relation holds also for the many-body wave function $|\Psi\rangle = |\Psi[n]\rangle$.

Consequently the solution of the Schrödinger equation (2.4) is now functional of n, a 3-variables quantity easier to handle with respect to the complete wave function. The possibility of finding the ground-state density that corresponds to the external potential v_0 is guaranteed by virtue of the Rayleigh-Ritz principle through the second important

Theorem 2.2. *(Hohenberg and Kohn II, 1964, Ref [95]). The energy functional $E_{v_0}[n]$ is minimized by the ground-state density n_0 that corresponds to the external potential v_0: $E_{v_0}[n] \geq E_{v_0}[n_0]$.*

Solution of $\hat{H}|0\rangle = \epsilon|0\rangle$ is then transformed to a minimization problem of $E_{v_0}[n]$ with respect to the variation of $n(\mathbf{r})$[1]. A trivial task if the energy functionals $T[n]$, $U[n]$, $V_0[n]$ were known. We should point out that the complexity of the problem is now moved into the possibility of inverting the relation between $\hat{H}$ and n (that is the determination of these functionals) or finding reasonable and suitable approximations for them.

This procedure allows to obtain directly the ground state properties of the system ($E_{v_0}[n]$, $|0\rangle$,...) and study its equilibrium. Since the Hamiltonian is functional of the ground state density, in principle all the other quantities like the

---

[1] Under the constraint of the total electron number N being fixed, that is obtained via the Lagrange multipliers method, where the parameter can be identified with the chemical potential.

excited states are achievable as functional of the density. Nevertheless, knowing the real dependence of $|\Psi\rangle$ on n would correspond to a complete knowledge of the system, i.e. the solution of the Schrödinger equation.

The most successful approach demonstrated to be the one presented by Kohn-Sham in 1965, that will be described in the following. Other approximations have been proposed e.g. by Thomas and Fermi in 1927 and can be found in literature [96–98]. In this work they substituted the electron-electron interaction U by the classical Hartree term and the kinetic energy T with a local density approximation using the one of a homogeneous electron gas. However the approach demonstrated to fail (for instance in reproducing the correct shell structure of the atoms or the chemical bonding) because $T[n]+U[n]$, that constitute the large part of the total energy, is hard to approximate.

2.3 Kohn-Sham Equations

A possibility to determine the energy functional is to refer to the one of a known simple system adapting it to the real problem. This is basically the Kohn-Sham (KS) approach, that starts from the

Definition 2.3. *(Kohn-Sham system, 1965, Ref [99]). Any system of interacting particles in the external potential v_0 can be mapped to a system of fictitious, non-interacting Kohn-Sham particles in the effective, local potential v_S such that both have the same ground-state density n_0: $H = T+U+V_0 \overset{n_0}{\longleftrightarrow} H_S = T_S+V_S$.*

Where $V_S[n] = \int d\mathbf{r}\; v_S(\mathbf{r})n(\mathbf{r})$ is a local, single-particle potential. As a consequence the Hohenberg and Kohn theorems (Ths. 2.1 and 2.2) hold also for the KS system and show that it is possible to access the real ground-state density n_0 (and all the other quantities that derive from it through theorem 2.1), via the minimization of the KS energy functional $E^{KS}[n] = T_S[n] + V_S[n]$. $T_S[n]$ is the kinetic energy for a system of N independent particles while V_S corresponds to the energy of the effective potential v_S determined as the one that makes the KS ground-state density reproduce the real system ground-state density n_0. Given v_S the Schrödinger equation for H_S reduces into a system of single-particle non-interacting Schrödinger equations:[2]

$$\left[-\frac{\nabla_\lambda^2}{2} + \int d\mathbf{r}\; v_S(\mathbf{r})n(\mathbf{r})\right]|\psi_\lambda^{KS}\rangle = \epsilon_\lambda^{KS}|\psi_\lambda^{KS}\rangle, \tag{2.8}$$

where λ labels the state. The system can be easily solved through a diagonalization, determining the single-particle wave functions $|\psi_\lambda^{KS}\rangle$ and the energy eigenvalues ϵ_λ^{KS} of the KS problem i.e., the ground state solution of both the KS and the real systems:

$$n(\mathbf{r}) = \sum_{\lambda=1}^{N} |\psi_\lambda^{KS}|^2. \tag{2.9}$$

In this way the kinetic energy functional of a system of non-interacting particles is known and given by:

$$T_S[n] = \sum_{\lambda=1}^{N} \langle\psi_\lambda^{KS}|\left(-\frac{\nabla^2}{2}\right)|\psi_\lambda^{KS}\rangle \tag{2.10}$$

---

[2] In the following I will adopt atomic units ($e = m_e = \hbar = 1$) to simplify the notation.

a much easier form with respect to the one of the real system. In order to obtain an expression for the effective potential $v_S[n]$ we can rewrite the energy functional of the interacting system $E_{v_0}[n]$ adding and subtracting $T_S[n]$ plus an Hartree energy term $V_H[n]$:[3]

$$E_{v_0}[n] = T_S[n] + V_H[n] + V_0[n] + V_{XC}[n], \tag{2.11}$$

where:

$$V_H[n] = \frac{1}{2}\iint d\mathbf{r}d\mathbf{r}'\ n(\mathbf{r})v_H(\mathbf{r},\mathbf{r}')n(\mathbf{r}), \tag{2.12}$$

$$V_{XC}[n] = T + U - V_H - T_S. \tag{2.13}$$

$v_H = \int d\mathbf{r}'\ \frac{n(\mathbf{r}')}{|\mathbf{r}-\mathbf{r}'|}$ is the functional derivative of V_H with respect to the density, while V_{XC} denotes the *exchange-correlation* energy that includes the part of the energy functional that is not explicitly known (named Stupidity energy by Feynmann [100]). Until $T_S + V_H$ is rather close to $T+U$ of the real system V_{XC} is small and can be approximated in a rough way obtaining a good description of the system. The energy functional of both systems, the interacting and the auxiliary one, takes its minimum at the same density n_0. As a consequence of the second theorem of Hohenberg and Kohn (Th. 2.2) one can apply the variational principle to both functionals (under the constraint of n being V-representable[4]) obtaining the following relation:

$$v_S(\mathbf{r},[n_0]) = v_0(\mathbf{r}) + v_H(\mathbf{r},[n_0]) + v_{XC}(\mathbf{r},[n_0]) \tag{2.14}$$

$$v_{XC}(\mathbf{r},[n_0]) = \frac{\delta V_{XC}}{\delta n(\mathbf{r})}|_{n_0}. \tag{2.15}$$

It is possible to demonstrate that v_{XC} is the local exchange correlation energy per particle, that is the electrostatic interaction energy of a particle with its DFT exchange-correlation hole n_{XC}[5] and should fulfill the sum rule:

$$\int d\mathbf{r}'\ n_{XC}(\mathbf{r},\mathbf{r}';n) = -1. \tag{2.16}$$

Eqs. (2.8) and (2.14) represent the KS equations that satisfy definition 2.3. The single-particle potential v_S now depends on the density and this set of equation has to be solved in a self-consistent procedure. Starting from a guess density $\tilde{n}$ it is possible to determine v_H and v_{XC} (i.e., v_S), and to calculate the new wave functions and density solving the single-particle Schrödinger equations (2.8). This process can be iterated until the differences between the densities at different steps vanishes or/and the energy converges to its minimum value. This is guaranteed by the second theorem of Hohenberg and Kohn (Th. 2.2).

The energy of the interacting system E_{tot} is recovered through the total

---

[3] $V_H[n]$ represents the classical electrostatic energy of interaction between the electrons.

[4] That is, to belong to the ensemble of physical potentials that have a non-degenerate ground-state. This is a not trivial constraint to be imposed while varying the density.

[5] $v_{XC}(\mathbf{r},[n]) = \int d\mathbf{r}'\ \frac{1}{2}\frac{n_{XC}(\mathbf{r},\mathbf{r}';n)}{|\mathbf{r}'-\mathbf{r}|}$.

energy E_{tot}^{KS} of the non interacting one being:

$$\begin{aligned} E_{tot}^{KS} &= \sum_{\lambda=1}^{N} \epsilon_{\lambda}^{KS} = T_S[n] + V_S[n] \\ &= T_S + \int d\mathbf{r}\ v_0(\mathbf{r}) n(\mathbf{r}) + \iint d\mathbf{r} d\mathbf{r}'\ n(\mathbf{r}) v_H(\mathbf{r},\mathbf{r}') n(\mathbf{r}) \\ &\quad + \int d\mathbf{r}\ v_{XC}(\mathbf{r}) n(\mathbf{r})|_{n=n_0} \end{aligned} \tag{2.17}$$

that substituted in Eq. (2.11) gives:

$$E_{tot}^{el} = E_{tot}^{KS} - \frac{1}{2}\int d\mathbf{r}\ v_H(\mathbf{r}) n(\mathbf{r}) + V_{XC}[n] - \int d\mathbf{r}\ v_{XC}(\mathbf{r}) n(\mathbf{r}). \tag{2.18}$$

In order to have the total energy of the entire system one should add the term due to the Coulomb nuclei interaction previously drawn out by the BO approximation.

During the years the first formulation of the HK theorems (Ths. 2.1 and 2.2) and the KS scheme have been developed reducing the theoretical constraints i.e. the possibility to apply KS-DFT to spin-polarized materials or the underlying necessity of the density being V-representable.

The latter problem has been overcome by Levy and Lieb proposing a minimization procedure with the new requirement of $n(\mathbf{r})$ being N-representable i.e., the density should correspond to an antisymmetric many-body wave function with fixed number N of electrons. This avoids the uniqueness minimum problem and allows to apply DFT to V-degenerate ground-states.

Further improvements with respect to the original Kohn-Sham work (e.g. spin inclusion) have been developed during the years and a detailed introduction can be found in [101].

2.3.1 Exchange and Correlation potential

All the previous equations have been formally exact, except for the Born-Oppenheimer approximation. However, the lack of an explicit functional for V_{XC} obliges to take it in an approximated form.[6] The majority of the calculations today are performed in the *local-density approximation* (LDA) introduced by Kohn and Sham in 1965 [99]. Similar to the Thomas-Fermi approximation, the system is locally considered as an interacting homogeneous electron gas: the density around a certain spatial point $\mathbf{r}$ is uniform and the $v_{XC}[n]$ functional reduces to a mere function ϵ_{XC}^{hom} of $n(\mathbf{r})$:

$$V_{XC}[n] = \int d\mathbf{r}\ v_{XC}(\mathbf{r},[n]) n(\mathbf{r}) \longrightarrow V_{XC}^{LDA}[n] = \int d\mathbf{r}\ \epsilon_{XC}^{hom}(n(\mathbf{r})) \tag{2.19}$$

where

$$\epsilon_{XC}^{hom} = \epsilon_{X}^{hom} + \epsilon_{C}^{hom}, \quad \text{with} \quad \epsilon_{X}^{hom} = -\frac{3}{4}\left(\frac{3}{\pi}\right)^{1/3} n^{1/3}(\mathbf{r}). \tag{2.20}$$

In this particular approximation $\epsilon_{XC}^{hom}(n)$ has an analytical solution for the exchange part (Eq. (2.20)) while exist reliable parametrizations of the correlation

---

[6] One notices that when the term is neglected the Hartree approximation is recovered.

function derived from quantum Monte-Carlo simulations of the homogeneous electron gas [102, 103]. LDA demonstrated successful in the calculation of ground-state properties of a variety of physical systems: from solids to nanostructures and even molecules where the density significantly deviates from the homogeneous assumption. Typically the lattice parameters, the bond lengths and the ground state energies are in excellent agreement with the experimental results within few percents for covalent, metallic and ionic bonds. While the same approximation works worse for weak bonding situations as Hydrogen bonds or Van der Waals forces.

However, the LDA energy functional does not cancel exactly the self-energy interaction of the Hartree term resulting in a wrong asymptotic behavior of the XC potential in finite systems.[7] There are other attempts that go beyond the LDA describing in a more accurate way the *exchange-correlation* functional. Examples are the *generalized-gradient approximation* (GGA)[8] [104], the *optimized effective potential* (OPM) [105] as the *exact-exchange* (EXX) where the exchange part is exactly treated [106], or the *hybrid functionals*[9] [107, 108].

2.3.2 Kohn-Sham Bandstructure and Bandgap

The orbitals and eigenvalues of Eq. (2.8) do not have a direct physical meaning. As they have been derived they permit uniquely to construct the real electronic density obtaining the ground-state properties. Hence, they do not give any direct access to informations about e.g. the excited states.[10] The Kohn-Sham energies ϵ_λ^{KS} and wave functions ψ_λ^{KS} of the fictitious set of independent electrons do not correspond to the ones of the real system and do not reproduce its *quasi-particle* band structure (which is measured e.g., in a photo-emission experiment). In insulators or semiconductors only the energy of the *highest occupied state* (HOMO) coincides with the exact ionization-energy of the system as shown by Janak's theorem [109].[11] Instead one can use TDDFT or Green's function formalism to study quasi-particle energies and neutral/charged excitations. Despite this, LDA-KS energies and wave functions remain a good starting point for these perturbative calculations (e.g. in GW-approximation calculations). Moreover, in a system where correlation effects are small, LDA-KS energies can be considered as a first approximation for the real quasi-particle band structure. In many cases they demonstrated capable of well reproducing the band dispersion $\epsilon_\lambda(\mathbf{k})$ of the valence and excited states, although the latter are underestimated

---

[7] It presents an exponential decay whereas it should behave as $\frac{1}{|\mathbf{r}|}$.

[8] In GGA non-local corrections are introduced threating v_{XC} as function of both the density and its gradient. In this case v_{XC} can describe also fast variations of the density, whereas in LDA are approximated as negligible.

[9] Hybrid functionals incorporate part of the exact exchange as derived from Hartree-Fock, together with XC from other sources (i.e. empirical or ab initio GW calculations). Some parameters establish the reciprocal weight of these two components.

[10] It is wrong to assert that through DFT it is *formally* not possible to know the excited states of the system. As previously stated, the external potential and all its derived quantities as the many-body wave functions $|\Psi\rangle$ are functionals of the ground-state density. In principle one can determine these functionals and $|\Psi\rangle$ corresponding to the excited states, although this demonstrates very complicated.

[11] Janak's theorem descends from the earlier Koopmans's theorem, enunciated in 1934 by Koopmans for molecules [110]. It states that in closed-shell Hartree-Fock theory, the first ionization energy of a molecular system is equal to the orbital energy of the highest occupied molecular orbital (HOMO).

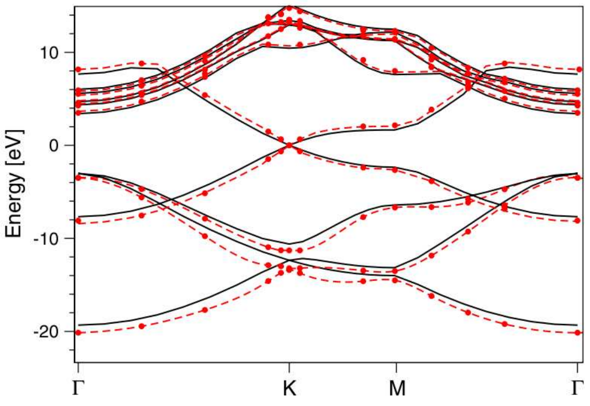

Figure 2.1: LDA-KS (black solid line) and quasi-particle (red dashed line) band structure of graphene (Reproduced from [111], Copyright ©2008 by The American Physical Society).

by an almost **k**-independent amount with respect to the experimental measurements (see Figs. (2.1) and (2.2)). This discrepancy is intrinsic of the KS formalism [112–115] depending on the properties of the adopted XC kernel. In insulating or semiconducting materials the fundamental energy gap (named also the *quasi-particle* gap) is defined as the difference between the largest addition energy and the smallest removal energy of an electron (i.e. the electron affinity $E_{tot}(N) - E_{tot}(N+1)$ and the ionization potential $E_{tot}(N-1) - E_{tot}(N)$):

$$E_{gap} = [E_{tot}(N-1) - E_{tot}(N)] - [E_{tot}(N) - E_{tot}(N+1)] \tag{2.21}$$

that corresponds to the difference between the two *HOMO* levels of the N and *N+1* particles systems. Thanks to Janak's theorem in exact DFT (or provided that v_{XC} is a good approximation for the real functional) these energies are given by the highest occupied KS states $\psi^{KS}_{(HOMO)}$:

$$E_{gap} = \epsilon^{KS}_{N+1}(N+1) - \epsilon^{KS}_{N}(N). \tag{2.22}$$

On the other hand, what one obtains within a single KS-DFT calculation with N particles are the KS-eigenvalues ϵ^{KS}_{N+1} and ϵ^{KS}_{N}[12] of the ground state density, and is immediate to recognize a discrepancy between the real and the KS band gaps [112–115]:

$$E^{KS}_{gap} = \epsilon^{KS}_{N+1}(N) - \epsilon_{N}(N) \tag{2.23}$$

$$E_{gap} - E^{KS}_{gap} = \epsilon^{KS}_{N+1}(N+1) - \epsilon^{KS}_{N+1}(N) = \Delta_{XC}. \tag{2.24}$$

The latter quantity Δ_{XC} is related to the non-analytic behavior i.e., the derivative discontinuity, of the real XC potential subjected to variation of the particles number N. This is in contrast with LDA (or other approximations as GGA) where V_{XC} is a continuous function of the electrons number. The discrepancy between the Kohn-Sham and the quasi-particle energy gap is shown in Fig. (2.3). Further details can be found in [116].

---

[12] They correspond to the energies of the lowest unoccupied state (LUMO) and the HOMO state respectively.

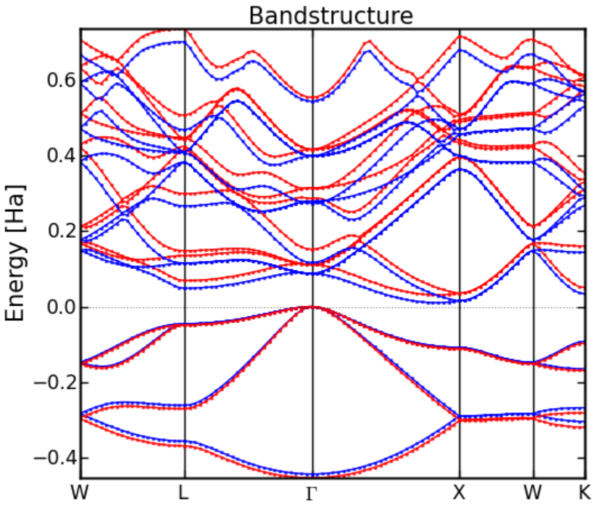

Figure 2.2: KS (blue line) and quasi-particle (red line) band structure of bulk silicon (Reproduced from `http://exciting-code.org`).

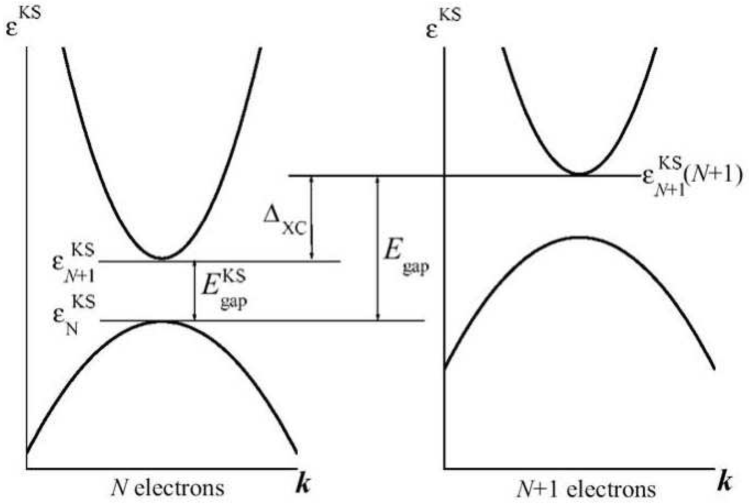

Figure 2.3: On the left: Kohn-Sham band structure (HOMO and LUMO states) of a N particles semiconductor; on the right: Kohn-Sham band structure of the $N+1$ particles system. The shift Δ_{XC} due to the addition of an electron to the conduction band is shown through the comparison of their energetic levels.

2.4 Ionic Contribution and Geometry Optimization

As stated before, the solution of the KS equations allows to obtain all the information about the N-body electronic problem. According to the BO approximation the total energy of the system is obtained through the summation of the electronic contribution and its interaction with the ionic potential (i.e., E^{el}_{tot} given by Eq (2.18)) plus the nuclei interaction:$E_{tot} = E^{el}_{tot} + E^{ion}_{int}$. The latter is the classical Coulomb interaction of point-particles for finite systems that can be obtained via the Ewald method [117] of infinite-charges summation in infinite materials like crystals. In the latter case the divergent terms of E_{tot} arising from the Coulomb long range potential mutually cancel for neutral-charge materials. However, it is always possible to impose an uniform charged background to neutralize systems with non-zero charge (as ionized molecules); this does not affect the dynamics or the physical quantities of interest as the density distribution.

Accordingly to the results obtained so far, given the nuclei position (i.e., the structure of the system) one can solve numerically the ground-state problem in the DFT framework. Unfortunately the equilibrium geometry is usually unknown. One can still use the DFT informations to find the structure that i) minimize the total energy or ii) make forces vanish. The first criterion can be easily applied to simple systems i.e. in the determination of the bond length of a bi-atomic molecule or the lattice parameters of a crystal obtained as the values that minimize the energy. Despite this, if one handles complex structures it becomes hard to consider all the degrees of freedom of the system and it is usually more convenient to move each atoms accordingly to the forces acting on it looking for the equilibrium configuration. These forces can be computed directly from the total energy:

$$\mathbf{F}_J = -\nabla_{\mathbf{R}_J} E_{tot} \tag{2.25}$$

thanks to the Hellmann-Feynman theorem [118, 119].

The total energy E_{tot} has an explicit dependence on the positions $\mathbf{R}_J$ and an implicit one through the electronic density n determined in the BO approximation Eq. (2.3). The latter dependence demonstrated unimportant since it vanishes, as shown by Slater [120], and does not contribute to $\mathbf{F}_J$. Therefore, $\nabla_{\mathbf{R}_J} E_{tot}$ reduces to the derivation of the only terms depending directly on the variables $\mathbf{R}_J$: V_0 of E^{el}_{tot} and E^{ion}_{int}. The former describes the interaction of the electrons in the nuclei (of charge Z_I) potential:

$$\begin{aligned} V_0 &= \int d\mathbf{r}\ v_0(\mathbf{r}) n(\mathbf{r}) \\ &= \int d\mathbf{r} \sum_I \frac{Z_I}{|\mathbf{r}-\mathbf{R}_I|} n(\mathbf{r}), \end{aligned} \tag{2.26}$$

giving the force:

$$\begin{aligned} \mathbf{F}^{V_0}_J &= -\nabla_{\mathbf{R}_J} V_0 \\ &= -\int d\mathbf{r}\ Z_J \frac{(\mathbf{r}-\mathbf{R}_J)}{|\mathbf{r}-\mathbf{R}_J|^3} n(\mathbf{r}). \end{aligned} \tag{2.27}$$

It coincides also with the energy of the nucleus J^{th} in the electric field generated by the electrons, according to the third principle of the dynamics.[13] The force between the nuclei instead reads:

$$\begin{aligned}\mathbf{F}^{ion}_{int\ J} &= -\nabla_{\mathbf{R}_J} E^{ion}_{int} \\ &= \sum_{I\neq J} Z_I Z_J \frac{(\mathbf{R}_I - \mathbf{R}_J)}{|\mathbf{R}_I - \mathbf{R}_J|^3},\end{aligned} \tag{2.28}$$

giving the total force acting on nucleus J^{th}:

$$\mathbf{F}_J = -\int d\mathbf{r}\ Z_J \frac{(\mathbf{r} - \mathbf{R}_J)}{|\mathbf{r} - \mathbf{R}_J|^3} n(\mathbf{r}) + \sum_{I\neq J} Z_I Z_J \frac{(\mathbf{R}_I - \mathbf{R}_J)}{|\mathbf{R}_I - \mathbf{R}_J|^3}. \tag{2.29}$$

This result is obtained considering the nuclei density $n^{ion}_J(\mathbf{r}) = Z_J\delta(\mathbf{r}-\mathbf{R}_J)$ i.e., approximating the nuclei as point-particles. When a particular distribution is employed (as in the case of the pseudopotential that will be presented later) n^{ion} can be determined from V_0 of the J^{th} atom (V_{0J}) using the Poisson equation that gives:

$$n^{ion}_J(\mathbf{r}) = -\frac{1}{4\pi}\nabla^2 V_{0J}(\mathbf{r}), \tag{2.30}$$

with a final force:[14]

$$\begin{aligned}\mathbf{F}_J = &-\iint d\mathbf{r}d\mathbf{r}'\ n^{ion}_J(\mathbf{r}')n(\mathbf{r})\frac{(\mathbf{r}-\mathbf{r}')}{|\mathbf{r}-\mathbf{r}'|^3} \\ &+ \sum_{I\neq J}\iint d\mathbf{r}d\mathbf{r}'\ n^{ion}_I(\mathbf{r})n^{ion}_J(\mathbf{r}')\frac{(\mathbf{r}-\mathbf{r}')}{|\mathbf{r}-\mathbf{r}'|^3}.\end{aligned} \tag{2.31}$$

As a consequence no further calculations are required once n_0 and $E_{tot}[n_0]$ are known. Their knowledge allows a variety of applications: structure relaxation, defect-induced deformation, surface reconstruction as well as the study of phononic-modes. Looking for the equilibrium structure it is possible to proceed through many algorithms that have been proposed in literature. All of them involve an iterative process where the electronic KS equation is solved up to self-consistency and subsequently the Hellmann-Feynman forces are evaluated from the new $E_{tot}[n_0]$. Then nuclei's positions are adjusted via different criteria that shall take into account the history of the iterations and try to optimize the convergence making it faster.

2.5 Numerical Details

The numerical calculations have been performed using a plane-waves basis set and norm-conserving pseudopotential for the description of the ions. I have used AbInit-package [121] in order to determine the ground-state structures

---

[13] Indeed Eq. (2.27) has the same expression as the Coulomb force played by the electron density n with electric field $E^{el}(\mathbf{r}) = \int d\mathbf{r}'\ n(\mathbf{r}')\frac{(\mathbf{r}'-\mathbf{r})}{|\mathbf{r}'-\mathbf{r}|^3}$ on a charge Z_J in the position $\mathbf{R}_J$.

[14] Since the distribution of a single ion is always localized avoiding overlaps among nuclei, for the Gauss theorem the second term of this equation is equal to the one of the point-particles interaction of Eq. (2.29).

and properties within DFT-LDA, and further the 2LIGHT-code [72] to calculate the linear and nonlinear optical response functions of the materials. In the following I will briefly address some numerical details and the necessary convergence tests. For a detailed introduction to the practical implementation of the DFT formalism one can refer to [121].

2.5.1 Plane-Waves Basis Set

The main task of the DFT-KS scheme is the solution of the single-particle Schrödinger equation that permits to determine $n(\mathbf{r})$. Once one refers to a crystal lattice or a periodic system, equations and wave functions are significantly simplified by means of Bloch's theorem. Moreover plane-waves become the natural basis set to represent its states:

$$|\psi_\lambda^{KS}(\mathbf{r})\rangle = |\psi_{n\mathbf{k}}(\mathbf{r})\rangle = \psi_{n\mathbf{k}}(\mathbf{r}) = u_{n\mathbf{k}}(\mathbf{r})\, e^{i\mathbf{k}\cdot\mathbf{r}} = \sum_{\mathbf{G}} c_{\mathbf{G}}(n\mathbf{k}) e^{i\mathbf{G}\cdot\mathbf{r}}\, e^{i\mathbf{k}\cdot\mathbf{r}}, \quad (2.32)$$

where λ can be identified by the band index and wave-vector $n, \mathbf{k}$. $\mathbf{k}$ is a continuous variable[15] belonging to the 1^{st} Brillouin Zone that identifies the reduced momentum of the state and $\mathbf{G}$ are the discrete reciprocal lattice vectors. The Schrödinger equation in this basis is represented by a secular equation where the new variables are the coefficients $c_{\mathbf{G}}(n\mathbf{k})$; the corresponding Hamiltonian is obtained applying $\langle e^{i\mathbf{G}'\cdot\mathbf{r}}|$ to the KS equation where $|\psi_\lambda^{KS}(\mathbf{r})\rangle$ is replaced by its Bloch's expansion (Eq. (2.32)). It is:

$$\sum_{\mathbf{G}} \hat{H}_{\mathbf{G}\mathbf{G}'}(\mathbf{k}) c_{\mathbf{G}}(n\mathbf{k}) = \epsilon_{c_{\mathbf{G}}(n\mathbf{k})} c_{\mathbf{G}}(n\mathbf{k}) \quad (2.33)$$

$$\begin{aligned}\hat{H}_{\mathbf{G}\mathbf{G}'}(\mathbf{k}) =& \frac{1}{2}|\mathbf{k}+\mathbf{G}|^2 \delta_{\mathbf{G},\mathbf{G}'} + V_{ext}(\mathbf{k}+\mathbf{G}, \mathbf{k}+\mathbf{G}') + \\ & V_H(\mathbf{G}-\mathbf{G}') + V_{XC}(\mathbf{G}-\mathbf{G}').\end{aligned} \quad (2.34)$$

This basis demonstrates to be very efficient and shows several advantages: i) plane-waves are a complete set of orthogonalized functions where the quality of the sampling can be easily improved increasing the number of considered waves. ii) Its definition is independent on the system but only depends on the simulation cell, and does not require a knowledge of the atomic orbitals involved or the atomic positions. iii) The equations are considerably simplified in the reciprocal space, in particular the differential terms as the kinetic energy or the Hartree potential (evaluated from the Poisson equation) reduce to simple products. iv) Passing through direct and Fourier space with plane-waves is also computationally efficient thanks to the Fast Fourier Transform (FFT) algorithm.

Because of these advantages it is usually convenient to treat with the same basis also systems with one or more finite dimension i.e., surfaces and nanowires or alternatively bulk solids with point defects (that lack of the correct lattice symmetry) or superlattices. For confined systems this can be done by inserting vacuum to cut the material and imposing the periodic *Born-von Karman*

---

[15] This is the case of Bloch's states where periodic boundary conditions are applied resulting in an infinite dimension material, whereas for real systems $\mathbf{k}$ is discrete and becomes continuous only in the thermodynamic limit.

boundary conditions at the edge of the simulation cell.[16] Instead, for treating defects it is usually sufficient to consider multiples of the primitive cell, so that the periodic constraint is preserved by default. The method takes the name of *supercell technique*. In both cases the size along the confined/multiple directions must be increased in order to avoid interaction among the different replica. This has to be checked through convergence tests.

Nowadays it is highly exploited since it demonstrated successful even for the simulation of small confined systems as molecules, where the states are strongly localized and there is a complete lack of periodicity. It permits also accurate calculations of systems like surfaces or multi-quantum wells where the translational invariance along one or more directions makes other kind of basis (i.e., localized basis sets) very inefficient.

As for the real space, the reciprocal coordinates determined by $\mathbf{k}$ and $\mathbf{G}$, should be finite and discrete for practical implementation. This is achieved 1) considering the plane-waves up to a certain threshold value of their modulus and 2) using a k-point grid.

1) Plane-Wave Energy Cut-off

As stated above the kinetic energy in reciprocal space assumes the simpler form:

$$-\frac{\nabla^2}{2} \rightarrow \frac{(\mathbf{k}+\mathbf{G})^2}{2}. \tag{2.35}$$

It is therefore natural to define a cut-off energy E_{cut} to truncate the infinite expansion over the $\mathbf{G}$ vectors as:

$$\frac{(\mathbf{k}+\mathbf{G})^2}{2} < E_{cut}. \tag{2.36}$$

This approximation is possible since the coefficients $c_{\mathbf{G}}(\mathbf{k}n)$ of Eq. (2.32) vanish exponentially when increasing the associated kinetic energy. As a consequence the first terms are typically the most important. Nevertheless the approximation can be systematically improved including higher spatial-frequency contributions by increasing the cut-off energy.

E_{cut} is obviously dependent on the system of interest, but additionally it reveals to be dependent on the physical quantity that one intend to study. Indeed, calculation of ground-state or formation energies need very accurate results and convergence is slow while increasing the cut-off, because every improvements in the basis will lower the total energy. At the same time relaxations, lattice parameters or molecular bond-length studies converge very quickly with respect to E_{cut} since one compares different system geometries. In these cases the variations of the total energy related to the different atomic configuration and density are always greater than the systematic error that is associated to the basis truncation.

There are other technical details related to this topic as the discontinuous increase of the numbers of the plane waves that can be found on [121].[17]

---

[16] It is not possible to describe finite systems with a finite set of plane-waves. Consequently, imposing periodic boundary conditions becomes mandatory, in analogy to what is numerically done to perform Fourier transformations of localized functions.

[17] Since we map the problem into a discrete $\mathbf{G}$ grid, increasing the sphere radius E_{cut} of

2) ***k*-point Grid**

Evaluating the quantity of interest $n(\mathbf{r})$ from the Bloch's states $|\psi_{n\mathbf{k}}(\mathbf{r})\rangle$ we should perform an integration over the vectors $\mathbf{k}$ that belong to the 1^{st} Brillouin Zone ($\Omega_{0\mathbf{k}}$):

$$n(\mathbf{r}) = \sum_n \frac{1}{\Omega_{0\mathbf{k}}} \int_{\Omega_{0\mathbf{k}}} d\mathbf{k}\ |\psi_{n\mathbf{k}}(\mathbf{r})| f(\epsilon_{n\mathbf{k}}) \tag{2.37}$$

where $f(\epsilon_{n\mathbf{k}})$ represents the occupation number of the band n at point $\mathbf{k}$. Again, it is not possible to treat numerically the continuum and the space $\Omega_{0\mathbf{k}}$ should be discretized. Wave functions are usually slowly varying in $\mathbf{k}$ and can be considered constant for two $\mathbf{k}$ points that are close together. This makes the sample of the Brillouin Zone by a discrete set of $\mathbf{k}$ points a good approximation to the integral. As for plane waves, the resulting error can be systematically reduced increasing the density of the $\mathbf{k}$-point grid.

The KS equations for a crystal (Eq. 2.33) should be solved for each sampling point $\mathbf{k}$. In order to reduce the computational effort there have been several attempts to construct representative mesh with the fewest number of points. Among these, Monkhorst-Pack [122] grids demonstrated particularly efficient: they are regular grids invariant under the point symmetries of the system. The calculation can then be restricted to points belonging to the Irreducible Brillouin Zone Ω_0^{IRR} that are symmetrically inequivalent, while the other contribute only to the weight factor $w_{\mathbf{k}}$ of the former in the summation:

$$n(\mathbf{r}) = \sum_n \sum_{\Omega_0^{IRR}} w_{\mathbf{k}} |\psi_{n\mathbf{k}}(\mathbf{r})| f(\epsilon_{n\mathbf{k}}) \tag{2.38}$$

The number of $\mathbf{k}$-points is consequently considerably decreased. The symmetry of the cell may also be used to further reduce the number of needed $\mathbf{k}$-points. Moreover, shifting the origin of the grid may improve convergence with $\mathbf{k}$-points [123].

In the following we will study only insulating and semiconducting materials at the temperature of $0\,K$. The occupations number will then restrict to the value of 1 at eigenvalue below the Fermi energy ($\epsilon_F > \epsilon_{n\mathbf{k}}$) and 0 above that level; summation of Eqs. (2.37), (2.38) is then performed only on the core and valence states.

2.5.2 Pseudopotential

Up to now we have considered all the electrons involved in the many-body problem. However, only *valence* electrons participate to chemical bonds and interactions among the atoms in a material. They are responsible of its structural and electronic properties hence should be accurately described. Until one does not move to the high energy regime also the optical processes (e.g. absorption, second harmonic generation ...) are determined entirely by the valence electrons,

---

Eq. (2.36) or varying the grid (e.g. modifying the lattice parameter) will change of a discrete amount the number of plane waves. This sudden change can affect the other quantities as the total energy, introducing discontinuities. The problem is usually avoided defining smearing and damping functions on $u_{n\mathbf{k}}(\mathbf{G})$ close to $|\mathbf{G}|$ cut-off.

whereas *core* electrons are confined in a region close to the atomic nucleus. This consideration allows to neglect their direct involvement as a variable of the many-body problem, regarding to their effects as an external contribution[18].

As stated above, core wave functions and density n_c are almost independent on the chemical environment and can be assumed to be equal to their atomic configuration (*frozen-core approximation*). Therefore they can be obtained from an all-electron calculation for a single atom, and subsequently included together with their effects in the nuclei potential they surround, forming a fixed *frozen-ion*.

The DFT calculation should then take into account only valence electrons and density n_v. Nevertheless the procedure demonstrates complex because core electrons are fermions indistinguishable from the valence ones with which they interact. Consequently one should still impose the constraint to valence wave functions to be orthogonal to the core states. In addition the XC functional $V_{XC}[n_c + n_v]$ is nonlinear and it becomes not trivial to separate the two contributions $V_{XC}[n_c] + V_{XC}[n_v]$ without introducing further approximations. This condition is fulfilled when the two densities n_c and n_v are spatially separated so that their overlap is zero and XC energy vanishes. It happens roughly when core states form a close shell, as in the materials object of this thesis (this is obviously an approximation that may lead to errors e.g., in the estimation of the total energy [124]).

The *frozen-core approximation* allows also to solve further problems related to the plane waves basis set. Indeed the ion Coulomb interaction presents a singularity at the nucleus, that is not completely removed by the screening effect of the core electrons. As a consequence their wave functions rapidly oscillate and the same is induced by orthogonality on the valence states in the core region. An accurate description of the latter would then require high-frequency plane waves with large cut-off energy.

Again, the observation of what is effectively important to describe the properties of the materials shows that chemical bounds are largely independent on the behavior of valence wave functions inside the core region. The simple idea that derives from this consideration is to replace the real KS eigenfunctions with other *pseudo*-functions that have the same chemical properties and shape outside a certain core region, while being smoother and node-free inside it. This would make the KS algorithm numerically simpler and faster, requiring a smaller number of basis plane waves. The purpose can be obtained redefining the ion-potential (given by the nucleus and the core electrons from an all-electron calculation), with a *pseudopotential* that removes completely the core orbitals from the simulation. It should confine the strong changes within a cut-off radius and eliminate the Coulomb singularity in order to soften the valence eigenfunctions. Provided that some constraints are fulfilled, as:

- the preservation of the KS energies,
- the conservation of the KS wave functions outside a sphere of cut-off radius r_c, together with their logarithmic derivative (the scattering properties) at the surface of the sphere,
- the conservation of the total density inside the sphere,[19]

---

[18] Similar to what has been done for ions within the BO approximation.

[19] This is required only for norm-conserving pseudopotential.

- the pseudopotential $\hat{V}_{ext}^{ps}$ must be a spherically symmetric hermitian linear operator,

one can fit the remaining parameters to soften the valence wave function inside a core region of radius r_c. These pseudopotentials can be substituted directly into the external potential in the KS equation.

The first attempts (in the 1960's) of constructing these screened potential where empirically designed to fit experiments. Nowadays it exists a variety of *ab initio* pseudopotential satisfying additional requirements as norm conserving, portability and the inclusion of nonlocal terms in order to correctly reproduce the different phase shift and scattering properties for each angular momentum components of the wave function [125].

Among the schemes proposed in literature, we restricted our applications to the Troullier-Martin type. Further details can be found in [126].

Chapter 3

Time Dependent Density Functional Theory

The theory based on the Runge-Gross Theorem gives the electronic density of the system as function of an external perturbing potential. Describing this variation within the linear-response formalism allows to obtain the physical response quantities of interest that are related to the experiments.

3.1 Study of the Excited States of a System

As discussed in the previous chapter DFT addresses the equilibrium ground-state properties of the system. If one desires to obtain informations on the excited states (necessary to describe e.g. photoemission spectroscopy, absorption, optical band gaps, transport etc.) the only possibility is to adopt a more efficient Hamiltonian that can describe these processes. Such an Hamiltonian cannot depend on the simple variation of density in space (as in DFT) but should depend on quantities able to describe dynamical variations of the system. There are two main approaches: i) by allowing the system to follow a time-dependent external potential and reproducing the dynamical properties of the system through its evolution; ii) via the study of the correlation functions of particles propagating through the system. The former approach is based on the Time Dependent Density Functional Theory and studies the excitations of the system by linking variations in time of the electronic density with the corresponding variations of an external acting potential. The latter approach is based on the Many-Body Perturbation Theory (MBPT). It describes the propagation of one or more particles in an interacting system through the Green's functions: these are the so-called *quasi-particles* experimentally observed. As a consequence the knowledge of the physics and the implementation of new approximations are more intuitive in MBPT.[1] On the contrary, in TDDFT as for DFT, all the unknown quantities are condensed in a unique term, the *exchange-correlation* kernel which is more difficult to treat and approximate. However it has been demonstrated that it is possible to establish a link between the two

---

[1] The advantage of MBPT methods and Green's functions is that one can systematically improve the approximations taking into account particular physical processes represented in the form of Feynman diagrams.

theories [127–130]. This makes possible to take advantage of the improvements and accuracy obtained within MBPT transferring them into the more efficient formalism of TDDFT. This is actually the method adopted in this thesis. All the results presented are obtained within TDDFT both for the linear and nonlinear optical response functions.

Time Dependent Density Functional Theory is founded on the same basic ideas that make DFT a powerful and efficient formalism to treat the ground-state properties. Generalizing the physical situation to the description of a system subjected to a *time-dependent* external perturbation, it is possible to follow its dynamics from the knowledge of its electronic density $n(\mathbf{r}, t)$ (that now depends on the time). The first calculations have been performed by Peuckert [131], Zangwill and Soven [132], but the first rigorous formal justification of the approach was provided by Runge, Gross and Kohn [133, 134] in 1984/85 and will be briefly introduced in the next paragraphs. A recent overview of the current developments in TDDFT can be found in [130, 135–137].

3.1.1 Runge-Gross Theorem

The starting point is the *time-dependent* Schrödinger equation (Eq. 2.1) in the BO approximation, where the external potential (the nucleus plus an external time-dependent perturbing scalar field) and the wave functions vary with time:

$$i\frac{\partial}{\partial t}|\Psi(t)\rangle = \hat{H}|\Psi(t)\rangle. \tag{3.1}$$

The Hamiltonian is defined as

$$\hat{H} = \hat{T} + \hat{U} + \widehat{V_{ext}}(t), \quad V_{ext}(t) = \int d\mathbf{r}\ v_{ext}(\mathbf{r}, t) n(\mathbf{r}, t), \quad |\Psi(t_0)\rangle = |\Psi_0\rangle \tag{3.2}$$

in analogy with Eq. (2.5). Runge and Gross have shown that it is possible to achieve a one-to-one connection between the time-dependent electronic density $n(\mathbf{r}, t)$ and the external potential $V_{ext}(t)$ that determines uniquely the system[2] and its eigenstates $|\Psi[n(t)] >$:

Theorem 3.1. *(Runge and Gross I, 1984, Ref [133]). The densities* $n(\mathbf{r}, t)$ *and* $n'(\mathbf{r}, t)$ *evolving from a common initial state* $|\Psi_0\rangle$ *at* t_0 *under the influence of the two Taylor expandable potentials* $v_{ext}(\mathbf{r}, t)$ *and* $v'_{ext}(\mathbf{r}, t)$ *differ, if and only if the potentials differ by more than a time-dependent constant* $v_{ext}(\mathbf{r}, t) - v'_{ext}(\mathbf{r}, t) \neq c(t)$.

As a consequence the Hamiltonian is determined by the density up to a free time-dependent function $c(t)$. This function is unknown but demonstrates irrelevant for the calculation of the observables of the system. Indeed it introduces a time-dependent phase-factor in the wave functions that cancels out when the expectation values of operators are calculated[3] $\hat{O}([n], t) = \langle\Psi([n], t)|\hat{O}|\Psi([n], t)\rangle$. Moreover any physical observable becomes functional of the time-dependent density n.

The theorem is the equivalent of the first Hohenberg and Kohn Th. 2.1; on the other hand, it is not possible to establish a counterpart of the theorem 2.2

---

[2] In analogy with DFT: $\hat{T}$ and $\hat{U}$ are the same for all the physical systems and only V_{ext} distinguish among them determining the Hamiltonian.

[3] This is true until we are not considering derivative or integral operator on time t.

based on the energy minimization. Indeed the total energy E_{tot} is no more conserved and it does not exist a minimization principle for E. One should consider instead the principle of stationary action applied to the quantum-mechanical action. This principle asserts that the equation of motion for the system i.e. the Schrödinger equation (Eq. 3.1) with solution $|\Psi(t)\rangle$ that satisfies the initial condition $|\Psi_0\rangle$ at $t = t_0$, is a stationary point of the quantum-mechanical integral action $\mathcal{A}$ defined as:[4]

$$\mathcal{A} = \int_{t_0}^{t_1} dt \; \langle\Psi(t)|i\frac{\partial}{\partial t} - H|\Psi(t)\rangle. \tag{3.3}$$

Thanks to theorem 3.1 the action is now a functional of the density too, which can be found as solution of the Euler-Lagrange equations, as stated by the

Theorem 3.2. *(Runge and Gross II, 1984, Ref [133]). For a given initial state $|\Psi_0\rangle$ at t_0, the action $A_{v_0}[n]$ becomes stationary at the density $n_0(\mathbf{r}, t)$ that corresponds to the external potential $v_0(\mathbf{r}, t)$: $[\delta\mathcal{A}_{v_0}[n]/\delta n(\mathbf{r}, t)]_{n_0} = 0$.*

Now finding the density that makes stationary the action integral means to find the solution of the system since all the other observables are derived from it accordingly to theorem 3.1.

3.1.2 Kohn-Sham Equations

Analogous to DFT, we do not have complete knowledge of the action functional $\mathcal{A}[n]$. Again, it is useful to manage with known quantities. It can be introduced a Kohn-Sham fictitious non-interacting system of N particles, that gives exactly the same density under the effect of an effective potential $v_S(\mathbf{r}, t)$, as proposed by Gross and Kohn [134]. Once the V-representability of $n(\mathbf{r}, t)$ has been provided[5] [138], for every electronic density exists a potential v_S functional of n. The application of the stationary condition to the variation of the action implies that the KS system should satisfy a set of *time-dependent Kohn-Sham equations*:

$$i\frac{\partial}{\partial t}|\psi_\lambda^{KS}(t)\rangle = \left(-\frac{\nabla^2}{2} + v_S\right)|\psi_\lambda^{KS}(t)\rangle. \tag{3.4}$$

The density n_0 solution of both the real and fictitious system is given by:

$$n(\mathbf{r}, t) = \sum_{\lambda=1}^{N} \left|\psi_\lambda^{KS}(\mathbf{r}, t)\right|^2. \tag{3.5}$$

---

[4] Definition (3.3) presents problems of causality violation since it is badly defined and lacks of the ingredients necessary to construct orbital functionals and XC functionals with memory [137]. E.g. neither the time-dependent Schrödinger equation can be recovered as stationary point of this action when the constraint of n being V-representable is applied. The problem can be overcome in the framework of Keldysh theory, declaring the variable t on the Keldysh time-contour as proposed by van Leeuven in [137, 138].

[5] The Runge-Gross theorem has been demonstrated for $v_0(t)$ expandable around t_0. Previous demonstrations required periodic $v_0(t)$ or static potentials with a small time-dependent perturbation (as in the linear response theory). Later Runge-Gross theorem has been demonstrated valid also for Laplace transformable switch-on potentials starting from the ground-state. Nowadays people believe that the theorem has a more general validity, although there is still no general proof.

One should relate the effective potential v_S to the action of the real system $\mathcal{A}_{v_0}$. Adding and subtracting the kinetic term $\mathcal{T}_S$ of the non interacting KS system and the Hartree contribution $\mathcal{A}_H$ (similar to what has been done for the DFT energy functional of Eq. (2.11)) it is possible to decompose the action as:

$$\mathcal{A}_{v_0}[n] = \mathcal{T}_S[n] + \mathcal{A}_H[n] + \mathcal{A}_0[n] + \mathcal{A}_{XC}[n]. \tag{3.6}$$

Here $\mathcal{A}_0$ indicates the part of the action integral generated by the external potential v_0, while all the unknown terms have been isolated in the exchange-correlation action $\mathcal{A}_{XC}$ defined as:

$$\mathcal{A}_{XC}[n] = \mathcal{T} + \mathcal{U} - \mathcal{T}_S - \mathcal{A}_H. \tag{3.7}$$

In this way the variational principle applied to $\mathcal{A}_{v_0}$ and $\mathcal{A}_{KS}$[6] (the action of the fictitious KS system) at the density distribution $n_0(\mathbf{r}, t)$ that is a stationary point for both the actions, allows to obtain an expression for v_S

$$v_S(\mathbf{r}, t, [n_0]) = v_0(\mathbf{r}, t) + v_H(\mathbf{r}, t, [n_0]) + v_{XC}(\mathbf{r}, t, [n_0]) \tag{3.8}$$

with the common Hartree potential (now for a time-dependent density) v_H and v_{XC} defined as:

$$v_H(\mathbf{r}, t) = \int d\mathbf{r}' \; \frac{n(\mathbf{r}', t)}{|\mathbf{r} - \mathbf{r}'|} \tag{3.9}$$

$$v_{XC}(\mathbf{r}, t) = \left[\frac{\delta \mathcal{A}_{XC}[n]}{\delta n(\mathbf{r}, t)} \right]_{n_0}. \tag{3.10}$$

The set of equations (3.4) and (3.8) here defined is a coupled system. Starting from an initial condition and an approximated expression for v_{XC} the system can be propagated substituting the new density $n(\mathbf{r}, t)$ of Eq. (3.5) into Eq. (3.8). Again, the KS wave functions do not have a direct physical meaning and are only used to construct the true density distribution of the system.

3.1.3 Exchange-Correlation Functional

The exchange-correlation potential $v_{XC}(\mathbf{r}, t)$ is generally unknown and the introduction of approximations becomes mandatory as in DFT. In TDDFT v_{XC} is much more complex than the ground state one: it is functional of the whole history of the density $n(\mathbf{r}, t)$ between $[t_0, t_1]$ as suggested by Eq. (3.3) and of the initial conditions $|\Psi_0\rangle$ and $|\psi_0^{KS}\rangle$ for the interacting and non-interacting systems[7]. The latter dependence means that it is possible to find more than one initial wave function corresponding to an assigned n_0. This would lead to different v_S for a given evolution. However, in the special case of non-degenerate ground state starting condition, the initial wave functions are functionals of the density only and the *initial-state dependence* disappears by virtue of the first

---

[6] For the non-interacting particle system $\mathcal{A}_{KS} = \mathcal{T}_S + \mathcal{A}_S$ with $\mathcal{A}_S$ the action corresponding to the effective potential v_S.

[7] Indeed the Hartree and external terms inside v_S are local in time because of the nature of the Coulomb interaction in the non-relativistic limit; the same kinetic term is instantaneous. Therefore these quantities are regardless of the initial condition or the time-evolution of the system, whose dependency is only contained in the v_{XC} term.

Hohenberg and Kohn theorem 2.1. This is the usual case for TDDFT applications.

The XC potential still remains a complex quantity, especially because of its *memory* of the past configurations of the system up to t_0, that makes it nonlocal in time and difficult to treat. Several approximations have been introduced, as the Adiabatic Local Density Approximation (ALDA) [130, 139]. It describes v_{XC} as a static kernel, local both in time and space (in analogy with LDA). The exchange-correlation functional becomes hence a mere function of the density at a fixed position and instant: $v_{XC}^{ALDA}(\mathbf{r}, t, [n]) = v_{XC}^{LDA}(n(\mathbf{r}, t))$. Although it did not obtain such good successes as its ground state counterpart, it is still widely adopted. The *independent particle*, *random phase* and the *alpha kernel* [130, 140] approximations used in this thesis will be presented more in detail later. The original work of Runge and Gross has been further developed and extended in the last years and for a complete discussion readers can refer to [137].

3.2 Time-Dependent Density Response Theory

The theory of the linear and nonlinear response function can be applied to the TDDFT in order to study the effects of a small perturbation on the system. As previously stated $n(\mathbf{r}, t)$ represents the key quantity and all the physical properties can be described in terms of the density, its variation and its response functions. Here I present its derivation up to the second perturbative order and its link with the KS independent-particles response function.

3.2.1 Response Functions

The behavior of a system under the influence of an external perturbation is called its *response*. More accurately it can be defined as the change in the expectation values of a certain operator of the system when a perturbation is applied (e.g. the total magnetization as function of an external magnetic field). Considering a small perturbation $\varphi(t)$ to the *unperturbed Hamiltonian* $\hat{H}_0$, within the interaction picture,[8] one can formally expand an observable $\hat{A}$ in orders of the interaction:

$$\begin{aligned}\hat{A}(1)[\varphi] =& \hat{A}(1)_0 + \int_{t_0}^{t_1} d2 \, \frac{\delta \hat{A}(1)}{\delta \varphi(2)} \varphi(2) + \frac{1}{2!} \int_{t_0}^{t_1} \int_{t_0}^{t_2} d2d3 \, \frac{\delta^2 \hat{A}(1)}{\delta \varphi(2) \delta \varphi(3)} \varphi(2) \varphi(3) \\ & + \dots \end{aligned} \tag{3.11}$$

where, for simplicity, we have adopted the notation $(\mathbf{r}_1, t_1) \equiv (1)$ etc. Coefficients of this expansion are the i^{th} order response functions of the system $\chi_A^{(i)}$:

$$\chi_A^{(1)}(1,2) = \frac{\delta \hat{A}(1)}{\delta \varphi(2)} \qquad \chi_A^{(2)}(1,2,3) = \frac{\delta^2 \hat{A}(1)}{\delta \varphi(2) \delta \varphi(3)}. \tag{3.12}$$

---

[8] The interaction picture is the most useful scheme in quantomechanics to study the evolution of a system subjected to the switching on of an external perturbation. The total Hamiltonian $\hat{H}$ is given by the unperturbed and the interacting ones: $\hat{H} = \hat{H}_0 + \hat{H}_I(t)$. $\hat{H}_I(t) = \hat{O}\varphi(t)$ depends on the particular coupling of the perturbation with the system (i.e. the explicit expression of the force or the interaction) as obtained through the fluctuation-dissipation theorem in Kubo's response theory [69, 141, 142].

These coefficients do not depend on the perturbing quantity in the limit $\varphi \to 0$ and correspond to the variation of the operator $\hat{A}$ with respect to the perturbation. For a physical system the causality condition holds and χ_A is function of the time interval only and not of the absolute times:

$$\chi_A^{(1)}(\mathbf{r}_1, t_1, \mathbf{r}_2, t_2) = \chi_A^{(1)}(\mathbf{r}_1, \mathbf{r}_2, t_1 - t_2) \quad t_1 > t_2, \tag{3.13}$$

with the condition $(t_1 > t_2)$. In the case of homogeneous systems also its spatial dependence $(\mathbf{r}_1, \mathbf{r}_2)$ becomes function of their distance $|\mathbf{r}_1 - \mathbf{r}_2|$. Other properties can be obtained for specific spatial symmetries or distributions, or depending on the nature of the interaction (i.e. if it is local then χ becomes local too: $\chi_A^{(1)}(\mathbf{r}_1, \mathbf{r}_2, t_1 - t_2) = \chi_A^{(1)}(\mathbf{r}_2, t_1 - t_2)\delta(\mathbf{r}_2 - \mathbf{r}_1)$).

The applied perturbation φ usually does not coincide with the *interacting Hamiltonian* $\hat{H}_I$ and Eqs. (3.12) implies the derivation of a composite function of the perturbation. Imagine this coupling is expressed through an operator $\hat{O}_I$ so that the Hamiltonian becomes:

$$\hat{H}(t) = \hat{H}_0 + \hat{H}_I(t), \qquad \text{with} \tag{3.14}$$

$$\hat{H}_I(t) = \hat{O}_I(t)\varphi(t) = \int d\mathbf{r}\ \hat{O}_I(\mathbf{r}, t)\varphi(\mathbf{r}, t). \tag{3.15}$$

As an example, in the particular case of the interaction with an external electric potential ϕ^{ext} $\hat{H}_I$ is given by:

$$\begin{gathered} \hat{H}_I(t) = \int d\mathbf{r}\ \hat{\rho}(\mathbf{r}, t)\phi^{ext}(\mathbf{r}, t), \qquad \text{with} \\ \hat{O}_I(\mathbf{r}, t) = \hat{\rho}(\mathbf{r}); \quad \varphi(\mathbf{r}, t) = \phi^{ext}(\mathbf{r}, t). \end{gathered} \tag{3.16}$$

It is then possible to derive a general form for $\chi_A^{(i)}$ depending only on the coupling $\hat{O}_I$ and the observable $\hat{A}$:

$$\chi_{AO}^{(1)}(1, 2) = -i\theta(t_1 - t_2)\langle[\hat{A}(1), \hat{O}_I(2)]\rangle, \tag{3.17}$$

$$\chi_{AOO}^{(2)}(1, 2, 3) = -\theta(t_1 - t_2)\theta(t_1 - t_3)T\langle[[\hat{A}(1), \hat{O}_I(2)], \hat{O}_I(3)]\rangle, \tag{3.18}$$

with T the *time-ordered product* of the operators. These expressions have been obtained originally by Kubo for the linear response theory [69, 141] and later generalized to higher orders [143].

3.2.2 TDDFT Linear Density Response Function

As a consequence of theorem 3.1, once solved Eq. (3.4), the true charge density and any derived quantity can be obtained. In the experimental condition of a system originally in its ground state to which is applied an external perturbing field at time t_0, the physical description can pass through the study of its density in a DFT and TDDFT calculation. At time $t < t_0$ the density n_0 and the KS wave functions $|\psi_\lambda^{KS}(t_0)\rangle$ are uniquely determined within DFT, while the evolution of the system can hence be followed in TDDFT.

Nevertheless, when the external field is small and can be considered as a perturbation to the initial Hamiltonian, it is not even necessary to solve Eq. (3.4). Accordingly to Eq. (3.12) the response of the system becomes independent on the perturbation and can be derived directly from the ground-state expectation values (by means of the fluctuation-dissipation theorem [69, 141]). In particular, for the KS independent particles system χ can be easily evaluated leading to an efficient formulation of the response (linear and nonlinear) in the TDDFT framework. Let's see the derivation for the linear case and its generalization to the second order.

Let's make the assumption of knowing the exact KS functional v_S of Eq. (3.8). Hence the density and its variation in time coincides with the exact variation of the real system $n(\mathbf{r}, t)$. As a consequence the induced variation of the density at the first order is the same whether one derives it as function of the real interacting potential or of the TD-KS one (see section 3.1.2 or [133]):

$$\begin{aligned} \delta n^{(1)}(1) &= \int d2\ \chi^{(1)}(1,2)\delta v_{ext}(2) && (3.19)\\ &= \int d2\ \chi_0^{(1)}(1,2)\delta v_S(2), && (3.20) \end{aligned}$$

where

$$\chi^{(1)}(1,2) = \frac{\delta n(1)}{\delta v_{ext}(2)} \qquad \chi_0^{(1)}(1,2) = \frac{\delta n(1)}{\delta v_S(2)}. \tag{3.21}$$

It is then possible to establish a link between the full response function χ,[9] that describes the reaction of the system to the perturbing field, and the non-interacting KS response functions χ_0. Since v_S is derived as function of v_{ext} from Eq. (3.8) one can apply the chain rule in the definition of the full polarizability obtaining:

$$\chi^{(1)}(1,2) = \frac{\delta n(1)}{\delta v_{ext}(2)} = \int d3\ \frac{\delta n(1)}{\delta v_S(3)}\frac{\delta v_S(3)}{\delta v_{ext}(2)} = \int d3\ \chi_0^{(1)}(1,3)\frac{\delta v_S(3)}{\delta v_{ext}(2)}. \tag{3.22}$$

Recalling Eq. (3.8) the derivative of the KS potential with respect to the external perturbation can be further developed as

$$\begin{aligned} \frac{\delta v_S(3)}{\delta v_{ext}(2)} &= \frac{\delta[v_{ext}(3) + v_H(3) + v_{XC}(3)]}{\delta v_{ext}(2)} \\ &= \delta(3,2) + \int d4\ \frac{\delta[v_H(3) + v_{XC}(3)]}{\delta n(4)}\frac{\delta n(4)}{\delta v_{ext}(2)} && (3.23)\\ &= \delta(3,2) + \int d4\ [v(3,4) + f_{xc}(3,4)]\chi^{(1)}(4,2), \end{aligned}$$

with v the Coulomb potential that corresponds to the functional derivative of the Hartree potential v_H. f_{xc} is the *exchange-correlation kernel* defined as the functional derivative of v_{XC}:

$$f_{xc}(1,2) = \frac{\delta v_{XC}(1)}{\delta n(2)}. \tag{3.24}$$

Substituting Eq. (3.23) into Eq. (3.22) one finds the link between the interacting and non-interacting response functions under the form of a Dyson equation:

$$\chi^{(1)}(1,2) = \chi_0^{(1)}(1,2) + \int d3d4\ \chi_0^{(1)}(1,3)[v(3,4) + f_{xc}(3,4)]\chi^{(1)}(4,2), \tag{3.25}$$

---

[9] Usually χ is called the *full polarizability.*

or, in a simplified notation without indexes:

$$\chi^{(1)} = \chi_0^{(1)} + \chi_0^{(1)}(v + f_{xc})\chi^{(1)}. \tag{3.26}$$

Equation (3.26) can be solved by inversion and is exact in the framework of the linear response theory (i.e. under the assumption of small perturbing field). Provided that v_{XC} and hence f_{xc} are known, the physical quantities of interest, as the response function χ, can be obtained directly from χ_0. Actually χ_0 has a formulation in terms of the ground state quantities only, as will be shown later. All the influence of the many-body effects are contained into f_{xc}.

The Exchange-Correlation Kernel

The importance of the kernel f_{xc} is crucial since it contains all the informations about the response and the screening internal to the medium. When the external field perturbs the system, changes are induced in the internal quantities like the Hartree potential v_H and the exchange-correlation potential v_{XC}. This corresponds to the screening of the external potential δv_{ext} due to the interaction between the electrons given by $\delta v_H + \delta v_{XC}$ in Eq. (3.23). The Hartree term accounts for their classical Coulomb interaction while the exchange-correlation term depends on their quantum nature.

The Dyson equation (3.26) incorporates directly all these self-screening effects into χ so that it could describe directly the total response of the system in terms of the external field only in Eq. (3.19). Therefore χ is much more complex than the corresponding independent particle response χ_0. This can also be seen in their different dependence on the shape of the material or their behavior for finite and infinite systems [144, 145]. It is immediate to notice that, being f_{xc} the functional derivative of v_{XC}, it is in practice unknown and suitable approximations should be found.

3.2.3 TDDFT Nonlinear Density Response Function

What has been obtained for the linear response can be further generalized to higher orders [135]. Recalling Eq. (3.12) the second order interacting and non-interacting density-susceptibilities $\chi^{(2)}$ are defined as:

$$\begin{aligned}
\chi^{(2)}(1,2,3) &= \frac{\delta^2 n(1)}{\delta v_{ext}(2)\delta v_{ext}(3)} = \frac{\delta\chi^{(1)}(1,2)}{\delta v_{ext}(3)} \\
\chi_0^{(2)}(1,2,3) &= \frac{\delta^2 n(1)}{\delta v_S(2)\delta v_S(3)} = \frac{\delta\chi_0^{(1)}(1,2)}{\delta v_S(3)}.
\end{aligned} \tag{3.27}$$

They can be interpreted as a perturbative variation of the first order responses, once the first derivative has been identified with $\chi^{(1)}/\chi_0^{(1)}$ respectively. Substituting the Dyson equation (3.25) into the first of Eqs. (3.27) and defining for simplicity $v(1,2) + f_{xc}(1,2) \equiv f_{vxc}(1,2)$, one obtains:

$$\chi^{(2)}(1,2,3) = \frac{\delta\chi_0^{(1)}(1,2)}{\delta v_{ext}(3)} + \int d4d5\ \frac{\delta[\chi_0^{(1)}(1,4)f_{vxc}(4,5)\chi^{(1)}(5,2)]}{\delta v_{ext}(3)}. \tag{3.28}$$

Retaining only the second-order variations it reduces to:

$$\begin{aligned}\chi^{(2)}(1,2,3) =&\frac{\delta\chi_0^{(1)}(1,2)}{\delta v_{ext}(3)}+\\ &\int d4d5\ \frac{\delta\chi_0^{(1)}(1,4)}{\delta v_{ext}(3)}f_{vxc}(4,5)\chi^{(1)}(5,2)+\\ &\int d4d5\ \chi_0^{(1)}(1,4)\frac{\delta f_{vxc}(4,5)}{\delta v_{ext}(3)}\chi^{(1)}(5,2)+\\ &\int d4d5\ \chi_0^{(1)}(1,4)f_{vxc}(4,5)\frac{\delta\chi^{(1)}(5,2)}{\delta v_{ext}(3)}.\end{aligned} \tag{3.29}$$

The functional derivative $\frac{\delta f_{vxc}}{\delta v_{ext}}$ in the third term of the previous summation can be reduced to the exchange-correlation part only of the kernel $\frac{\delta f_{xc}}{\delta v_{ext}}$ since v corresponds to the Coulomb potential and is independent by variations in v_{ext}. This functional derivative can be further developed considering f_{xc} function of v_{ext} through the density as:

$$\frac{\delta f_{xc}(4,5)}{\delta v_{ext}(3)} = \int d6\ \frac{\delta f_{xc}(4,5)}{\delta n(6)}\frac{\delta n(6)}{\delta v_{ext}(3)} = \int d6\ g_{xc}(4,5,6)\chi^{(1)}(6,3), \tag{3.30}$$

where g_{xc} is the second functional derivative of the exchange-correlation potential v_{XC} and contains the higher orders three-body interactions.

Again, we want to establish a relation between the interacting and non-interacting second-order response functions. Introducing the chain rule (differentiating with respect to v_S), substituting Eqs. (3.23), (3.25) and considering the definition of $\chi_0^{(2)}$ (3.27) one achieves the final result (for a detailed derivation refers to Appendix A.1):

$$\begin{aligned}\chi^{(2)}(1,2,3) =&\chi_0^{(2)}(1,2,3) + \int d4d5\ \chi_0^{(2)}(1,4,3)f_{vxc}(4,5)\chi^{(1)}(5,2)+\\ &\int d4d5\ \chi_0^{(2)}(1,2,4)f_{vxc}(4,5)\chi^{(1)}(5,3)+\\ &\int d4d5d6d7\ \chi_0^{(2)}(1,5,4)f_{vxc}(5,6)\chi^{(1)}(6,2)f_{vxc}(4,7)\chi^{(1)}(7,3)+\\ &\int d4d5d6\ \chi_0^{(1)}(1,4)g_{xc}(4,5,6)\chi^{(1)}(6,3)\chi^{(1)}(5,2)+\\ &\int d4d5\ \chi_0^{(1)}(1,4)f_{vxc}(4,5)\chi^{(2)}(5,2,3).\end{aligned} \tag{3.31}$$

This is a second-order Dyson equation. This equation has a more complex structure than the linear one, reflecting the nature of the physical process that involves electron transitions between three levels. Starting from the second-order Kohn-Sham response $\chi_0^{(2)}$, that describes it neglecting any possible interaction among the electrons (the internal screening), the Hartree and exchange-correlation interactions are added systematically by $\chi^{(1)}$, that modulates the independent particle response. This means that its is necessary to know the linear solution in order to solve the second-order Dyson equation. The repeated occurrence of $\chi^{(1)}$ indicates also that the underlying interaction is mainly of linear nature, i.e. it can be decomposed in successive two bands transitions. Only the g_{xc} kernel accounts for a real three-body interaction mixing together three electronic states (this physical insight is more intuitive when the diagrammatic representation of Feynman is adopted).

There is another way to write the previous equation expressing the interacting solution $\chi^{(2)}$ as function of the other quantities. It reveals useful for further consideration on its physical meaning and properties. Collecting the terms containing $\chi^{(2)}$ on the left and rearranging all the others on the right hand side, equation (3.31) can be rewritten in the final form:

$$\begin{aligned}\int d5 \left[\delta(1,5) - \int d4\ \chi_0^{(1)}(1,4) f_{vxc}(4,5)\right] \chi^{(2)}(5,2,3) = \\ \int d4d5\ \chi_0^{(2)}(1,5,4) \left[\delta(2,5) + \int d6\ f_{vxc}(5,6)\chi^{(1)}(6,2)\right] \cdot \\ \left[\delta(3,4) + \int d7\ f_{vxc}(4,7)\chi^{(1)}(7,2)\right] + \\ \int d4d5\ \chi_0^{(1)}(1,4) g_{xc}(4,5,6)\chi^{(1)}(6,3)\chi^{(1)}(5,2),\end{aligned} \tag{3.32}$$

or, using a compact notation as for the linear case, the expression can be simplified as:

$$\left[\hat{1} - \chi_0^{(1)} f_{vxc}\right] \chi^{(2)} = \chi_0^{(2)} \left[\hat{1} + f_{vxc}\chi^{(1)}\right] \left[\hat{1} + f_{vxc}\chi^{(1)}\right] + \chi_0^{(1)} g_{xc}\chi^{(1)}\chi^{(1)}. \tag{3.33}$$

The quantities $[\hat{1} - \chi_0^{(1)} f_{vxc}]$ and $[\hat{1} + f_{vxc}\chi^{(1)}]$ can be expressed in terms of the first order response functions only via the first order Dyson Eq.(3.26):

$$\left[\hat{1} - \chi_0^{(1)} f_{vxc}\right] = \chi_0^{(1)} \left[\chi^{(1)}\right]^{-1} \tag{3.34}$$

$$\left[\hat{1} + f_{vxc}\chi^{(1)}\right] = \left[\chi_0^{(1)}\right]^{-1} \chi^{(1)}, \tag{3.35}$$

Substituting Eq. (3.34) and (3.35) into (3.33) and multiplying by the inverse term $\chi^{(1)}[\chi_0^{(1)}]^{-1}$ on the left side of both the members of the equation, we finally achieve the solution:

$$\chi^{(2)} = \chi^{(1)} \left[\chi_0^{(1)}\right]^{-1} \chi_0^{(2)} \left[\chi_0^{(1)}\right]^{-1} \chi^{(1)} \left[\chi_0^{(1)}\right]^{-1} \chi^{(1)} + \chi^{(1)} g_{xc}\chi^{(1)}\chi^{(1)}. \tag{3.36}$$

Alternatively, one can avoid inverse quantities and express all in terms of the f_{vxc} and g_{xc} kernels:

$$\chi^{(2)} = \left[\hat{1} + \chi^{(1)} f_{vxc}\right] \chi_0^{(2)} \left[\hat{1} + f_{vxc}\chi^{(1)}\right] \left[\hat{1} + f_{vxc}\chi^{(1)}\right] + \chi^{(1)} g_{xc}\chi^{(1)}\chi^{(1)}, \tag{3.37}$$

where $\chi^{(1)}[\chi_0^{(1)}]^{-1}$ has been obtained from Eq. (3.35) multiplying for the correct inverse functions:

$$\left[\hat{1} + \chi^{(1)} f_{vxc}\right] = \chi^{(1)} \left[\chi_0^{(1)}\right]^{-1}. \tag{3.38}$$

Insight in the Nonlinear Solution

Eq. (3.37) is useful because it allows to observe the role of the internal screening on the second-order response. First lets introduce the dielectric function, defined in the linear approximation as the correlation function between the total effective potential and the external one:

$$v_{tot}(1) = \int d2\ \epsilon^{-1}(1,2) v_{ext}(2), \qquad \text{with} \quad \epsilon^{-1}(1,2) = \frac{\delta v_{tot}}{\delta v_{ext}}. \tag{3.39}$$

The inverse dielectric function ϵ^{-1} acts as a screening for the external potential and contains the many-body interaction of the material.

The total potential is given by the external perturbing one plus its interaction with the induced charge density displacement $\delta n^{(1)} = \chi^{(1)} \delta v_{ext}$ (from the definition of the density response of Eq. (3.19)). The expression of the latter interaction depends on the nature of the probe. If the probe can be considered as classical (e.g. an electromagnetic field described by photons) then $v_{tot} = v_{ext} + v_H$. One has the so-called *test-particle* (TP) case:

$$\begin{aligned} \epsilon^{-1}_{TP}(1,2) = \frac{\delta v_{tot}(1)}{\delta v_{ext}(2)} &= \delta(1,2) + \int d3\ \frac{\delta v_H(1)}{\delta n(3)} \frac{\delta n(3)}{\delta v_{ext}(2)} \\ &= \delta(1,2) + \int d3\ v(1,3) \chi^{(1)}(3,2) \\ &= 1 + v\chi^{(1)} \qquad \text{(in the compact form).} \end{aligned} \tag{3.40}$$

Otherwise, if the probe is an electron, it can test also the screening of the exchange-correlation interaction with the induced charge, described by the potential v_{XC}. Therefore the total potential $v_{tot} = v_{ext} + v_H + v_{XC}$ corresponds to the definition of v_S of Eq. (3.8). This is the case of the *test-electron* (TE) probe:

$$\epsilon^{-1}_{TE}(1,2) = \frac{\delta v_{tot}(1)}{\delta v_{ext}(2)} = \frac{\delta v_S(1)}{\delta v_{ext}(2)} \tag{3.41}$$

that has already been calculated in Eq. (3.23):

$$\begin{aligned} \epsilon^{-1}_{TE}(1,2) &= \delta(1,2) + \int d3\ \left[v(1,3) + f_{xc}\right] \chi^{(1)}(3,2) \\ &= 1 + f_{vxc}\chi^{(1)} \qquad \text{(in a compact form).} \end{aligned} \tag{3.42}$$

The screening function of the TE case is the one that occurs in the Dyson equation (3.37) that hence can be rewritten as:

$$\begin{aligned} \chi^{(2)} = &\left[\epsilon^{-1}_{TE}(2\omega)\right]^T \chi^{(2)}_0(2\omega,\omega,\omega) \epsilon^{-1}_{TE}(\omega) \epsilon^{-1}_{TE}(\omega) + \\ &\chi^{(1)}(2\omega) g_{xc}(2\omega,\omega,\omega) \chi^{(1)}(\omega) \chi^{(1)}(\omega). \end{aligned} \tag{3.43}$$

Inverting the definition in Eq. (3.41) so that $\delta v_S = \epsilon^{-1}_{TE} \delta v_{ext}$, it becomes clear that ϵ^{-1}_{TE} transforms the external perturbing potential v_{ext} into the KS potential v_S. This is exactly the role of the two terms on the right side of $\chi^{(2)}_0$. Applying an external field δv_{ext} is transformed by ϵ^{-1}_{TE} into a KS field on which can act the second-order independent particle susceptibility $\chi^{(2)}_0$.

The transposed term $[\epsilon_{TE}^{-1}]^T$ as well as the g_{xc} kernel come both from the second-order derivative of $\frac{\delta^2 v_S}{\delta v_{ext} \delta v_{ext}}$ in the derivation of $\chi^{(2)}$ and do not have any counterpart in the linear response. They can be identified as the second-order screening and the second-order three-body interaction of the process.

Chapter 4

Second Harmonic Generation

The second harmonic generation process involves the absorption of two equal photons and the emission of a third one with twice their energy due to energy conservation. This mechanism is described by the polarization of the medium, in particular by the second-order polarization when it is expanded through perturbation theory in term of the total electric field. It is possible to relate this macroscopic polarization to the microscopic one. Once it has been established that the long wavelength limit holds, the latter is derived from the nonlinear density response of TDDFT seen in the previous chapter.

Since its formulation is obtained as a function of the KS response function from the Dyson equation, we provide the derivation of the exact expression for the independent particles KS susceptibility in a periodic system using Bloch states and a plane wave basis.

4.1 Microscopic Derivation

In section 3.2, I have briefly introduced the response theory in a perturbative approach and its derivation for the density response function in TDDFT. The second harmonic process instead describes the interaction and the response of the system to an external electromagnetic radiation. Formally it can be identified with the (macroscopic) polarization of the material $\mathbf{P}_M$. This polarization can be expanded in term of the macroscopic total electric field $\mathbf{E}$:

$$\begin{aligned}\mathbf{P}_M(1) &= \mathbf{P}_M^{(1)}(1) + \mathbf{P}_M^{(2)}(1) + \mathbf{P}_M^{(3)}(1) + \dots \\ &= \chi_M^{(1)}(1,2)\mathbf{E}(2) + \chi_M^{(2)}(1,2,3)\mathbf{E}(2)\mathbf{E}(3) + \chi_M^{(3)}(1,2,3,4)\mathbf{E}(2)\mathbf{E}(3)\mathbf{E}(4) + \dots\end{aligned} \tag{4.1}$$

where $\chi_M^{(i)}$ are the optical responses being $\chi_M^{(1)}$ the linear term and the others the nonlinear ones. χ_M is called the *dielectric susceptibility* of the material. These response functions are characteristic of the observed system, therefore they should be determined from its microscopic structure within a quantum-mechanical approach.

In the following I will show that it is possible, according to Ref. [146] and [68], to determine the microscopic polarization up to the second order from the induced current, establishing a relation between the dielectric susceptibility and the TDDFT density response function.

Usually one wants to compare with spectroscopy experiments. A system in its equilibrium many-body state $|\Psi(t_0)\rangle$ is stimulated starting from a certain instant t_0 and its reaction is observed. Consequently one can think to describe the system within perturbation theory, starting from an unperturbed Hamiltonian $\hat{H}_0$ and switching on at $t = t_0$ the external field that couples with the system through an interaction Hamiltonian $\hat{H}_I$:

$$\hat{H} = \hat{H}_0 + \hat{H}_I(t). \tag{4.2}$$

This approach can be simply described in the *interaction picture*, where the wave functions and the operators are defined as:[1]

$$|\Psi^{(I)}(t)\rangle = e^{iH_0t}|\Psi^{(S)}(t)\rangle, \tag{4.3}$$

$$\hat{O}_I^{(I)} = e^{iH_0t}\hat{O}_I^{(S)}e^{-iH_0t}. \tag{4.4}$$

and in particular

$$\hat{H}_I^{(I)} = e^{iH_0t}\hat{H}_I^{(S)}e^{-iH_0t}. \tag{4.5}$$

The convenient point is that the evolution operator depends only on the known eigenvalue and eigenfunctions of the unperturbed Hamiltonian, while the Schrödinger equation and its solution become:

$$\partial_t|\Psi^{(I)}(t)\rangle = -iH_I^{(I)}(t)|\Psi^{(I)}(t)\rangle, \tag{4.6}$$

$$|\Psi^{(I)}(t)\rangle = |\Psi^{(I)}(t_0)\rangle - i\int_{t_0}^{t} dt_1\; H_I^{(I)}(t_1)|\Psi^{(I)}(t_1)\rangle. \tag{4.7}$$

Substituting iteratively Eq. (4.7) into itself[2] in the right hand side integral, one obtains the solution expressed as summation of different orders of the interaction $\hat{H}_I$. Retaining only terms up to the second order we have:[3]

$$\begin{aligned} |\Psi(t)\rangle =& |\Psi(t_0)\rangle - i\int_{t_0}^{t} dt_1\; H_I(t_1)|\Psi(t_0)\rangle \\ &+ \int_{t_0}^{t} dt_1 \int_{t_0}^{t_1} dt_2\; H_I(t_1)H_I(t_2)|\Psi(t_0)\rangle + \O(3). \end{aligned} \tag{4.8}$$

When one evaluates the expectation value of an operator $\hat{O}(t)$ (I will indicate it with the simplified notation $\langle\hat{O}\rangle = \langle\Psi(t)|\hat{O}|\Psi(t)\rangle$) adopting the solution Eq. (4.8), also $\langle\hat{O}\rangle$ is decomposed in different orders of the perturbation H_I. They can be collected and re-arranged through the Baker-Campbell-Hausdorff

---

[1] Here the superscript (I) and (S) stand respectively for the interaction and Schrödinger pictures.

[2] Equation (4.7) is a Dyson Equation for $|\Psi\rangle$, where $|\Psi(t_0)\rangle$ represents the unperturbed solution.

[3] From now on the superscript label of the interaction picture (I) will be omitted.

formula as [147]:

$$\begin{aligned}\langle\hat{O}(t)\rangle =&\langle\hat{O}(t_0)\rangle + \delta\langle\hat{O}(t)\rangle^{(1)} + \delta\langle\hat{O}(t)\rangle^{(2)} + \emptyset(3) = \\ =&\langle\hat{O}(t_0)\rangle - i\int_{t_0}^{t} dt_1\ \langle\Psi(t_0)|[\hat{O}(t),\hat{H}_I(t_1)]|\Psi(t_0)\rangle \\ &- i\int_{t_0}^{t} dt_1 \int_{t_0}^{t_1} dt_2\ \langle\Psi(t_0)|[[\hat{O}(t),\hat{H}_I(t_1)],\hat{H}_I(t_2)]|\Psi(t_0)\rangle + \emptyset(3),\end{aligned} \tag{4.9}$$

where the expression has been truncated at the second order.

Starting from this general result one can obtain the dielectric susceptibility and the polarization that arise when the system interacts with a perturbing electromagnetic field described by its scalar and vector potentials ($\phi^P, \mathbf{A}^P$). In this particular case $\hat{H}$ takes the form:[4]

$$\hat{H}(t) = \hat{H}_0\left(\hat{\mathbf{j}} - \frac{1}{c}\rho(\mathbf{r},t)\mathbf{A}^P(\mathbf{r},t)\right) + \int d\mathbf{r}\ \rho(\mathbf{r},t)\phi^P(\mathbf{r},t), \tag{4.10}$$

where $\hat{H}_0$, which is function of the current-density $\hat{H}_0(\mathbf{j})$ in the unperturbed case, now becomes function of $\mathbf{j} - \frac{1}{c}\rho(\mathbf{r},t)\mathbf{A}^P(\mathbf{r},t)$. Whereas, the *free* current-density $\hat{\mathbf{j}}$ and the density $\hat{\rho}$ of Eq. (4.10) are defined as:

$$\hat{\mathbf{j}}(\mathbf{r}) = \frac{1}{2}\left[\Psi^*\nabla\Psi - \Psi\nabla\Psi^*\right] \tag{4.11}$$

$$\hat{\rho}(\mathbf{r}) = |\Psi(\mathbf{r})|^2 \tag{4.12}$$

The *free* current-density $\mathbf{j}(\mathbf{r},t)$ has been substituted with the *total* current-density $\mathbf{j}_{tot}(\mathbf{r},t)$ (the additional induced term originates from the interaction of the electronic charge $\hat{\rho}$[5] in the presence of the vector potential $\mathbf{A}^P$):[6]

$$\hat{\mathbf{j}}_{tot} = \hat{\mathbf{j}} - \frac{1}{c}\rho(\mathbf{r},t)\mathbf{A}^P(\mathbf{r},t). \tag{4.13}$$

At the same time the electronic charge of the system in the presence of the electric potential ϕ^P gives rise to the last term of Eq. (4.10). Working on this equation it is then possible to isolate the interaction terms of the Hamiltonian H_I (I define for simplicity $\tilde{\mathbf{A}}^P = \frac{1}{c}\mathbf{A}^P$):

$$\hat{H}_I(t) = -\int d\mathbf{r}\ \hat{\mathbf{j}}(\mathbf{r})\tilde{\mathbf{A}}^P(\mathbf{r},t) + \int d\mathbf{r}\ \hat{\rho}(\mathbf{r})\phi^P(\mathbf{r},t) + \frac{1}{2}\int d\mathbf{r}\ \hat{\rho}(\mathbf{r})\left[\tilde{\mathbf{A}}^P(\mathbf{r},t)\right]^2. \tag{4.14}$$

Eq. (4.14) can be collected accordingly to the perturbative order into linear and second-order terms:

$$\begin{aligned}\hat{H}_I^{(1)}(t) &= -\int d\mathbf{r}\ \hat{\mathbf{j}}(\mathbf{r})\tilde{\mathbf{A}}^P(\mathbf{r},t) + \int d\mathbf{r}\ \hat{\rho}(\mathbf{r})\phi^P(\mathbf{r},t), \\ \hat{H}_I^{(2)}(t) &= \frac{1}{2}\int d\mathbf{r}\ \hat{\rho}(\mathbf{r})\left[\tilde{\mathbf{A}}^P(\mathbf{r},t)\right]^2.\end{aligned} \tag{4.15}$$

---

[4] I am always considering atomic units $e = m_e = \hbar = 1$.

[5] From now on the density operator will be identified as $\hat{\rho}$ and its expectation value will be $\langle\hat{\rho}\rangle = \langle\Psi|\hat{\rho}|\Psi\rangle$ instead of n. Indeed in the following $\hat{n}$ could be confused with the *operator number* that gives the occupation numbers of an electronic state and n with the band index when the explicit expression of the KS response function is derived.

[6] This derives from the substitution of the free linear momentum of the electronic system with the additional term arising from the perturbing field: $\hat{\mathbf{p}} \to \hat{\mathbf{p}} - \frac{1}{c}\int d\mathbf{r}\ \rho(\mathbf{r},t)\mathbf{A}^P(\mathbf{r},t)$. The current-density is its local form.

One can now use the results of Eq. (4.9) to obtain the corrections at each order in $(\phi^P, \mathbf{A}^P)$ given a certain operator $\hat{A}$. From Maxwell equations the microscopic polarization of the medium, the quantity of interest, is defined as:

$$\hat{\mathbf{j}}_{tot}(\mathbf{r},t) = \frac{\partial}{\partial t}\mathbf{P}(\mathbf{r},t), \tag{4.16}$$

that in frequency-space domain becomes:

$$\hat{\mathbf{j}}_{tot}(\mathbf{r},\omega) = -i\omega\mathbf{P}(\mathbf{r},\omega). \tag{4.17}$$

It is then possible to establish a direct link among the linear (and nonlinear) optical response of the system $\mathbf{P}^{(i)}$ and its microscopic current-density response functions at every order.

4.1.1 Current-Density Derivation

The total current-density because of Eq. (4.17) becomes the key quantity of the microscopic SHG process. It can be evaluated accordingly to Eq. (4.9) choosing $\hat{O} = \hat{\mathbf{j}}_{tot}$ and substituting Eq. (4.14) into Eq. (4.9):

$$\begin{aligned}\langle\hat{\mathbf{j}}_{tot}(\mathbf{r},t)\rangle =&\langle\hat{\mathbf{j}}_{tot}(\mathbf{r},t_0)\rangle - i\int_{t_0}^{t} dt_1\ \langle[\hat{\mathbf{j}}_{tot}(\mathbf{r},t),\hat{H}_I(t_1)]\rangle \\ &- \int_{t_0}^{t} dt_1 \int_{t_0}^{t_1} dt_2\ \langle[[\hat{\mathbf{j}}_{tot}(\mathbf{r},t),\hat{H}_I(t_1)],\hat{H}_I(t_2)]\rangle + \dots\ .\end{aligned} \tag{4.18}$$

The first order correction of the total current $\delta\langle\hat{\mathbf{j}}_{tot}\rangle^{(1)}$ in a simplified notation is:

$$\delta\langle\hat{\mathbf{j}}_{tot}(1)\rangle^{(1)} = -\langle\hat{\rho}(1)\rangle\tilde{\mathbf{A}}^P(1) - i\int_{t_0}^{t_1} dt_2\ \langle\Big[\hat{\mathbf{j}}(1),\hat{H}_I^{(1)}(2)\Big]\rangle, \tag{4.19}$$

where the first term comes from the zero-order (since the perturbation is already present in the definition of $\hat{\mathbf{j}}_{tot}$) and the other from the first order interaction. Further developing the terms substituting $\hat{H}_I^{(1)}$ of Eq. (4.15) one gets:[7]

$$\begin{aligned}\delta\langle\hat{\mathbf{j}}_{tot}(1)\rangle^{(1)} =& -\langle\hat{\rho}(1)\rangle\tilde{\mathbf{A}}^P(1) + i\int d\mathbf{r}_2\int_{t_0}^{t_1} dt_2\ \langle\Big[\hat{\mathbf{j}}(1),\hat{\mathbf{j}}(2)\Big]\rangle\tilde{\mathbf{A}}^P(2) \\ &- i\int d\mathbf{r}_2\int_{t_0}^{t_1} dt_2\ \langle\Big[\hat{\mathbf{j}}(1),\hat{\rho}(2)\Big]\rangle\phi^P(2).\end{aligned} \tag{4.20}$$

These terms can be identified according to Eqs. (3.11) and (3.12) as the first order response functions of the system. In order to find an expression that is consistent with our definition of Eq. (3.17), let's introduce the *step function* $(\int_{t_0}^{t_1} dt_2 = \int_{t_0}^{\infty} dt_2\ \theta(t_1 - t_2))$:

$$\begin{aligned}\delta\langle\hat{\mathbf{j}}_{tot}(1)\rangle^{(1)} =& -\langle\hat{\rho}(1)\rangle\tilde{\mathbf{A}}^P(1) + i\int d\mathbf{r}_2\int_{t_0}^{\infty} dt_2\ \theta(t_1-t_2)\langle\Big[\hat{\mathbf{j}}(1),\hat{\mathbf{j}}(2)\Big]\rangle\tilde{\mathbf{A}}^P(2) \\ &- i\int d\mathbf{r}_2\int_{t_0}^{\infty} dt_2\ \theta(t_1-t_2)\langle\Big[\hat{\mathbf{j}}(1),\hat{\rho}(2)\Big]\rangle\phi^P(2).\end{aligned} \tag{4.21}$$

---

[7] Since I have adopted the simplified notation $(\mathbf{r}_1,t_1) = (1)$ I represent the integrals $\iint d\mathbf{r}_1 dt_1$ as $\int d1$, making explicit the extremes if necessary. When the integration is performed upon only one of the variables $\mathbf{r}$ or t, I will use $\int d\mathbf{r}_1$ or alternatively $\int dt_1$.

It is now immediate to identify the response functions $\chi^{(1)}_{\mathbf{jj}}$ and $\chi^{(1)}_{\mathbf{j}\rho}$ in the form of Eq. (3.17):

$$\begin{aligned}\delta\langle\hat{\mathbf{j}}_{tot}(1)\rangle^{(1)} =& -\langle\hat{\rho}(1)\rangle\tilde{\mathbf{A}}^P(1) - \int d\mathbf{r}_2 \int_{t_0}^{\infty} dt_2\ \chi^{(1)}_{\mathbf{jj}}(1,2)\tilde{\mathbf{A}}^P(2)\\ &+ \int d\mathbf{r}_2 \int_{t_0}^{\infty} dt_2\ \chi^{(1)}_{\mathbf{j}\rho}(1,2)\phi^P(2).\end{aligned} \tag{4.22}$$

Time-Fourier transforming these quantities in the frequency space (choosing the arbitrary variable $t_0 = -\infty$, see App. B for the conventions adopted for Fourier transforms) it takes the form:

$$\begin{aligned}\delta\langle\hat{\mathbf{j}}_{tot}(\mathbf{r}_1,\omega)\rangle^{(1)} =& -\langle\hat{\rho}(\mathbf{r}_1)\rangle\tilde{\mathbf{A}}^P(\mathbf{r}_1,\omega) - \int d\mathbf{r}_2\ \chi^{(1)}_{\mathbf{jj}}(\mathbf{r}_1,\mathbf{r}_2,\omega)\tilde{\mathbf{A}}^P(\mathbf{r}_2,\omega)\\ &+ \int d\mathbf{r}_2\ \chi^{(1)}_{\mathbf{j}\rho}(\mathbf{r}_1,\mathbf{r}_2,\omega)\phi^P(\mathbf{r}_2,\omega).\end{aligned} \tag{4.23}$$

This expression can be further modified using gauge invariance (see [146] and appendix D for the complete derivation) and one gets:

$$\delta\langle\hat{\mathbf{j}}_{tot}(\mathbf{r}_1,\omega)\rangle^{(1)} = \frac{i}{\omega}\langle\hat{\rho}(\mathbf{r}_1)\rangle\mathbf{E}^P(\mathbf{r}_1,\omega) + \frac{i}{\omega}\int d\mathbf{r}_2\ \chi^{(1)}_{\mathbf{jj}}(\mathbf{r}_1,\mathbf{r}_2,\omega)\mathbf{E}^P(\mathbf{r}_2,\omega), \tag{4.24}$$

where the electric perturbing field $\mathbf{E}^P$ determined by the external potentials $(\phi^P, \mathbf{A}^P)$ is defined as:

$$\begin{aligned}\mathbf{E}^P(\mathbf{r},t) &= -\nabla\phi^P(\mathbf{r},t) - \frac{1}{c}\frac{\partial}{\partial t}\mathbf{A}^P(\mathbf{r},t)\\ \mathbf{E}^P(\mathbf{r},\omega) &= -\nabla_{\mathbf{r}}\phi^P(\mathbf{r},\omega) + \frac{i\omega}{c}\mathbf{A}^P(\mathbf{r},\omega).\end{aligned} \tag{4.25}$$

Defining the *quasi-susceptibility*[8] $\tilde{\alpha}^{(1)}$ as:

$$\tilde{\alpha}^{(1)}(\mathbf{r}_1,\mathbf{r}_2,\omega) \equiv \frac{1}{\omega^2}\left[-\chi_{\mathbf{jj}}(\mathbf{r}_1,\mathbf{r}_2,\omega) - \langle\hat{\rho}(\mathbf{r}_2)\rangle\delta(\mathbf{r}_1-\mathbf{r}_2)\right], \tag{4.26}$$

Eq. (4.24) can be rewritten as:

$$\delta\langle\hat{\mathbf{j}}_{tot}(\mathbf{r}_1,\omega)\rangle^{(1)} = -i\omega\int d\mathbf{r}_2\ \tilde{\alpha}^{(1)}(\mathbf{r}_1,\mathbf{r}_2,\omega)\mathbf{E}^P(\mathbf{r}_2,\omega), \tag{4.27}$$

The linear correction to the polarization $\mathbf{P}^{(1)}$ is then given in real and reciprocal space by:[9]

$$\mathbf{P}^{(1)}(\mathbf{r}_1,\omega) = \int d\mathbf{r}_2\ \tilde{\alpha}^{(1)}(\mathbf{r}_1,\mathbf{r}_2,\omega)\mathbf{E}^P(\mathbf{r}_2,\omega), \tag{4.28}$$

$$\mathbf{P}^{(1)}(\mathbf{q}_1+\mathbf{G}_1,\omega) = \sum_{\mathbf{G}_2}\ \tilde{\alpha}^{(1)}(\mathbf{q}_1+\mathbf{G}_1,\mathbf{q}_1+\mathbf{G}_2,\omega)\mathbf{E}^P(\mathbf{q}_1+\mathbf{G}_2,\omega). \tag{4.29}$$

---

[8] It is called quasi-susceptibility or quasi-polarizability because it is related to the perturbing field $\mathbf{E}^P$. The *polarizability* is the one related to the total field $\mathbf{E}$.

[9] For the reciprocal space the expression is obtained through a Fourier transform over the spatial variable $\mathbf{r}$ considering a periodic medium. This is the case of crystal lattices but the assumption can be extended also to non periodic systems as presented in section 2.5.1, where constructing a supercell allows to impose boundary conditions for the usage of a plane waves basis set.

The same calculation can be performed for the second-order current-density (which is linked to $\mathbf{P}^{(2)}$). Collecting all the second-order terms of Eq. (4.18) and recognizing the response functions of Eq. (3.18), one obtains the final form:

$$\begin{aligned}
&\delta\langle\hat{\mathbf{j}}_{tot}(1)\rangle^{(2)} = -\frac{1}{2}\int d2\ \chi^{(1)}_{\mathbf{j}\rho}(1,2)\left[\tilde{\mathbf{A}}^{P}(2)\right]^{2}\\
&+\int d2\ \left[\chi^{(1)}_{\rho\mathbf{j}}(1,2)\tilde{\mathbf{A}}^{P}(1)\tilde{\mathbf{A}}^{P}(2)-\chi^{(1)}_{\rho\rho}(1,2)\tilde{\mathbf{A}}^{P}(1)\phi^{P}(2)\right]\\
&+\frac{1}{2}\iint d2d3\ \left[\chi^{(2)}_{\mathbf{jjj}}(1,2,3)\tilde{\mathbf{A}}^{P}(2)\tilde{\mathbf{A}}^{P}(3)+\chi^{(2)}_{\mathbf{j}\rho\rho}(1,2,3)\phi^{P}(2)\phi^{P}(3)\right]\\
&-\frac{1}{2}\iint d2d3\ \left[\chi^{(2)}_{\mathbf{jj}\rho}(1,2,3)\tilde{\mathbf{A}}^{P}(2)\phi^{P}(3)+\chi^{(2)}_{\mathbf{j}\rho\mathbf{j}}(1,2,3)\phi^{P}(2)\tilde{\mathbf{A}}^{P}(3)\right].
\end{aligned}\tag{4.30}$$

Using the same kind of argument, through gauge invariance relations (see Appendix D for a complete derivation) one gets:

$$\begin{aligned}
&\delta\langle\hat{\mathbf{j}}_{tot}(\mathbf{r},\omega_1)\rangle^{(2)} = -\iint d\mathbf{r}_2 d\mathbf{r}_3 \iint d\omega_2 d\omega_3\ \delta(\omega_1-\omega_2-\omega_3)\\
&\frac{1}{\omega_2\omega_3}\mathbf{E}^{P}(\mathbf{r}_2,\omega_2)\mathbf{E}^{P}(\mathbf{r}_3,\omega_3)\left[-\frac{1}{2}\chi^{(2)}_{\mathbf{jjj}}(\mathbf{r}_1,\mathbf{r}_2,\mathbf{r}_3,\omega_2,\omega_3)-\right.\\
&\left.\chi^{(1)}_{\rho\mathbf{j}}(\mathbf{r}_1,\mathbf{r}_2,\omega_2)\delta(\mathbf{r}_1-\mathbf{r}_3)-\frac{1}{2}\chi^{(1)}_{\mathbf{j}\rho}(\mathbf{r}_1,\mathbf{r}_2,\omega_2+\omega_3)\delta(\mathbf{r}_2-\mathbf{r}_3)\right].
\end{aligned}\tag{4.31}$$

Now one has a direct link between $\mathbf{P}^{(2)}$ and $\mathbf{E}^{P}$, that can be expressed through the *second-order quasi-susceptibility* $\tilde{\alpha}^{(2)}$ as:

$$\begin{aligned}
\mathbf{P}^{(2)}(\mathbf{r_1},\omega_\mathbf{1}) = \iint d\mathbf{r}_2 d\mathbf{r}_3 \iint d\omega_2 d\omega_3\ \delta(\omega_1-\omega_2-\omega_3)\\
\tilde{\alpha}^{(2)}(\mathbf{r}_1,\mathbf{r}_2,\mathbf{r}_3,\omega_2,\omega_3)\mathbf{E}^{P}(\mathbf{r}_2,\omega_2)\mathbf{E}^{P}(\mathbf{r}_3,\omega_3)
\end{aligned}\tag{4.32}$$

where $\tilde{\alpha}^{(2)}$ has been defined from Eq. (4.31) as

$$\begin{aligned}
&\tilde{\alpha}^{(2)}(\mathbf{r}_1,\mathbf{r}_2,\mathbf{r}_3,\omega_2,\omega_3) = -\frac{i}{\omega_2\omega_3(\omega_2+\omega_3)}\left[\frac{1}{2}\chi^{(2)}_{\mathbf{jjj}}(\mathbf{r}_1,\mathbf{r}_2,\mathbf{r}_3,\omega_2,\omega_3)+\right.\\
&\left.+\chi^{(1)}_{\rho\mathbf{j}}(\mathbf{r}_1,\mathbf{r}_2,\omega_2)\delta(\mathbf{r}_1-\mathbf{r}_3)+\frac{1}{2}\chi^{(1)}_{\mathbf{j}\rho}(\mathbf{r}_1,\mathbf{r}_2,\omega_2+\omega_3)\delta(\mathbf{r}_2-\mathbf{r}_3)\right].
\end{aligned}\tag{4.33}$$

In the momentum space Eq. (4.32) becomes:

$$\begin{aligned}
&\mathbf{P}^{(2)}(\mathbf{q}_1+\mathbf{G}_1,\omega_1) =\\
&\sum_{\mathbf{q}_2\mathbf{G}_2}\sum_{\mathbf{G}_3}\int d\omega_2\ \tilde{\alpha}^{(2)}(\mathbf{q}_1+\mathbf{G}_1,\mathbf{q}_2+\mathbf{G}_2,\mathbf{q}_1-\mathbf{q}_2+\mathbf{G}_3,\omega_2,\omega_1-\omega_2)\\
&\mathbf{E}^{P}(\mathbf{q}_2+\mathbf{G}_2,\omega_2)\mathbf{E}^{P}(\mathbf{q}_1-\mathbf{q}_2+\mathbf{G}_3,\omega_1-\omega_2).
\end{aligned}\tag{4.34}$$

4.2 Longitudinal Perturbation

As I have shown in the previous derivations, the current-density variation allows to get the complete knowledge of the polarization of a medium at each perturbative order. Although it exists an ab-initio formalism that describes the system in terms of the current, the Time Dependent Current-Density Functional Theory (TDCDFT), so far it has proved to be premature for practical application on ab-initio optical calculations. TDCDFT indeed, has not yet reached a level of development comparable to the TDDFT. Calculation methods and algorithms are still improving and, more important, the development of approximated forms for the f_{xc} kernel that goes beyond the LDA nowadays represents an open task. Because of these reasons, one may want to rely on well established TDDFT, which demonstrated to be efficient especially treating an perturbing field in a perturbative approach (see section 3.2).

In this perspective it is possible to pass from the current-density to the density through the continuity equation

$$\nabla_{\mathbf{r}}\hat{\mathbf{j}}(\mathbf{r},t) = \partial_t \hat{\rho}(\mathbf{r},t), \tag{4.35}$$

that shows a correlation between the two quantities. This differential equation takes a useful linear expression in the space of frequencies and reciprocal vectors:

$$\mathbf{q}\cdot\hat{\mathbf{j}}(\mathbf{q},\omega) = i\omega\hat{\rho}(\mathbf{q},\omega) \tag{4.36}$$

that holds at each order:

$$\mathbf{q}\cdot\delta\langle\hat{\mathbf{j}}(\mathbf{q},\omega)\rangle^{(i)} = i\omega\delta\langle\hat{\rho}(\mathbf{q},\omega)\rangle^{(i)}. \tag{4.37}$$

This equation establish a direct link between the density $\hat{\rho}$ and the current $\hat{\mathbf{j}}$. More precisely, it is the longitudinal component of the induced current $\mathbf{q}\cdot\hat{\mathbf{j}}$ that is proportional to the density. It is a general condition and shows how TDDFT and theories that describe the system in terms of the density only cannot manage in principle transverse electromagnetic perturbations. However, under the constraint that the perturbing field is longitudinal this correspondence permits to describe the longitudinal component of $\hat{\mathbf{j}}$ and hence $\mathbf{P}$ in terms of the density response functions only. It represents a good approximation for SHG even if the external electromagnetic field is not longitudinal, since for optical excitations in the visible range, one can assume that the system undergoes only *vertical transitions* $\mathbf{q} = 0$.[10] This can be easily seen in the real space considering that the typical wavelength λ of a photon in the visible range is around $10^3 - 10^4$ Å. Hence the long wavelength limit ($\lambda \to \infty$) with respect to the characteristic dimension of the system (i.e., the lattice parameter) holds and the field is seen by the system as constant. Therefore it can be locally approximated as uniform. In this case it does not have any meaning distinguishing between longitudinal and transverse perturbations [148], since $|\mathbf{q}| \simeq 0$ and no propagation direction is defined. The problem can therefore be treated in the hypothesis of longitudinal field without loss of generality. However, $\hat{\mathbf{q}}$ will describe the polarization of the electromagnetic field that is still defined. Under this assumption TDDFT can be applied rigorously to every perturbation. From now on I will always consider the limit $\mathbf{q} \to 0$ in all the demonstrations and calculations.

4.2.1 Density Derivation

Because of the continuity equation the important quantities are now the linear and nonlinear response functions of the density, that can be obtained with an

---

[10] Photons are massless particles. Their wavenumber $\mathbf{k}$ is proportional to the frequency $k = \frac{2\pi}{\lambda}$ and for frequency around the visible range the exchanged vector with the system is $\mathbf{k} \sim 10^{-3}$ Å $^{-1}$ and can be neglected.

approach similar to that used for the current. The first order density correction $\delta\langle\hat{\rho}_{tot}(1)\rangle^{(1)}$ derived developing Eq. (4.9) is:

$$\delta\langle\hat{\rho}_{tot}(1)\rangle^{(1)} = -\int d2\ \chi^{(1)}_{\rho\mathbf{j}}(1,2)\tilde{\mathbf{A}}^P(2) + \int d2\ \chi^{(1)}_{\rho\rho}(1,2)\phi^P(2). \tag{4.38}$$

With the same kind of calculation as for the current, expressing $\delta\langle\hat{\rho}_{tot}(1)\rangle^{(1)}$ as function of the electric field $\mathbf{E}^P$ in the frequencies and reciprocal spaces one has [146]:

$$\begin{aligned}\delta\langle\hat{\rho}_{tot}(\mathbf{r}_1,\omega)\rangle^{(1)} =& \frac{i}{\omega}\int d\mathbf{r}_2\ \chi^{(1)}_{\rho\mathbf{j}}(\mathbf{r}_1,\mathbf{r}_2,\omega)\mathbf{E}^P(\mathbf{r}_2,\omega),\\ \delta\langle\hat{\rho}_{tot}(\mathbf{q}_1+\mathbf{G}_1,\omega)\rangle^{(1)} =& \frac{i}{\omega}\sum_{\mathbf{G}_2}\chi^{(1)}_{\rho\mathbf{j}}(\mathbf{q}_1+\mathbf{G}_1,\mathbf{q}_1+\mathbf{G}_2,\omega)\mathbf{E}^P(\mathbf{q}_1+\mathbf{G}_2,\omega).\end{aligned} \tag{4.39}$$

In the case of the density it is interesting to notice that for neutral excitations, e.g. the absorption of one or more photon without emission of any electron (this is the case we are interested in), the total charge is conserved. Therefore, the overall variation of the density $\int d\mathbf{r}\delta\langle\rho(\mathbf{r})\rangle$ has to be zero for each perturbative order, in particular from Eq. (4.39):

$$\int d\mathbf{r}_1\ \delta\langle\hat{\rho}_{tot}(\mathbf{r}_1,\omega)\rangle^{(1)} = \int d\mathbf{r}_1\int d\mathbf{r}_2\ \chi^{(1)}_{\rho\mathbf{j}}(\mathbf{r}_1,\mathbf{r}_2,\omega)\mathbf{E}^P(\mathbf{r}_2,\omega) = 0 \tag{4.40}$$

Because this holds in general, independently on the applied perturbation $\mathbf{E}^P$ acting in a generic point $\mathbf{r}_2$, it means that the other term should be identically zero:

$$\begin{aligned}\int d\mathbf{r}_1\ \chi^{(1)}_{\rho\mathbf{j}}(\mathbf{r}_1,\mathbf{r}_2,\omega) = 0 \qquad & \forall\mathbf{r}_2\\ \chi^{(1)}_{\rho\mathbf{j}}(0,\mathbf{G}_2,\omega) = 0 \qquad & \forall\mathbf{G}_2.\end{aligned} \tag{4.41}$$

The last equation shows that $\chi^{(1)}_{\rho\mathbf{j}}$ vanish because of charge conservation in neutral excitations.

The second-order density correction instead reads:

$$\begin{aligned}\delta\langle\hat{\rho}_{tot}(1)\rangle^{(2)} =& -\frac{1}{2}\int d2\ \chi^{(1)}_{\rho\rho}(1,2)[\tilde{\mathbf{A}}^P(2)]^2\\ &+\frac{1}{2}\iint d2d3\ \left[\chi^{(1)}_{\rho\mathbf{jj}}(1,2,3)\tilde{\mathbf{A}}^P(2)\tilde{\mathbf{A}}^P(3) - \chi^{(1)}_{\rho\mathbf{j}\rho}(1,2,3)\tilde{\mathbf{A}}^P(2)\phi^P(3)\right]\\ &+\frac{1}{2}\iint d2d3\ \left[\chi^{(2)}_{\rho\rho\rho}(1,2,3)\phi^P(2)\phi^P(3) - \chi^{(1)}_{\rho\rho\mathbf{j}}(1,2,3)\phi^P(3)\tilde{\mathbf{A}}^P(2)\right].\end{aligned} \tag{4.42}$$

Using gauge invariance and expressing $\delta\langle\hat{\rho}_{tot}\rangle^{(2)}$ as function of $\mathbf{E}^P$, Eq. (4.42) can be rewritten in a form that will be useful in the following (see App. D.3):

$$\delta\langle\hat{\rho}_{tot}(1)\rangle^{(2)} = \frac{1}{2}\int d2d3\ \chi^{(2)}_{\rho\rho\rho}(\mathbf{q}_1,\mathbf{q}_2,\mathbf{q}_3,\omega_2,\omega_3)\frac{i|\mathbf{E}^P|(\mathbf{q}_2,\omega_2)}{|\mathbf{q}_2|}\frac{i|\mathbf{E}^P|(\mathbf{q}_3,\omega_3)}{|\mathbf{q}_3|}. \tag{4.43}$$

The last equation holds in general because of gauge invariance.

4.2.2 Optical Limit Considerations

As explained above, for SHG the long wavelength limit constitutes a good approximation. Its consequences can be further developed. Taking $\mathbf{q} \to 0$ the linear response $\chi_{\mathbf{j}\rho}$ vanishes,[11] whereas $\chi_{\rho\mathbf{j}}$ is zero because of charge conservation in neutral excitations. Then the quasi-susceptibilities of Eqs. (4.26), (4.33) depend only on the response functions $\chi^{(1)}_{\mathbf{jj}}$ and $\chi^{(2)}_{\mathbf{jjj}}$ that can be derived from the density ones, achieved via the TDDFT description of the system (see Eqs. (3.26) and (3.33)). In particular from the continuity equation [149, 150] one has:

$$\mathbf{q}_1 \cdot \chi^{(1)}_{\mathbf{jj}}(\mathbf{q}_1, \mathbf{q}_2, \omega) \cdot \mathbf{q}_2 = -\omega^2 \chi^{(1)}_{\rho\rho}(\mathbf{q}_1, \mathbf{q}_2, \omega) \tag{4.44}$$

$$\chi^{(1)LL}_{\mathbf{jj}}(\mathbf{q}, \mathbf{q}, \omega) = -\frac{\omega^2}{q^2} \chi^{(1)}_{\rho\rho}(\mathbf{q}, \mathbf{q}, \omega) \tag{4.45}$$

Where the superscript (L) stands for the longitudinal component (here is double, both in the perturbation and the response). At the second order instead it becomes (see Appendix D.3 for a complete derivation):

$$\chi^{(2)LLL}_{\mathbf{jjj}}(\mathbf{q}, \mathbf{q}, \mathbf{q}, 2\omega, \omega) = -i\frac{\omega^3}{q^3} \chi^{(2)}_{\rho\rho\rho}(\mathbf{q}, \mathbf{q}, \mathbf{q}, 2\omega, \omega). \tag{4.46}$$

A problem still exists connected with the limit $\mathbf{q} \to 0$ of the latter response function when inserted into the quasi-susceptibilities, which is vanishing and should be handled in a perturbative approach. However in the following section I will suppose the limits exists, handling this problem in a second time.

4.3 Response Function Derivation

Now, all the required knowledge for the determination of the polarization in terms of the response functions depend on the possibility of having an explicit form for Eqs. (3.17) and (3.18). These quantities have been expressed as function of the real wave functions and energies in the interaction picture. For an easier physical understanding I divide $\hat{O}$, the coupling of the field with the system in Eqs. (3.17) and (3.18), into its components $\hat{\rho}$ and $\hat{\mathbf{j}}$ that couples with φ^P and $\mathbf{A}^P$ respectively (see Eq. (4.14)). I derive then an explicit form of the linear and second-order response functions considering two general operators $\hat{B}$ and $\hat{C}$, that can be identified at the occurrence with the particular interaction terms ($\hat{\rho}$, $\hat{\mathbf{j}}$) that are involved. As an example, the linear case Eq. (3.17) can be rewritten as:

$$\chi^{(1)}_{AB}(1,2) = -i\theta(t_1 - t_2)\left(\langle \hat{A}^{(I)}(1)\hat{B}^{(I)}(2)\rangle - \langle \hat{B}^{(I)}(2)\hat{A}^{(I)}(1)\rangle\right). \tag{4.47}$$

---

[11] $\chi_{\mathbf{j}\rho}$ is obtained from gauge invariance calculation and vanish in the long wavelength limit.

Developing the two formula (the linear and nonlinear case) and translating them into the frequency domain one obtains the following results:[12]

$$\chi^{(1)}_{AB}(\mathbf{r}_1,\mathbf{r}_2,\omega) = \lim_{\eta\to 0^+}\sum_n \left(\frac{\langle\Psi_0|\hat{A}^{(S)}(1)|\Psi_n\rangle\langle\Psi_n|\hat{B}^{(S)}(2)|\Psi_0\rangle}{\omega-(E_n-E_0)+i\eta} - \right. \\ \left. - \frac{\langle\Psi_0|\hat{B}^{(S)}(2)|\Psi_n\rangle\langle\Psi_n|\hat{A}^{(S)}(1)|\Psi_0\rangle}{\omega+(E_n-E_0)+i\eta}\right) \tag{4.48}$$

or in a simplified notation where $\langle\Psi_i|\hat{A}^{(S)}(1)|\Psi_j\rangle = A_{ij}(1)$:

$$\chi^{(1)}_{AB}(\mathbf{r}_1,\mathbf{r}_2,\omega) = \lim_{\eta\to 0^+}\sum_n \left(\frac{A_{0n}(1)B_{n0}(2)}{\omega-(E_n-E_0)+i\eta} - \frac{B_{0n}(1)A_{n0}(2)}{\omega+(E_n-E_0)+i\eta}\right). \tag{4.49}$$

The second-order term instead becomes:[13]

$$\chi^{(2)}_{ABC}(\mathbf{r}_1,\mathbf{r}_2,\mathbf{r}_3,\omega_1,\omega_2,\omega_3) = \lim_{\eta\to 0^+}\sum_{nm}\delta(\omega_1-\omega_2-\omega_3) \\ \left(\frac{A_{0n}(1)B_{nm}(2)C_{m0}(3)}{(E_0-E_m+\omega_3+i\eta)(E_0-E_n+\omega_2+\omega_3+2i\eta} \right. \\ -\frac{B_{0n}(1)A_{nm}(2)C_{m0}(3)}{(E_0-E_m+\omega_3+i\eta)(E_n-E_m+\omega_2+\omega_3+2i\eta} \\ +\frac{C_{0n}(1)A_{nm}(2)B_{m0}(3)}{(E_n-E_0+\omega_3+i\eta)(E_n-E_m+\omega_2+\omega_3+2i\eta} \\ \left. -\frac{C_{0n}(1)B_{nm}(2)A_{m0}(3)}{(E_n-E_0+\omega_3+i\eta)(E_m-E_0+\omega_2+\omega_3+2i\eta}\right) \\ +(2\leftrightarrow 3)\,. \tag{4.50}$$

One can immediately notice that there are only two independent frequencies. ω_1, the one of the response, is given by the summation of the two perturbations ω_2 and ω_3. This process, called *frequencies summation*, in the particular case of $\omega_1 = \omega_2$ reduces to the second harmonic generation. While the first needs two different electromagnetic fields, the latter can take place in the presence of a single external perturbation. At the linear order the frequency is unique ω and there is no possibility of frequency composition. Frequency modification are always related to nonlinear effects.

4.3.1 TDDFT plane waves Independent Particle Derivation

Forms (4.49) and (4.50) are useful only once the real wave functions and energies are known. As discussed in chapters 2 and 3, this is not the case and one has to rely on the response functions of the independent KS system. In a second time the linear and nonlinear total response can be deduced solving the Dyson equations (3.26) and (3.33), as achieved in the TDDFT-response theory.

---

[12] In the following the operators $\hat{A}$, $\hat{B}$ and $\hat{C}$ are in the Schrödinger picture, that correspond to the same operators in the interaction picture at $t = t_0$.

[13] The last term $(2 \leftrightarrow 3)$ means that the previous terms should be considered in the addition also with the indexes (2) and (3) swapped.

The independent response functions are obtained in second quantization starting from the previous results. For the linear expression it becomes:

$$\chi^{(1)}_{0\ AB}(\mathbf{r}_1,\mathbf{r}_2,\omega) = \sum_{i,j}(f_i - f_j)\frac{\langle\psi_i(\mathbf{r}_1)|\hat{a}(\mathbf{r}_1)|\psi_j(\mathbf{r}_1)\rangle\langle\psi_j(\mathbf{r}_2)|\hat{b}(\mathbf{r}_2)|\psi_i(\mathbf{r}_2)\rangle}{(\epsilon_i - \epsilon_j + \omega + i\eta)} \tag{4.51}$$

with the lower-case letters $\hat{a}$, $\hat{b}$ and $\hat{c}$ (in the following equation) that indicates the corresponding single particle operators used to express $\hat{A}$, $\hat{B}$ and $\hat{C}$ in second quantization.[14]

For the second-order response instead one has:

$$\begin{aligned}\chi^{(2)}_{0\ ABC}(\mathbf{r}_1,\mathbf{r}_2,\mathbf{r}_3,\omega_2+\omega_3,\omega_2,\omega_3) = &\sum_{i,j,k}\frac{\langle\psi_i(\mathbf{r}_1)|\hat{a}(\mathbf{r}_1)|\psi_j(\mathbf{r}_1)\rangle}{(\epsilon_i - \epsilon_j + \omega_1 + \omega_2 + 2i\eta)}\\ &\Bigg[(f_i - f_k)\frac{\langle\psi_j(\mathbf{r}_2)|\hat{b}(\mathbf{r}_2)|\psi_k(\mathbf{r}_2)\rangle\langle\psi_k(\mathbf{r}_3)|\hat{c}(\mathbf{r}_3)|\psi_i(\mathbf{r}_3)\rangle}{(\epsilon_i - \epsilon_k + \omega_3 + i\eta)} +\\ &(f_j - f_k)\frac{\langle\psi_j(\mathbf{r}_3)|\hat{c}(\mathbf{r}_3)|\psi_k(\mathbf{r}_3)\rangle\langle\psi_k(\mathbf{r}_2)|\hat{b}(\mathbf{r}_2)|\psi_i(\mathbf{r}_2)\rangle}{(\epsilon_k - \epsilon_j + \omega_3 + i\eta)} +\\ &(2\leftrightarrow 3)\Bigg]\,.\end{aligned} \tag{4.52}$$

The derivation is general and holds for the eigenfunctions and eigenenergies ψ_i, ϵ_i of a single particle basis (i.e., an independent particle system). In the particular case of interest, they represents the KS wave functions and energies ψ^{KS}_λ, ϵ^{KS}_λ. If $\hat{A} = \hat{B} = \hat{C} = \hat{\rho}$ Eqs. (4.51) and (4.52) correspond to the responses of the independent particles KS system $\chi^{(1)}_0$, $\chi^{(2)}_0$ of Eqs. (3.21), (3.27).

Substituting to $\hat{a}$, $\hat{b}$, $\hat{c}$ the density single particle operator (i.e., $\hat{a}(\mathbf{r}_1) = \delta(\mathbf{r}_1 - \mathbf{r})$) and developing the two formula Eqs. (4.51), (4.52) in the basis of Bloch's states, the two independent particles susceptibilities take the expressions:

$$\chi^{(1)}_{0\ \rho\rho}(\mathbf{r}_1,\mathbf{r}_2,\omega) = \sum_{i,j}(f_i - f_j)\frac{\psi^*_i(\mathbf{r}_1)\psi_j(\mathbf{r}_1)\psi^*_j(\mathbf{r}_2)\psi_i(\mathbf{r}_2)}{(\epsilon_i - \epsilon_j + \omega + i\eta)} \tag{4.53}$$

$$\begin{aligned}\chi^{(2)}_{0\ \rho\rho\rho}(\mathbf{r}_1,\mathbf{r}_2,\mathbf{r}_3,\omega_2+\omega_3,\omega_2,\omega_3) = &\sum_{i,j,k}\frac{\psi^*_i(\mathbf{r}_1)\psi_j(\mathbf{r}_1)}{(\epsilon_i - \epsilon_j + \omega_2 + \omega_3 + 2i\eta)}\\ &\Bigg[(f_i - f_k)\frac{\psi^*_j(\mathbf{r}_2)\psi_k(\mathbf{r}_2)\psi^*_k(\mathbf{r}_3)\psi_i(\mathbf{r}_3)}{(\epsilon_i - \epsilon_k + \omega_3 + i\eta)} +\\ &(f_i - f_k)\frac{\psi^*_j(\mathbf{r}_3)\psi_k(\mathbf{r}_3)\psi^*_k(\mathbf{r}_2)\psi_i(\mathbf{r}_2)}{(\epsilon_i - \epsilon_k + \omega_2 + i\eta)} +\\ &(f_j - f_k)\frac{\psi^*_j(\mathbf{r}_3)\psi_k(\mathbf{r}_3)\psi^*_k(\mathbf{r}_2)\psi_i(\mathbf{r}_2)}{(\epsilon_k - \epsilon_j + \omega_3 + i\eta)} +\\ &(f_j - f_k)\frac{\psi^*_j(\mathbf{r}_2)\psi_k(\mathbf{r}_2)\psi^*_k(\mathbf{r}_3)\psi_i(\mathbf{r}_3)}{(\epsilon_k - \epsilon_j + \omega_2 + i\eta)}\Bigg]\,.\end{aligned} \tag{4.54}$$

---

[14] In second quantization the single particle operator $\hat{A}$ is expressed as $\hat{A} = \int d\mathbf{r}\ \psi^\dagger(\mathbf{r})\hat{a}(\mathbf{r})\psi(\mathbf{r})$ where $\psi^\dagger$, ψ are the field operators that create or annihilate a particle in $\mathbf{r}$. In the particular case of the density $\hat{a}(\mathbf{r}_1) = \delta(\mathbf{r}_1 - \mathbf{r})$ and

$$\langle\psi_i(\mathbf{r}_1)|\hat{a}(\mathbf{r}_1)|\psi_j(\mathbf{r}_1)\rangle = \int d\mathbf{r}\ \psi^*_i(\mathbf{r}_1)\delta(\mathbf{r}_1 - \mathbf{r})\psi_j(\mathbf{r}_1) = \psi^*_i(\mathbf{r}_1)\psi_j(\mathbf{r}_1).$$

At the same time one has (with $\hat{\mathbf{p}} = -i\nabla$ the linear momentum operator):

$$\chi^{(1)}_{0\ \rho\mathbf{j}}(\mathbf{r}_1, \mathbf{r}_2, \omega) = \sum_{i,j} (f_i - f_j) \frac{\psi_i^*(\mathbf{r}_1)\psi_j(\mathbf{r}_1)\psi_j^*(\mathbf{r}_2)\hat{\mathbf{p}}\psi_i(\mathbf{r}_2)}{(\epsilon_i - \epsilon_j + \omega + i\eta)} \tag{4.55}$$

So far the equations have been expressed for two incoming fields of frequency ω_2 and ω_3 with the general constraint that the second-order response has the frequency component $\omega_1 = \omega_2 + \omega_3$. The same holds in reciprocal space: $\mathbf{q}_1 = \mathbf{q}_2 + \mathbf{q}_3$. It is a general condition valid for the sum frequencies generation process. However now I want to restrict to the SHG case defined by $\omega_2 = \omega_3$. From now on I will pose them equal to ω. Due to all these relations that subsist among the variables I will also use a shorter notation for the susceptibility:

$$\chi^{(2)}_{0\ \rho\rho\rho}(\mathbf{q}_2 + \mathbf{q}_3 + \mathbf{G}_1, \mathbf{q}_2 + \mathbf{G}_2, \mathbf{q}_3 + \mathbf{G}_3, \omega_2 + \omega_3, \omega_2, \omega_3) \rightarrow \chi^{(2)}_{0\ \mathbf{G}_1\mathbf{G}_2\mathbf{G}_3}(\mathbf{q}_2, \mathbf{q}_3, \omega).$$

The KS response functions are then obtained using the KS basis $\psi_i = \psi_\lambda^{KS}$, $\epsilon_i = \epsilon_\lambda^{KS}$, and expressing them on the Bloch states $|\psi_{\mathbf{k}n}\rangle$ of Eq. (2.32) the final form for SHG reads:

$$\begin{aligned}
\chi^{(2)}_{0\ \mathbf{G}_1\mathbf{G}_2\mathbf{G}_3}(\mathbf{q}_2, \mathbf{q}_3, \omega) = \frac{2}{V} \sum_{n,n',n'',\mathbf{k}} & \frac{\langle\psi_{n'\mathbf{k}}|e^{-i(\mathbf{q}_2+\mathbf{q}_3+\mathbf{G}_1)\mathbf{r}_1}|\psi_{n\mathbf{k}}\rangle}{\epsilon_{n\mathbf{k}} - \epsilon_{n'\mathbf{k}+\mathbf{q}_2+\mathbf{q}_3} + 2\omega + 2i\eta} \\
\Bigg\{ \Big[\langle\psi_{n'\mathbf{k}+\mathbf{q}_2+\mathbf{q}_3}|e^{i(\mathbf{q}_3+\mathbf{G}_3)\mathbf{r}_2}|\psi_{n''\mathbf{k}+\mathbf{q}_2}\rangle & \langle\psi_{n''\mathbf{k}+\mathbf{q}_2}|e^{i(\mathbf{q}_2+\mathbf{G}_2)\mathbf{r}_3}|\psi_{n\mathbf{k}}\rangle \Big] \cdot \\
\left[\frac{(f_{n\mathbf{k}} - f_{n''\mathbf{k}+\mathbf{q}_2})}{\epsilon_{n\mathbf{k}} - \epsilon_{n''\mathbf{k}+\mathbf{q}_2} + \omega + i\eta} \right. & + \left. \frac{(f_{n'\mathbf{k}+\mathbf{q}_2+\mathbf{q}_3} - f_{n''\mathbf{k}+\mathbf{q}_2})}{\epsilon_{n''\mathbf{k}+\mathbf{q}_2} - \epsilon_{n'\mathbf{k}+\mathbf{q}_2+\mathbf{q}_3} + \omega + i\eta} \right] + \\
\Big[\langle\psi_{n'\mathbf{k}+\mathbf{q}_2+\mathbf{q}_3}|e^{i(\mathbf{q}_2+\mathbf{G}_2)\mathbf{r}_2}|\psi_{n''\mathbf{k}+\mathbf{q}_3}\rangle & \langle\psi_{n''\mathbf{k}+\mathbf{q}_3}|e^{i(\mathbf{q}_3+\mathbf{G}_3)\mathbf{r}_3}|\psi_{n\mathbf{k}}\rangle \Big] \cdot \\
\left[\frac{(f_{n\mathbf{k}} - f_{n''\mathbf{k}+\mathbf{q}_3})}{\epsilon_{n\mathbf{k}} - \epsilon_{n''\mathbf{k}+\mathbf{q}_3} + \omega + i\eta} \right. & + \left. \frac{(f_{n'\mathbf{k}+\mathbf{q}_2+\mathbf{q}_3} - f_{n''\mathbf{k}+\mathbf{q}_3})}{\epsilon_{n''\mathbf{k}+\mathbf{q}_3} - \epsilon_{n'\mathbf{k}+\mathbf{q}_2+\mathbf{q}_3} + \omega + i\eta} \right] \Bigg\}.
\end{aligned} \tag{4.56}$$

As stated before, it is not immediate to obtain the limit $\mathbf{q} \rightarrow 0$ since $\chi_0^{(2)}$ vanishes. As a consequence one cannot substitute directly $\mathbf{q} = 0$ but has to expand the Bloch functions in $\mathbf{q}$ using perturbation theory up to the second order both for the energies and the wave functions (I am considering semiconductors and insulators for which $f_{n,\mathbf{k}+\mathbf{q}} = f_{n,\mathbf{k}}$ and is $\mathbf{k}$-independent).[15]

4.3.2 Optical Limit through Perturbation Theory

$|\psi_{n\mathbf{k}}\rangle$ is solution of the Bloch Hamiltonian [151]:

$$\hat{H}_{\mathbf{k}}|\psi_{n\mathbf{k}}\rangle = \left[-\frac{1}{2}\nabla^2 + V_{nl} \right] |\psi_{n\mathbf{k}}\rangle = \epsilon_{n\mathbf{k}}|\psi_{n\mathbf{k}}\rangle \tag{4.57}$$

with V_{nl} a generic nonlocal periodic lattice potential, that can be identified with the total potential V_{ext} or the ionic pseudopotential. Decomposing the

---

[15] This corresponds considering all the terms in $\chi_0^{(2)}$ = that are proportional to $|\mathbf{q}|^3$, the higher non-vanishing order. Indeed because of equation (4.46) and the finite limit for $\chi^{(2)LLL}_{\mathbf{jjj}}(\mathbf{q} \rightarrow 0)$, once one expands $\chi_0^{(2)}$ in powers of $\mathbf{q}$ the terms up to $|\mathbf{q}|^2$ must vanish and the one proportional to $|\mathbf{q}|^3$ is the only one that remains in Eq. (4.46) when the limit is performed.

wave functions on the Bloch states of Eq. (2.32), the periodic term $|u_{n\mathbf{k}}\rangle$ is solution of the equation:[16]

$$h_{\mathbf{k}}|u_{n\mathbf{k}}\rangle \left[\frac{1}{2}k^2 - i\mathbf{k}\nabla - \frac{1}{2}\nabla^2 + e^{-i\mathbf{kr}}V_{nl}e^{i\mathbf{kr}}\right]|u_{n\mathbf{k}}\rangle = \epsilon_{n\mathbf{k}}|u_{n\mathbf{k}}\rangle. \tag{4.58}$$

Accordingly to Eq. (4.56), the Bloch functions and energies depends on the linear momentum $\mathbf{k}+\mathbf{q}$. The periodic part of $|\psi_{\mathbf{k}+\mathbf{q}n}\rangle$, $|u_{n\mathbf{k}+\mathbf{q}}\rangle$, becomes the solution of the corresponding Hamiltonian $h_{\mathbf{k}+\mathbf{q}}$:

$$h_{\mathbf{k}+\mathbf{q}}|u_{n\mathbf{k}+\mathbf{q}}\rangle = \epsilon_{n\mathbf{k}+\mathbf{q}}|u_{n\mathbf{k}+\mathbf{q}}\rangle \tag{4.59}$$

$$h_{\mathbf{k}+\mathbf{q}} = \left[\frac{1}{2}(\mathbf{k}+\mathbf{q})^2 - i(\mathbf{k}+\mathbf{q})\nabla - \frac{1}{2}\nabla^2 + e^{-i(\mathbf{k}+\mathbf{q})\mathbf{r}}V_{nl}e^{i(\mathbf{k}+\mathbf{q})\mathbf{r}}\right]. \tag{4.60}$$

It is possible to identify Eq. (4.59) with Eq. (4.58) where the variable $\mathbf{k}$ is substituted with $\mathbf{k} \to \mathbf{k}+\mathbf{q}$. In the long wavelength limit $\mathbf{q} \to 0$ one can think $h_{\mathbf{k}+\mathbf{q}}$ and its eigenvalues/eigenvectors being the perturbed Hamiltonian of the unperturbed $h_{\mathbf{k}}$.[17]. Rearranging the terms of Eq. (4.59) according to their respective order of $\mathbf{q}$, the perturbation Hamiltonian can be written as $h_{\mathbf{k}+\mathbf{q}} = h_{\mathbf{k}} + h_{1,\mathbf{k}} + h_{2,\mathbf{k}} + \O(3)$, with:

$$h_{1,\mathbf{k}} = \mathbf{kq} - i\mathbf{q}\nabla + \left[e^{-i\mathbf{kr}}V_{nl}e^{i\mathbf{kr}}, i\mathbf{qr}\right], \tag{4.61}$$

$$\begin{aligned} h_{2,\mathbf{k}} = \frac{1}{2}q^2 + \mathbf{qr}e^{-i\mathbf{kr}}V_{nl}e^{i\mathbf{kr}}\mathbf{qr} - \frac{1}{2}(\mathbf{qr})^2 e^{-i\mathbf{kr}}V_{nl}e^{i\mathbf{kr}} - \\ - \frac{1}{2}e^{-i\mathbf{kr}}V_{nl}e^{i\mathbf{kr}}(\mathbf{qr})^2. \end{aligned} \tag{4.62}$$

These perturbations and the relative corrections to the eigenstates $|u_{n\mathbf{k}}\rangle$ can be obtained also for the complete wave functions $|\psi_{n\mathbf{k}}\rangle$. Indeed, considering $H_{\mathbf{k}+\mathbf{q}} = H_{\mathbf{k}} + H_{1,\mathbf{k}} + H_{2,\mathbf{k}} + \O(3)$ one has:

$$\begin{aligned} h_{1,\mathbf{k}}|u_{n\mathbf{k}}\rangle &= e^{-i\mathbf{kr}}H_{1,\mathbf{k}}|\psi_{n\mathbf{k}}\rangle \\ h_{2,\mathbf{k}}|u_{n\mathbf{k}}\rangle &= e^{-i\mathbf{kr}}H_{2,\mathbf{k}}|\psi_{n\mathbf{k}}\rangle, \end{aligned} \tag{4.63}$$

that gives

$$\begin{aligned} H_{1,\mathbf{k}} =& - i\mathbf{q}\nabla + [V_{nl}, i\mathbf{qr}] = i\mathbf{q}\left[H_{\mathbf{k}}, \mathbf{r}\right] \\ =& \mathbf{qv} \end{aligned} \tag{4.64}$$

$$\begin{aligned} H_{2,\mathbf{k}} =& \frac{1}{2}q^2 + \mathbf{qr}V_{nl}\mathbf{qr} - \frac{1}{2}(\mathbf{qr})^2 V_{nl} - \frac{1}{2}V_{nl}(\mathbf{qr})^2 \\ =& \frac{1}{2}q^2 + \frac{1}{2}\left[\mathbf{qr}, [V_{nl}, \mathbf{qr}]\right] \\ =& -\frac{i}{2}\left[\mathbf{qr}, \mathbf{qv}\right], \end{aligned} \tag{4.65}$$

where the velocity operator $\mathbf{v}$ is given by $\mathbf{v} = \mathbf{q} + i\left[V_{nl}, \mathbf{r}\right]$. One can notice that V_{nl} enters through its commutator with the position operator $\mathbf{r}$. Therefore only

---

[16] It is obtained developing the Hamiltonian for the full Bloch states $e^{i\mathbf{kr}}|u_{n\mathbf{k}}\rangle$ and then dividing by the exponential term $e^{i\mathbf{kr}}$. It results that $h_{\mathbf{k}} = e^{-i\mathbf{kr}}H_{\mathbf{k}}$.

[17] Here the perturbation is identified with the exchanged linear momentum $\mathbf{q}$.

its nonlocal part, that does not commute, contributes to these Hamiltonians. $H_{1,\mathbf{k}}$ and $H_{2,\mathbf{k}}$ allow to obtain the energy and wave functions corrections within Time-Independent Perturbation Theory.

The energy corrections (see Appendix C for a complete derivation) developed up to the second order become:

$$\begin{aligned}\epsilon^{(1)}_{n\mathbf{k}} &= \langle\psi_{n\mathbf{k}}|H_{1,\mathbf{k}}|\psi_{n\mathbf{k}}\rangle \\ &= \langle\psi_{n\mathbf{k}}|\mathbf{qv}|\psi_{n\mathbf{k}}\rangle\end{aligned} \tag{4.66}$$

$$\begin{aligned}\epsilon^{(2)}_{n\mathbf{k}} &= \sum_{m\notin D_n}\frac{|\langle\psi_{m\mathbf{k}}|H_{1,\mathbf{k}}|\psi_{n\mathbf{k}}\rangle|^2}{\epsilon_{n\mathbf{k}}-\epsilon_{m\mathbf{k}}} + \langle\psi_{n\mathbf{k}}|H_{2,\mathbf{k}}|\psi_{n\mathbf{k}}\rangle \\ &= \sum_{m\notin D_n}\frac{|\langle\psi_{m\mathbf{k}}|\mathbf{qv}|\psi_{n\mathbf{k}}\rangle|^2}{\epsilon_{n\mathbf{k}}-\epsilon_{m\mathbf{k}}} - \frac{i}{2}\langle\psi_{n\mathbf{k}}|\left[\mathbf{qr},\mathbf{qv}\right]|\psi_{n\mathbf{k}}\rangle,\end{aligned} \tag{4.67}$$

with $\epsilon_{n\mathbf{k}+\mathbf{q}} = \epsilon_{n\mathbf{k}} + \epsilon^{(1)}_{n\mathbf{k}} + \epsilon^{(2)}_{n\mathbf{k}} + \emptyset(3)$. The wave functions instead are given by:

$$\begin{aligned}|\psi^{(1)}_{n\mathbf{k}}\rangle &= \sum_{m\notin D_n}\frac{\langle\psi_{m\mathbf{k}}|H_{1,\mathbf{k}}|\psi_{n\mathbf{k}}\rangle}{\epsilon_{n\mathbf{k}}-\epsilon_{m\mathbf{k}}}|\psi_{m\mathbf{k}}\rangle \\ &= \sum_{m\notin D_n}\frac{\langle\psi_{m\mathbf{k}}|\mathbf{qv}|\psi_{n\mathbf{k}}\rangle}{\epsilon_{n\mathbf{k}}-\epsilon_{m\mathbf{k}}}|\psi_{m\mathbf{k}}\rangle\end{aligned} \tag{4.68}$$

$$\begin{aligned}|\psi^{(2)}_{n\mathbf{k}}\rangle &= \sum_{m\notin D_n}\sum_{p\notin D_n}\frac{\langle\psi_{m\mathbf{k}}|H_{1,\mathbf{k}}|\psi_{p\mathbf{k}}\rangle\langle\psi_{p\mathbf{k}}|H_{1,\mathbf{k}}|\psi_{n\mathbf{k}}\rangle}{(\epsilon_{n\mathbf{k}}-\epsilon_{p\mathbf{k}})(\epsilon_{n\mathbf{k}}-\epsilon_{m\mathbf{k}})}|\psi_{m\mathbf{k}}\rangle \\ &\quad - \langle\psi_{n\mathbf{k}}|H_{1,\mathbf{k}}|\psi_{n\mathbf{k}}\rangle\sum_{m\notin D_n}\frac{\langle\psi_{m\mathbf{k}}|H_{1,\mathbf{k}}|\psi_{n\mathbf{k}}\rangle}{(\epsilon_{n\mathbf{k}}-\epsilon_{m\mathbf{k}})^2}|\psi_{m\mathbf{k}}\rangle \\ &\quad + \sum_{m\notin D_n}\frac{\langle\psi_{m\mathbf{k}}|H_{2,\mathbf{k}}|\psi_{n\mathbf{k}}\rangle}{(\epsilon_{n\mathbf{k}}-\epsilon_{m\mathbf{k}})}|\psi_{m\mathbf{k}}\rangle \\ &\quad - \frac{1}{2}\sum_{m\notin D_n}\frac{|\langle\psi_{m\mathbf{k}}|H_{1,\mathbf{k}}|\psi_{n\mathbf{k}}\rangle|^2}{(\epsilon_{n\mathbf{k}}-\epsilon_{m\mathbf{k}})^2}|\psi_{n\mathbf{k}}\rangle \\ &= \sum_{m\notin D_n}\sum_{p\notin D_n}\frac{\langle\psi_{m\mathbf{k}}|\mathbf{qv}|\psi_{p\mathbf{k}}\rangle\langle\psi_{p\mathbf{k}}|\mathbf{qv}|\psi_{n\mathbf{k}}\rangle}{(\epsilon_{n\mathbf{k}}-\epsilon_{p\mathbf{k}})(\epsilon_{n\mathbf{k}}-\epsilon_{m\mathbf{k}})}|\psi_{m\mathbf{k}}\rangle \\ &\quad - \langle\psi_{n\mathbf{k}}|\mathbf{qv}|\psi_{n\mathbf{k}}\rangle\sum_{m\notin D_n}\frac{\langle\psi_{m\mathbf{k}}|\mathbf{qv}|\psi_{n\mathbf{k}}\rangle}{(\epsilon_{n\mathbf{k}}-\epsilon_{m\mathbf{k}})^2}|\psi_{m\mathbf{k}}\rangle \\ &\quad - \sum_{m\notin D_n}\frac{i}{2}\frac{\langle\psi_{m\mathbf{k}}|\left[\mathbf{qr},\mathbf{qv}\right]|\psi_{n\mathbf{k}}\rangle}{(\epsilon_{n\mathbf{k}}-\epsilon_{m\mathbf{k}})}|\psi_{m\mathbf{k}}\rangle \\ &\quad - \frac{1}{2}\sum_{m\notin D_n}\frac{|\langle\psi_{m\mathbf{k}}|\mathbf{qv}|\psi_{n\mathbf{k}}\rangle|^2}{(\epsilon_{n\mathbf{k}}-\epsilon_{m\mathbf{k}})^2}|\psi_{n\mathbf{k}}\rangle\end{aligned} \tag{4.69}$$

with D_n the degenerate subspace of the eigenvectors with energy equal to $\epsilon_{n\mathbf{k}}$. In the particular case of $\epsilon_{n\mathbf{k}}$ being non-degenerate, $D_n \equiv n$.

The wave function is given by: $|\psi_{n\mathbf{k}+\mathbf{q}}\rangle = e^{i\mathbf{qr}}(|\psi_{n\mathbf{k}}\rangle + |\psi^{(1)}_{n\mathbf{k}}\rangle + |\psi^{(2)}_{n\mathbf{k}}\rangle + \emptyset(3))$. These formulas, substituted in Eq. (4.56) gives the desired KS second-order density response $\chi^{(2)}_0$, that I will not present here because of the lengthy expression. The matrix elements are here evaluated in the *velocity gauge*, but the final result can be demonstrated to be in agreement with the one of Hughes and Sipe [48, 50, 152] evaluated in the *length gauge* [153]. More informations about the correspondences between the two gauges can be found in appendix D.4.

4.4 Macroscopic Derivation

In the previous sections I have shown the microscopic derivation of the second-order response function. This has been achieved applying perturbation theory to the TDDFT formalisms. Nevertheless, it is not sufficient in order to compare with experimental results. Experiments on semiconducting materials as the ones of interest are usually performed on macroscopic samples in the laboratory environment. Also the optical phenomena (reflection, propagation, transmission) can be quantified by a number of parameters that determine the properties of the medium at the macroscopic level. Therefore the macroscopic response of the system that is measured must be linked to the microscopic one that has been derived so-far. This process corresponds to a spatial average over a distance that is large with respect to the lattice parameter, as shown by Ehrenreich in Ref. [146]. It is obtained by averaging the parts of the microscopic quantities that are periodic with respect to the lattice. The two responses (macroscopic and microscopic) generally differ because of the microscopic inhomogeneities of the system that make the induced polarization locally different. Differences can arise also from the microscopic order that differs from the macroscopic one (an example is given by anti-ferromagnetic materials, where the microscopic order given by well defined alignment of the electronic spins is averaged to zero at a macroscopic level). The starting point is again the definition of the polarization[18]

$$\begin{aligned}\mathbf{P}_M(1) &= \mathbf{P}_M^{(1)}(1) + \mathbf{P}_M^{(2)}(1) + \dots \\ &= \chi_M^{(1)}(1,2)\mathbf{E}(2) + \chi_M^{(2)}(1,2,3)\mathbf{E}(2)\mathbf{E}(3) + \dots\end{aligned} \tag{4.70}$$

where $\mathbf{E}$ corresponds to the *total* macroscopic electric field, given by the external and the induced ones. The SHG process is then defined by the second-order macroscopic polarization:

$$\mathbf{P}_M^{(2)}(1) = \chi_M^{(2)}(1,2,3)\mathbf{E}(2)\mathbf{E}(3), \tag{4.71}$$

with the constraint that the two frequencies of the fields $\mathbf{E}(\omega_2)$, $\mathbf{E}(\omega_3)$ are equal: $\omega_2 = \omega_3$. $\chi_M^{(i)}$, as well as other optical quantities as ϵ_M (the dielectric function responsible of the linear response), cannot be obtained directly by averaging the microscopic expressions of $\mathbf{P}^{(1)}$ and $\mathbf{P}^{(2)}$ Eqs. (4.28) and (4.32). These are function of the external perturbing field $\mathbf{E}^P$ and should be first reformulated in terms of $\mathbf{E}$. The average is then performed by taking the $\mathbf{G} = 0$ component (this is a general theorem that holds for periodic functions).

---

[18] This definition holds for materials that lack of an intrinsic polarization when $\mathbf{E}^P = 0$.

4.4.1 Derivation of the Perturbing Field as Function of the Total Field

The dielectric susceptibility is obtained from the polarization as seen before. An useful derivation of the different $\mathbf{P}^{(i)}$ orders can be obtained considering the displacement vector $\mathbf{D}$ in Maxwell's equations. Let's now introduce their microscopic form in the usual c.g.s units:[19]

$$\nabla \cdot \mathbf{D} = 4\pi \rho^{ext} \tag{4.72}$$

$$\nabla \times \mathbf{E} = -\frac{\partial_t}{c}\mathbf{B} \tag{4.73}$$

$$\nabla \times \mathbf{H} = \frac{\partial_t}{c}\mathbf{D} + \frac{4\pi}{c}\mathbf{j}^{ext} \tag{4.74}$$

$$\nabla \cdot \mathbf{B} = 0 \tag{4.75}$$

where $\rho^{ext}, \mathbf{j}^{ext}$ are the sources of the external field

$$\nabla \cdot \mathbf{E}^{ext} = 4\pi \rho^{ext} \tag{4.76}$$

and $\mathbf{E}$ is the *total* field given by the external and the induced one:

$$\begin{aligned} \nabla \cdot \mathbf{E} = \nabla \cdot \mathbf{E}^{ext} + \nabla \cdot \mathbf{E}^{ind} = \\ = 4\pi\rho^{ext} + 4\pi\rho^{ind} = 4\pi\rho^{tot}. \end{aligned} \tag{4.77}$$

The last equation, together with Maxwell's equation (4.72) and the definition of the polarization vector $-\nabla \cdot \mathbf{P} = \rho^{ind}$, gives the displacement vector $\mathbf{D}$:

$$\mathbf{D} = \mathbf{E} + 4\pi\mathbf{P}. \tag{4.78}$$

I will not consider the magnetization of the material ($\mathbf{M} = 0$, so that $\mathbf{B} = \mathbf{H} + \mathbf{M} = \mathbf{H}$). The previous equations can be transformed from the differential form into a linear one in the frequencies-momenta space through a Fourier transform. Maxwell's equations then read:

$$i(\mathbf{q}+\mathbf{G}) \cdot \mathbf{D}(\mathbf{q}+\mathbf{G},\omega) = 4\pi\rho^{ext}(\mathbf{q}+\mathbf{G},\omega) \tag{4.79}$$

$$(\mathbf{q}+\mathbf{G}) \times \mathbf{E}(\mathbf{q}+\mathbf{G},\omega) = \frac{\omega}{c}\mathbf{B}(\mathbf{q}+\mathbf{G},\omega) \tag{4.80}$$

$$(\mathbf{q}+\mathbf{G}) \times \mathbf{B}(\mathbf{q}+\mathbf{G},\omega) = -\frac{\omega}{c}\mathbf{D} - \frac{4\pi i}{c}\mathbf{j}^{ext}(\mathbf{q}+\mathbf{G},\omega) \tag{4.81}$$

$$i(\mathbf{q}+\mathbf{G}) \cdot \mathbf{B}(\mathbf{q}+\mathbf{G},\omega) = 0. \tag{4.82}$$

Equation (4.78) for the microscopic electric displacement vector becomes:

$$\begin{aligned} \mathbf{D}(\mathbf{q}+\mathbf{G},\omega) &= \mathbf{E}(\mathbf{q}+\mathbf{G},\omega) + 4\pi\mathbf{P}(\mathbf{q}+\mathbf{G},\omega) \\ &= \mathbf{E}(\mathbf{q}+\mathbf{G},\omega) + 4\pi(\mathbf{P}^{(1)}(\mathbf{q}+\mathbf{G},\omega) + \mathbf{P}^{(2)}(\mathbf{q}+\mathbf{G},\omega)) \end{aligned} \tag{4.83}$$

where $\mathbf{P}$ has been developed up to the second order.

$\mathbf{D}$ can be related to $\mathbf{E}^{ext}$ thanks to equations (4.76) and (4.79), that give:

$$\begin{aligned} \nabla \cdot \mathbf{D} &= \nabla \cdot \mathbf{E}^{ext} \\ (\mathbf{q}+\mathbf{G}) \cdot \mathbf{D}(\mathbf{q}+\mathbf{G},\omega) &= (\mathbf{q}+\mathbf{G}) \cdot \mathbf{E}^{ext}(\mathbf{q}+\mathbf{G},\omega) \\ \mathbf{D}^{L}(\mathbf{q}+\mathbf{G},\omega) &= \mathbf{E}^{ext,L}(\mathbf{q}+\mathbf{G},\omega). \end{aligned} \tag{4.84}$$

---

[19] The velocity of light is expressed by c, while $\epsilon_0, \mu_0 = 1$.

Combining the Eqs. (4.80) and (4.81) instead one has:

$$\begin{aligned}&(\mathbf{q}+\mathbf{G})\times[(\mathbf{q}+\mathbf{G})\times\mathbf{E}(\mathbf{q}+\mathbf{G},\omega)] = \\ &-\frac{\omega^2}{c^2}\mathbf{D}(\mathbf{q}+\mathbf{G},\omega)-\frac{4\pi i\omega}{c^2}\mathbf{j}^{ext}(\mathbf{q}+\mathbf{G},\omega)\end{aligned} \tag{4.85}$$

$$\begin{aligned}&[(\mathbf{q}+\mathbf{G})\cdot\mathbf{E}(\mathbf{q}+\mathbf{G},\omega)](\mathbf{q}+\mathbf{G})-|\mathbf{q}+\mathbf{G}|^2\mathbf{E}(\mathbf{q}+\mathbf{G},\omega) = \\ &\qquad -\frac{\omega^2}{c^2}\mathbf{D}(\mathbf{q}+\mathbf{G},\omega)-\frac{4\pi i\omega}{c^2}\mathbf{j}^{ext}(\mathbf{q}+\mathbf{G},\omega),\end{aligned} \tag{4.86}$$

where the relation $\mathbf{a}\times(\mathbf{b}\times\mathbf{c}) = (\mathbf{a}\cdot\mathbf{c})\mathbf{b}-(\mathbf{a}\cdot\mathbf{b})\mathbf{c}$. In the absence of external currents ($\mathbf{j}^{ext}=0$), projecting Eq. (4.86) on both hand-sides on the transverse component gives:

$$\mathbf{E}^T(\mathbf{q}+\mathbf{G},\omega) = \frac{\omega^2}{c^2|\mathbf{q}+\mathbf{G}|^2}\mathbf{D}^T(\mathbf{q}+\mathbf{G},\omega). \tag{4.87}$$

The last equation in the case of long wavelengths $\mathbf{q}\to 0$ so that $\lambda \gg 1$, one has $\frac{\omega}{c} \ll 1$ that makes all the terms with $\mathbf{G}\neq 0$ vanish being their limit $\frac{0}{G^2}$. As a consequence only the macroscopic component of the transverse total field remains.

4.4.2 Macroscopic response

The derivation of the second-order macroscopic response is a nontrivial task, because one wants to pass from the induced microscopic fluctuations obtained in the response theory to the knowledge of the macroscopic polarization of equation (4.1). The most difficult goal is to pass from the external field $\mathbf{E}^{ext}$ that is macroscopic, to the total electric field $\mathbf{E}$ that is microscopic since it contains also the contribution of the microscopic induced fields i.e., the crystal local fields effects.

The total field $\mathbf{E}$ can be considered in general as the sum of the perturbing field $\mathbf{E}^P$ and the response field $\mathbf{E}^R$.

If one choses $\mathbf{E}^P = \mathbf{E}^{ext}$ so that $\mathbf{E}^R = \mathbf{E}^{ind}$ as done by Ehrenreich [146] for cubic crystal, the results is more physically intuitive. Nevertheless, it demonstrated extremely difficult to treat a general crystal lattice and another choice of the fields presented by Del Sole and Fiorino [68] should be adopted. Other definitions of $\mathbf{E}^P$ and $\mathbf{E}^R$ are formally exact and possible in the response theory: It means moving part of the response already into the unperturbed Hamiltonian, i.e. in the linear case redefining

$$\hat{H} = \hat{H}_0 + \hat{H}_I = \hat{H}'_0 + \hat{H}'_I \tag{4.88}$$

with different unperturbed states, but keeping the same total Hamiltonian. Hence it has the same behavior of the system subjected to the external perturbation.[20] According to Ref. [68] for a general crystal symmetry it reveals convenient to split the induced part of the total electric field into its longitudinal and transverse components:

$$\mathbf{E}^{ind} = \mathbf{E}^{ind,L} + \mathbf{E}^{ind,T}. \tag{4.89}$$

---

[20] One can find an analogy in Many-Body Perturbation Theory in the arbitrariness of the choice of the G_0 Green's function. E.g., one can include or not the Hartree term into the unperturbed Hamiltonian so that $G_0 \to G_H$. The quantities into the Dyson equation (the self-energy Σ) will change, but the full-interacting G will be the same in both the cases.

The perturbing field $\mathbf{E}^P$ as considered before, should then be redefined in order to have a complete knowledge of the two main quantities: the unperturbed Hamiltonian,[21] and the perturbing field $\mathbf{E}^P$ as obtained from the Kubo response theory [69]. If one considers as Ref. [146] $\mathbf{E}^P = \mathbf{E}^{ext}$ then $\mathbf{E}^{ind}$ contains both $\mathbf{E}^{ind,L}$ given by the instantaneous Coulomb interaction between the electrons and $\mathbf{E}^{ind,T}$ that originates from their retarded Coulomb interaction [68]. The latter is extremely complicated and for noncubic crystals precludes the knowledge of the unperturbed states, making this particular choice of $\mathbf{E}^P$ unuseful. On the contrary, including the induced transverse response directly in the perturbing field i.e.,

$$\mathbf{E}^P = \mathbf{E}^{ext} + \mathbf{E}^{ind,T} = \mathbf{E} - \mathbf{E}^{ind,L}, \tag{4.90}$$

permits to have a simpler non-retarded Hamiltonian whose states (including the longitudinal perturbation) can be more easily evaluated. In addition it has the advantage that the perturbing field is macroscopic as both its component $\mathbf{E}^{ext}$ and $\mathbf{E}^{ind,T}$. This makes easier its macroscopic average, that is present in the subsequent derivation.

Further developing this general assumption I can now find the expression of $\mathbf{P}_M$ passing from the perturbing field $\mathbf{E}^P$ to the total field $\mathbf{E}$. From the definition of the displacement vector Eq. (4.83), looking at its longitudinal component one has:

$$\begin{aligned}\mathbf{D}^L(\mathbf{q}+\mathbf{G},\omega) &= \mathbf{E}^L(\mathbf{q}+\mathbf{G},\omega) + 4\pi\mathbf{P}^L(\mathbf{q}+\mathbf{G},\omega)\\ &= \mathbf{E}^{ext,L}(\mathbf{q}+\mathbf{G},\omega) + \mathbf{E}^{ind,L}(\mathbf{q}+\mathbf{G},\omega) + 4\pi\mathbf{P}^L(\mathbf{q}+\mathbf{G},\omega)\end{aligned} \tag{4.91}$$

and substituting $\mathbf{D}^L$ from Eq. (4.84), one obtains that

$$\begin{aligned}\mathbf{E}^{ind,L}(\mathbf{q}+\mathbf{G},\omega) &= -4\pi\mathbf{P}^L(\mathbf{q}+\mathbf{G},\omega)\\ \mathbf{E}^{ind,L}(\mathbf{q}+\mathbf{G},\omega) &= -4\pi\frac{\mathbf{q}+\mathbf{G}}{|\mathbf{q}+\mathbf{G}|}P^L(\mathbf{q}+\mathbf{G},\omega).\end{aligned} \tag{4.92}$$

From Eqs. (4.90) and (4.92) the total field in its microscopic and macroscopic formulation becomes:

$$\mathbf{E}(\mathbf{q}+\mathbf{G},\omega) = \mathbf{E}^P(\mathbf{q}+\mathbf{G},\omega) - 4\pi\frac{\mathbf{q}+\mathbf{G}}{|\mathbf{q}+\mathbf{G}|}P^L(\mathbf{q}+\mathbf{G},\omega) \tag{4.93}$$

$$\mathbf{E}(\mathbf{q},\omega) = \mathbf{E}^P(\mathbf{q},\omega) - 4\pi\frac{\mathbf{q}}{|\mathbf{q}|}P^L(\mathbf{q},\omega) \tag{4.94}$$

where the macroscopic component of the field Eq. (4.94) has been obtain from the microscopic average posing $\mathbf{G} = 0$.

According to the formulation of the first order microscopic polarization as it has been obtained in Eq. (4.29), its macroscopic component becomes:

$$\mathbf{P}^{(1)}(\mathbf{q},\omega) = \tilde{\alpha}^{(1)}(\mathbf{q},\mathbf{q},\omega)\mathbf{E}^P(\mathbf{q},\omega). \tag{4.95}$$

Substituting $\mathbf{E}^P$ as obtained from Eq. (4.94) into (4.95)

$$\mathbf{P}^{(1)}(\mathbf{q},\omega) = \tilde{\alpha}^{(1)}(\mathbf{q},\mathbf{q},\omega)\mathbf{E}(\mathbf{q},\omega) + 4\pi\tilde{\alpha}^{(1)}(\mathbf{q},\mathbf{q},\omega)\frac{\mathbf{q}}{|\mathbf{q}|}P^L(\mathbf{q},\omega) \tag{4.96}$$

---

[21] It gives access to the unperturbed states ad as a consequence to all the observable one is interested in, as the dielectric susceptibility. see section 3.2.1.

and expanding $P^L = \frac{\mathbf{q}}{|\mathbf{q}|} \cdot \mathbf{P}$ up to the second order in $\mathbf{P} = \mathbf{P}^{(1)} + \mathbf{P}^{(2)}$, it is then possible to get a relation between the polarization and the total electric field only:

$$\begin{aligned}\mathbf{P}^{(1)}(\mathbf{q},\omega) =& \tilde{\alpha}^{(1)}(\mathbf{q},\mathbf{q},\omega)\mathbf{E}(\mathbf{q},\omega) \\ &+ 4\pi\tilde{\alpha}^{(1)}(\mathbf{q},\mathbf{q},\omega)\frac{\mathbf{q}}{|\mathbf{q}|}\frac{\mathbf{q}}{|\mathbf{q}|} \cdot \Big(\mathbf{P}^{(1)}(\mathbf{q},\omega) + \mathbf{P}^{(2)}(\mathbf{q},\omega)\Big).\end{aligned} \tag{4.97}$$

Further manipulating the equation, adding $\mathbf{P}^{(2)}$ to both hand sides and then collecting $(\mathbf{P}^{(1)} + \mathbf{P}^{(2)})$ at the left member, one has:

$$\begin{aligned}\left[1 - 4\pi\tilde{\alpha}^{(1)}(\mathbf{q},\mathbf{q},\omega)\frac{\mathbf{q}}{|\mathbf{q}|}\frac{\mathbf{q}}{|\mathbf{q}|}\cdot\right]\Big(\mathbf{P}^{(1)}(\mathbf{q},\omega) + \mathbf{P}^{(2)}(\mathbf{q},\omega)\Big) = \\ \tilde{\alpha}^{(1)}(\mathbf{q},\mathbf{q},\omega)\mathbf{E}(\mathbf{q},\omega) + \mathbf{P}^{(2)}(\mathbf{q},\omega).\end{aligned} \tag{4.98}$$

It is then possible to obtain the value of $\mathbf{P} = \mathbf{P}^{(1)} + \mathbf{P}^{(2)}$:

$$\begin{aligned}\mathbf{P}(\mathbf{q},\omega) &= \mathbf{P}^{(1)}(\mathbf{q},\omega) + \mathbf{P}^{(2)}(\mathbf{q},\omega) \\ &= A^R(\mathbf{q},\omega)\tilde{\alpha}^{(1)}(\mathbf{q},\mathbf{q},\omega)\mathbf{E}(\mathbf{q},\omega) + A^R(\mathbf{q},\omega)\mathbf{P}^{(2)}(\mathbf{q},\omega),\end{aligned} \tag{4.99}$$

where the tensor A^R is defined from Eq. (4.98) as

$$A^R(\mathbf{q},\omega) = \left[1 - 4\pi\tilde{\alpha}^{(1)}(\mathbf{q},\mathbf{q},\omega) \cdot \frac{\mathbf{q}}{|\mathbf{q}|}\frac{\mathbf{q}}{|\mathbf{q}|}\right]^{-1} \tag{4.100}$$

$$= 1 + 4\pi\frac{\tilde{\alpha}^{(1)}(\mathbf{q},\mathbf{q},\omega)}{1 - 4\pi\tilde{\alpha}^{(1),LL}(\mathbf{q},\mathbf{q},\omega)} \cdot \frac{\mathbf{q}}{|\mathbf{q}|}\frac{\mathbf{q}}{|\mathbf{q}|}. \tag{4.101}$$

and comes from the *right-hand* longitudinal contraction of the quasi-susceptibility tensor $\tilde{\alpha}^{(1)}$, whereas $\tilde{\alpha}^{(1),LL}$ corresponds to its longitudinal-longitudinal contraction. It is possible to define an analogous tensor A^L for its *left-hand* longitudinal contraction:

$$A^L(\mathbf{q},\omega) = \left[1 - 4\pi\frac{\mathbf{q}}{|\mathbf{q}|}\frac{\mathbf{q}}{|\mathbf{q}|} \cdot \tilde{\alpha}^{(1)}(\mathbf{q},\mathbf{q},\omega)\right]^{-1} \tag{4.102}$$

$$= 1 + 4\pi\frac{\mathbf{q}}{|\mathbf{q}|}\frac{\mathbf{q}}{|\mathbf{q}|} \cdot \frac{\tilde{\alpha}^{(1)}(\mathbf{q},\mathbf{q},\omega)}{1 - 4\pi\tilde{\alpha}^{(1),LL}(\mathbf{q},\mathbf{q},\omega)}. \tag{4.103}$$

Now $\mathbf{P}$ as it has been derived can be substituted in the definition of the macroscopic electric displacement vector Eq. (4.83) obtaining:

$$\begin{aligned}\mathbf{D}(\mathbf{q},\omega) &= \mathbf{E}(\mathbf{q},\omega) + 4\pi(\mathbf{P}^{(1)}(\mathbf{q},\omega) + \mathbf{P}^{(2)}(\mathbf{q},\omega)) \\ &= \mathbf{E}(\mathbf{q},\omega) + 4\pi A^R(\mathbf{q},\omega)\tilde{\alpha}^{(1)}(\mathbf{q},\mathbf{q},\omega)\mathbf{E}(\mathbf{q},\omega) + 4\pi A^R(\mathbf{q},\omega)\mathbf{P}^{(2)}(\mathbf{q},\omega).\end{aligned} \tag{4.104}$$

The terms that are linear in the electric field correspond to the linear response of the system i.e., the tensor of the macroscopic dielectric function ϵ_M:[22]

$$\begin{aligned}\epsilon_M(\mathbf{q},\omega) &= 1 + 4\pi A^R(\mathbf{q},\omega) \cdot \tilde{\alpha}^{(1)}(\mathbf{q},\mathbf{q},\omega), \\ &= 1 + 4\pi\tilde{\alpha}^{(1)}(\mathbf{q},\mathbf{q},\omega) \cdot A^L(\mathbf{q},\omega)\end{aligned} \tag{4.105}$$

where all is expressed in terms of averaged $\mathbf{G} = 0$ macroscopic quantities.

---

[22] This derives from its definition for linear materials $\mathbf{D} = \epsilon\mathbf{E}$ and holds also for nonlinear systems, where all the other contributions are included into the nonlinear optical coefficients: $\mathbf{D} = \epsilon\mathbf{E} + 4\pi\chi^{(2)}\mathbf{E}\mathbf{E} + \emptyset(3)$.

Second Order Macroscopic Response

Equation (4.104) of the former section contains an additional term, that accounts for the second-order nonlinear response of the system.[23] This nonlinear part that I will call for simplicity $\mathbf{D}^{(2)}$ is given by:

$$\mathbf{D}^{(2)}(\mathbf{q},\omega) = 4\pi A^R(\mathbf{q},\omega)\mathbf{P}^{(2)}(\mathbf{q},\omega). \tag{4.106}$$

It is the *macroscopic* second-order displacement vector, obtained from the average of the microscopic polarization $\mathbf{P}^{(2)}$. This term can be expressed also as function of the macroscopic polarization, as defined in Eq. (4.78)):

$$\mathbf{D}(\mathbf{q},\omega) = \mathbf{E}(\mathbf{q},\omega) + 4\pi\left(\mathbf{P}^{(1)}_M(\mathbf{q},\omega) + \mathbf{P}^{(2)}_M(\mathbf{q},\omega)\right). \tag{4.107}$$

$$\mathbf{D}^{(2)}(\mathbf{q},\omega) = 4\pi\mathbf{P}^{(2)}_M(\mathbf{q},\omega) \tag{4.108}$$

Imposing the two definition to be equal, the macroscopic second-order polarization $\mathbf{P}^{(2)}_M$ of Eq. (4.71) becomes:

$$\mathbf{P}^{(2)}_M(\mathbf{q},\omega) = A^R(\mathbf{q},\omega)\mathbf{P}^{(2)}(\mathbf{q},\omega). \tag{4.109}$$

Again, as done for the linear case one should express the microscopic polarization as function of the total field to obtain an expression for the macroscopic second-order susceptibility $\chi^{(2)}_M$. Since the microscopic polarization $\mathbf{P}^{(2)}$ is already second order in the perturbing field $\mathbf{E}^P$ it is sufficient to use the linear relation between the total and the perturbing fields to have a second order expression in $\mathbf{E}$. With this consideration Eq. (4.97) can be truncated to the first order retaining only $\mathbf{P}^{(1)}$[24] and reduces to:

$$\mathbf{P}^{(1)}(\mathbf{q},\omega) = \tilde{\alpha}^{(1)}(\mathbf{q},\mathbf{q},\omega)\mathbf{E}(\mathbf{q},\omega) + 4\pi\tilde{\alpha}^{(1)}(\mathbf{q},\mathbf{q},\omega)\frac{\mathbf{q}}{|\mathbf{q}|}\frac{\mathbf{q}}{|\mathbf{q}|}\cdot\mathbf{P}^{(1)}(\mathbf{q},\omega). \tag{4.110}$$

Substituting the averaged microscopic polarization $\mathbf{P}^{(1)}$ with Eq. (4.95) and collecting $\mathbf{E}$ and $\mathbf{E}^P$ on the opposite sides of the equation one obtains:

$$\begin{aligned}\mathbf{E}(\mathbf{q},\omega) &= \left[1 - 4\pi\frac{\mathbf{q}}{|\mathbf{q}|}\frac{\mathbf{q}}{|\mathbf{q}|}\cdot\tilde{\alpha}^{(1)}(\mathbf{q},\mathbf{q},\omega)\right]\mathbf{E}^P(\mathbf{q},\omega)\\ &= A^{L\ -1}(\mathbf{q},\omega)\mathbf{E}^P(\mathbf{q},\omega),\end{aligned} \tag{4.111}$$

$$\mathbf{E}^P(\mathbf{q},\omega) = A^L(\mathbf{q},\omega)\mathbf{E}(\mathbf{q},\omega). \tag{4.112}$$

Once this equivalence is introduced in the expression of the microscopic second-order polarization (see Eq. (4.34)), $\mathbf{P}^{(2)}$ can be written as:[25]

$$\begin{aligned}\mathbf{P}^{(2)}(\mathbf{q},\omega) = \sum_{\mathbf{q}'}\int d\omega'\ &\tilde{\alpha}^{(2)}(\mathbf{q},\mathbf{q}',\mathbf{q}-\mathbf{q}',\omega_1,\omega-\omega')\\ A^L(\mathbf{q}',\omega')A^L(\mathbf{q}-\mathbf{q}',\omega-\omega')&\mathbf{E}(\mathbf{q}',\omega')\mathbf{E}(\mathbf{q}-\mathbf{q}',\omega-\omega').\end{aligned} \tag{4.113}$$

---

[23] One should have further developed the polarization in order to include and study higher corrections.

[24] $\mathbf{P}^{(2)}$ would give rise to higher order corrections.

[25] Being $\mathbf{G} = 0$ equation (4.34) is considerably simplified. The link is immediate, identifying $(\mathbf{q}_1, \omega_1)$ with $(\mathbf{q}, \omega)$ and $(\mathbf{q}_2, \omega_2)$ with $(\mathbf{q}', \omega')$.

The macroscopic polarization is then:

$$\begin{aligned}\mathbf{P}_M^{(2)}(\mathbf{q},\omega) = \sum_{\mathbf{q}'}\int d\omega'\ A^R(\mathbf{q},\omega)\tilde{\alpha}^{(2)}(\mathbf{q},\mathbf{q}',\mathbf{q}-\mathbf{q}',\omega',\omega-\omega') \\ A^L(\mathbf{q}',\omega')A^L(\mathbf{q}-\mathbf{q}',\omega-\omega')\mathbf{E}(\mathbf{q}',\omega')\mathbf{E}(\mathbf{q}-\mathbf{q}',\omega-\omega')\end{aligned} \tag{4.114}$$

and from the definition of the macroscopic second-order dielectric susceptibility $\chi_M^{(2)}$ in the reciprocal space:[26]

$$\mathbf{P}_M^{(2)}(\mathbf{q},\omega) = \sum_{\mathbf{q}'}\int d\omega'\ \chi_M^{(2)}(\mathbf{q},\mathbf{q}',\mathbf{q}-\mathbf{q}',\omega,\omega',\omega-\omega')\mathbf{E}(\mathbf{q}',\omega')\mathbf{E}(\mathbf{q}-\mathbf{q}',\omega-\omega') \tag{4.115}$$

One has finally the relation between the microscopic ($\tilde{\alpha}^{(2)}$) and the macroscopic nonlinear polarization of matter. In addition, it allows to link $\chi_M^{(2)}$ with the microscopic response $\tilde{\alpha}^{(2)}$:

$$\begin{aligned}&\chi_M^{(2)}(\mathbf{q},\mathbf{q}',\mathbf{q}-\mathbf{q}',\omega,\omega',\omega-\omega') = \\ &\quad A^R(\mathbf{q},\omega)\tilde{\alpha}^{(2)}(\mathbf{q},\mathbf{q}',\mathbf{q}-\mathbf{q}',\omega',\omega-\omega')A^L(\mathbf{q}',\omega')A^L(\mathbf{q}-\mathbf{q}',\omega-\omega').\end{aligned} \tag{4.116}$$

In the particular case of second harmonic generation $\omega = 2\omega'$:

$$\begin{aligned}&\chi_M^{(2)}(\mathbf{q},\mathbf{q}',\mathbf{q}-\mathbf{q}',2\omega,\omega) = \\ &\quad A^R(\mathbf{q},\omega)\tilde{\alpha}^{(2)}(\mathbf{q},\mathbf{q}',\mathbf{q}-\mathbf{q}',\omega,\omega)A^L(\mathbf{q}',\omega)A^L(\mathbf{q}-\mathbf{q}',\omega).\end{aligned} \tag{4.117}$$

Link to TDDFT

The last equation presented in the previous section is not yet useful. Before one should express the second-order microscopic quasi-susceptibility $\tilde{\alpha}^{(2)}$, as obtained in Eq. (4.33) from the TD-Response Function Theory, in terms of the TDDFT density response $\chi_{\rho\rho\rho}^{(2)}$. The quasi-susceptibility $\tilde{\alpha}^{(2)}$ contains three response functions: $\chi_{\mathbf{jjj}}^{(2)}$, $\chi_{\rho\mathbf{j}}^{(1)}$ and $\chi_{\mathbf{j}\rho}^{(1)}$. The last two vanish in the limit $\mathbf{q}\to 0$ as seen in section (4.2), whereas $\chi_{\mathbf{jjj}}^{(2)}$ is related to $\chi_{\rho\rho\rho}^{(2)}$ through its longitudinal component in Eq. (4.46) via the continuity equation. Consequently from TDDFT one does not have the knowledge of the complete $\tilde{\alpha}^{(2)}$ and $\chi_M^{(2)}$, but only of their longitudinal elements (they are tensor whose elements can be decomposed into directions perpendicular or parallel with respect to the polarizations vectors $\mathbf{q}$).

Considering only the longitudinal component of the dielectric susceptibility $\chi_M^{(2)}$ means projecting it along the directions of $\mathbf{q}_2+\mathbf{q}_3$, $\mathbf{q}_2$, $\mathbf{q}_3$.[27] For simplicity of notation I will call $P_{\mathbf{q}}$ the projection operator along $\hat{\mathbf{q}}$: $P_{\mathbf{q}} = \frac{\mathbf{q}}{|\mathbf{q}|}\frac{\mathbf{q}}{|\mathbf{q}|}$.

---

[26] It has been obtained Fourier transforming Eq. (4.71).

[27] As $\tilde{\alpha}^{(2)}$ has been derived, one should project on left for the outgoing polarization $\mathbf{q}_1 = \mathbf{q}_2+\mathbf{q}_3$ and on right for the two incoming electric fields $\mathbf{q}_2$, $\mathbf{q}_3$. The projection along a certain direction $\hat{\mathbf{q}}$ of a tensor T (e.g. it can be $\tilde{\alpha}$ or χ) is given as usual by $T_{\mathbf{q}}\hat{\mathbf{q}} = (T\cdot\hat{\mathbf{q}})\hat{\mathbf{q}} = T\cdot\frac{\mathbf{q}}{|\mathbf{q}|}\frac{\mathbf{q}}{|\mathbf{q}|}$. This projection operator $\frac{\mathbf{q}}{|\mathbf{q}|}\frac{\mathbf{q}}{|\mathbf{q}|}$ correspond to a 3×3 matrix in space, whose elements are given by

$$\frac{1}{|\mathbf{q}|^2}\begin{pmatrix} q_x \\ q_y \\ q_z \end{pmatrix}\begin{pmatrix} q_x & q_y & q_z \end{pmatrix} = \frac{1}{|\mathbf{q}|^2}\begin{pmatrix} q_x^2 & q_xq_y & q_xq_z \\ q_yq_x & q_y^2 & q_yq_z \\ q_zq_x & q_zq_y & q_z^2 \end{pmatrix}.$$

What one is interested in is the second-order macroscopic polarization $\mathbf{P}_M^{(2)}$ of Eq. (4.1). In particular, because of the limits of TDDFT that can describe only the longitudinal response to a longitudinal perturbation, one restricts to the calculation of $\mathbf{P}_M^{(2)\ L}$ once assumed $\mathbf{E}$ being longitudinal ($\mathbf{E} = \mathbf{E}^L$).[28] $\mathbf{P}_M^{(2)\ L}$ is then given by

$$\begin{aligned}
&\mathbf{P}_M^{(2)\ L}(\mathbf{q}_2+\mathbf{q}_3, 2\omega) = \\
&\quad = P_{\mathbf{q}_2+\mathbf{q}_3} \cdot \mathbf{P}_M^{(2)}(\mathbf{q}_2+\mathbf{q}_3, 2\omega) = \\
&\quad = P_{\mathbf{q}_2+\mathbf{q}_3} \cdot \chi_M^{(2)}(\mathbf{q}_2+\mathbf{q}_3, \mathbf{q}_2, \mathbf{q}_3, 2\omega, \omega) \cdot \mathbf{E}(\mathbf{q}_2, \omega) \cdot \mathbf{E}(\mathbf{q}_3, \omega) = \\
&\quad = P_{\mathbf{q}_2+\mathbf{q}_3} \cdot \chi_M^{(2)}(\mathbf{q}_2+\mathbf{q}_3, \mathbf{q}_2, \mathbf{q}_3, 2\omega, \omega) \cdot P_{\mathbf{q}_2} E(\mathbf{q}_2, \omega) \cdot P_{\mathbf{q}_3} E(\mathbf{q}_3, \omega).
\end{aligned} \tag{4.118}$$

The quantity that is then needed is the longitudinal second-order susceptibility $\chi_M^{(2)\ LLL}$ that reads:

$$\begin{aligned}
&\chi_M^{(2)\ LLL}(\mathbf{q}_2+\mathbf{q}_3, \mathbf{q}_2, \mathbf{q}_3, 2\omega, \omega) = \\
&\quad = P_{\mathbf{q}_2+\mathbf{q}_3} \cdot \chi_M^{(2)}(\mathbf{q}_2+\mathbf{q}_3, \mathbf{q}_2, \mathbf{q}_3, 2\omega, \omega) \cdot P_{\mathbf{q}_2} \cdot P_{\mathbf{q}_3} \\
&\quad = P_{\mathbf{q}_2+\mathbf{q}_3} \cdot A^R(\mathbf{q}_2+\mathbf{q}_3, \omega)\tilde{\alpha}^{(2)}(\mathbf{q}_2+\mathbf{q}_3, \mathbf{q}_2, \mathbf{q}_3, 2\omega, \omega) \\
&\qquad A^L(\mathbf{q}_2, \omega) \cdot P_{\mathbf{q}_2} A^L(\mathbf{q}_3, \omega) \cdot P_{\mathbf{q}_3}.
\end{aligned} \tag{4.119}$$

Projections of the tensors $A^{R,L}$ takes a simple form considering the expressions Eqs. (4.101), (4.103):

$$\begin{aligned}
P_{\mathbf{q}} \cdot A^R(\mathbf{q}, \omega) &= A^L(\mathbf{q}, \omega) \cdot P_{\mathbf{q}} \\
&= P_{\mathbf{q}} + 4\pi P_{\mathbf{q}} \cdot \frac{\tilde{\alpha}^{(1)}(\mathbf{q}, \mathbf{q}, \omega)}{1 - 4\pi\tilde{\alpha}^{(1),LL}(\mathbf{q}, \mathbf{q}, \omega)} \cdot P_{\mathbf{q}} \\
&= \epsilon_M^{LL}(\mathbf{q}, \omega) P_{\mathbf{q}}.
\end{aligned} \tag{4.120}$$

Where $\epsilon_M^{LL}(\mathbf{q}, \omega)$ correspond to the longitudinal longitudinal contraction of the dielectric function:

$$\begin{aligned}
\epsilon_M^{LL}(\mathbf{q}, \omega) &= P_{\mathbf{q}} \cdot \epsilon_M(\mathbf{q}, \omega) \cdot P_{\mathbf{q}} \\
&= \frac{P_{\mathbf{q}}}{1 - 4\pi\tilde{\alpha}^{(1),LL}(\mathbf{q}, \mathbf{q}, \omega)}.
\end{aligned} \tag{4.121}$$

The longitudinal second-order susceptibility then reads:

$$\begin{aligned}
\chi_M^{(2)\ LLL}(\mathbf{q}_2+\mathbf{q}_3, \mathbf{q}_2, \mathbf{q}_3, 2\omega, \omega) &= 4\pi\epsilon_M^{LL}(\mathbf{q}_2+\mathbf{q}_3, 2\omega)\epsilon_M^{LL}(\mathbf{q}_2, \omega)\epsilon_M^{LL}(\mathbf{q}_3, \omega) \\
&\quad P_{\mathbf{q}_2+\mathbf{q}_3} \cdot \tilde{\alpha}^{(2)}(\mathbf{q}_2+\mathbf{q}_3, \mathbf{q}_2, \mathbf{q}_3, 2\omega, \omega) \cdot P_{\mathbf{q}_2} \cdot P_{\mathbf{q}_3}.
\end{aligned} \tag{4.122}$$

As previously pointed out, the condition deriving from the continuity equation (4.36) links the current longitudinal projection to the density (see Appendix

---

[28] As stated above, in the long wavelength limit this assumption does not represent a constraint since it holds the equivalence of longitudinal and transverse fields for vanishing wave vector. Indeed the field does not propagate and the only light polarization defines $\mathbf{q}$. Under this assumption $\mathbf{E}$ can be written as

$$\mathbf{E} = \mathbf{E}^L \equiv P_{\mathbf{q}} E.$$

D.3). This equation can then be exploited in order to obtain an expression for $P_{\mathbf{q}}\chi^{(2)}_{\mathbf{jjj}} = P_{\mathbf{q}}\tilde{\alpha}^{(2)}$ as functions of $\chi^{(2)}_{\rho\rho\rho}$:

$$\begin{aligned} \mathbf{q}\cdot\hat{\mathbf{j}}(\mathbf{q},\omega) &= i\omega\hat{\rho}(\mathbf{q},\omega) \\ |\mathbf{q}|P_{\mathbf{q}}\cdot\hat{\mathbf{j}}(\mathbf{q},\omega) &= i\omega\hat{\rho}(\mathbf{q},\omega) \end{aligned} \tag{4.123}$$

The microscopic quasi-susceptibility $\tilde{\alpha}^{(2)}$ of Eq. (4.33) when Fourier transformed in reciprocal space takes the form:

$$\tilde{\alpha}^{(2)}(\mathbf{q}_2+\mathbf{q}_3,\mathbf{q}_2,\mathbf{q}_3,\omega_2,\omega_3) = -\frac{i}{\omega_2\omega_3(\omega_2+\omega_3)}\frac{1}{2}\chi^{(2)}_{\mathbf{jjj}}(\mathbf{q}_2+\mathbf{q}_3,\mathbf{q}_2,\mathbf{q}_3,\omega_2,\omega_3) \tag{4.124}$$

where $\chi^{(2)}_{\rho\mathbf{j}}$ is zero and $\chi^{(2)}_{\mathbf{j}\rho}$ vanish in the long wavelength limit. Using then Eq. (4.123) allow to obtain the longitudinal projection of $\tilde{\alpha}^{(2)}$ as:

$$\begin{aligned} &P_{\mathbf{q}_2+\mathbf{q}_3}\cdot\tilde{\alpha}^{(2)}(\mathbf{q}_2+\mathbf{q}_3,\mathbf{q}_2,\mathbf{q}_3,2\omega,\omega)\cdot P_{\mathbf{q}_2}\cdot P_{\mathbf{q}_3} = \\ &\frac{1}{2}\frac{1}{|\mathbf{q}_2+\mathbf{q}_3|q_2q_3}\chi^{(2)}_{\rho\rho\rho}(\mathbf{q}_2+\mathbf{q}_3,\mathbf{q}_2,\mathbf{q}_3,2\omega,\omega) \end{aligned} \tag{4.125}$$

giving then

$$\begin{aligned} \chi^{(2)\ LLL}_{M}(\mathbf{q}_2+\mathbf{q}_3,\mathbf{q}_2,\mathbf{q}_3,2\omega,\omega) &= -2\pi\frac{1}{|\mathbf{q}_2+\mathbf{q}_3|q_2q_3} \\ \epsilon^{LL}_{M}(\mathbf{q}_2+\mathbf{q}_3,2\omega)\epsilon^{LL}_{M}(\mathbf{q}_2,\omega)\epsilon^{LL}_{M}(\mathbf{q}_3,\omega)&\chi^{(2)}_{\rho\rho\rho}(\mathbf{q}_2+\mathbf{q}_3,\mathbf{q}_2,\mathbf{q}_3,2\omega,\omega). \end{aligned} \tag{4.126}$$

It is clear that the TDDFT response is modulated in frequency by three different dielectric functions at frequency ω and 2ω. Moreover it is evident that only $\chi^{(2)\ LLL}_{M}$ can be evaluated from the density response, although in the limit $\mathbf{q}\to 0$ valid for optical processes this does not represent a limitation for the applicability of TDDFT.

The scalar quantity $\chi^{(2)\ LLL}_{M}$ constitute only one element of the whole tensor $\chi^{(2)}_{M}$, identified by the polarization vectors $(\mathbf{q}_2,\mathbf{q}_3)$. It is however possible to reduce the independent elements through symmetry consideration on the crystalline structure, and finding relations between the remaining components. In this way $\chi^{(2)\ LLL}_{M}$ can provide more information than the ones strictly connected to the particular choice of $(\mathbf{q}_2,\mathbf{q}_3)$ when necessary. This will be addressed more in detail once the specific structures I present in this work will be analized. As an example I present here the final result for the cubic symmetry, whose tensor has only one independent element, $\chi^{(2)}_{xyz}$ that reads:

$$\chi^{(2)}_{xyz}(2\omega) = -\frac{i}{24}\epsilon(\mathbf{x},2\omega)\epsilon(\mathbf{y},\omega)\epsilon(\mathbf{z},\omega)\chi^{(2)}_{\rho\rho\rho}(\mathbf{x},\mathbf{y},\mathbf{z},2\omega,\omega). \tag{4.127}$$

The module of these tensor elements is the quantity experimentally measured.

Chapter 5

The 2light code

The 2LIGHT code [72, 73] has been written by the European Theoretical Spectroscopy Facility (ETSF) group of Palaiseau[1] and it implements the ab-initio calculation of the SHG process. The code is based originally on DP [154], another ETSF code for the linear optic calculation in solids. During my PHD research activity I have developed the code at many different levels: i) introducing new features as the possibility of renormalization of the results when vacuum is inluded in the simulation cell, ii) optimizing the code for better performances also reducing the memory requirements, and iii) implementing a parallel version of the latter in order to make calculations faster. All this work, that constituted the majority of my activity, was necessary in order to simulate the system of interest, for which ab initio SHG calculations demonstrated to be expensive both in terms of memory and cpu-time requirement.

SHG computation in practice

The practical calculation of the SHG response function $\chi^{(2)}$, accordingly to the formalism presented in this thesis, is performed in two steps:

- the solution of the KS system (wave functions and eigenvalues) through a DFT calculation,
- the computation of the KS and full response functions $\chi_0^{(2)}$, $\chi^{(2)}$ via the developed SHG formalism.

The first calculation exploits the existing open-source code ABINIT [121]. It is a *package whose main program allows one to find the total energy, charge density and electronic structure of systems made of electrons and nuclei (molecules and periodic solids) within Density Functional Theory, using pseudo-potentials and a plane waves or wavelet basis.* ABINIT *also includes options to optimize the geometry according to the DFT forces and stresses, or to perform molecular dynamics simulations using these forces,* [...]. ABINIT *is a project that favours development and collaboration.*[2]

---

[1] Laboratoire des Solides Irradiés, Ecole Polytechnique, Palaiseau (France).

[2] This introduction has been taken from the ABINIT package's presentation at *http://www.abinit.org.*

DFT calculations on a converged and relaxed system obtained with ABINIT constitute the starting point of the subsequent SHG calculation. The latter is performed with the code 2LIGHT that will be presented more in detail in the following section. Input quantities are the DFT Kohn-Sham wave functions $\psi_{n\mathbf{k}}^{KS}(\mathbf{r})$ and the respective single particle energies $\epsilon_{n\mathbf{k}}^{KS}$ (as seen in chapter 4 equation (4.56)) that are stored in an unique ABINIT's output file with the "`KSS`" extension.

The linear and SHG spectra can be obtained from the KS response functions of Eq. (4.54) and (4.53), introducing them into the Dyson equations (3.26), (3.33) providing a suitable f_{xc} kernel.

Further details on ABINIT, a description of the input parameters and its usage can be found in [121] and on the code's website *http://www.abinit.org* where tutorials are also provided. In the following I will give only the necessary numerical details concerning the calculation variables of physical meaning presented in section 2.5.

5.1 2light Input Description

The KSS file, where the Kohn-Sham wave functions and eigenvalues are stored, constitutes the main input of the calculation from which 2LIGHT gets also the informations about the cell geometry (its dimension, the number, position and species of the atoms) and the set of parameters upon which the calculation is performed (e.g., the **k**-mesh, the maximum band index and the planewaves used to describe the wave functions). These quantities are fixed in the DFT simulation while the SHG parameters are then chosen seeking for convergence in the following 2LIGHT calculation.

5.1.1 Numerical Details

Input quantities are provided on a plane wave basis, obtained imposing periodic boundary conditions at the cell's border and describing the system in terms of its Bloch's states. As I have briefly introduced in section 2.5 some approximations and truncations of the basis have to be imposed in order to have a limited number of quantities to be stored in memory by the calculator, making the calculation feasible in reasonable time. This of course cannot be regardless of the convergence of the results as discussed previously, and tests are always necessary. Only where meaningful I will present convergence studies, while elsewhere I will give the technical details of the calculation and its convergence parameters.

As for the DFT calculation, there are technological and practical limitations that do not allow calculations on the complete basis and series the main quantities have been expressed on (i.e., the infinite vacuum states or the plane wave basis). Here I provide a list of the parameters[3] that have to be set in a SHG calculation performed with the 2LIGHT code, and their relative description.

---

[3] Some of the parameters are identical to the ones of DP [154], especially the structure of the input files.

Numerical Approximations to Physical Quantities:

- ω **range**: it is the frequency range within the calculation of $\chi^{(2)}$ is performed. It is identified by three parameters **omegai**, **omegae** and **domega** that represent respectively the start, end and step values of the frequency grid on which the spectrum is evaluated.

- **npwwfn**: the parameter establishes the number of plane waves to be used in the description of the KS single particle states. By default it is reduced to be equal to the number of plane waves in the last closed shell.[4] Alternatively one can choose the number of closed shells **npwsh**.

- **nbands**: it represents the maximum band index to be considered in the construction of the KS susceptibilities. To obtain the whole $\chi^{(2)}$ at each frequency one would require all the empty states. Nevertheless, reducing into a certain frequency range the transitions that are far away from the band gap are not involved, contributing to the higher frequency spectrum only.[5] It is then possible to truncate the summation to $N \leq$**nbands**.

- **lomo**: this parameter is the counterpart of **nbands** for the occupied states. If one is looking at low energies only the highest valence states are involved (or the corresponding *pseudo*-states if pseudopotentials are used).

- **npwmat**: it is the number of **G** vectors to be considered in the representation of the microscopic KS response functions matrices. $\chi_0^{(1)}(\mathbf{G}_1, \mathbf{G}_2, \omega)$ is then represented in the reciprocal space as a two dimensional matrix of range **npwmat**×**npwmat**, while $\chi_0^{(2)}(\mathbf{G}_1, \mathbf{G}_2, \mathbf{G}_3, 2\omega, \omega)$ will be a three-dimensional matrix.

Code Optimizations and Developments:

There are other parameters internal to the code, that can be set up in order to improve the speed of the calculation. I do not report here their detailed description because they have no physical meaning, nevertheless they are fundamental for the computation. In order to pursue the studies here presented, and improving the performance of 2LIGHT, they have been necessary various modifications and developments. This has constituted a prominent part of my activity, and in the following I will briefly present my work on the code.

(I) **Restart capabilities**. In 2light are implemented two restart possibilities: one on the transitions-cycle i.e., the summations that give $\chi_0^{(1)}$ and $\chi_0^{(2)}$ in Eqs. (4.53) and (4.54), and another one on the **G** vectors of these matrices. The first permits to reload an interrupted calculation storing intermediate results. The last one instead allow to improve the calculation

---

[4] As described in sec. 2.5 the number of plane waves n_{pw} does not vary continuously increasing the cutoff energy E_{cut}. If **npwwfn** does not match one of these n_{pw} values, the last shell is not closed. It means that along different directions in the reciprocal space one is considering a different cutoff and plane waves, loosing the symmetry and consequently impoverishing the accuracy of the result.

[5] This can be directly seen in the summations of Eqs. (4.53) and (4.54), where contributions from transitions that are too far in energy from the frequencies of interest give large denominators making their terms negligible.

using a larger **npwmat** parameter to describe the susceptibility matrices starting from a previous calculation on a smaller matrix's dimension. This is particularly useful during convergence tests over **npwmat**. Indeed the $\chi_0^{(2)}$ matrix dimension is proportional to $(\mathbf{npwmat})^3$ and calculations become quickly very long and memory consuming. Hence it revealed useful to avoid double counting of the elements that are already available from a previous calculation.

(II) **Grid separation**. The principal summation of Eqs. (4.53) and (4.54) are performed respectively on 2 and 3 band indexes for each k-point belonging to the grid over which one samples the Brillouin Zone.[6] Since terms belonging to different k-points are independent, the grid can be decomposed in smaller sub-grids diminishing computational requirements both for the DFT and SHG calculations. Subsequently, through an appropriate setting of the input parameters it is possible to collect the various responses over the different grids in a *total* response function. During this operation the required memory is not increased and calculation results faster. In addition the convergence over the chosen k-points set can always be improved adding new grids to the final results. This feature avoids time and resources wasting that are present if convergence is studied on a single k-points grid.[7]

(III) **Division of $\chi_0^{(i)}$ matrices for memory saving**. The microscopic KS response functions $\chi_0^{(1)}$ and $\chi_0^{(2)}$ are matrices of order $(\mathbf{npwmat})^2$ and $(\mathbf{npwmat})^3$ in the $\mathbf{G}-$vectors. The memory required to store the second one can be significant when local fields (they will be defined later in this chapter) are important and slowly converging. This translates in high values of **npwmat**. In order to reduce this bottleneck that did not allow big calculations, I have modified the code 2LIGHT redefining the algorithm and subroutines for the calculation of $\chi_0^{(2)}$. Now the cubic matrix can be divided into layers, storing data and performing calculation on several $(\mathbf{npwmat})^2$ matrices, that are allocated and used separately, consequently saving memory.

(IV) **Re-definition of the transitions cycle.** I have implemented a new procedure for the evaluation of the second-order KS response function. The original cycle over the transition elements in Eq. (4.54) (i.e., the sum over the states identified by the band index and the k-point) has been reorganized without loosing of speed performance. The memory requirements relative to the calculation of $\chi_0^{(2)}$ are now independent of the total number of transitions. This means that the computational resources are independent of the size and complexity of the system and fixed a priori

---

[6] For computational needs one has to approximate the integration over the full Brillouin Zone with a finite summation over a sampling grid of reciprocal k-points.

[7] This improvement was mandatory to perform studies on big size systems such as the Si/CaF$_2$ interface presented below, where already DFT calculations need a large amount of resources and time. Hence every unnecessary double-counting or re-calculation should be avoided. Before, converging over the k-mesh meant running various calculations each time increasing the grid and solving the KS secular equation for all its points. Now one can retain the old grid running the calculation for the new added points only.

by the user.[8] Before the cange, this represented a great bottleneck of the code, preventing the simulation of the large-size systems as the ones presented in this thesis. Indeed the memory previously required to store all the transitions involved, could easily pass e.g. the 120 GByte available on a typical computing node where calculations have been performed.[9] This because of the nonlinear increase of the transitions, that in first approximation can be related to (**nbands**)^3 since the SHG process and more generally $\chi_0^{(2)}$ involves combinations of three-bands indexes (see section 4 Eq. (4.56)). When the dimension of the system is increased (e.g. using supercell methods) this number rapidly increase too. As an example, on the smaller Si/CaF$_2$ interface system presented in chapter 6, the memory requirement for a converged result has been diminished from 80 GBytes down to 4 GBytes with the new procedure, without loosing speed in the overall calculation.

(V) **Parallelization of the code.** The other limitation I have encountered during the simulations corresponds to the large amount of time required to evaluate the linear and especially the nonlinear response. This time is roughly proportional to the number of transitions and to the dimension of the $\chi_0^{(i)}$ matrices. To improve the performances of the code, making feasible simulations that would else be too long, a parallel version of the code has been implemented. This work has been done during my PHD activity thanks to the support and resources of the HPC-Europa2 project, in collaboration with the GENCI-CINES HPC center in Montpellier. The parallelization strategy has been focused on two part of the code where the majority of the time is spent. At first the calculation of the transition elements i.e., $\langle\psi_{n\mathbf{k}}|H_{1,2\ \mathbf{k}}|\psi_{n\mathbf{k}}\rangle$ of Eqs. (4.66)-(4.69) when perturbation theory is applied to the limit $\mathbf{q} \to 0$. Secondly I have parallelized the cycles for the evaluation of $\chi_0^{(1)}$, $\chi_0^{(2)}$, where the summation over the different transition elements is performed. This has been achieved through a shared memory paradigm, using OpenMP. The code is not entirely parallel hence one does not expect a linear scaling. Nevertheless, the efficiency of these two parallel parts is almost linear especially if applied to big size systems where the time spent in the creation of the parallel environment becomes negligible with respect to the one spent in the calculation.

5.2 Available Approximations

So far, I have introduced the numerical approximations that are intrinsic to the possibility to perform a finite calculation of the SHG response of the system (e.g., the **npwwfn** and **npwmat** parameters). Other approximations instead arise from the unknown response of the system (the exchange correlation terms) that have be included into the functional derivative v_{XC} of the DFT potential and the TDDFT kernel f_{xc}. The first has been exhaustively treated in chapter 2

---

[8] For this purpose it has been introduced a new computation flag named **nt2_elements** that fix the number of iteration to be stored at each calculation step.

[9] The majority of the results here presented have been obtained thanks to the resources of the CINECA-HPC center. In particular calculations have been performed on the *sp6* cluster with 32 cores per node and 120 GBytes of RAM per node. Therefore it represents the limit of the available memory for the serial calculation.

while the second will be deepened in this section describing the several levels of approximation implemented in 2LIGHT.

The main characteristic of adopting TD Perturbation Theory to TDDFT is that the final response can be obtained through a Dyson equation both for the linear (Eq. (3.26)) and the nonlinear case (Eq. (3.33)):

$$\chi^{(1)} = \chi_0^{(1)} + \chi_0^{(1)}(v + f_{xc})\chi^{(1)} \tag{5.1}$$

$$\left[\hat{1} - \chi_0^{(1)} f_{vxc}\right]\chi^{(2)} = \chi_0^{(2)}\left[\hat{1} + f_{vxc}\chi^{(1)}\right]\left[\hat{1} + f_{vxc}\chi^{(1)}\right] + \chi_0^{(1)} g_{xc}\chi^{(1)}\chi^{(1)}. \tag{5.2}$$

In the usual frequency-momenta space it becomes [47,50,70ArtLEO]:[10]

$$\begin{aligned}
&\sum_{\mathbf{G}_2}\left[\delta_{\mathbf{G},\mathbf{G}_2} - \sum_{\mathbf{G}_1}\chi^{(1)}_{0,\mathbf{G}\mathbf{G}_1}(2\mathbf{q},2\mathbf{q},2\omega) f_{vxc,\mathbf{G}_1\mathbf{G}_2}(2\mathbf{q},2\mathbf{q},2\omega)\right]\times \\
&\chi^{(2)}_{\mathbf{G}_2,\mathbf{G}',\mathbf{G}''}(2\mathbf{q},\mathbf{q},\mathbf{q},2\omega,\omega) = \sum_{\mathbf{G}_1\mathbf{G}_3}\chi^{(2)}_{0,\mathbf{G},\mathbf{G}_1,\mathbf{G}_3}(2\mathbf{q},\mathbf{q},\mathbf{q},2\omega,\omega)\times \\
&\qquad\left[\delta_{\mathbf{G}'',\mathbf{G}_3} + \sum_{\mathbf{G}_4} f_{vxc,\mathbf{G}_3\mathbf{G}_4}\chi^{(1)}_{\mathbf{G}_4\mathbf{G}''}(\mathbf{q},\mathbf{q},\omega)\right]\times \\
&\qquad\left[\delta_{\mathbf{G}',\mathbf{G}_1} + \sum_{\mathbf{G}_2} f_{vxc,\mathbf{G}_1\mathbf{G}_2}\chi^{(1)}_{\mathbf{G}_2\mathbf{G}'}(\mathbf{q},\mathbf{q},\omega)\right] + \\
&\sum_{\mathbf{G}_1\mathbf{G}_2\mathbf{G}_3}\chi^{(1)}_{0,\mathbf{G}\mathbf{G}_1}(2\mathbf{q},2\mathbf{q},2\omega) g_{xc,\mathbf{G}_1\mathbf{G}_2\mathbf{G}_3}(2\mathbf{q},\mathbf{q},\mathbf{q},2\omega,\omega)\times \\
&\qquad\chi^{(1)}_{\mathbf{G}_2\mathbf{G}'}(\mathbf{q},\mathbf{q},\omega)\chi^{(1)}_{\mathbf{G}_3\mathbf{G}''}(\mathbf{q},\mathbf{q},\omega).
\end{aligned} \tag{5.3}$$

One should notice that $\chi_0^{(i)}$ are the KS *density response functions* and $\chi^{(i)}$ the full density response functions $\chi^{(1)}_{\rho\rho}$, $\chi^{(2)}_{\rho\rho\rho}$. The latter should be substituted into Eq. (4.126) thanks to its relation with the density-current response $\chi^{LLL}_{\mathbf{jjj}}$ to get the desired second-order dielectric susceptibility $\chi^{(2)}_M$.

Thanks to the form the second-order response takes, it is straightforward to improve the accuracy of the results when necessary. Indeed one can use more sophisticated f_{vxc}, g_{xc} kernels and better describe the tensors increasing the **G**-vectors expansion (i.e., the dimension of the $\chi_0^{(i)}$ matrices) before the final result is averaged at $\mathbf{G} = 0$. Up to now there are different levels of approximation that have been implemented into 2LIGHT.

---

[10] The tensors $\chi^{(1)}(\mathbf{q}_1 + \mathbf{G}_1, \mathbf{q}_2 + \mathbf{G}_2, \omega)$ depends on $\mathbf{q} + \mathbf{G}$, where the vectors **G** belong to the reciprocal lattice. Hence they are a discrete variable and $\chi^{(1)}$ can then be represented as a matrix over **G** indexes:

$$\chi^{(1)}(\mathbf{q}_1 + \mathbf{G}_1, \mathbf{q}_2 + \mathbf{G}_2, \omega) = \chi^{(1)}_{\mathbf{G}_1,\mathbf{G}_2}(\mathbf{q}_1, \mathbf{q}_2, \omega).$$

The same holds for the KS response function that can be represented as $\chi^{(1)}_{0,\mathbf{G}_1\mathbf{G}_2}$ and the nonlinear responses $\chi^{(2)}_{0,\mathbf{G}_1\mathbf{G}_2\mathbf{G}_3}$, $\chi^{(2)}_{\mathbf{G}_1\mathbf{G}_2\mathbf{G}_3}$. This compact notation makes clearer the meaning of **G**-vectors basis expansion and its numerical truncation, showing that the Dyson equations consists of matrices products. The macroscopic average $\mathbf{G} = 0$ is then performed once the final microscopic result $\chi^{(1)}$, $\chi^{(2)}$ are evaluated from the Dyson equation retaining all the **G**-vectors.

Here I present the ones adopted in this thesis. Higher order variations of the exchange-correlation kernels are neglected in the following, imposing $g_{xc} = \frac{\delta^2 v_{XC}}{\delta\rho\delta\rho} = 0$. I will now describe in details the approximations to the second-order Dyson-like equation (5.2). They are adopted at the same time in the linear response of Eq. (5.1).

5.2.1 Independent Particle Approximation in the SHG spectrum

Independent Particle Approximation (IPA) is the simplest approximation to Eq. (5.2) and represents the standard approach used in literature so far [13, 22, 50, 54, 57, 70, 152]. It is obtained treating the electrons as non-interacting particles. This means that all the many-body effects are neglected posing $f_{xc} = 0$.[11] At the same time also local fields effects are not considered restricting the **G**-vector expansion to the only $\mathbf{G}_1, \mathbf{G}_2, \mathbf{G}_3 = 0$ elements. This means to consider the macroscopic average of $\chi_0^{(i)}$ when the Dyson equation is evaluated. All the involved quantities become scalar objects. Hence the off-diagonal elements, that enter in the matrices products or inversions, are here neglected (the meaning will be treated more in detail in the local field approximation).

With this particular choice only the Coulomb potential $f_v = v$ remains, and solving the Dyson equations one has:

$$\chi^{(1)} = \chi_0^{(1)} + \chi_0^{(1)} v \chi^{(1)} \tag{5.4}$$

$$\chi^{(2)} = \left[1 + \chi^{(1)} v\right] \chi_0^{(2)} \left[1 + v\chi^{(1)}\right] \left[1 + v\chi^{(1)}\right]. \tag{5.5}$$

Now, recognizing that

$$\left[\epsilon^{LL}\right]^{-1} = 1 + v\chi^{(1)} = 1 + \chi^{(1)} v \tag{5.6}$$

because they are scalar quantities in IPA, $\chi^{(2)}$ becomes:

$$\chi^{(2)} = \left[\epsilon^{LL}\right]^{-1} \chi_0^{(2)} \left[\epsilon^{LL}\right]^{-1} \left[\epsilon^{LL}\right]^{-1} \tag{5.7}$$

The latter substituted to $\chi^{(2)}_{\rho\rho\rho}$ in Eq. (4.126) gives:

$$\begin{aligned} \chi_M^{(2)\ LLL}&(\mathbf{q}_2 + \mathbf{q}_3, \mathbf{q}_2, \mathbf{q}_3, 2\omega, \omega) = \\ &- 2\pi \frac{1}{(q_2 + q_3) q_2 q_3} \epsilon_M^{LL}(\mathbf{q}_2 + \mathbf{q}_3, 2\omega) \\ &[\epsilon_M^{LL}(\mathbf{q}_2 + \mathbf{q}_3, 2\omega)]^{-1} \chi_0^{(2)}(\mathbf{q}_2 + \mathbf{q}_3, \mathbf{q}_2, \mathbf{q}_3, 2\omega, \omega) \\ &[\epsilon_M^{LL}(\mathbf{q}_2, \omega)]^{-1} \epsilon_M^{LL}(\mathbf{q}_2, \omega) [\epsilon_M^{LL}(\mathbf{q}_3, \omega)]^{-1} \epsilon_M^{LL}(\mathbf{q}_3, \omega) \\ &= -2\pi \frac{1}{|\mathbf{q}_2 + \mathbf{q}_3| q_2 q_3} \chi_0^{(2)}(\mathbf{q}_2 + \mathbf{q}_3, \mathbf{q}_2, \mathbf{q}_3, 2\omega, \omega). \end{aligned} \tag{5.8}$$

Thus, in the IPA the macroscopic susceptibility corresponds to the microscopic response of the non-interacting system. This is physically intuitive since one is neglecting the many-body interaction posing the exchange-correlation potential

---

[11] I remind that $f_{vxc} = f_v + f_{xc}$ where the Hartee functional f_v coincides with the bare Coulomb potential $f_v = \frac{\delta v_H}{\delta\rho} = v$ and $f_{xc} = \frac{\delta v_{XC}}{\delta\rho}$ is the exchange-correlation functional.

equal to zero. Nevertheless it is not trivial because everything pass through two Dyson equations and is modulated by three dielectric functions in Eq. (4.126).

It is immediate to notice that this approximation is simple since no particular knowledge of f_{xc} is required and from a computational point of view is the less time and memory consuming since the **G** expansion series are reduced to one point. For this reason it represents the standard approach in literature to the study of complex and big-size systems, as the ones considered in this thesis. The IPA, although is a drastic simplification, can however get some important features of the real response and reveals a good starting point. Its validity and accuracy depend mainly on the physical nature of the system under investigation, as I will show later in the results. Therefore, in materials where local fields and many-body effects are small, already IPA can provide a trustful description of the material.

5.2.2 Local Fields in the Random Phase Approximation

This approximation is obtained retaining only the microscopic variation in the induced Hartree potential, thus still neglecting the exchange and correlation interaction between the electrons: $f_{vxc} = f_v = v$. This is called the Random Phase Approximation (RPA) [130]. With respect to IPA the microscopic quantities are described on the **G**-basis[12] keeping their **G** dependence. Retaining higher **G** vectors means that density variation up to the atomic scale are considered. The following microscopic induced field, in turn, can then polarize the material nearby, contributing to the overall perturbation. Since these fields are rapidly varying as the underlying microscopic density from which they are originated, the response depends locally on the lattice structure and these effects are called *crystal local fields effects* (LF). Depending on how much rapid variations are, the **G** basis should be improved to correctly describe it.

Contrary to IPA, all these microscopic induced polarization effects are taken into account when solving the linear and nonlinear Dyson equation:

$$\sum_{\mathbf{G}_2}\left[\delta_{\mathbf{G},\mathbf{G}_2} - \sum_{\mathbf{G}_1}\chi^{(1)}_{0,\mathbf{G}\mathbf{G}_1} v_{\mathbf{G}_1\mathbf{G}_2}\right]\chi^{(2)}_{\mathbf{G}_2,\mathbf{G}',\mathbf{G}''} =$$
$$\sum_{\mathbf{G}_1\mathbf{G}_3}\chi^{(2)}_{0,\mathbf{G},\mathbf{G}_1,\mathbf{G}_3}\left[\delta_{\mathbf{G}'',\mathbf{G}_3} + \sum_{\mathbf{G}_4} v_{\mathbf{G}_3\mathbf{G}_4}\chi^{(1)}_{\mathbf{G}_4\mathbf{G}''}\right]\left[\delta_{\mathbf{G}',\mathbf{G}_1} + \sum_{\mathbf{G}_2} v_{\mathbf{G}_1\mathbf{G}_2}\chi^{(1)}_{\mathbf{G}_2\mathbf{G}'}\right]. \tag{5.9}$$

The macroscopic average is then performed at the end of the calculation posing $\mathbf{G} = \mathbf{G}' = \mathbf{G}'' = 0$.

A more intuitive example of the different behavior of the IPA and RPA responses is provided by the dielectric function $\epsilon_M(\omega)$ [155]. It is connected to the inverse of the microscopic dielectric function $\epsilon_{\mathbf{G}\mathbf{G}'(\mathbf{q},\omega)}$ through the macroscopic average:

$$\epsilon_M(\omega) = lim_{\mathbf{q}\to 0}\frac{1}{\epsilon^{-1}_{\mathbf{G}\mathbf{G}'}(\mathbf{q},\omega)|_{\mathbf{G}=\mathbf{G}'=0}} \tag{5.10}$$

In IPA $\epsilon_{\mathbf{G}\mathbf{G}'}(\mathbf{q},\omega) = \epsilon_{00}(\mathbf{q},\omega)$ is a scalar quantity and one gets $\epsilon_M(\omega) = lim_{\mathbf{q}\to 0}\epsilon_{00}(\mathbf{q},\omega)$. In RPA instead one should invert the full matrix $\epsilon_{\mathbf{G}\mathbf{G}'}(\mathbf{q},\omega)$

---

[12] As previously stated, for practical reason one restrict the calculation to a converged set of **G**-vectors i.e, one represents χ as square (or cubic) matrices.

before averaging. In the inversion process all the off-diagonal terms of $\epsilon_{\mathbf{GG}'}$ describing the microscopic nonlocal fields are mixed with the diagonal ones. In particular they enter in $\epsilon^{-1}_{\mathbf{GG}'}(\mathbf{q},\omega)|_{\mathbf{G}=\mathbf{G}'=0}$ modifying the macroscopic averaged response.

At the second order, formulas are more complex and many terms weight in the final response, just remembering that the dielectric susceptibility $\chi^{(2)}$ is obtained from Eq. (4.126) where the result of the Dyson equation is modulated by three dielectric functions. It is therefore difficult to predict how they modify the IPA response or understand through which quantities of Eq. (5.9) they have the major contribution. I will show a detailed analysis in chapter 6.

As LF effects have been described, it is immediate to notice that their importance depends entirely on the nature of the system. In particular they revealed essential when the material presents inhomogeneities, defects or other characteristic that give rise to rapid variations in the microscopic polarization, whereas they demonstrated negligible for highly homogeneous systems. This holds also for sharp macroscopic discontinuities, as in the presence of an interface or a surface, or for finite system where LF could give rise to depolarization effects [145]. This is in agreement also with the outcomes of the macroscopic Effective Medium Theory [145, 156]. Their importance will be treated more in detail later while presenting the results. In general one should expect a redistribution of the oscillator strength that leads to shift the peaks in the linear and SHG spectra towards higher energies, decreasing the overall intensity in order to preserve the *f-sum rule* [157, 158]. However their influence is generally unpredictable especially in the case of sharp discontinuity materials like interfaces or surfaces.

Tests should always be performed to check the relative importance of LF effects inclusion when possible. Up to now only few ab initio studies that include LF have been presented in literature [64, 66, 67], while the majority of the studies are performed in the IPA. This is because of the great difficulty to develop a theory as the one proposed here, where LF can be easily identified in the formalism and equations. Moreover their inclusion greatly affects the computational effort increasing both the memory ($\chi^{(2)}$ matrices are proportional to $(\mathbf{npwmat})^3$) and time requirements.

5.2.3 Adiabatic Local Density Approximation

This particular kernel has been already presented in section 3. It provides a first approximation to the exchange and correlation kernel that is neglected in the previous cases. It is the time-dependent generalization of the LDA in DFT. Assuming the LDA exchange correlation potential $v_{XC}(\mathbf{r},t,[\rho])$ being local in space and instantaneous in time (this approximation takes the name of Adiabatic Local Density Approximation ALDA) [135]:

$$v_{XC}^{ALDA}(\mathbf{r},t,[\rho]) = v_{XC}^{LDA}(\rho(\mathbf{r},t)), \tag{5.11}$$

the TDDFT kernel named TDLDA takes the form

$$\begin{aligned} f_{xc}^{ALDA}(\mathbf{r}_1,\mathbf{r}_2,t_1,t_2) &= \delta(\mathbf{r}_1-\mathbf{r}_2)\delta(t_1-t_2)\frac{\delta v_{XC}^{LDA}(\rho(\mathbf{r}_1,t_1))}{\delta\rho(\mathbf{r}_2,t_2)} \\ &= \delta(\mathbf{r}_1-\mathbf{r}_2)\delta(t_1-t_2)\left.\frac{\delta v_{XC}^{LDA}(\rho(\mathbf{r}_1,\omega))}{\delta\rho(\mathbf{r}_2,\omega)}\right|_{\omega=0}. \end{aligned} \tag{5.12}$$

Because of its instantaneous nature it neglects the memory effects (it is a static kernel) while its locality get rid of the nonlocal XC density interaction. It is a first drastic approximation to the unknown f_{xc} nevertheless, as LDA demonstrated successful in a variety of systems, even TDLDA works well e.g. for excitation properties of finite systems or electron energy loss spectroscopy (EELS) and ion X-ray scattering spectroscopy (IXSS) in extended matter. However it fails in the calculation of optical ($q = 0$) spectra of solids [130, 159, 160] due to the wrong asymptotic behavior of the exchange-correlation kernel [159]. In particular for this kind of system it only slightly improves the RPA optical absorption [159, 161] or the second harmonic generation spectra [72–74] with minor modifications. For this reason it is not appreciated as a good candidate for optics and SHG spectroscopy going beyond the RPA, and other ways should be followed.

5.2.4 Quasi-Particles Corrections

In chapter 2 I have presented in detail the problem of the gap underestimation that arise in DFT, especially if LDA is adopted. Differences among the KS eigenenergies $(\epsilon_{n\mathbf{k}} - \epsilon_{m\mathbf{k}})$ as the ones present at the denominators of $\chi_0^{(i)}$ in Eqs. (4.66)-(4.69), can give rise to deviations from the correct results. One should then provide a correction to the non-interacting band-structure in order to consider the exact *quasi-particle* energies, determined by the screening of the hole the electron lefts behind.

Indeed one can see the neutral excitation process in three steps:

(I) the electron is excited from its initial state and leaves a hole behind it.

(II) This hole interacts both with the system and the promoted electron. In the first case it is seen as a positive charge that attracts the neighboring electrons, surrounding itself of a cloud of opposite charge. This rearrangement of the system density is a screening effect, that mediates the interaction of the bare excited particle with the KS system. The union of the particle together with its screening takes the name of *quasi-particle*.[13] This can be thought as a single particle process and is well accounted for in MBPT Hedin's equations [162, 163], in particular by the first order Green's function. The Green's function describes the propagation of the *quasi-particle* and allows to obtain information about the *quasi-particle*'s energies (from its poles) and wave functions. This set of five connected equations is usually solved in the GW Approximation for the Self-Energy, where eigenfunctions are supposed not to vary from the intial LDA-KS and one cycle of Hedin's equations provides the *quasi-particle* energy corrections. For further details please refer to [162, 164–168].

(III) The last step is represented by the direct interaction of the hole with the promoted electrons. Both of them are interacting with the medium, hence locally modifying the surrounding environment, i.e., they can be thought

---

[13] This can be interpreted as a reorganization of the system once the electron has been promoted from state n to state m in order to get the minimum energy configuration. Indeed the KS ground state of a DFT calculation with $N - 1$ electrons does not correspond to the ground state of a N independent particles system where the topmost electron has been eliminated.

as quasi-particles. However, these quasi-particles are not independent and propagate during their lifetime interacting each other by Coulomb attraction. This two-body interaction between the electron and the hole is called the exciton, and its influence on the final optical response is identified as the *excitonic effects*. Later in this chapter these effects will be treated more in detail.

In the Kohn Sham system the non-interacting nature of the particles shifts all these dynamical informations in the exchange correlation kernel. However they are lost in the LDA and this lack translates in a general shift of the peaks position.

The third step is complicated involving two-particle effects that should be accounted in the f_{xc} kernel. The second one is instead a single-particle process, whose effects can be directly included in the KS system modifying the energies and wave functions at the basis of the KS response calculation instead of considering later them into f_{xc}.[14] This means toprovide the exact *quasi-particles* structure e.g., using more sophisticated XC potentials in the DFT calculation. However, it turns out that in many semiconducting materials the effect of quasi-particles consists in a almost constant shift of the conduction states in the band structure. This justifies the *scissor operator* (SO) correction here adopted. For the wave functions instead the KS states are usually very close to the real ones. In MBPT approaches, and GW Approximation, usually corrections are neglected and KS eigenstates are used.

Scissor Operator Correction

Real quasiparticle band structure can be approximated via a rigid shift of the KS conduction bands, avoiding a longer and expensive MBPT calculation of the quasiparticle states. This is a rough approximation justified by experience in many materials (e.g. for silicon Fig. (2.2), GaAs, graphene Fig. (2.1) etc., although it does not work in general), that demonstrated to be valid also for second-order response [72–74, 152, 169], being able to reproduce the spectra and in particular the correct position of the peaks.

Shift of the conduction states however introduces non-trivial implications to the calculation of SHG [57] because of the non-locality of the scissor operator. This in particular creates new terms when the optical limit $\mathbf{q} \to 0$ is performed modifying the perturbed and unperturbed Hamiltonians.[15] The scissor operator $\hat{S}$ takes the form:

$$\hat{S} = \Delta \sum_n (1 - f_n)|\psi_n\rangle\langle\psi_n| \tag{5.13}$$

being Δ the constant energy shift, f_n the occupation number so that $(1 - f_n)$ makes the correction acts to the only empty states (I am supposing an insulating

---

[14] Here I am considering the response of the system in TDDFT. Hence the true f_{xc} is expected to give the real response and correctly reproduce the conduction states although starting from a less accurate initial guess as the KS-LDA. Nevertheless, the better is the starting point and the reproduction of the excited levels, the more f_{xc} and its effects can be negligible.

[15] As seen in Eqs. (4.64) and (4.65) and derived, expanding the Bloch's states on $\mathbf{q}$ it appears a commutator between the potential and the density $[V_{nl}, \mathbf{r}]$. As a consequence the nonlocal part of V_{nl} give a nonvanishing term. In this case also the scissor operator that does not commute with $\mathbf{r}$ will contribute.

or semiconduting material), and $|\psi_n\rangle$ the KS states.[16] This formula corresponds to the hypothesis that the real eigenstates $|\psi_n\rangle$ are really close to the KS ones (so that their difference can be neglected) and only the energies of the conduction bands are incremented by the constant positive factor Δ. Applying perturbation theory in order to develop the states and energies corrections at different orders for $\mathbf{q} \to 0$, the ground-state SO-corrected unperturbed Hamiltonian ($\hat{H}_{SO}$) becomes:

$$\hat{H}_{SO} = \frac{1}{2}\nabla^2 + V_{nl} + \hat{S}. \tag{5.14}$$

Whereas without considering the SO it was (cfr. Eq. (4.57)):

$$\hat{H}_{\mathbf{k}} = \frac{1}{2}\nabla^2 + V_{nl}, \tag{5.15}$$

that is the usual Hamiltonians whose wave functions and energies are obtained from the DFT(-LDA) ground state calculations expressed on the Bloch's states. Because of the non-locality of $\hat{S}$, the velocity operator $\mathbf{v} = \mathbf{q} + [V_{nl}, \mathbf{r}]$ that appears through the commutator $[\mathbf{qr}, \mathbf{qv}]$ in the second order corrections $\epsilon^{(2)}_{n\mathbf{k}}$, $|\psi^{(2)}_{n\mathbf{k}}\rangle$ of Eqs. (4.67) and (4.69) has a new term:

$$\mathbf{v}_{SO} = \mathbf{q} + [(V_{nl} + \hat{S}), \mathbf{r}]. \tag{5.16}$$

consequently one finds that (see derivation in Appendix E)

$$\langle\psi_n|\mathbf{v}_{SO}|\psi_m\rangle = \langle\psi_n|\mathbf{v}|\psi_m\rangle \frac{\epsilon^{SO}_{n\mathbf{k}} - \epsilon^{SO}_{m\mathbf{k}}}{\epsilon_{n\mathbf{k}} - \epsilon_{m\mathbf{k}}}. \tag{5.17}$$

Supposing $\Delta = 0$ one recovers the original result, while important changes can be introduced with increasing Δ that appears in the form $[\mathbf{r}, [\hat{S}, \mathbf{r}]]$ into the second order corrections.

In linear optics the contribution of the scissor operator can be identified with an almost rigid shift of the spectra to higher energies of a quantity Δ. In nonlinear processes as second harmonic generation it keeps the function of shift but in a more convoluted way. Indeed an unequal mixing of increased and unmodified energies in the transitions[17] makes it difficult to predict the real effect of the SO At first approximation it correspond to a rough shift of $\frac{\Delta}{2}$ of the whole SHG spectra.

It is important to remark that the possibility of including a scissor operator has been straightforwardly demonstrated for SHG [152] deriving the correction to the equations. There is instead no justification to the direct substitution of GW eigenvalues avoiding the modification of the Hamiltonian.[18] The assumption that LDA and GW (or SO) wave functions are equal and are both eigenfunction of their respective Hamiltonian, does not imply that the two Hamiltonian

---

[16] Here for simplicity I avoid to put the $\mathbf{k}$ dependence since Δ and hence $\hat{S}$ are the same for each $\mathbf{k}$-vector.

[17] The easiest way to comprehend it is to remember that SHG is described by many terms, between which there are also three-bands transitions given by valence-valence-conduction states or valence-conduction-conduction states. Hence the corrections enters twice in some terms and once in the others. As a result the shift is different and mixed in a non trivial way. Moreover $\chi^{(2)}$ is following multiplied by three dielectric functions with their own shifts.

[18] As it has been done for the SO correction, with the introduction of $\hat{S}$ in Eq. (5.14).

are equivalent, so that their eigenvalues $\epsilon_{n\mathbf{k}}, \epsilon_{n\mathbf{k}}^{GW}$ can be straightforwardly exchanged in the response expression.[19] Indeed, H^{LDA} is local whereas H^{GW} contains the GW-*self energy* term $\hat{\Sigma}$ that is nonlocal. So, there should be a correction term (as found for the SO) that arises from the $[(V_{nl}+\hat{\Sigma}), \mathbf{r}]$ commutator and change the calculation of the optical matrix elements [67, 68, 152, 170]. As a consequence, one cannot substitute the GW (or SO) energies, that stem from a nonlocal Hamiltonian, to $\epsilon_{n\mathbf{k}}$ into Eqs. (4.66-eq:bloch-k-wf-corr2) and Eq. (4.56) without introducing the correction term.[20] This substitution will neglect some terms giving wrong results. People in the past have misunderstood and have made mistakes on this.

GW corrections are then difficult to be implemented, increasing the complexity of the SHG calculation and are not yet available in the 2LIGHT code. The possibility of using a SO correction instead, has been implemented in 2LIGHT (it is described by the **soenergy** input variable), and can then be used in every SHG calculation as it is independent of the subsequent choice of f_{xc}.[21] All the approximations presented in this chapter can then be performed on top of the SO one. Remembering that for semiconductors DFT-LDA is far from the experimental gap, it becomes important to apply this energy correction, although it is a very basic approximation.

5.2.5 MBPT-TDDFT link

The great simplification that one achieves condensing all the informations in a unique variable, the density $\rho(\mathbf{r}, t)$, makes the link with other physical quantities complex and of difficult interpretation. This applies also to f_{xc} and g_{xc}. These kernels contain all the dynamical exchange and correlation effects that acts on the response of a system to an external perturbation. As stated above, they are generally unknown quantities and one should provide approximated expressions as the ones considered in this chapter in order to study the response. However, going beyond RPA becomes soon very difficult not only for computational limits but also for theoretical analysis. Indeed, given a physical approximation, because of the complexity of the XC functional it is usually hard to derive an expression for f_{xc}. The same holds for the opposite i.e., starting from a designed approximated expression and understanding the physics behind it as the effects that have been included or neglected.

With this regard it demonstrated useful to establish a link between TDDFT and Many-Body Perturbation Theory, where the physics of the system is more intuitively expressed in terms of the correlations Green's functions. They are more complex quantities that at the first order describe the propagation in space and time of a particle/hole inside the material, at second order depicts the evolution of two interacting particle and so on. Green's functions are useful since one consider *quasi*-particles and their reciprocal interaction while propagating. They contains more informations about the system than the density at the cost

---

[19] That is, considering the GW hamiltonian H^{GW} an operator of the same form and nature of the LDA one H^{LDA} but only more accurate, giving the correct eigenstates energy values. In that case, direct substitution of $\epsilon_{n\mathbf{k}}$ with $\epsilon_{n\mathbf{k}}^{GW}$ would be justified, improving the H^{LDA} reasults only.

[20] In Eq. (4.56) it is also evident that LDA-DFT energy differences are required toghether with the corrected (GW or SO) ones in the response calculation.

[21] This is true unless f_{xc} does not contain any information about the quasiparticle energy correction i.e., the screening of the system.

of the simplicity of equations and formulas. In particular TDDFT has the great advantage to represent low dimensional quantities i.e. $\rho(\mathbf{r}, t) = \rho(1)$ while the first order Green's function is a two-point quantity $G(\mathbf{r}, t; \mathbf{r}', t') = G(1; 2))$ and the second order is a four-point quantity $G_2(1, 2; 3, 4)$, while f_{xc} that describes the same second-order effects depends on only two points: $f_{xc}(1, 2)$. This translate in more efficient numerical algorithms for TDDFT, provided an exchange correlation kernel able to get the same informations contained in the Green's functions formalism.

Excitonic Effects and the Alpha Kernel

Following this line there are many works devoted to the transfer of knowledge achieved in MBPT to TDDFT. The prominent examples are provided by the NANO-QUANTA kernel, derived from the contraction of the Bethe-Saltpeter Equation (BSE) [127, 171, 172], and the *long range alpha-kernel* [140]. Both of them aim to include *excitonic effects*. They are a two particle process describing the mutual interaction of the excited electron-hole pair created by the interaction with the external field (i.e. through the absorption of photons). In semiconductors for example, once the electron is promoted from the valence to the conduction state it lefts behind itself an empty state: the *hole*. They feel the reciprocal Coulomb attraction and the screening provided by the surrounding electronic density, modifying the evolution of the system and its response. Their importance is linked to the nature of the material. In general excitonic effects demonstrated important in a variety of systems, in particular for optical neutral excitations e.g. in the absorption (see Ref. [127]). Literature has systematically improved their description for linear optical processes, but there is still a lack in the application to nonlinear optics and in the SHG only few attempts have been proposed [64, 67, 72, 73].

Excitons are correctly described by BSE in MBPT and the derived NANO-QUANTA kernel contains the same information describing excitonic effects at the same level of accuracy. However, it requires a computational effort close to the one needed to solve BSE due to the complex structure of the kernel, and for this reason it reveals inadequate for practical applications and has not been yet implemented into the code 2LIGHT.

The *alpha kernel* here adopted [140, 171] instead has demonstrated to be a good simplification able to catch the effects of moderate electron-hole interactions, as the ones characteristic of silicon. This static kernel is obtained from the intuition [159] that failure of TDLDA are related to the wrong behavior of its long-range contribution that is missing due to the locality of the approximation. This interaction is mainly given by the Coulomb particle-hole attraction, mediated and softened by the screening of the other electrons. At first approximation it can then be thought as a Coulomb interaction whose reduced strength is given by a multiplicative factor α. f_{xc}^{LRC}[22] has then been defined [140, 171] as:

$$\begin{aligned} f_{xc}^{LRC}(\mathbf{r}_1, \mathbf{r}_1) &= -\frac{\alpha}{4\pi|\mathbf{r}_1 - \mathbf{r}_2|} \\ f_{xc}^{LRC}(\mathbf{q} + \mathbf{G}) &= -\frac{\alpha}{|\mathbf{q} + \mathbf{G}|^2}. \end{aligned} \tag{5.18}$$

---

[22] LRC superscript stands for Long-Range Correlation kernel.

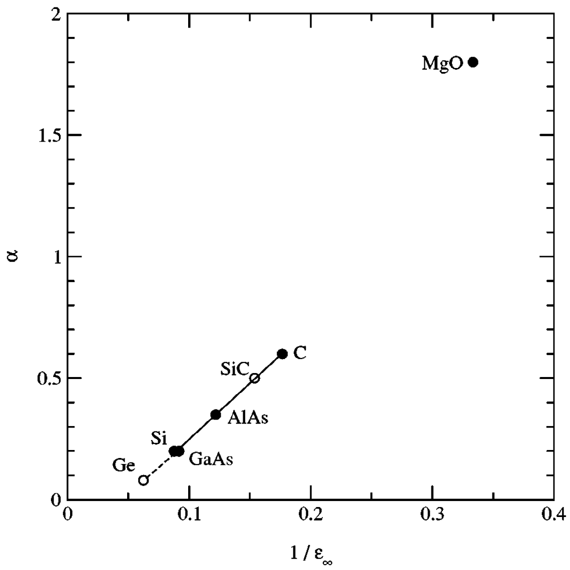

Figure 5.1: Material dependence of the parameter α with respect to the inverse of the dielectric constant. Filled circles: α fitted to reproduce BSE optical spectra; solid line: linear fit (using Eq. (5.19)) for $\alpha(\epsilon_\infty^{-1})$ on filled circles; empty circles calculated from Eq. (5.19). (Reproduced from [140], Copyright ©2004 by The American Physical Society).

In general α is a parameter that represents the average of the dynamical dependence of the real f_{xc} kernel for a given frequency range. This physical intuition is also motivated by the NANO-QUANTA kernel once is averaged over the frequency and considering the limit $\mathbf{q} \to 0$, that gives the trend $\frac{1}{q^2}$. Moreover, according to its derivation the kernel α has been supposed to be equal to the attractive screened-Coulomb interaction $W = \epsilon^{-1}v$. This shows that f_{xc} hence α should be negative and roughly proportional to the inverse of the static dielectric function ϵ_∞. In particular for linear optics it has been shown that exists a well respected general trend for semiconducting materials, given by [140]:

$$\alpha = 4.615\epsilon_\infty^{-1} - 0.213 \tag{5.19}$$

as can be seen in figure (Fig. 5.1). This law allows to guess reasonable values also for other materials unless ϵ_∞^{-1} is small, i.e. one is considering semiconductors with a large screening that makes exciton's interaction weak. Unless this trend is good it provides the possibility of estimating the excitonic correction[23] to the optical spectra of new materials without adding computational complexity beyond the RPA where ϵ_∞ is evaluated: that is, without solving the BSE or evaluating more complicated expressions for f_{xc}. Indications presented in the work of Botti *et al.* [140] show that the range of materials where f_{xc}^{LRC} works well coincide to materials dominated by continuum excitons.[24] Differences between BSE and the *alpha* kernel become evident instead when studying strongly

---

[23] The validity of this correction has been proven for absorption spectra in a large variety of materials through a comparison of the results with BSE calculations [140].

[24] It means the material has small to moderate electron-hole interaction.

bound excitons, because of its static approximation[25] (e.g., in solid argon that exhibits a strongly localized Frenkel exciton) or when the real f_{xc} is no more well reproduced by the screened-Coulomb interaction W.[26]

It has been observed for linear optics that the general effect of the *alpha* kernel is to redistribute oscillator strength. This can lead as a consequence to an apparent shift of peaks. For second harmonic generation, up to now excitons have shown an almost constant increase of the total response of the system Refs. [72–74]. Is however more difficult to predict their effects that are mixed through all the quantities appearing in Eq. (4.126).

All the results presented in this thesis regarding excitonic effects have been obtained using the long range *alpha* kernel.

---

[25] Indeed it becomes mandatory to keep the dynamic frequency dependency in order to reproduce the different excitonic peaks of the experimental spectra, while α gives only an average that fits all these features together into an unique single-excitation model.

[26] I.e., it is no more a good approximation the one adopted for the derivation of the kernel $f_{xc} = W$.

Chapter 6

The Si/CaF$_2$ Interface

As discussed in the introduction, second-harmonic generation has been largely used for materials characterization [13–15, 17, 71, 82, 173]. It can give multiple information on the structural [22, 27, 58, 59, 70, 92, 174, 175] and electronic properties of materials by detecting the modifications induced by the presence of adsorbates [14], stress [13] or external perturbing electromagnetic fields [176] and also permitting an in situ monitoring of dynamical processes [14, 15].

Sensitivity of SHG to the symmetry of the system is at the basis of all these different applications. Since SHG is dipole forbidden in centro-symmetric materials [2], a distinctive structural and electronic characterization of complex materials such as interfaces, surfaces, nanostructures or defects can be obtained from the signal originated by the symmetry-broken regions [2, 17, 27, 70, 71, 175]. Meanwhile, the surrounding bulk environment (if possessing the inversion symmetry) does not contribute. This makes of SHG a great selective spectroscopic tool.

An example is provided by the Si/Ge superlattices where SHG [17, 92] exhibits an increase of about one order of magnitude with respect to the crystalline system if the structure presents defects. Even the atomic angle and bond-length distortion inside materials as bulk silicon can be detected and measured thorough SHG as function of an applied external stress, as it has been shown in [13].

Moreover, SHG demonstrated sensitive not only to microscopic deviations from the centro-symmetric structure, but also to the macroscopic breaking of the symmetry due to surfaces and interfaces. Fig. (6.1) shows that the SHG signal originates in the interface between two centro-symmetric materials. It is characteristic of their contact region, whereas elsewhere it cannot take place because of selection rules.[1] With this regard, SHG has been investigated both experimentally and theoretically for a large variety of interfaces [17].

---

[1] Silicon has a small bulk contribution to the SHG process arising from higher-order term as the electric-quadrupole and the magnetic-dipole [2]. An example is provided by the third-order dielectric susceptibility $\chi^{(3)}_M$ once an external static field $\mathbf{E}_{dc}$ is applied. It polarize the system breaking the inversion symmetry and allowing SHG. This process is called *electric field induced second harmonic* (EFISH) generation and give rise to frequency doubling: $\mathbf{P}_E(2\omega) = \chi^{(3)}_M \mathbf{E}(\omega)\mathbf{E}(\omega)\mathbf{E}_{dc}$. The intensity of these higher-order processes is usually smaller with respect to the second-order one and can be detected only when the second-order vanish. In interfaces $\chi^{(2)}_M$ dominates; because of this, hereafter I will neglect the higher-order contributions.

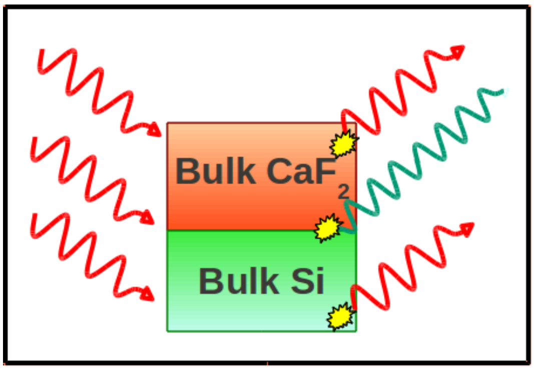

Figure 6.1: Second-Harmonic Generation process in the Si/CaF$_2$ interface. The two bulk materials cannot generate the double-frequency signal because of their inversion-symmetry. The SHG signal is genertated by light interaction with the interface region where the symmetry is broken.

Here I present an ab initio study of the Si/CaF$_2$ interface [82]. In this contest, Si/CaF$_2$ interface is a suitable material because of its optical and electronic properties, being a well-controlled semiconductor/insulator interface with potential technological importance [177–179]. Indeed, thanks to the small mismatch between the two lattice parameters, it is possible to grow epitaxially Si-CaF$_2$ nanostructures by superimposing semiconducting and insulating slabs in a multi-quantum well [180, 181]. It consents to exploit the relation between optical properties and quantum confinement effects of Si [86, 87, 177–179, 181, 182] whereas CaF$_2$ plays the role of an excellent insulator. In fact, its 12 eV energy gap makes this material transparent in a wide frequency range.

Because of these two factors i.e., i) the possibility of technologically design the energy gap via the silicon quantum confinement, and ii) the complete transparency of CaF$_2$ into the window of visible light, the interface demonstrates useful for photovoltaic and optoelectronic applications. In particular in solar cells, a different opening of the electronic and optical gaps, that can be achieved depositing Si slabs of various thickness in a multi-quantum well structure,[2] would enlarge the devices absorbtion frequency-range increasing the efficiency. Meanwhile CaF$_2$ provides that sunlight propagates deep into the material without loss of intensity, so that an higher number of Si slab can be superimposed.

However, these optical properties, in particular in the low-energy region (i.e. visible light), strongly depend on the interface electronic-states [85–87, 181]. In fact, interface states enters into the electronic gap varying its dispersion along the wave vectors **k** and generally reducing the gap. Moreover crystal local-field effects become important around that region due to the sharp variation of the potential inside the lattice, consequently modifying the final optical response.

As a result, the interface is a competing effect with respect to the quantum-confinement. Understanding the influence of this competition on the final response has become then a mandatory task for practical applications of Si/CaF$_2$

---

[2] In the present case I am considering multi-layers structures. Also in 2- and 3-dimensional confined structures, such as nano-wires and nano-dots, one can observe the quantum confinement effect playing on silicon and opening its electronic gap. In these cases the gap opening depends respectively on the width or the diameter of the structure [183]

and the interfaces in general [21, 22, 54, 67]. Therefore, a great effort has been devoted to analyze these states. In particular, literature presents a lot of works focused on the understanding of the possible geometrical configuration that determines them [85, 88, 89, 182], and its dependency on the growth conditions [76, 77]. This represented an open question for a decade in the 90's, animating a long discussion with several experimental and theoretical studies. Nowadays there is general agreement about the crystalline structure, although some controversies are still opened [76, 77].

Besides the linear optics, the Si/CaF$_2$ interface has also important nonlinear optical properties which have been investigated experimentally by Heinz *et al.* [82] in 1989. They used optical second harmonic to probe the electronic transitions in order to understand the distinctive nature of the interface region.

In linear optics, at these frequencies, interface effects are hidden by the intense bulk response of Si (e.g. in absorption spectra). Therefore, SHG spectroscopy revealed an useful technique to investigate the same system in the absence of the underlying bulk contribution, thanks to it symmetry-broken selectivness. In fact, both silicon and calcium fluoride are centro-symmetric and do not contribute to the SHG signal that becomes distinctive of the insulator-semiconductor discontinuity (see Fig. (6.1)). Through SHG Heinz, Himpsel and Palange [82] observed directly the interface electronic transitions. In particular they achieved information from the peaks of the SHG spectrum on the direct electronic transition between the HOMO-LUMO states at the special point Γ.

This experimental work constitutes then an opportunity for comparison with our calculated spectra, allowing the test and study of several topics object of this thesis.

I) It is the first time the code 2LIGHT and the formalism presented in chapter 4 are applied to a complex system as the Si/CaF$_2$ interface. Only bulk systems with a limited amount of atoms were studied before [13, 72–75]. As a consequence, the comparison with the experiment represent an ideal test for the accuracy of the method once applied to complex materials.

II) Knowledge of the accuracy of the calculation can give informations on the capabilities of SHG ab initio simulations, ever for predictive application to unknown interfaces.[3]

III) As for linear optics, ab initio studies of SHG allow to gain knowledge on the different effects contributing to the final response e.g., the crystal local-field or the excitonic effects. This is not always possible in experiments where one collects their resulting total response. Comparison among different level of approximations and the experiments indeed, allows one to estimate their importance, obtaining informations both on the nature of the system and on the second-harmonic generation process.

IV) So far, SHG ab initio calculations have been restricted to the independent particle approximation and eventually to small-size systems when more accurate approximations have been adopted. Therefore, there is still a need to deepen our knowledge of the physics behind the process, extending

---

[3] Experimentally SHG measurements represent a nontrivial task and it is not always possible to perform accurate studies [17].

the *first-principle* studies to a larger variety of materials, as the interface here proposed.

V) Finally, the comparison will permit to confirm experimental analysis concerning the nature of the interface with respect to the growing conditions. The interface structure of [82] is indeed experimentally unknown, contrary to the studied ab initio system. Because of the high sensitivity of SHG, matching of the spectra would then represent a confirmation of the correspondence between the two structures. All these considerations justify the use of ab initio SHG simulations not only on the interpretation and study of structures, but also as a theoretical predictive tool that could guide both new experiments and the design of innovative materials.

6.1 The 1989 Experiment

In the 80's Himpsel *et al.* dedicated part of their work to the study of the epitaxial interface of Si/CaF$_2$ [78, 79, 81–83]. In particular in Ref. [82] they studied its resonant second-harmonic and sum-frequency (SF) spectra. These three-wave-mixing signals have been obtained by exposing the sample to laser radiation from a tunable source. In the first case tunable laser light is employed and after spectral filtering of the frequency-doubled reflected radiation coming from the interface, the SHG signal is collected. In SF generation instead, the spectrum is obtained mixing the tunable source with another laser operating at fixed frequency (of 1.17 eV). Again, reflected radiation pass thorough a frequency filter and is following amplified by a photomultiplier. The tunable radiation is produced from a dye laser pumped by second harmonic radiation coming from a Q-switched Nd-doped yttrium aluminum garnet (Nd:YalG) laser. Its radiation constitutes also the fixed frequency laser employed in SF measurements.

They obtained a significant signal, easily measurable, with weakly focused laser beam (diameter>1 mm) and a laser fluence far below the damage threshold ($\sim$ 1 mJ), in the range of $[2.2 - 2.5]eV$. Pulses of 5 ns where employed and using a parallel optical path they registered possible variations in the intensity of the pump radiation[4] that have been considered and compensated in the SHG spectrum (obtained as function of the incoming radiation intensity).

They detected p-polarized three-wave mixing radiation produced by excitation with a p-polarized beam incident on the sample with an angle of 80° from the interface normal. In this configuration it is obtained the $\chi^{(2)}_{M\ zzz}$ element of the second-order dielectric susceptibility tensor. The contributions from the topmost CaF$_2$ and the underlying Si surfaces demonstrated to be negligible together with higher-order terms (magnetic-dipole and electric quadrupole moments) arising from bulk Si (cfr. [82]). Figure (6.2) shows the mesured SHG and SF spectra for the $\chi^{(2)}_{M\ zzz}$ component in the Si(111)/CaF$_2$ interface of [82]. The SHG and SF spectra are plotted as function of the dye laser photon energy i.e., the varying ingoing radiation. The two spectra present the same resonant

---

[4] When the dye laser frequency is modified, the outgoing frequency can have a different intensity. It is therefore necessary to account for it i.e., considering the ratio between the SHG (I_{SHG}) and the laser (I_l) intensities $\frac{I_{SHG}}{I_l}$ instead of the bare SHG signal while analyzing the spectrum.

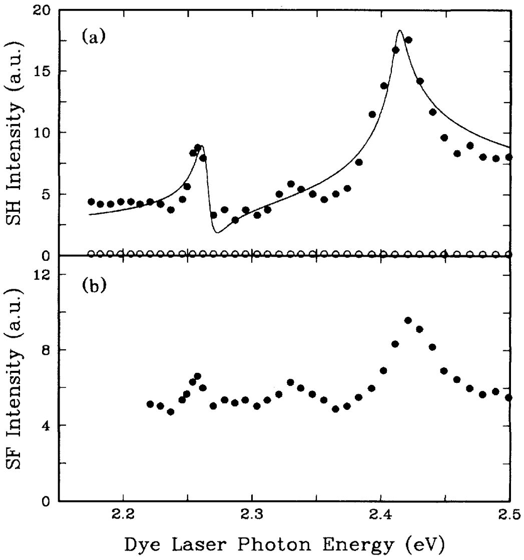

Figure 6.2: Resonant three-wave-mixing signals associated with $\chi^{(2)}_{M\ zzz}$ as a function of the energy of a photon from the tunable dye laser. (a) Results for the SHG process and (b) the SF generation mixing the dye laser output with a photon of fixed energy (1.17 eV). The filled simbols refer to signals from the Si(111)/CaF$_2$ sample. The open symbols refers to a Si(111) surface covered by native oxide showing the contribution of the underlying Si surface being negligible. The solid curve in (a) is a fit to theory presented in [82] (Reproduced from [82], Copyright ©1989 by The American Physical Society).

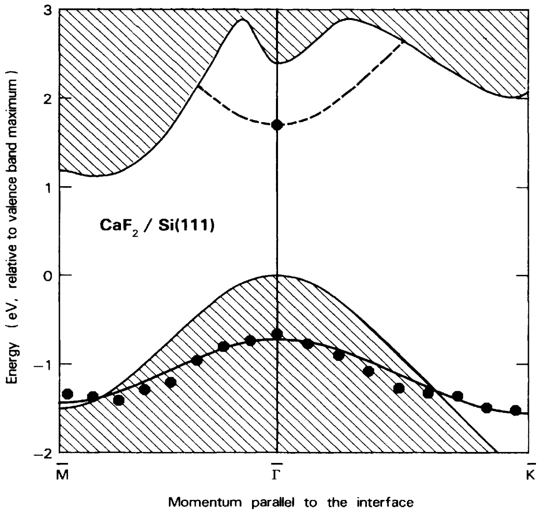

Figure 6.3: Band-gap structure of the Si(111)/CaF$_2$ interface. (Reproduced from [82], Copyright ©1989 by The American Physical Society).

peak at the same fundamental frequency (the one of the dye laser).[5] This made the authors conclude that the peak arises from a direct transition at the Si(111)/CaF$_2$ interface. They associate the strong peak at about 2.4 eV to the vertical gap (HOMO-LUMO) transition at the Γ point Fig (6.3) [81, 83]. It is originated by the bonding and anti-bonding matching of the Ca$^+$(4s) and the hybridized Si(sp3) orbitals at the interface [78].

6.2 The Si(111)/CaF$_2$ Structure

6.2.1 Experimental Sample

The Si(111)/CaF$_2$ samples studied in [82] consisted of a layer of about 500 Å of CaF$_2$ grown epitaxially on top of Si(111) crystal surface. This is allowed by the similar crystal structures of the two materials and the small lattice mismatch of $\sim 0.6\%$ at room temperature. CaF$_2$ has been grown with molecular-beam epitaxy (MBE) technique on an initial Si(111) substrate at a temperature of $[700 \div 750]$°C. The silicon presented a clean (7×7) surface reconstruction [81, 82].[6] After the first layers growth, MBE deposition can continue at lower temperature, diminishing the lattice mismatch. This improves the growing conditions and increases the achievable CaF$_2$ thickness.

The electronic configuration (and consequently the SHG spectrum) is directly related to the geometrical one. The latter has represented an open ques-

---

[5] One can considers as an example the peak at 2.42 eV as an example. In SHG spectrum the second harmonic photon has an energy that is twice the one of the dye laser i.e., 4.84 eV. In SF instead the final photon possesses an energy of $1.17 + 2.4 = 3.59$ eV.

[6] It has been obtained through a previous annealing at higher temperature and a subsequent slow cooling. The surface cleanness and reconstruction has been verified by LEED and photoelectron spectroscopy.

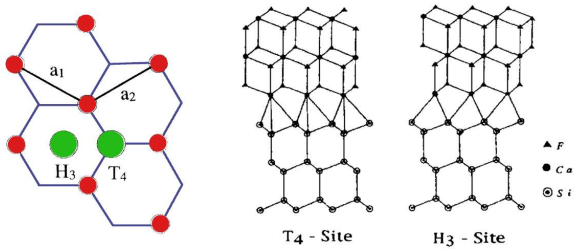

Figure 6.4: Top view of the Si surface unit cell (left). The two possible adsorption sites T_4 and H_3 for the Ca atom in the CaF layer at the interface are shown by shaded atoms. The basis vectors of the hexagonal unit cell are indicated. Frontal view of the T_4 and H_3 interfaces are compared on the right.

tion [76, 77, 79, 84, 85, 89, 90, 182], particularly because of its dependence on the growing conditions of the sample. In particular, the geometrical structure of the experimental sample [82] is unknown.

Experimental Studies on the Interface Geometry

The match between the latest studies on the effects of growth parameters on the structural interface features [76, 77] and the sample synthesis conditions described by [82], allow to predict for the experimental interface a T_4 configuration (see Fig. (6.4)) with B-type orientation [77, 85] Fig. (6.5). In this particular configuration Ca atoms at the interface are in T_4 high symmetry sites Fig. (6.4) while one fluorine of the first layer is lost at the interface after the dissociation of the CaF$_2$ molecule [76, 79], and the other occupies the H_3 sites (see Fig. (6.4)).

In Ref. [89], Zegenhagen claims, for the interface grown at temperature close to the one of Heinz *et al.*,[7] a mixture of domain structures characterized by both the T$_4$ and H$_3$ bonding sites for calcium. This appears in the sub-monolayer coverages [89], and depends on the cleanness of the surface and a possible nonuniform growth, as following discussed in [76], whereas there is no evidence of that mixture for clean substrate and thicker coverages [76] as in the experiment of Ref. [82]. Therefore, I am confident that T$_4$ is the correct interface geometry that reproduce the experimental sample.

Formation Energy study

In addition to the above considerations, as further check I have performed a study of the formation energy of the two interfaces (see Fig. (6.6)). A comparison between the multi-quantum wells structure where the two materials match in the T$_4$ and H$_3$ configurations respectively, show that the first is energetically favored with respect to the latter. Evaluating the formation energy of a particular interface as the difference between its total energy and the chemical potential μ of its single components (N_X is the number of X species atoms)

$$E_{form} = E_{tot} - N_{Ca}\mu_{Ca} - N_F\mu_F - N_{Si}\mu_{Si} \qquad (6.1)$$

---

[7] Samples of Ref. [89] has been grown at temperatures between [450 ÷ 770]°C.

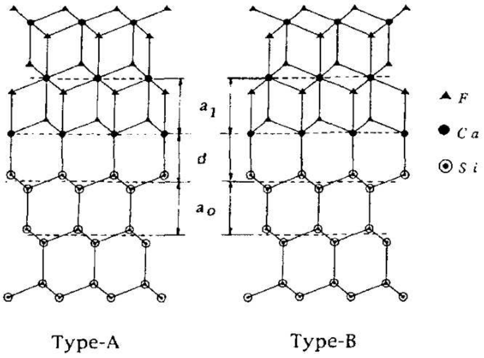

Figure 6.5: Two types of epitaxial relations of the Si(111)/CaF$_2$ interface: for type-A (left) and for type-B (right). Interlayer spaces a$_1$, d, a$_0$ are different among the two materials and the interface.

I obtained:

$$\begin{aligned} E_{form}(H_3) - E_{form}(T_4) &= 47Ha \\ E_{form}(H_3) &> E_{form}(T_4). \end{aligned} \tag{6.2}$$

These studies have been performed with the Abinit code, on a Si(111)/CaF$_2$ interface where 5 double layers of Si and 4/5 layers of CaF$_2$ alternates in a multi-quantum well structure presenting a particular matching face (cfr. Fig. (6.6)).[8] These test structures have been studied in analogous works [86, 87, 177, 184] on Si/CaF$_2$ and constituted a good starting point. In particular, relaxation of the cell dimension allows to obtain the (x, y) *inplane* lattice parameters that minimize the interface stress between the two materials. This value of $a_{xy} \simeq 5.40$Å is the one I adopt in the following also in the single interface structure.

The formation energy result, together with the experimental studies previously presented [76, 77], identify T$_4$ as the most probable structure for the experimental samples I am comparing with.

6.2.2 Simulation Cell Structure

I have studied the T$_4$ B-type configuration of Si/CaF$_2$ in Density-Functional Theory within Local-Density Approximation using the plane-wave pseudopotential method as implemented in the ABINIT package [121].

Si/CaF$_2$ Pseudopotentials

For Si I have adopted the pseudopotential used in [72]. It is built in a Troullier-Martin scheme and has been already tested in literature for linear and nonlinear calculations [13, 72, 74]. Whereas, for CaF$_2$ they do not exists tested pseudopotentials for nonlinear optics. I have chosen Fritz-Haber Institute (FHI) pseu-

---

[8] The adopted pseudopotential and the parameters of these test-systems are the same of the single interface system presented in the next section, to which I remand for further details.

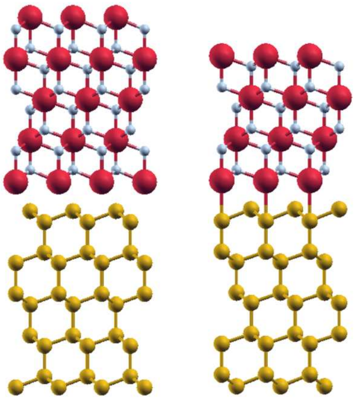

Figure 6.6: H_3 interface multilayers system (left) and T_4 interface multilayers system (right). Five double layers of silicon (yellow balls) have been considered for both the structures, while calcium fluoride (Ca is shown in red and fluorine in grey) has a different thickness to recover the periodicity along **z**.

dopotentials obtained in a Troullier-Martin scheme present in the Abinit package (see *http://www.abinit.org/downloads/psp-links*). The linear optical spectra of bulk CaF$_2$ and multi-quantum well test structures have been compared with [87, 184], obtaining a reasonable agreement. Calcium contributes with one 4s electron to the interface states [78, 82, 83, 86, 182], together with an unpaired Si electron in the $sp3$ hybridized orbital. Spatial separation and the negligible exchange-correlation interaction between 4s and core/semi-core electrons in the underlying closed shells, make possible to consider only 4s valence electrons.

Bulk CaF$_2$ system is well described when looking at its structural properties, as obtained by comparing the lattice parameter with the experimental one or the interface bond-lengths that will be presented in the following. The optical response of bulk CaF$_2$ instead, could be influenced by the semi-core electrons (as observed for other compounds). However, for the experimental energies of interest [82], CaF$_2$ is completely transparent being a large gap insulator. As a consequence its bulk states do not contribute to the final linear and nonlinear spectra and one can freeze semi-core electrons in the pseudopotential approximation.

Fluorine does not contribute directly to the interface. It desorbs far away from it after the molecule dissociations, and the one which remains links to Ca atoms only.

Performing a relaxation of the silicon and calcium fluoride bulk systems and of their lattice parameters, I have obtained respectively $a_{\mathrm{CaF_2}} = 5.410$ Å and $a_{\mathrm{Si}} = 5.389$ Å, with a lattice mismatch of 0.4%. These theoretical values calculated at 0 K well reproduce the experimental values $a_{\mathrm{CaF_2}} = 5.447$ Å and $a_{\mathrm{Si}} = 5.430$ Å at 6.4 K [185].

Single Interface Structure

The experiment has been performed on a single interface between a Si substrate and a 500 Å thick CaF$_2$ insulating slab. Because of computational limits it is prohibitive to reproduce that size, and I have proceeded starting from a smaller system of about 5 Å of silicon and 6 Å of CaF$_2$, then increasing their thickness up to convergence of the SHG spectra. Since the insulating and semiconducting slabs assume rapidly the bulk structure below the interface i.e., the centro-symmetry, one expects that the SHG signal originates from a region of few angstrom around the interface.

The system has been built aligning the growth direction with the z axis, so that the interface lies in the xy plane. In order to have a single-interface system[9] I have built a supercell introducing vacuum into the simulation cell on top of the CaF$_2$. It avoids interaction between the different replica and breaks the multi-layer structure created by the periodic-boundary conditions in absence of the vacuum. The dangling-bonds of the external surfaces have been passivated with hydrogen atoms.[10]

The experimental thickness of CaF$_2$ makes it possible a modification of the substrate lattice parameter close to the interface due to the stress, although the mismatch between a_{CaF_2} and a_{Si} is very small. Choosing the in-plane lattice parameter as the one of Si, CaF$_2$ or values within, should be negligible. However, I take the relaxed in-plane lattice parameter of $a_{xy} \simeq 5.40$ Å to diminish this stress.[11]

To further reduce the required computational resources, I have considered the unitary cell given by the basis vectors ($\mathbf{X}$, $\mathbf{Y}$, $\mathbf{Z}$):

$$\mathbf{C} = \begin{pmatrix} \mathbf{X} = & \frac{1}{2}\mathbf{x} + \frac{1}{2}\mathbf{y} \\ \mathbf{Y} = & -\frac{1+\sqrt{3}}{4}\mathbf{x} - \frac{1-\sqrt{3}}{4}\mathbf{y} \\ \mathbf{Z} = & \mathbf{z} \end{pmatrix} \tag{6.3}$$

where $\mathbf{x}$, $\mathbf{y}$ are the basis vector of the Si(CaF$_2$) FCC cell and $\mathbf{z}$ is the total height of the interface plus the vacuum. The cell $\mathbf{C}$ is obtained passing from the FCC cell to the tetragonal unitary cell $\mathbf{C}'$:

$$\mathbf{C}' = \begin{pmatrix} \mathbf{x}' = & \frac{1}{2}\mathbf{x} + \frac{1}{2}\mathbf{y} \\ \mathbf{y}' = & -\frac{1}{2}\mathbf{x} + \frac{1}{2}\mathbf{y} \\ \mathbf{z}' = & \mathbf{z} \end{pmatrix} \tag{6.4}$$

and then rotating the $\mathbf{y}'$ axis to 120° from x (i.e. considering the unitary hexagonal cell of the Si(111) interface):

$$\mathbf{C} = \begin{pmatrix} \mathbf{X} = & \mathbf{x}' \\ \mathbf{Y} = & -\frac{1}{2}\mathbf{x}' + \frac{\sqrt{3}}{2}\mathbf{y}' \\ \mathbf{Z} = & \mathbf{z}' \end{pmatrix} \tag{6.5}$$

---

[9] One cannot use the multilayer structure because it generate spurious contributions to the SHG process arising from the interferences between the various layers in the superlattice, as it happens e.g., in Si/Ge superlattices [21].

[10] For hydrogen I have used a FHI Troullier-Martin pseudopotential obtained from [121].

[11] This has been done through a DFT relaxation on the multy-layer T$_4$ system. The Si/CaF$_2$ interface is easier relaxed in a multi-layers structure [86, 87, 177]. In the single interface, because of the vacuum, the stress is partially redistributed along z, interfering with the in-plane relaxation. One should then use thicker slabs to have the internal part of the system resembling the bulk, but this would require a greater computational effort.

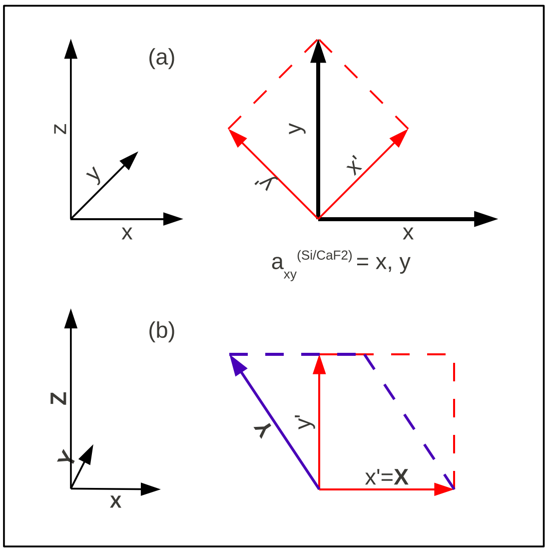

Figure 6.7: Relation among the primitive vectors of the simulation cell $C = (\mathbf{X}, \mathbf{Y}, \mathbf{Z})$ Eq. (6.3) and the silicon FCC cell $C = (\mathbf{x}, \mathbf{y}, \mathbf{z})$ Eq. (6.5) passing through $C' = (\mathbf{x}', \mathbf{y}', \mathbf{z}')$ Eq. (6.4). Top view of the interface-plane on the right.

as seen in Fig. (6.7). The last transformation is useful when defining the atomic positions in terms of the reduced coordinates (i.e., with respect to the primitive vectors) for the silicon crystal structure.[12]

6.3 SHG Calculation

The in-plane structure presents 120° symmetry-rotation angle around the normal to the interface, as observed by the experiment [82]. It corresponds to a primitive hexagonal symmetry, as confirmed by the results of the DFT relaxation.

To compare with the experiment I have calculated $|\chi^{(2)}_{zzz}|$ which corresponds to light polarized along the $\mathbf{z}$ direction i.e., perpendicular to the interface (as discussed in [82] and in section 6.1). In the formalism presented in chapter 4, considering hexagonal geometry $\chi^{(2)}_{zzz}$ is related to the second-order response function $\chi^{(2)}_{\rho\rho\rho}$ as follows:[13]

$$\chi^{(2)}_{zzz}(2\omega) = -\frac{i}{4}\epsilon^{LL}_{M}(\mathbf{z}, 2\omega)\chi^{(2)}_{\rho\rho\rho}(2\mathbf{z}, \mathbf{z}, \mathbf{z}, 2\omega, \omega, \omega)\epsilon^{LL}_{M}(\mathbf{z}, \omega)\epsilon^{LL}_{M}(\mathbf{z}, \omega), \tag{6.6}$$

where the polarization vectors $\mathbf{q}$ have been identified with $\mathbf{z}$.

---

[12] The ($\mathbf{X}$, $\mathbf{Y}$) axis forms an angle of 120°. In this coordinate system the (x, y) reduced atomic coordinates assume the simple values of 0, $\frac{1}{3}$, $\frac{2}{3}$.

[13] Full derivation can be found in Appendix F.1.

6.3.1 SHG Spectra Normalization

The systems I have studied contains a vacuum slab that breaks the structure along the **z** direction. The response of the system, as discussed in chapter 4 gives a signal that is characteristic of the whole simulation cell. In bulk materials this coincide to a signal normalized to the volume. Varying the size of the cell does not modify the final response.[14]

For surfaces, interfaces and similar structures, built introducing the vacuum instead, the empty part of the simulation cell does not contribute to the response, although entering in the normalization factor of the equations.

E.g., the integrals deriving from the products $\langle\psi_{n\mathbf{k}}|\psi_{n'\mathbf{k}'}\rangle$ are all performed on the volume of the simulation cell V: $\frac{1}{V}\int_V d\mathbf{r}$. As a consequence also the vacuum part is considered when evaluating the linear and the second-order responses. This can be seen directly in Eq. (4.56) where the term $\frac{1}{V}$ appears in front of the summation that gives the contribution of all the two- and three-bands transitions. It is immediate to notice that for a given system, different thicknesses of the surrounding vacuum will give different responses (see App. G.1.3 for a detailed discussion). Consequently, it is not clear which is the real physical situation that reproduces the experiment.

Let's start from analogous consideration on a similar system: a surface. The surface is determined by its nature as the region between *two semi-infinite* media: the material and the vacuum.[15] This is justified once looking to the experimental environment (e.g. in absorption spectroscopy). The probe (the light) examines a region defined by the substrate and the vacuum inside the experimental chamber. Both the sample and the chamber are macroscopic therefore the probe see them as infinite.

With this assumption the surface is the matching between two *semi-infinite* dielectric media. Reporting this idea into the finite dimension of the simulation cell, it means considering the surface composed of an equal amount of vacuum and material: $V_{sys} = V_{vac}$. V_{sys} is the volume of the material and V_{vac} the void inside the simulation cell.

This interpretation holds also for interfaces, as the matching between two semi-infinite medium (regarding the vacuum as a medium of dielectric function $\epsilon = 1$, even the surface can be considered as an interface between matter and vacuum).

In the Si(111)/CaF$_2$ samples of [82], Si and CaF$_2$ have both a great size compared with the interface region probed by the light. Therefore, accordingly to the previous considerations it can be thought as defined by two semi-infinite media. Consequently an equal amount of both should be considered. However, in my simulation cell I have a different configuration. Actually, three dielectrics materials are present: the silicon, the calcium fluoride and the vacuum.

The essential nature of the Si(111)/CaF$_2$ system is characterized by the interface between the semiconductor and the insulator. In particular calcium fluoride at the frequency I am looking at is completely transparent. Therefore, optically it behaves exactly as the vacuum on top of it and they can be thought together as forming an unique CaF$_2$ insulating slab. I decide then to consider the vacuum and the CaF$_2$ as the semi-infinite insulator, and the silicon as the semi-

---

[14] This holds for processes that are proportional to the volume i.e., the linear optics or SHG in bulk materials as GaAs.

[15] Here I suppose the sample is micrometric so that can be considered macroscopic.

infinite semiconductor. The results here proposed are then obtained considering almost an equal amount of these two media.

Renormalization

Considering the same amount of insulating and semiconducting material in the Si(111)/CaF_2 interface is usually a waste of resources. One of the two slabs could indeed converge within a smaller thickness. Therefore, in order to contain the calculation, it is useful to define a renormalization procedure that allows to pass from the response of a system to another one with a different insulator-semiconductor ratio (see Appendix G.1.3 for further details). For practical reasons I have then simulated smaller systems converting their response to the adopted convention of 50%/50% silicon/insulator percentage. In particular, the SHG response has been renormalized keeping fixed the silicon volume and renormalizing the CaF_2-vacuum thickness to the one of silicon. This because a larger silicon region contributes to the signal with respect to the calcium fluoride one (as I will show later).

6.4 Studied Systems and Convergence Tests

I have studied different systems, increasing respectively:

I) the vacuum thickness to avoid interaction among the replica,

II) the insulating CaF_2 slab and

III) the silicon thickness.

I tested the convergence of the various systems looking at the IPA-SHG signal. Because of its simpler equations, the independent-particle reveals to be the best approximation for comparison among different systems. In IPA indeed, peaks are uniquely identified by the two- and three-bands transition of Eq. (4.56) at the corresponding denominator energies. On the contrary, once LF or excitonic effects are introduced, transitions at different energies are mixed both in the second-order Dyson equation (Eq. (3.31)) and in the final response Eq. (4.126) where $\chi^{(2)}_{\rho\rho\rho}$ is further convoluted with three dielectric functions at different frequencies. One loses the direct peak-transition correspondence and consequently the identities of the peaks. Therefore, peaks close to the same energies can have different origins while going beyond IPA.[16] IPA reveals then the best choice for comparison among different structures while testing convergence.

In the particular case of testing the thickness of the silicon slab, also the scissor operator correction to the DFT energies has to be taken into account. Indeed for silicon, the quantum confinement effects due to the finite height of the semiconductor opens the gap. As studied elsewhere [186], the gap opening is different depending on the size of silicon and tends to the bulk value while increasing its thickness. The different confinement hence reflects in a different shift of the peaks position, that have to be corrected applying the SO correction. In particular, the SO energy correction Δ (cfr. Eq. (5.13)) has been taken to reproduce the experimental gap of 2.4 eV at the Γ point [82].

---

[16] Moreover, in the particular case of the Si(111)/CaF_2 interface, introduction of the LF generally soften the spectra making less clear and more difficult to identify differences.

For each of these systems I will then provide the convergence parameters of the DFT and SHG calculations.[17]

6.4.1 Vacuum Convergence

Si(111)(3dl)/CaF$_2$(4l)

I started from a system composed of 3 double layers (dl) of Si(111) and 4 layers (l) of insulating CaF$_2$, see Fig. (6.8). The total height of the cell is 50.3 Å. The equilibrium configuration of the system has been obtained thorough a DFT relaxation of the atomic positions with the Abinit code. The DFT convergence parameters are:

1. **E**$_{cut}$ represents the energy cutoff over the plane waves (i.e., the maximum module of the **G** vectors). I have chosen this cutoff in order to converge the total energy within $5 \cdot 10^{-5}\%$.

2. **toldfe** establishes the threshold value for DFT convergence. When the difference of the total energy between two following step is smaller than this value, the self-consistent KS cycle is considered to be converged.

3. **k**-grids; it gives the number of points along the three reciprocal-space directions that define the grid over which the KS Hamiltonian is solved. The grids here presented are all Monkhorst-Pack grids, centered in $(\frac{1}{2}, \frac{1}{2}, \frac{1}{2})$. I considered a grid (N, N, M) to be converged once differences in the total energy between it and the finest one $(N+2, N+2, M+2)$ is below $7 \cdot 10^{-5}$ %.[18]

4. **tolmxf** is the force threshold for the relaxation cycle. Only if the force acting on each atom is below **tolmxf** relaxation is considered as converged.

5. **toldff** is the force threshold considered by Abinit while converging the KS self-consistent cycle for the electronic density during the relaxation procedure.

I have always performed a convergence test of the **E**$_{cut}$ value and the **k**-grids, testing also values beyond the desired accuracy in order to be confident of their convergence. After the relaxation of the system with **toldff**, I have always performed a DFT cycle in order to improve and better converge the electronic density, choosing a more stringent **toldfe** threshold parameter. Using it directly into the relaxation procedure, where numerous self-consistent DFT cycle are performed, would have increase the computational effort without significantly improving the ion dynamics. For the Si(111)(3dl)/CaF$_2$($4l$) system and the ones presented in the following, I have adopted the parameters of Tab. (6.1).[19]

---

[17] Since nonlinear optical properties requires more accurate parameters then the linear ones, I perform both the calculation with the same values converged for the SHG spectrum. Indeed the linear response is a necessary ingredient to obtain the nonlinear one through the second-order Dyson equation. Convergence of the latter implies necessary convergence of the former. The linear quantities are given in output by 2light together with the nonlinear ones.

[18] Because of the different dimension along the z component M can be smaller than the number of points along the x, y direction in reciprocal space.

[19] These values are over-converged for the smaller systems therefore revealed accurate also for the bigger structures presented in the following.

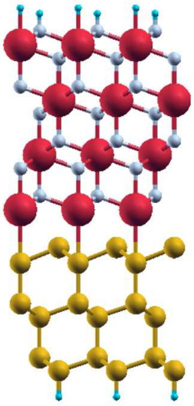

Figure 6.8: Si(111)(3dl)/CaF_2(4l) B-type, T_4 single interface system. The silicon (yellow) and the calcium fluoride (respectively Ca in red and F in grey) slabs are terminated both with H atoms (light-blue).

E_{cut}	100 Ha
toldfe	10^{-12} Ha
k-grid	$8 \times 8 \times 1$
tolmxf	$5 \cdot 10^-5$ Ha/bohr
toldff	$5 \cdot 10^-6$ Ha/bohr

.

Table 6.1: DFT parameters for the Si(111)/CaF_2 systems.

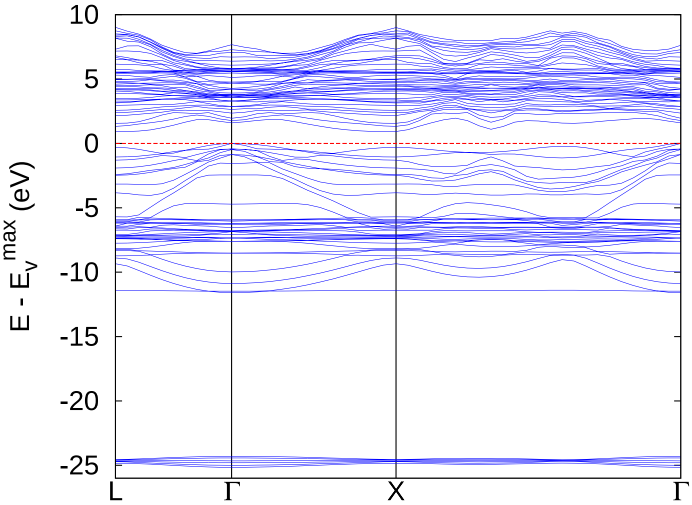

Figure 6.9: Band structure of the Si(111)(3dl)/CaF$_2$(4l) interface along the $L - \Gamma - X - \Gamma$ path. The zero has been taken as the valence maximum.

The final structure is composed of $\sim$ 8.4 Å of CaF$_2$ and $\sim$ 12.2 Åof Si.[20] The vacuum present into the cell is $\sim$ 30 Å. Afterwards, I have evaluated the band structure of the system along the $L - \Gamma - X - \Gamma$ special points path, Fig. (6.9). It presents an indirect-gap of 0.92 eV at $\Gamma - L$ and $\Gamma - X$ and a direct gap at Γ of 1.59 eV. The smalles direct transition take place at the L, X special points.

The IPA-SHG spectra has been obtained considering a scissor operatore defined as $\Delta = 0.81$ eV, correcting the DFT gap at Γ in order to recover the experimental one. The input density has been taken from the previous DFT calculation. Due to the small energy range I am looking at (the experiment has been performed in a 0.4 eV energy window) it is necessary to achieve an high accuracy of the second-harmonic calculation. The tested converged parameters used in the 2LIGHT code are reported in Tab. (6.2) whereas the IPA result is presented in Fig. (6.10).

The silicon slab is smaller if compared with the insulating one (the vacuum plus the CaF$_2$). Therefore, spectra have been normalized according to the renormalization procedure presented in Appendix G.1.3 to the 50%/50% semiconductor/insulator ratio (as discussed in section 6.3.1) keeping the Si height as reference. The same has been applied to all the other systems presented in the following once $V_{Si} \neq V_{CaF_2} + V_{vac}$.

Vacuum Convergence Test on Si(111)(3dl)/CaF$_2$(4l)

The SHG response of the same system has been evaluated inserting a vacuum of respectively 20 and 40 Å into the simulation cell. The DFT and SHG parameters used in the previous calculation (Tabs. 6.1, 6.2) demonstrated to be converged even for these two systems. IPA-SHG responses of the three systems

---

[20] The height of a slab is evaluated from its surface (identified as the middle point between the Si-H/Ca-H bond) and the interface (identified as the middle of the Si-Ca bond).

	IPA
npwwfn	2997
nband	90
lomo	34
npwmat	1
k-grid	1152
SO	0.81
domega	0.004
broad	0.013

Table 6.2: Parameters of the 2LIGHT calculation on Si(111)(3dl)/CaF$_2$(4l). **k**-grid indicates the number of *random* **k**-points used in the calculation to better sample the first Brillouin Zone. I have applied a gaussian broadening (**broad**) of 0.013 eV to the theoretical results.

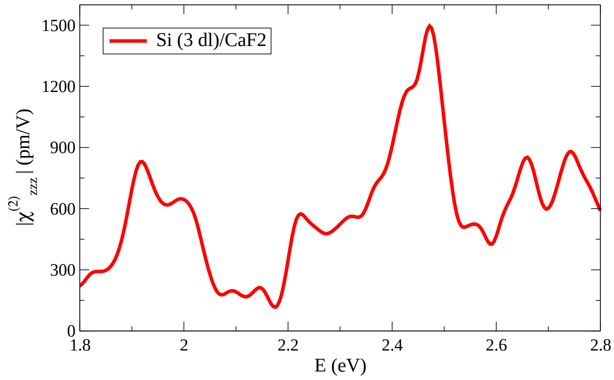

Figure 6.10: IPA-SHG spectrum of the Si(111)(3dl)/CaF$_2$(4l) system with 30 Å of vacuum into the simulation cell.

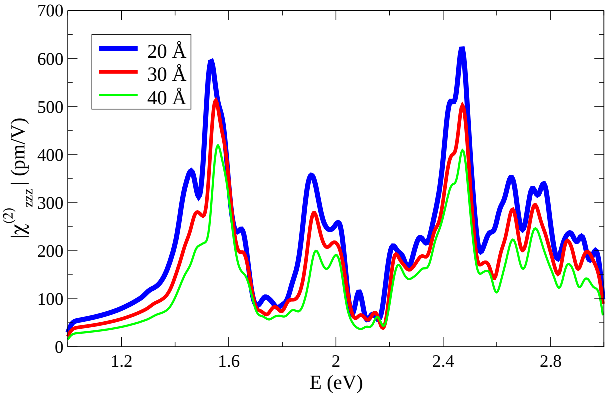

Figure 6.11: Comparison among the IPA second harmonic generation spectra for the Si(111)(3dl)/CaF$_2$(4l) with respectively 20 Å (blue curve), 30 Å (red curve) and 40 Å (green curve) of vacuum into the simulation cell. The results have not been renormalized.

are compared in Fig. (6.11) and the same spectra are reported in Fig. (6.12) once an appropriate renormalization factor has been applied to make the three systems coincide to a cell with a 50%/50% insulator/semiconductor ratio (the Si height has been taken as reference). As can be seen 30 Å represents an accurate choice of the height of the vacuum slab. It permits to avoid interference among the Si and CaF$_2$ surfaces of different replica in the SHG response. From now on, all the following systems are constructed inserting 30 Å of vacuum on top of the CaF$_2$ slab.

6.4.2 Insulator Thickness Convergence

Si(111)(6dl)/CaF$_2$(4l)

I started from a system composed of 6 dl of Si(111) and 4 layers of insulating CaF$_2$; the height of the simulation cell is 59.6 Å (see Fig. (6.13)). Again, the equilibrium configuration of the system has been obtained through a DFT relaxation of the atomic positions with the DFT convergence parameters of Tab. 6.1. The total thickness of the silicon slab is $\sim$ 17.7 Å and the one of the insulating CaF$_2$ is $\sim$ 12.2 Å. In Fig. (6.14) is plotted the band dispersion along the $L-\Gamma-X-\Gamma$ path. The systems present an indirect gap of 0.70 eV between the Γ and L points and a direct gap of 1.14 eV at the L and X points. The DFT-LDA direct gap at Γ of 1.47 eV in the following SHG-IPA calculation corrected through a scissor operator of $\Delta = 0.93$ eV to recover the experimental value. The converged SHG parameters are reported in Tab. (6.3).

The same calculation has been performed on the system where the insulating slab has been doubled up to 21.6 Å of thickness (i.e. 7 layers of calcium fluoride). The height of the cell has been consequently increased to 68.8 Å and the geometry has been relaxed with the DFT parameters of Tab. 6.1. For completeness the band structure has been reported in Fig. (6.15). The converged SHG parameters are reported in Tab. (6.3).

The two spectra are compared in Fig. (6.16), where the Si(111)/CaF$_2$(7l)

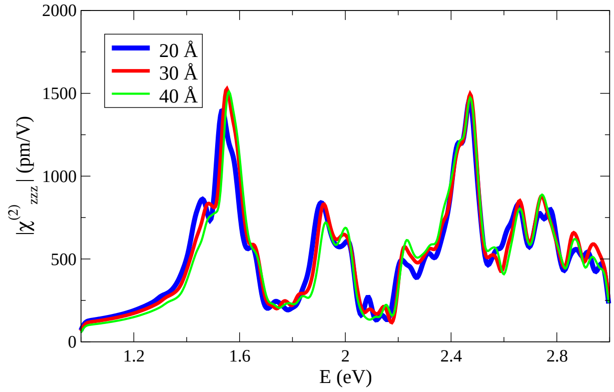

Figure 6.12: Comparison among the IPA second harmonic generation spectra for the Si(111)(3dl)/CaF$_2$(4l) with respectively 20 Å (blue curve), 30 Å (red curve) and 40 Å (green curve) of vacuum into the simulation cell. The results have been renormalized to a simulation cell composed of an equal amount of insulator and semiconductor material, keeping the silicon thickness as reference.

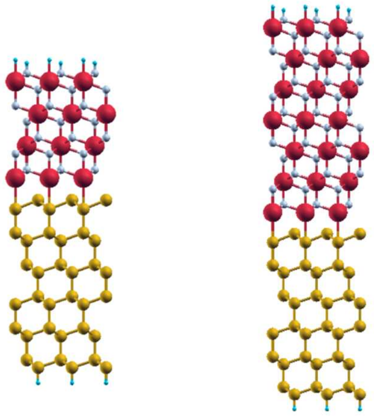

Figure 6.13: Si(111)(6dl)/CaF$_2$(4l) system (left) and Si(111)(6dl)/CaF$_2$(7l) system (right). The silicon (yellow) thickness is fixed whereas the calcium fluoride (respectively Ca in red and F in grey) slab is varied. Both the surfaces are terminated with H atoms (light-blue).

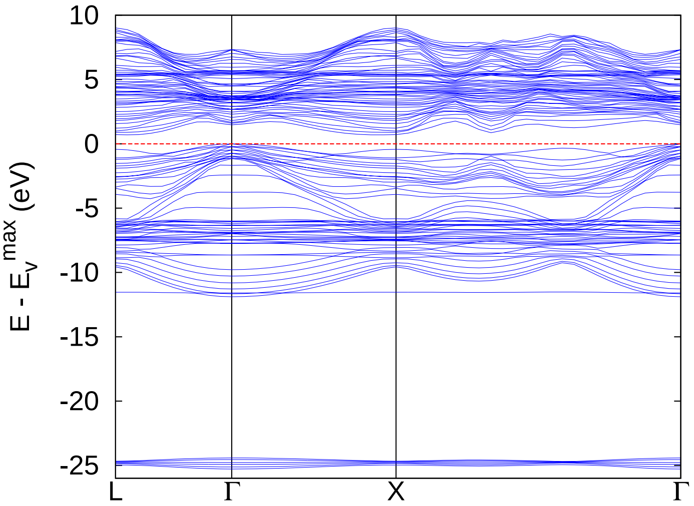

Figure 6.14: Band structure of the Si(111)(6dl)/CaF$_2$(4l) interface along the $L - \Gamma - X - \Gamma$ path. The zero has been taken as the valence maximum.

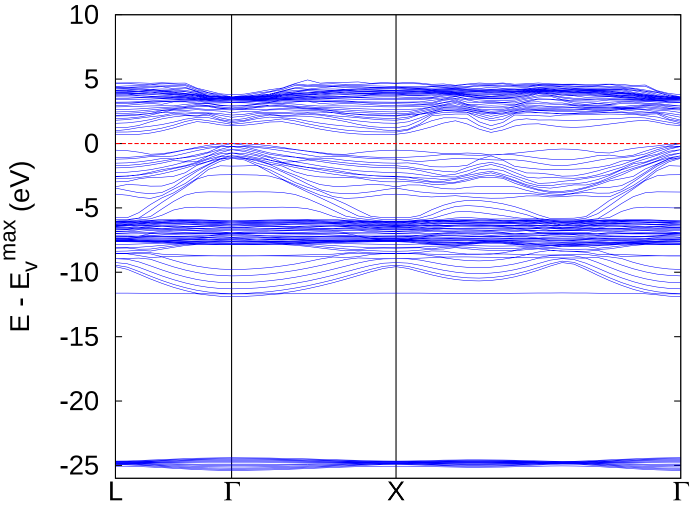

Figure 6.15: Band structure of the Si(111)(6dl)/CaF$_2$(7l) interface along the $L - \Gamma - X - \Gamma$ path. The zero has been taken as the valence maximum.

	(4l)	(7l)
npwwfn	2997	3989
nband	105	120
lomo	34	55
npwmat	1	1
k-grid	960	960
SO	0.93	0.93
domega	0.004	0.004
broad	0.013	0.013

Table 6.3: Parameters of the IPA 2LIGHT calculation on Si(111)/CaF$_2$(4l) and Si(111)/CaF$_2$(7l) systems.

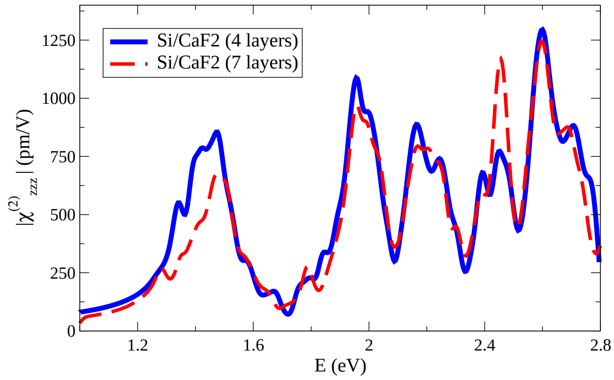

Figure 6.16: Comparison of the IPA-SHG spectra for the Si(111)(6dl)/CaF$_2$(4l) system (blue straight line) and the Si(111)(6dl)/CaF$_2$(7l) system (red dashed line). doubling the thickness of the insulating slab the spectra is almost unaffected.

response has been renormalized to the volume of the Si(111)/CaF$_2$(4l) system.

They agree within a good accuracy. The peaks of both the systems have the same energy positions and the shape of the two spectra coincide. This shows that only the first interface layers of the CaF$_2$ contributes to the interface SHG optical signal. Adding new insulator layers will introduce bulk states that are far from the energy gap (calcium fluoride possesses an energy gap of about 8 eV for the used pseudopotentials). Because of the inversion symmetry they do not contribute to the SHG spectrum. Moreover, already for the linear optics where the transition are allowed, they enter only in the high part of the spectrum, far from the studied energies because of the large energy gap of CaF$_2$. In conclusion, the CaF$_2$ after the first layers does not enter in the interface SHG signal. Adding new states does not modify the response. This is due to its transparency that makes it behave as the overhanging vacuum, justifying the assumption of considering vacuum and CaF$_2$ as an unique transparent insulating slab.

From now on I will consider only four layers of CaF$_2$.

6.4.3 Semiconductor Thickness Convergence

As done for CaF$_2$, I have studied the active region of silicon contributing to the interface SHG response. Silicon should give the most important contribution to the spectrum with respect to CaF$_2$. Its states are indeed close to the energy gap, describing transitions in the low energy part of the optical signal. Moreover, the effects of the interface propagates deep in the volume. This can be se from the relaxation of the layers beyond the interface. Whereas CaF$_2$ is almost unaffected and achieve soon the bulk geometry, the distance among the first Si layers is reduced close to the interface and increases progressively converging after the first four double layers to the bulk configuration. One expects hence that all that region, where the centro-symmetry is lost, originates the SHG process. The high sensitivity of SHG to the symmetry can even go deeper into the substrate being related to the electronic configuration (i.e. the deformation of the electronic orbitals) more than to the nuclei geometry. As a consequence silicon thickness has to be increased until the bulk configuration is recovered. This define the active region of silicon.

The surface, as a symmetry-broken region, can contribute to the final SHG process. It becomes then mandatory to keep the same configuration (i.e., the same surface SHG-signal) in order identify and distinguish it from the interface spectrum, as will be later presented in section 6.5. Therefore, each time I increase the cell, I add 3 double layers of silicon, that correspond to the Si(111) unit of repetition keeping the same surface configuration.

Si(111)(9dl)/CaF$_2$(4l)

I keep ~ 12.2 Å of CaF$_2$ increasing the Si thickness up to 9 double layers achieving a semiconducting slab of 27.0 Å (for a total height of 68.9 Å of the simulation cell). The parameter of the DFT relaxation are the ones of Tab. 6.1. Fig. (6.17) shows the relaxed geometry while Fig. (6.18) shows the band structure of the system. The relaxation do not modify anymore the interface and surface geometry. That is, the distances among the silicon layers forming these regions is unchanged. All the new Si inserted into the cell increases then the bulk slab inside the semiconductor i.e., the geometry of the interface and the surface are both converged within 9dl-27.0 Å of silicon.

Whereas the maximum of the valence band (HOMO) continues to be positioned at the Γ point, the minimum of the conduction band is close to the X point slightly shifted. The system presents an indirect gap of 0.60 Å whereas the optical gap is still at the X and L points, with a value of 1.12 Å. The DFT-LDA direct gap at Γ of 1.41 eV has been then corrected introducing a scissor operator of $\Delta = 0.99$ eV to the whole band structure. The converged SHG parameters are given in Tab. 6.4 and the renormalized spectra is reported in Fig. (6.19).

Si(111)(12dl)/CaF$_2$(4l)

The system has been then increased to 12 double layers of silicon, obtaining a thickness of 36.3 Å and a simulation cell height of 78.1 Å. Relaxing the system after the introduction of 3dl of bulk Si inside the semiconductor, I have verified that the maximum force acting on the ions is already below the force-threshold of **tolmxf**$= 5{\cdot}10^{-}5$ Ha/bohr, without performing any relaxation cycle. Again, the DFT parameter are the ones of Tab. 6.1, whereas in Fig. (6.17) and Fig. (6.20)

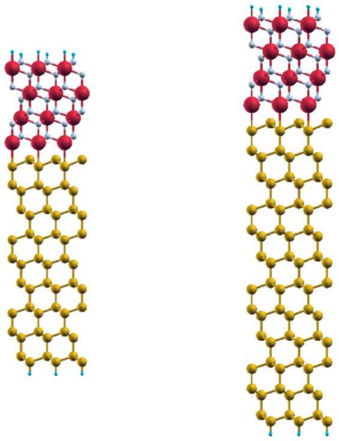

Figure 6.17: Si(111)(9dl)/CaF$_2$(4l) system (left) and Si(111)(12dl)/CaF$_2$(4l) system (right). The silicon (yellow) thickness is increased while the calcium fluoride (respectively Ca in red and F in grey) is is kept fixed. Both the surfaces are terminated with H atoms (light-blue).

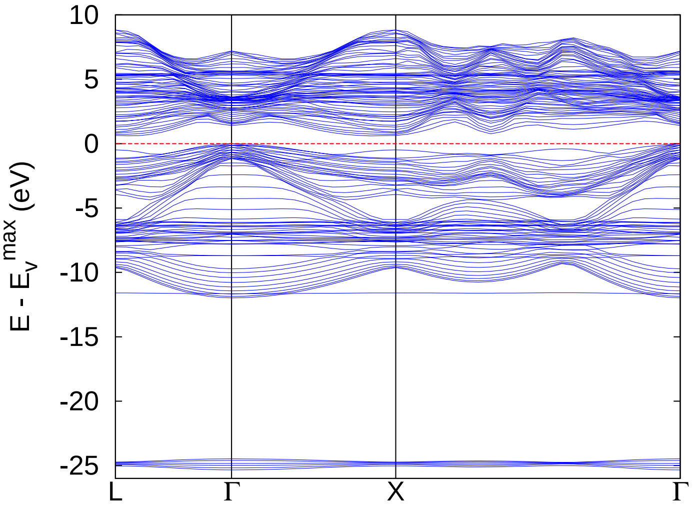

Figure 6.18: Band structure of the Si(111)(9dl)/CaF$_2$(4l) interface along the $L-\Gamma-X-\Gamma$ path. The zero has been taken as the valence maximum.

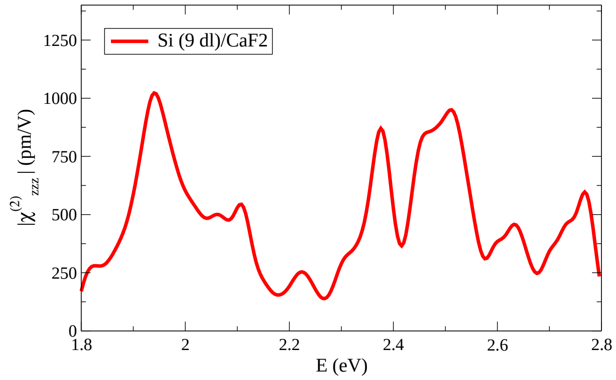

Figure 6.19: IPA second harmonic generation spectra for the Si(111)(9dl)/CaF$_2$(4l) system. The spectrum has been normalized to 50%/50% silicon/insulator ratio.

	9 dl	**12 dl**	**15 dl**
npwwfn	3989	3989	4493
nband	110	115	130
lomo	45	55	60
npwmat	1	1	1
k-grid	960	640	608
SO	0.099	1.03	1.065
domega	0.004	0.004	0.004
broad	0.013	0.013	0.013

Table 6.4: Parameters of the IPA 2LIGHT calculation on Si(111)(9dl)/CaF$_2$, Si(111)(12dl)/CaF$_2$ and Si(111)(15dl)/CaF$_2$ systems.

they are reported respectively the geometry and the band structure of the system.

The indirect gap is given by the same HOMO-LUMO transition of the Si(111)(9dl)/CaF$_2$($4l$) system, with a value of 0.55 eV. The DFT-LDA optical gap at X reads 1.11 eV whereas the one at the Γ points is equal to 1.37 eV. In the optical simulation I have therefore adopted a scissor operator identified by Δ = 1.03 eV. The others SHG parameters are listed in Tab. 6.4 and the spectrum is reported in Fig. (6.21).

Si(111)(15dl)/CaF$_2$(4l)

The last studied system is the single interface of Si(111)/CaF$_2$ with 15 double layers of silicon, for a total thickness of 45.6 Å of the semiconductor, 12.2 Å of CaF$_2$ insulator, 30 Å of vacuum and a simulation cell of 87.4 Å height (see Fig. (6.22))

The maximum force acting on the ions are below the force-threshold of **tolmxf**$= 7 \cdot 10^-5$ Ha/bohr. For the self-consistent DFT cycle the parameter of Tab. 6.1 demonstrated to be sufficiently accurate accordingly to the total energy threshold of $5 \cdot 10^{-5}$% chosen in section 6.4.1. Bigger **k**-grids or values of $\mathbf{E}_{cut}$

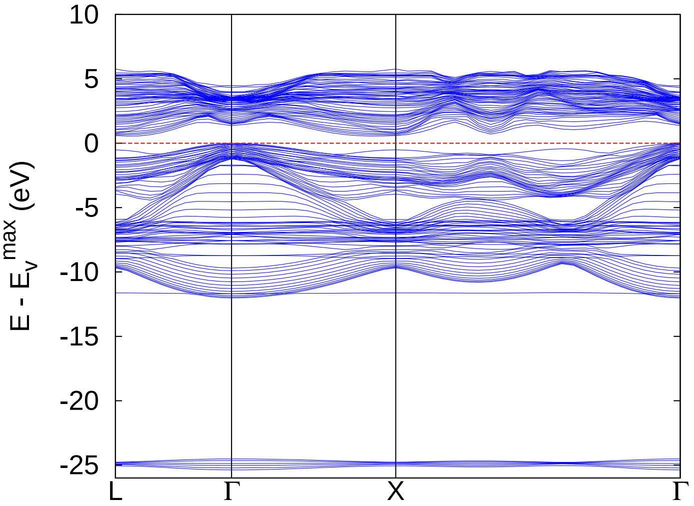

Figure 6.20: Band structure of the Si(111)(12dl)/CaF_2(4l) interface along the $L-\Gamma-X-\Gamma$ path. The zero has been taken as the valence maximum.

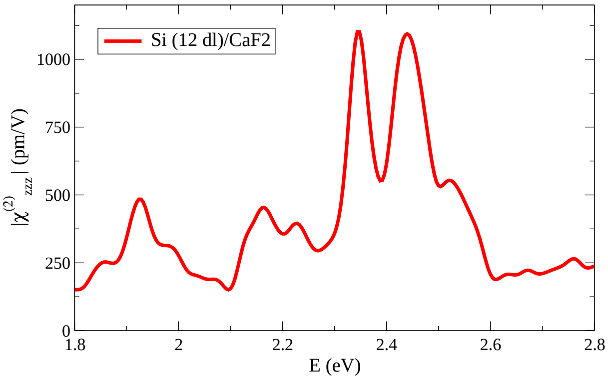

Figure 6.21: IPA second harmonic generation spectra for the Si(111)(12dl)/CaF_2(4l) system. The spectrum has been normalized to 50%/50% silicon/insulator ratio.

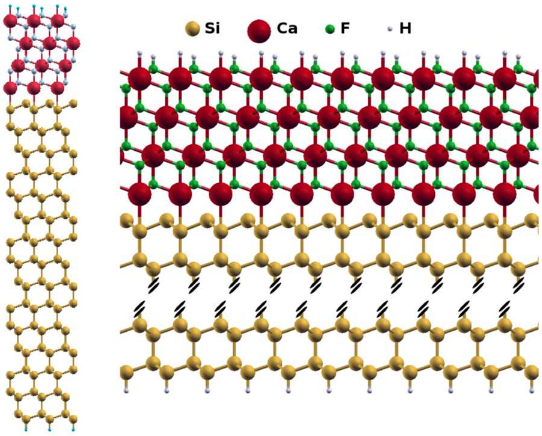

Figure 6.22: Si(111)(15dl)/CaF$_2$(4l) system (left). On the right is shown the interface region and the two surfaces.

give rise to corrections that are below that value. The geometrical configuration at the interface is in good agreement with the atomic distances measured by Tromp *et al.* [88].

The direct gap at Γ (Fig. (6.23)) measures 1.335 eV, consequently the scissor operator has been chosen as $\Delta = 1.065$ eV. The others SHG parameters are listed in Tab. 6.4. Since the insulating silicon reached the same height of the CaF$_2$ plus vacuum volume, the signal does not require to be renormalized. The spectrum is shown in Fig. (6.24) and the convergence parameters are listed in Tab. (6.4).

Comparison of the results

In Figs. (6.25-6.28) the second harmonic spectra of the different single-interface system presented in section 6.4.3 are compared. Convergence of the spectra, as seen in 6.4.2, is mainly motivated by the position of the main peaks and by the overall shape of the spectra in the interesting energy range. Therefore, the scissor operator revealed necessary in order to correct the DFT-LDA underestimation of the quasi-particle gap, positioning at the correct energy value the peaks arising from the resonant transitions.

In order to make clearer the comparison among the systems, I plotted only two systems at a time. As can be seen in Fig. (6.27), already at 36.3 Å of silicon (12dl) there is convergence in the shape of the spectra with respect to the former 9dl system.

The form of the peaks around 2.4 eV (the energy of the experimental measurements) becomes more defined and the SHG spectra is well converged. However, there is an important structure present both in the 9dl, 12dl systems at about $[1.8 \div 1.9]$ eV that is decreasing and disappears only when 15dl are considered. This big resonance arises from the bottom silicon surface, as will be shown in the next section 6.5 and as obtained in previous works presented in

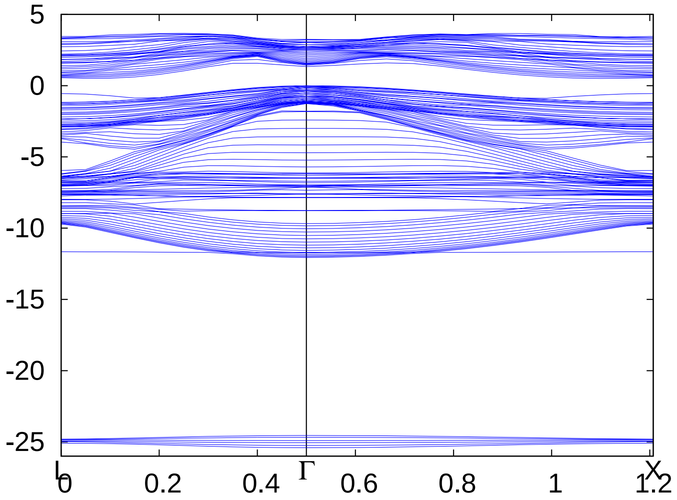

Figure 6.23: Band structure of the Si(111)(15dl)/CaF_2(4l) interface along the $L - \Gamma - X$ path. The zero has been taken as the valence maximum.

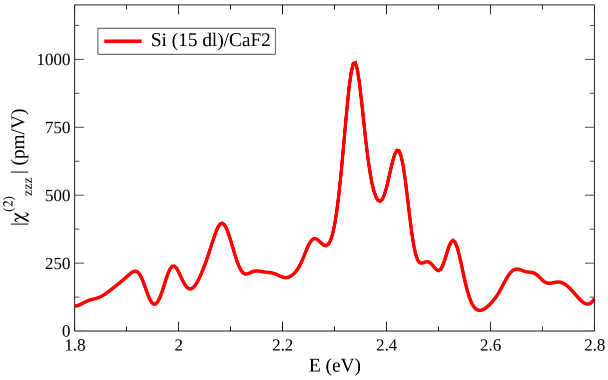

Figure 6.24: IPA second harmonic generation spectra for the Si(111)(15dl)/CaF_2(4l) system.

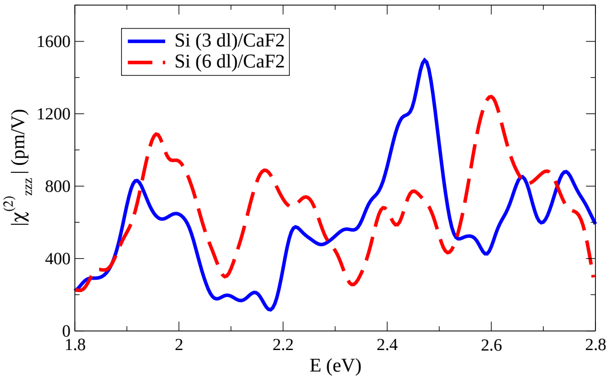

Figure 6.25: Comparison of the IPA second harmonic generation spectra between the Si(111)(3dl)/CaF$_2$(4l) (blue straight line) and the Si(111)(6dl)/CaF$_2$(4l) (red dashed line) systems.

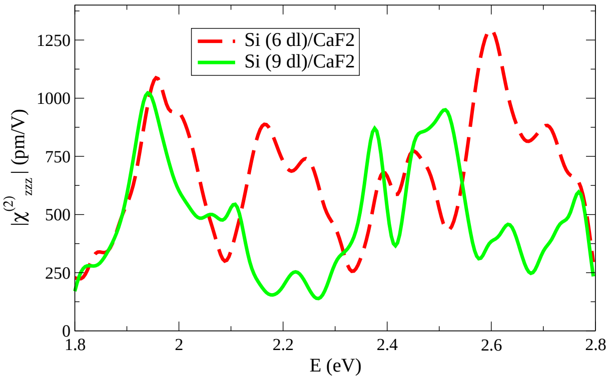

Figure 6.26: Comparison of the IPA second harmonic generation spectra between the Si(111)(6dl)/CaF$_2$(4l) (red dashed line) and the Si(111)(9dl)/CaF$_2$(4l) (green continuous line) systems.

literature [70].[21] Consequently I have chosen the Si(111)(15dl)/CaF$_2$(4l) system as the converged structure, where the surface contribution becomes negligible with respect to the interface signal that dominates. The active silicon region beyond the interface demonstrated to go deep into the substrate, more than what suggested by the structure relaxation that involves the first 3-4 double layers underlying the interface.

---

[21] Ref. [70] evaluates the contribution of an monohydride-terminated Si(111)(1×1)-H surface and the theoretical result corrected with a scissor operator shows an analogous peak at about 3.8 eV for the outgoing signal i.e., 1.9 eV for the input laser. This is exactly the peak found in our calculation. They found another peak at higher energy (∼2.25 eV), but in our system that structure is suppressed because of the presence of the interface and the different geometry, as will be shown later.

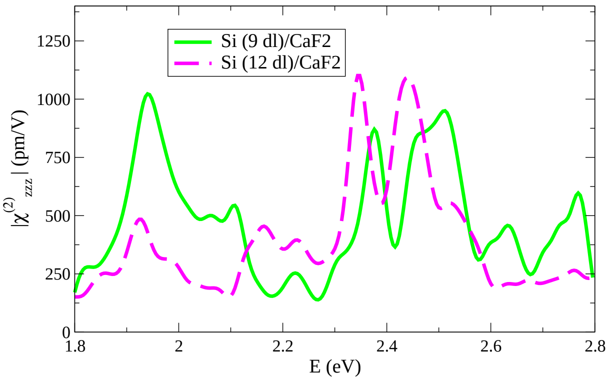

Figure 6.27: Comparison of the IPA second harmonic generation spectra between the Si(111)(9dl)/CaF$_2$(4l) (green continuous line) and the Si(111)(12dl)/CaF$_2$(4l) (magenta dashed line) systems.

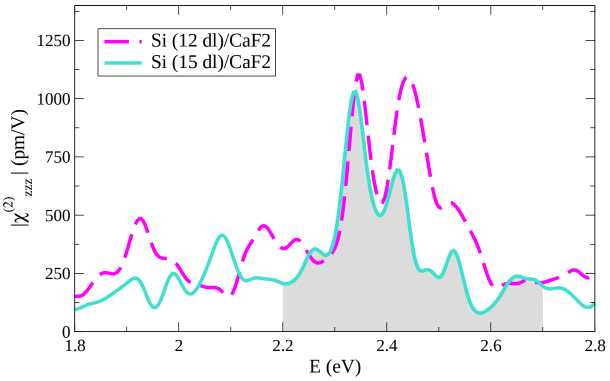

Figure 6.28: Comparison of the IPA second harmonic generation spectra between the Si(111)(12dl)/CaF$_2$(4l) (magenta dashed line) and the Si(111)(15dl)/CaF$_2$(4l) (light-blue continuous line) systems. The two spectra are converged in the energetic region of the interface (shaded area). The surface peak at about 1.9 eV is vanishing with respect to the interface signal that dominates.

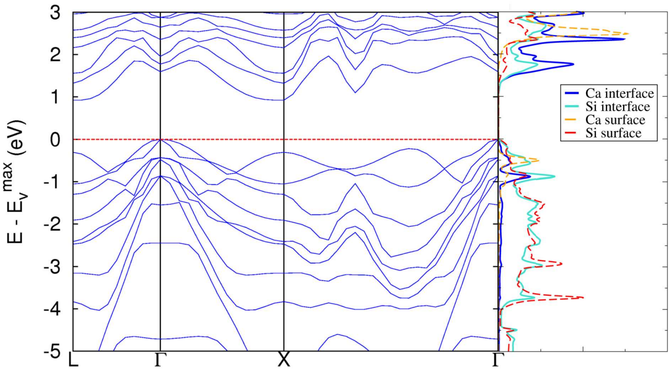

Figure 6.29: Energy-gap band structure for the Si(111)(3dl)/CaF$_2$ system (left). The projected density of states has been plotted (right) for the interface Ca (blue continuous line), Si (light-blue continuous line) atoms and the surface Ca (orange dashed line), Si (red dashed line) atoms. Silicon surface states are present into the energy gap.

6.5 Surface Signal

As observed in the previous section (Sec. 6.4.3), the two surfaces that appears in the simulation cell can have a proper SHG signal that mix with the one characteristic of the interface. Looking a the density of states for the CaF$_2$ hydrogenated surface (see Fig. (6.29)), one does not expect it to contribute to the SHG spectra at these low energies being far away from the considered energy. On the contrary, Si surface states enters directly in the gap region (and determines the HOMO state at X, the optical gap), and their contribution cannot be neglected.

Consequently further analysis should be performed to evaluate the contribution of the Si(111)-H surface. I studied the Si(111) slabs passivated on one surface with the H atoms as for the interface case, and on the other side with P and As atoms that saturates the dangling-bonds of silicon. I have then increased the Si thickness looking to the surfaces SHG spectra and their behavior. These do not coincide with real observed surface reconstruction, but are simple and useful for our purpose of determining the spurious features due to the presence of the Si(111)-H surface in our simulation cell.

H/Si(111)/As systems

The systems have been constructed in the usual way, substituting the topmost Si layer with an As atoms that bonds with its three dangling-bonds to the three underlying Si atoms. A vacuum height of 30 Å has been introduced into the simulation cell while the (x, y) lattice parameters have been taken to be the same of the former calculation. I have considered 6, 9 and 12 double layers of Si (see Fig. (6.30)).

Convergence parameter for the DFT calculation are presented in Tab. (6.5) I have performed both a relaxation of the cell parameter and a final self-consistent calculation of the ground state density of the system. In the silicon slab there

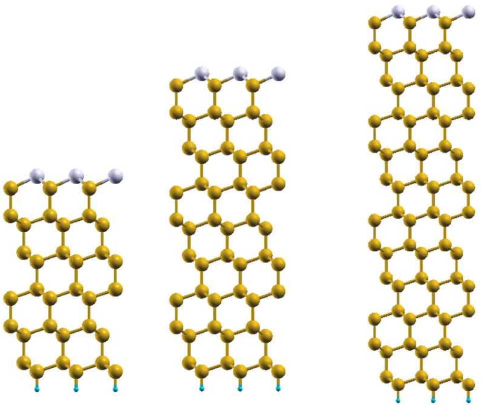

Figure 6.30: H/Si(111)(6dl)/As (left) H/Si(111)(9dl)/As (center) and H/Si(111)(12dl)/As (right) systems. The silicon (yellow) thickness is increased. The bottom surface is terminatd with hydrogen atoms (light-blue) while the upper surface is terminated with As atoms (white).

$\mathbf{E}_{cut}$	60 Ha
toldfe	10^{-12} Ha
k-grid	$9 \times 9 \times 1$
tolmxf	$5 \cdot 10^-5$ Ha/bohr
toldff	$5 \cdot 10^-6$ Ha/bohr

Table 6.5: Parameters of the DFT Abinit relaxation and following self-consistent density calculation for the H/Si(111)/As systems.

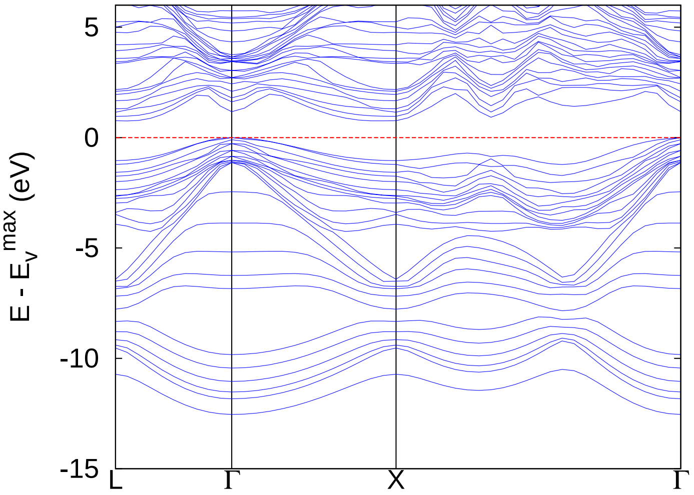

Figure 6.31: Band structure of the H/Si(111)(6dl)/As interface along the $L - \Gamma - X - \Gamma$ path. The zero has been taken as the valence maximum. The band dispersion around the gap is different with respect to the corresponding interface system (Fig. (6.14)).

are new surface states originating from the Si-As bond that modify the gap states dispersion, whereas the interface ones are not present. As an example, the optical gap due to band-folding is positioned at Γ (see Figs. (6.31-6.33)) contrary to what has been observed for the interface systems. As a consequence, the energy gap is no more the one of the interface for which the direct transition at Γ has been experimentally measured, and the SHG gap opening should be differently evaluated. Considering that the silicon quantum confinement is characteristic of the height of the silicon slab only, I decided to adopt the same SO correction of the corresponding Si(111)/CaF$_2$ interfaces. The SHG parameters for the H/Si(111)(6dl)/As, H/Si(111)(9dl)/As and H/Si(111)(12dl)/As systems are reported in Tab. (6.6) whereas the spectra are compared in Fig. (6.34). Convergence is achieved at 12 double layers of silicon. One finds the same struc-

	6dl	**9dl**	**12dl**
npwwfn	2489	2489	2493
nband	50	70	90
lomo	10	15	20
npwmat	1	1	1
k-grid	576	800	640
SO	0.93	0.99	1.03
domega	0.004	0.004	0.004
broad	0.013	0.013	0.013

Table 6.6: Parameters of the IPA 2LIGHT calculation on H/Si(111)($n$dl)/As systems.

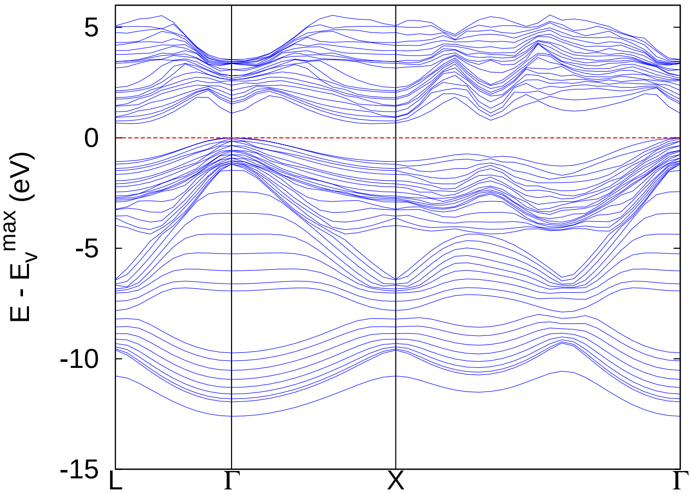

Figure 6.32: Band structure of the H/Si(111)(9dl)/As interface along the $L - \Gamma - X - \Gamma$ path. The zero has been taken as the valence maximum.

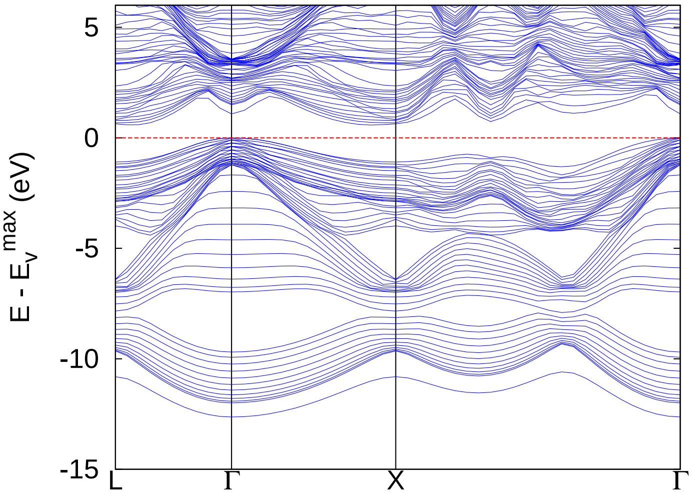

Figure 6.33: Band structure of the H/Si(111)(12dl)/As interface along the $L - \Gamma - X - \Gamma$ path. The zero has been taken as the valence maximum.

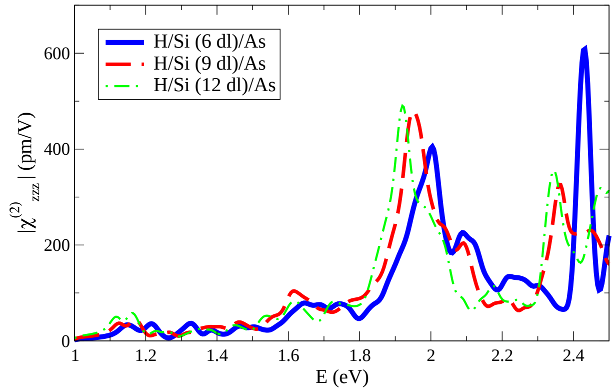

Figure 6.34: Comparison of the IPA second harmonic generation spectra between the H/Si(111)/As systems composed of 6 (blue straight line) 9 (red dashed line) and 12 double layers of silicon (green dashed-dotted line). The spectra are well converged already for 9dl. The peak at about 1.9 eV is consequently a characteristic of the silicon H-terminated surface.

ture at about 1.9 eV of the corresponding Si(111)/CaF$_2$ systems. In the present case the interface states are missing, substituted by a donor As atoms. The Si/As surface does not present dangling bonds and the Si surface is terminated with As atoms that links to the underlying three Si atoms. In the interface system instead, the Si slab is terminated with a unique Si-Ca bond. Therefore, the similarities between the two systems should arise from the hydrogenated Si(111) surface that, in conclusion, is responsible of the 1.9 eV peak.

H/Si(111)/P systems

The same test has been performed considering a P atom instead of As to saturate the surface silicon dangling-bonds. The bottom surfaces is again hydride-terminated Si(111) and I have considered 6 and 9 double layers composing the silicon slab (see Fig. fig:cellaSiP). Convergence parameter of Tab. (6.5) demonstrate to give results within the desired accuracy. In Figs.(6.36,6.37) are shown the band structures of the two systems. The SHG parameters for the H/Si(111)(6dl)/P and H/Si(111)(9dl)/P calculations are reported in Tab. (6.7) and the corresponding IPA-SHG spectra are shown in Fig. (6.38). Both of the systems show the same surface peak at about 1.9 eV although in this case H/Si(111)(6dl)/P is still converging. For my purpose the 9 double layers structure is sufficiently converged to compare with the previous results.

A comparison among the Si(111)(12dl)/CaF$_2$ and the H/Si(111)(12dl)/As and H/Si(111)(9dl)/P SHG spectra is shown in Fig. (6.39). The peaks around 1.9 eV is present in all the systems confirming to be characteristic of the hydrogenated surface, whereas the structures at higher energies are dependent on the topmost termination of silicon (i.e., the interface or the P/As surfaces).

The higher intensity of the interface signal around 2.4 eV shows that the interface signal is dominating over the surface response. This is clearer in Fig. (6.28) where increasing the Si thickness up to 15 dl the interface peaks are almost constant whereas the surface signal decrease. Therefore I consider

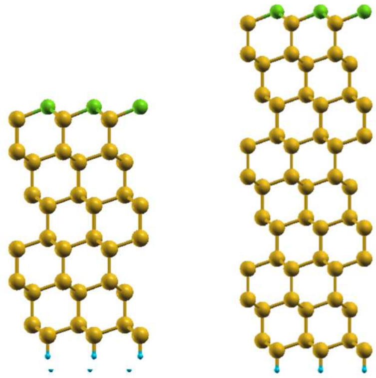

Figure 6.35: H/Si(111)(6dl)/P (left) H/Si(111)(9dl)/P (right). The silicon (yellow) thickness is increased. The bottom surface is terminatd with hydrogen atoms (light-blue) while the upper surface is terminated with P atoms (white).

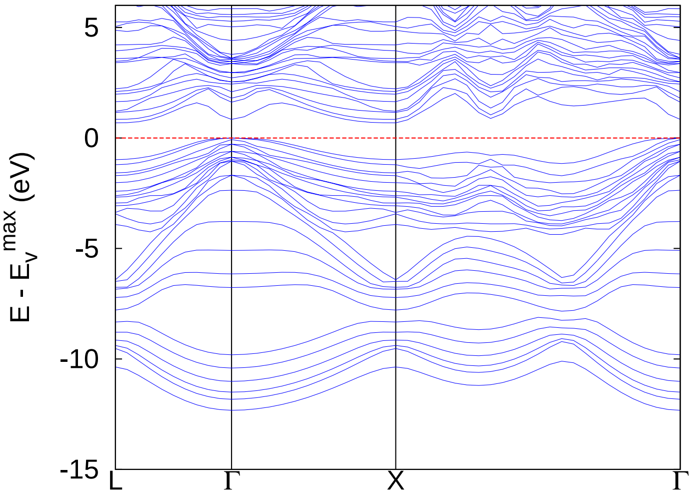

Figure 6.36: Band structure of the H/Si(111)(6dl)/P interface along the $L - \Gamma - X - \Gamma$ path. The zero has been taken as the valence maximum.

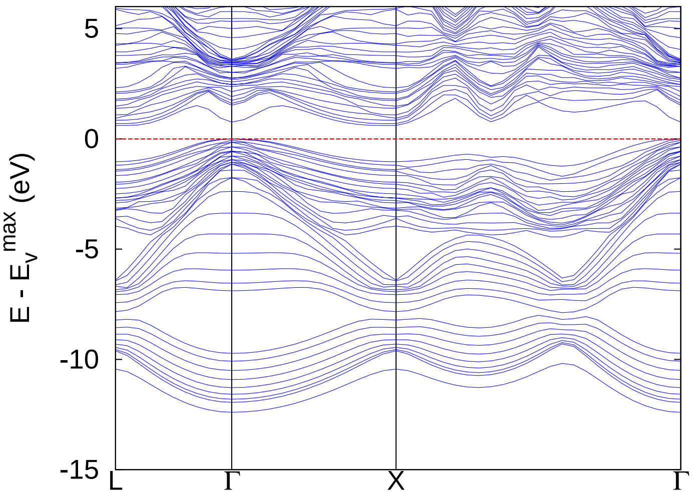

Figure 6.37: Band structure of the H/Si(111)(9dl)/P interface along the $L - \Gamma - X - \Gamma$ path. The zero has been taken as the valence maximum.

	6dl	**9dl**
npwwfn	2489	2489
nband	50	70
lomo	10	15
npwmat	1	1
k-grid	960	800
SO	0.93	0.99
domega	0.004	0.004
broad	0.013	0.013

Table 6.7: Parameters of the IPA 2light calculation of the H/Si(111)(6dl)/P and H/Si(111)(9dl)/P systems.

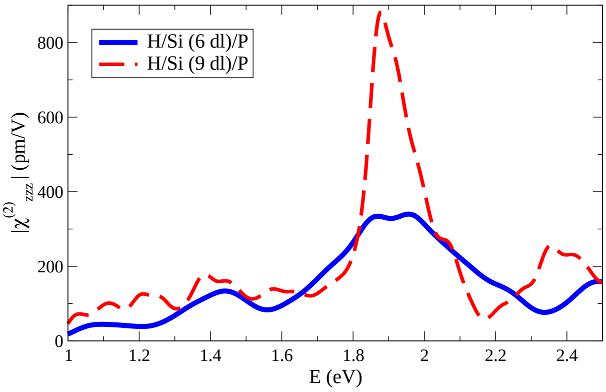

Figure 6.38: Comparison of the IPA second harmonic generation spectra between the H/Si(111)/P systems composed of 6 (blue straight line) and 9 (red dashed line) double layers of silicon. Again, the peak at about 1.9 eV reveals to be characteristic of the Si/H surface.

	IPA	LF-RPA	EXC
npwwfn	4493	4993	4993
nband	130	130	130
lomo	60	60	60
npwmat	1	11	11
k-grid	608	608	608
SO	1.065	1.065	1.065
alpha	0.0	0.0	-0.22355
domega	0.004	0.004	0.004
broad	0.013	0.013	0.013

Table 6.8: Parameters of the IPA and LF-RPA 2LIGHT calculation on Si(111)(15dl)/CaF$_2$(4l) system. Maximum values of **npwmat** have been tested up to 57 **G**-vectors per dimension of the $\chi^{(i)}$ matrices. Variations from **npwmat**= 11 demonstrated to be negligible in the present energy range.

the SHG signal of the Si(111)/CaF$_2$ interface to be converged with a silicon thickness of 45.6 Å and I chose the Si(111)(15dl)/CaF$_2$(4l) system for further analysis of the second harmonic generation process in the Si/CaF$_2$ interface.

6.6 Analysis of the SHG Spectrum

Once convergence in the IPA spectrum is achieved, I have studied the second-harmonic generation process at the Si(111)/CaF$_2$ interface introducing both the LF effects in the random phase approximation and the excitonic effects using the *alpha*-kernel according to the formalism and the equations presented in chapter 5.2. The SHG convergence parameter for the calculations are presented in Tab. (6.8). In Fig. (6.40) I report the calculated SHG spectra together with experimental data [82]. The experimental spectrum [82], originally in arbitrary units, has been reproduced for an easy comparison with our theoretical

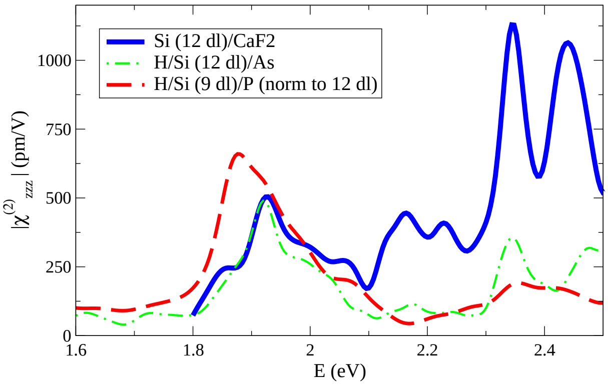

Figure 6.39: Comparison of the IPA second harmonic generation spectra of the Si(111)(12dl)/CaF$_2$ interface (blue stright line) and the response arising from the 12dl silicon slab passivated with As (green dashed-dotted line) and the 9dl slab whose upper surface has been passivated with P (red dashed line). The latter has been normalized to the silicon thickness of 12 dl for consistency in order to better compare with the other systems. The low energy peak is characteristic of the Si/H surface shared among the three structures, whereas the differences above 2.1 eV arise from the different termination of the silicon top-surface.

results. In the IPA response the energy position of the three main experimental peaks (2.26, 2.33 and 2.42 eV) are recovered but their relative intensities are wrong. In particular, the intensity of the second peak is strongly overestimated. When LF are included the energy position of the peaks remains practically unchanged while their height is in general diminished in this low energy region of the spectrum. The same trend has been observed for SiC and GaAs bulk semiconductors [72]. Nevertheless, with respect to these homogeneous systems, for Si/CaF$_2$ interface the SHG reduction and hence its dependence on LF effects is more important because of the discontinuity region. This behavior (i.e., the significant influence of LF on the spectrum) also occurs in the linear optic outcomes but with some noticeable differences. In fact, while IPA and LF absorption spectra almost coincide in that energy range, apart for a constant factor (Fig. (6.41)), IPA and LF SHG spectra present a different intensity modulation for each peak. This is the consequence of the specific local environment that surrounds the interface discontinuity where the SHG process is generated. In particular, in IPA the SHG peak at 2.33 eV seems to be the most important feature in the spectrum while with the inclusion of the LF this peak is drastically diminished with respect to the others.

Moreover the peaks at 2.26 and 2.42 eV substantially keep their relative intensity with the inclusion of the LF which also contributes to flatten out the peaked structure above 2.5 eV. Comparing with the experiment it is evident that only including the LF effects one can obtain a good agreement in terms of both energy positions and relative intensity of the peak structures.

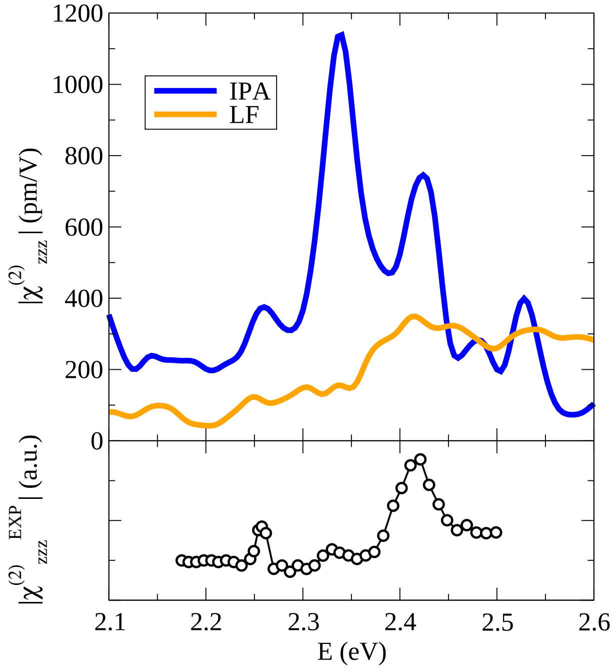

Figure 6.40: Second-harmonics generation spectra ($\chi^{(2)}_{zzz}$) calculated in IPA (blue line) and including LF (orange line). The experimental SHG spectrum from [82] is also reported (black line and circles) on the lower part of the graphic.

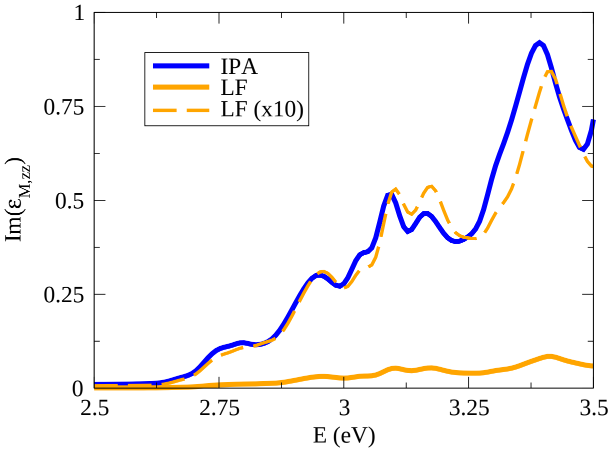

Figure 6.41: Absorption spectra ($\mathrm{Im}(\epsilon_{M,zz})$) in the **z** direction calculated in IPA (blue continuous line) and with inclusion of LF effects (orange continuous line). For a clearer comparison the LF curve has been multiplied by a factor of 10 (orange dashed line).

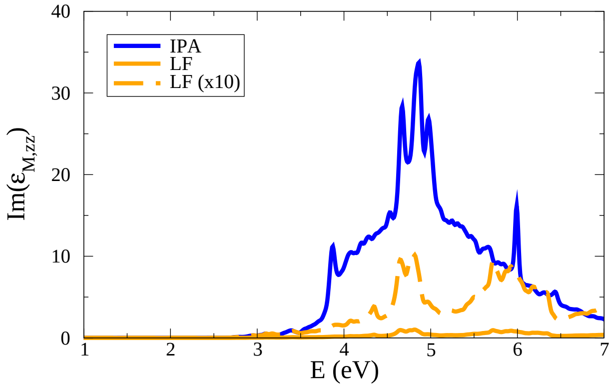

Figure 6.42: Absorption spectra ($\mathrm{Im}(\epsilon_{M,zz})$) in the **z** direction calculated in IPA (blue continuous line) and with inclusion of LF effects (orange continuous line). The energy range goes up to 7 eV including silicon bulk transitions. The depolarization effect caused by the sharp discontinuity shifts the IPA intensity at energies below the studied range. For a clearer comparison the LF curve has been multiplied by a factor of 10 (orange dashed line).

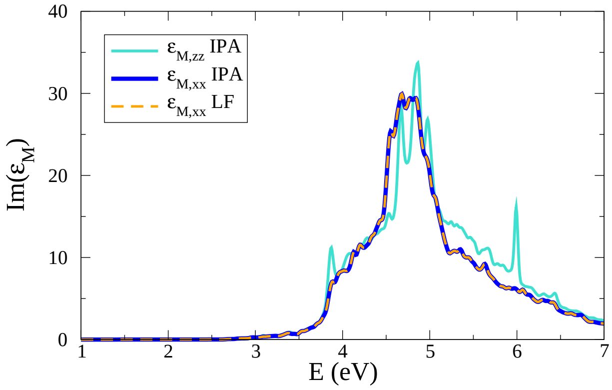

Figure 6.43: Absorption spectra ($\mathrm{Im}(\epsilon_{M,xx})$) evaluated with IPA (blue-continuous line) and with the inclusion of local-fields effects (orange-dashed line). The IPA curve of the $\mathrm{Im}(\epsilon_{M,zz})$ component has been reported for comparison (light-blue-continuous line).

6.6.1 Local Field Effects

In our approach, the effects of the crystal local fields enter through ϵ_M of Eq. (4.126) and through $\chi^{(2)}_{\rho\rho\rho}$ obtained from the second-order Dyson equation (Eq. (3.33)). In order to estimate the magnitude of these effects I have performed a comparative study with the linear absorption spectroscopy which is proportional to the imaginary part of ϵ_M (Eq. (4.121)).

The linear optical-absorption spectra for light polarized along the **z** direction are shown in Fig. (6.42). The presence of the LF strongly influences the linear optical properties of the system. In the IPA spectrum, at energy above ∼3.5 eV the silicon-bulk transitions start to be optically allowed and are much more numerous than the ones that take place at the interface, due to the different sizes of the two competing regions. As a result the latter are completely covered up. This becomes clear comparing e.g. the intensity of the Independent Particle Approximation (IPA) response (Fig. (6.42)) in the low energy part of the spectrum (i.e. where the bulk signal is absent, around 3 eV) with the total signal around 5 eV (where the curve is the sum of the bulk and the interface contributions): the former is 2 orders of magnitude smaller.

As a consequence, one can directly compare the linear and non-linear optical behaviors of the interface in the low part of the energy spectrum (Fig. (6.41)) only. LF effects strongly influences the absorption spectra in this energetic region: the whole intensity is lowered by about 10 times with respect to the independent particle response. However, the main features of the spectrum like the position of the peaks, the shape and the relative intensities are only slightly modified.

However, this is not an unexpected result. In a finite silicon structure (like the silicon slab of our calculations) or close to a surface/interface, the response at low energies along the confined direction is practically zero due to a depolarization effect [145, 187–189] while the main bulk peaks (i.e. the critical point energies E1 and E2) are shifted to higher energies. This effect is not present in the IPA calculation that cannot describe rapid variation of the potential in small regions and emerges when LF are introduced. Fig. (6.42) shows in fact the IPA bulk structure shifted[22] even out of the range of the calculation for the LF response. This depolarization effect arising from LF has already been studied in literature on similar Si-based systems like nanowires [145] surfaces [189] and nanodots [187, 188].

As suggested in Ref. [145], it is possible to compare and study their effects on the dielectric function along a direction where the system is infinite (in our case **x** or **y**). Here the system is homogeneous and one finds (Fig. (6.43)) that LF are almost negligible and the spectrum is not modified by the depolarization effect, as explained in Ref. [145]. As a consequence, this drastic intensity reduction is characteristic of the discontinuous direction z and negligible for the other more homogeneous components $\epsilon_{M,xx}$ and $\epsilon_{M,yy}$ (Fig. (6.43)).

These LF effects start to become relevant specifically for the calculation of the SHG coefficient $\chi^{(2)}_{M\ zzz}$ (as seen in Fig. (6.40)) i.e., when light is polarized along the **z** direction where the system is discontinuous. Similar to ϵ_M, one finds that their relevance is not true in general. Fig. (6.44) shows the SHG

---

[22] This is not a shift of the transition, hence a real shift of the IPA peak. It coincides with a remodulation of the oscillator strength that shifts the intensities (and consequently the peak) at higher energies.

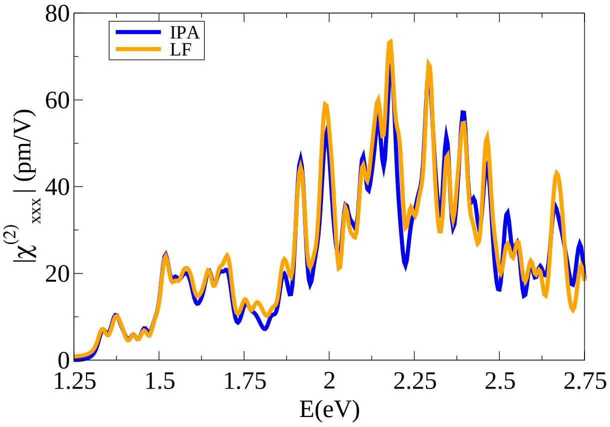

Figure 6.44: SHG spectra of the ($\chi^{(2)}_{M\ xxx}$) component calculated in the independent particle (IPA, blue line) and local fields (LF, orange line) approximations. LF effects are negligible along the homogeneous **x**, **y** directions.

$\chi^{(2)}_{M\ xxx} = \chi^{(2)}_{M\ yyy}$ spectra for light polarized in the **x** direction evaluated both in the independent particle approximation and introducing local fields. It is immediate to notice that because of the interface the signal does not vanish,[23] then the effects of LF demonstrated to be negligible with respect to IPA accuracy. In fact, along this direction the system is continuous and homogeneous and the SHG shares the same behavior of the linear response.

Analysis of the Local Field Effects

A direct study of the transitions contribution to the SHG process is possible only at the IPA level because, accordingly to our formalism, when LF are introduced $\chi^{(2)}_{zzz}$ is obtained through a second-order Dyson equation (Eq. 4.126) that mix linear and non-linear coefficients at different frequencies. Moreover, in the *velocity-gauge* several terms mixing two- and three-bands transitions contribute to the final response. As a consequence, it is not possible to identify particular transitions contributing to the final spectrum. Considering the *length-gauge* instead, Eq. (4.56) takes a simpler form in terms of three-states excitations and one can distinguish between transitions where the intermediate electronic state is a valence state (vvc transition) or a conduction one (vcc transition). The Si(111)/CaF$_2$ interface however show that the three major peaks of the IPA response contain both the two components Fig. (6.45). Since both contribute with the same order of magnitude to the main optical SHG peaks, it is not possible to relate the drastic decrease of the IPA peak at 2.33 eV when LF are included, with the suppression of a particular set of transitions, or the different nature of that peak.

Consequently, I developed another analysis method in order to understand which are the quantities that are mostly affected by the introduction of LF and

---

[23] For a pure hexagonal symmetry (as the one of Si(111)) the SHG component $\chi^{(2)}_{M\ xxx} = \chi^{(2)}_{M\ yyy}$ is identically zero because of symmetry selection rules (see App. F.1). In this case the interface breaks the symmetry and even these terms can exhibit a non-vanishing value.

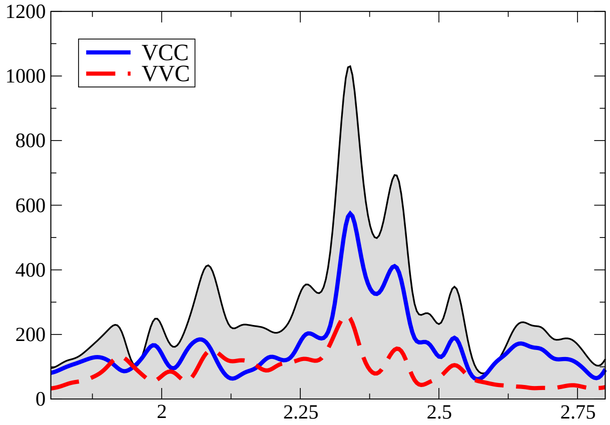

Figure 6.45: SHG-IPA spectra of the ($\chi^{(2)}_{M\ zzz}$) component calculated in the length-gauge. The VCC transitions (blue continuous line) and the VVC ones (red dashed line) signals are compared. Both the signal contributes to the main peaks of the total IPA spectrum (grey area).

which are responsible of the differences between the linear and non-linear cases. From Eq. (4.126) its is clear that the final response depends on the product of the dielectric function $\epsilon_{M,zz}$ with the density response function $\chi^2_{\rho\rho\rho}$.

From Figs. (6.41) and (6.42) it is evident that going beyond IPA the dielectric function is generally diminished by one order of magnitude, whereas the consequent decrease (about 10^{-3} arising from the three dielectric function that appear in Eq. (4.126)) is not observed in the SHG-LF result. As consequence LF produce a great enhancement of $\chi^{(2)}_{\rho\rho\rho}$ with respect to IPA that compensate the reduction.

Secondly I have investigated the non-uniform decrease of the SHG-IPA peaks when LF are included. It can be consequence of both the variation of the dielectric functions $\epsilon^{LL}_M(\mathbf{z}, \omega)$, $\epsilon^{LL}_M(\mathbf{z}, 2\omega)$ or of $\chi^{(2)}_{\rho\rho\rho}(\mathbf{z}, \mathbf{z}, \mathbf{z}, \omega, \omega)$. Therefore, I combined the different results:

(A) substituting in Eq. (4.126) the dielectric function ϵ^{LL}_M as obtained within the independent particle approximation, while including the local-field effects in the $\chi^{(2)}_{\rho\rho\rho}$ description (Fig. (6.46)).

(B) Studying the contribution of the single $\epsilon^{LL}_M(\mathbf{z}, \omega)$ or $\epsilon^{LL}_M(\mathbf{z}, 2\omega)$ quantities. The latter indeed contains frequencies where the bulk silicon is optically active in IPA and because of the depolarization effects LF drastically lower these structures (cfr. Fig. (6.42)). Results are reported in Fig. (6.47).

(C) In a similar way I have then evaluated the nonlinear optical spectra treating $\chi^{(2)}_{\rho\rho\rho}$ at the IPA level, while including LF effects into the dielectric functions (see Fig. (6.48)).

Comparison among these spectra and the ones of the IPA and LF calculation can give useful informations about the final form of the signal to which I am interested. Fig. (6.46) (A) show that when ϵ^{LL}_M is threat at the IPA level,

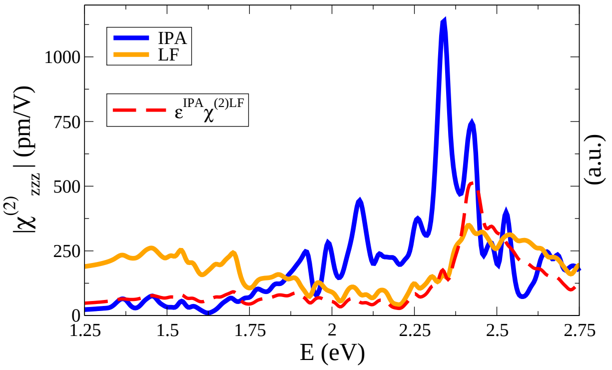

Figure 6.46: Comparison of the SHG ($\chi^{(2)}_{M\ zzz}$) spectra obtained within the IPA (blue line), including LF (orange line), and combining the IPA dielectric function $\epsilon_{M\ zz}$ and LF-$\chi^{(2)}_{\rho\rho\rho}$ (red dashed line) in Eq. (4.126). The latter curve is reported in arbitrary units (right hand-side scale). The curve recovers with good agreement the LF spectrum.

the peak at 2.33 eV disappears while the other are less affected, and one almost recover the SHG-LF curve. Hence, one can conclude that the different behavior of the linear response with respect to the SHG is contained in the $\chi^{(2)}_{\rho\rho\rho}$ quantity. From Fig. (6.47) (B) it is evident that the suppression of the peak at 2.33 eV is not due to the almost uniform decrease of interface states in the LF dielectric function (Fig (6.41)), neither to the shift of the bulk signal due to the depolarization effect in silicon (Fig. (6.42)). This indicates that the response is characteristic of the interface and is not enhanced by the presence of direct-bulk transitions that are missing in the LF absorption spectra.[24] The confirmation is provided by Fig. (6.48) (C) where the ϵ^{LL}_{M} LF spectra combined with the $\chi^{(2)}_{\rho\rho\rho}$ IPA curve recover the SHG-IPA result.

In conclusion it has been shown that interface local-field effects play an important role both for the linear as well as for the SHG spectrum, but the latter is almost independent of the former. All the information about the modifications of the SHG curve are mostly contained in $\chi^{(2)}_{\rho\rho\rho}$ response function, since the form of ϵ_M is almost unchanged and variations are small and slow with respect to the SHG range. This highlights how, for inhomogeneous systems where the potential undergoes rapid variations, the second-order density response functions $\chi^{(2)}_{\rho\rho\rho}$ become the key quantity for the SHG process and LF effects become predominant on the studied system.

6.6.2 Excitonic Effects

I have also studied the influence of the electronic effects on the interface SHG signal. Excitons have been described accordingly to the *alpha*-kernel f^{LRC}_{xc} presented in section 5.2 Eq. (5.18). The value of the binding constant α has been evaluated as in Eq. (5.19) from the static dielectric constant. The latter is obtained from the trace of the dielectric function tensor in the random phase

---

[24] Countrary to the Si(111)/H surface signal (Ref. [70]) where the enhancement of the SHG response has been shown to coincide with the E1, E2 bulk transitions.

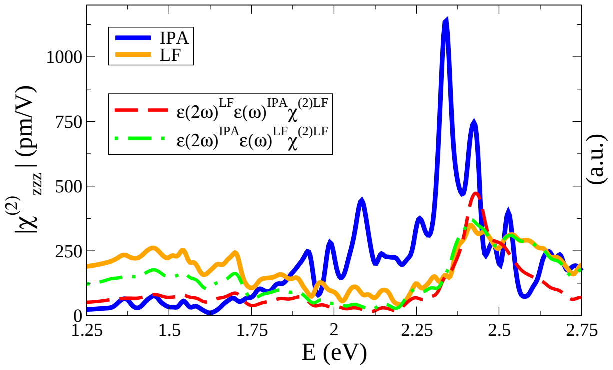

Figure 6.47: SHG ($\chi^{(2)}_{M\ zzz}$) spectra obtained considering separately $\epsilon_{M\ zz}(\omega)$, $\epsilon_{M\ zz}(2\omega)$ at the IPA and LF level of approximation (red dashed line) or viceversa (green dashed-dotted line). $\chi^{(2)}_{\rho\rho\rho}$ is taken in the LF-RPA, the results are in arbitrary units (right hand-side scale). The IPA (blue line) and LF (orange line) spectra are reported for comparison (left hand-side scale).

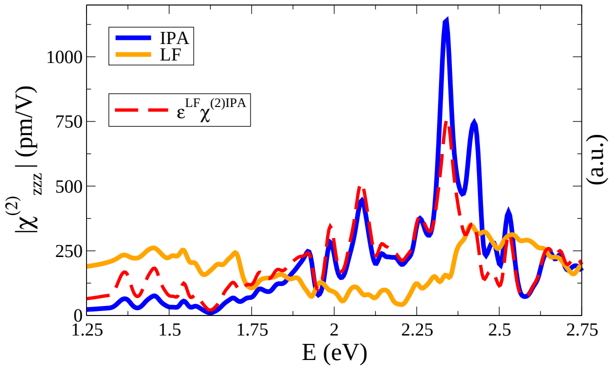

Figure 6.48: Comparison of the SHG ($\chi^{(2)}_{M\ zzz}$) spectra obtained within the IPA (blue line), including LF (orange line), and combining the LF dielectric function $\epsilon_{M\ zz}$ and the IPA-$\chi^{(2)}_{\rho\rho\rho}$ (red dashed line) in Eq. (4.126). The latter curve is reported in arbitrary units (right hand-side scale). The curve recovers with good agreement the IPA spectrum.

approximation (i.e., including the LF correction of section 5.2):

$$\begin{aligned}\epsilon_\infty &= \frac{1}{3}(\epsilon^{xx}(\omega=0)+\epsilon^{yy}(\omega=0)+\epsilon^{zz}(\omega=0)) = 4.52 \\ \alpha &= 0.81.\end{aligned} \tag{6.7}$$

In Tab. (6.8) are presented the converged parameter of the alpha-SHG calculations. The spectra is presented in Fig. (6.49). The importance of excitonic effects on the investigated Si(111)/CaF$_2$ interface is very small when compared to the LF one. Their contribution does not change at all the shape of SHG spectrum as calculated with LF.

Analogous studies have been performed on bulk semiconductors (GaAs, SiC). In particular in Refs. [72–74] using the same formalism and the serial version of 2LIGHT here adopted, they claim that only when one accounts for the excitonic effects obtain a very good agreement with the experimental second-harmonic generation spectrum. That consideration is explicitly related to a discussion on those systems. In general, the importance of LF and excitons depends on the physical nature of the system studied. LF carries out the information about the inhomogeneity of the system. Therefore, their effects are expected to be more important in the Si(111)/CaF$_2$ which has a discontinuity at the interface, than in bulk semiconductor (as GaAs).

From Fig. (6.49) is evident that the interface between Si and CaF$_2$ makes LF more important than excitons which contributes by just slightly and almost rigidly increasing the spectrum intensity. Moreover, as a test, I also varied α in a wider range of values as reported in Fig. (6.50). As can be seen, the role of the excitons on this particular system consists in a uniform variation of the general intensity of the system, that maintains unchanged the shape of the LF curve. In comparison, the local-fields effects play a much more important role modifying the form of the spectrum and smoothing in a selective way particular peaks.

This result, compared with the previous studies on bulk systems [72–74] underlines how the different physical nature of the systems determines the relative importance of these two effects. In the present case the interface is responsible of the SHG signal, making predominant the sharp variation of the potential in the interface region i.e. the local-fields, with respect to others many-body effects. This is an advancement in the comprehension of the SHG process, relating the nature of the system to the physics behind the process in order to obtain a good agreement with the experimental measurements.

6.7 Geometrical confirmation

Thanks to the knowledge of the systems acquired in the previous studies, as a test I have considered the Si(111)/CaF$_2$ interface in the B-type H_3 configuration. I have considered 12 double layers of silicon and four layers of CaF$_2$ with 30 Å of vacuum inside the simulation cell (see Fig. fig:cellaSiCaF2-H3). This configuration has been chosen in analogy with convergence parameters of T_4 interface. In Fig. (6.52) is shown the converged SHG spectra (convergence parameters are reported in Tab. (6.9)) where a scissor operator of 1.17 eV has been applied in order to open the direct energy gap at Γ to the experimental

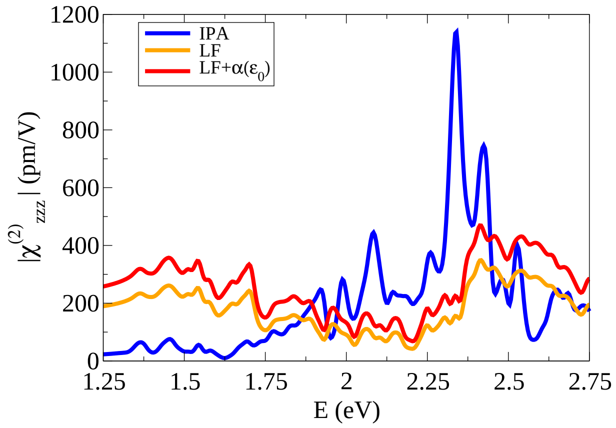

Figure 6.49: Second-harmonics generation spectra ($\chi^{(2)}_{zzz}$) calculated in IPA (blue line), including LF (orange line) and excitonic effects (red line).

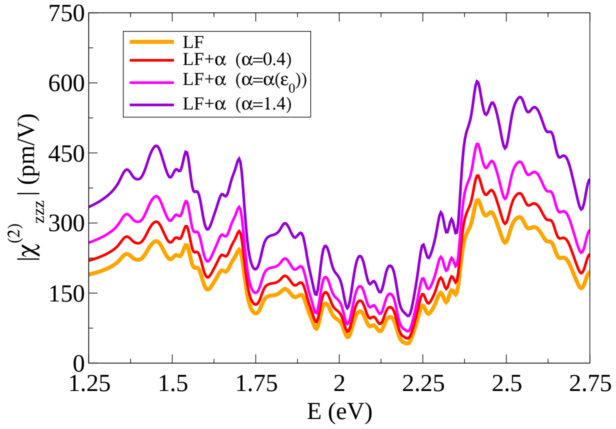

Figure 6.50: Second-harmonics generation spectra ($\chi^{(2)}_{zzz}$) including excitons contribution for different values of the parameter α, starting from $\alpha = 0$ i.e., the LF curve (orange line) up to te value $\alpha = 1.4$. The excitonic effects at the interface increase the outgoing signal although not changing its from even augmenting the electron-hole strength. For higher values of α the f^{LRC}_{xc} kernel is no more a good approximation.

Figure 6.51: Si(111)(12dl)/CaF$_2$(4l) system in the H_3 configuration.

value of 2.4 eV as obtained from the band structure (Fig. (6.53)). It is immediate to notice that neither IPA recovers the experimental data, nor LF that completely smooth down the spectrum giving an almost uniform background.

This results, together with the significant agreement obtained for the T_4 configuration, confirms the experimental investigations [76, 77] that attribute a T_4 B-type nature to the Si/CaF$_2$ interface grown at temperature above 700°C.

Conclusions

In conclusion, I have shown that an independent particle picture can give a qualitative description of the SHG process in the Si/CaF$_2$ interface, recover-

	IPA	LF-RPA
npwwfn	3999	3999
nband	124	124
lomo	40	40
npwmat	1	15
k-grid	912	912
SO	1.17	1.17
alpha	0.0	0.0
domega	0.004	0.004
broad	0.013	0.013

Table 6.9: Parameters of the IPA and LF-RPA 2LIGHT calculation on Si(111)(12dl)/CaF$_2$(4l) H_3 system.

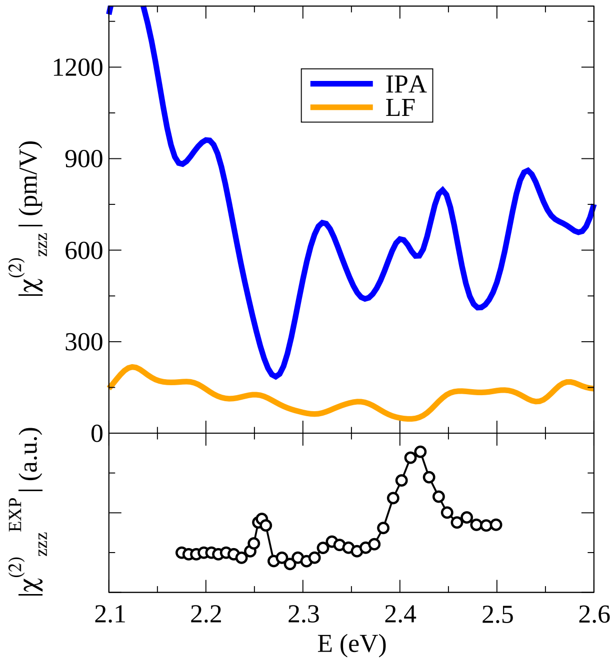

Figure 6.52: SHG spectra of the Si(111)/CaF$_2$ interface in the H_3 geometry. The ($\chi^{(2)}_{zzz}$) component is calcualted in IPA (blue line) and including LF (orange line). The experimental SHG spectrum from [82] is also reported (black line and circles) on the lower part of the graphic.

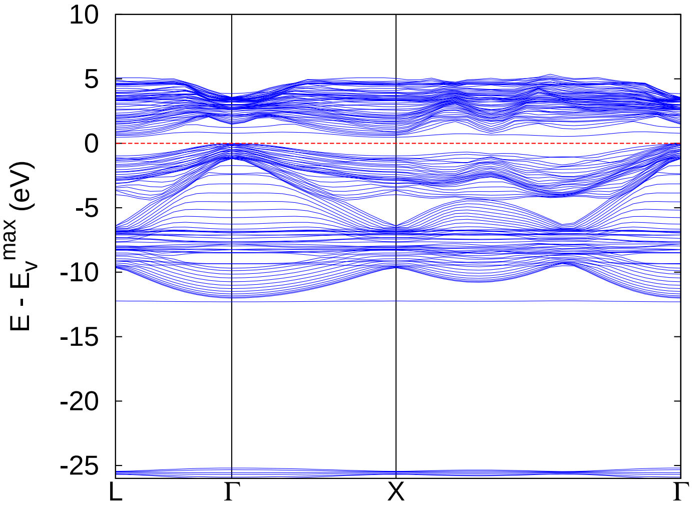

Figure 6.53: Band structure of the Si(111)/CaF$_2$ interface in the H_3 geometry along the $L-\Gamma-X-\Gamma$ path. The zero has been taken as the valence maximum.

ing the main features (in terms of energy peak position) originated from the anisotropies of the system. However, to match the spectral line shape of the experiment, LF effects become essential. In fact, LFs strongly influence the second-order nonlinear response close to the discontinuity region inducing a significant redistribution of the intensity. I demonstrated that this redistribution is largely more dramatic in nonlinear optical response than in the linear response. For SHG the lowering of the intensities is selective and not homogeneous while for absorption the shape of the spectrum is almost unchanged. My results have far-reaching consequences beyond the specific interface I have studied. The microscopic induced polarization can have large and unpredictable effects on the SHG process becoming essential for complex systems.

Chapter 7

Future Developments

Si/Ge Superlattices

In this chapter I will briefly introduce my work on the $(\mathrm{Si})_n/(\mathrm{Ge})_n$ superlattices. These are the preliminary results of a more detailed study that is, at the moment, in progress.

Si/Ge are of interest because of the particular properties they can assume in a superlattice structure. Actually, Because of quantum confinement it is possible to design the band dispersion close to the energy gap obtaining interesting electronic, optical and thermal-conductivity properties [190–193] Within the optical studies, also the nonlinear SHG process has been experimentally investigated [91, 92, 194–198]. In particular, considering the superposition of an equal amount of Si and Ge, if n (i.e., the number of Si and Ge layers) is even the crystal is centrosymmetric and the SHG signal vanishes, while for odd periodicity the nonlinear response is allowed and constructive interference among the periodic interfaces should give an intense harmonic radiation as theoretically predicted [21, 199, 200]. Further interest on these systems arise from the possibility to nanostructure these superlattices into different shapes e.g. constructing $(\mathrm{Si})_n/(\mathrm{Ge})_n$ nanowires [93].

These structures are experimentally obtained with MBE technique and nowadays, thanks to the latest technological developments, high control of the geometrical structure has been achieved and SHG has been measured [93, 196, 198] This allows to growth high, defect-free multilayers. In the past only low periodicity has been obtained and the even/odd layering has not been observed because of the growth errors (± 1 layer) that broaden the interfaces [195, 197]. Moreover, Zhang *et al.* [92] have observed, for superlattices grown on top of a Si(001) surface, that once the germanium thickness is over the value $n = 5$ layers there is a great enhancement (Fig. 7.1), of about one orders of magnitude, of the SHG response. This is due to the creation of nanometric *V-shape* misfit stacking fault defects (see Fig. 7.2) that originate from the lattice mismatch between Si and Ge.

Consequently, different kind of defects can be present and characterize the SHG process. In my work I have first addressed the role of defects in the $(\mathrm{Si})_n/(\mathrm{Ge})_n$ superlattices, trying to relate the different intensity and the form of the measured experimental spectra to their nature. In the future I will try

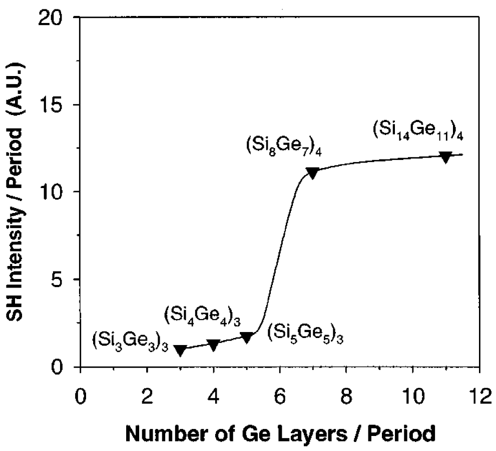

Figure 7.1: Experimental measurements of the Second Harmonic reflected intensity in (Si)$_n$/(Ge)$_m$ systems. A great enhancement has been observed once Ge thickness is over $m = 5$. (Reproduced from [92], Copyright ©1998 American Institute of Physics).

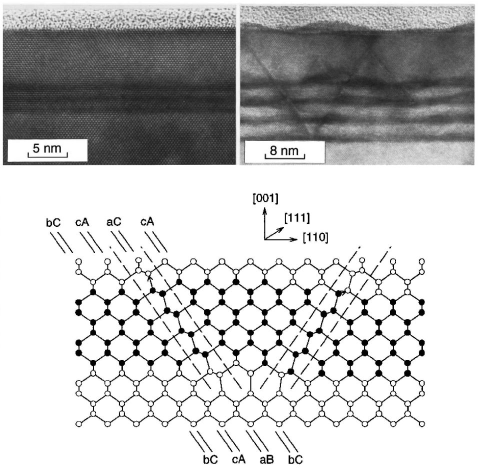

Figure 7.2: A defect-free (Si)$_3$/(Ge)$_3$ system (top left) and a *V-shape* misfit in (Si)$_5$/(Ge)$_5$ (top right) have been observed at TEM. (Reproduced from [92], Copyright ©1998 American Institute of Physics).

System	Å
Si_3/Ge_3	8.334
Si_4/Ge_4	11.113
Si_5/Ge_5	13.893
Si_7/Ge_7	19.455

Table 7.1: Height of the Si/Ge superlattice structure, considering the thickness of the Si slab plus the one of the Ge.

to compare the influence of other effects also, as the quantum confinement that appears once the superlattice is cut in a nanowire shape as in [93]. In the following some preliminary results are presented.

I have studied the $(\mathrm{Si})_n/(\mathrm{Ge})_n$ superlattices varying n from 3 up to 9 considering odd values and the even value $n = 4$ for comparison. The simulation cell $\mathbf{C}$ $(\mathbf{X}, \mathbf{Y}, \mathbf{Z})$ for even-periodic system is obtained passing from the FCC cell $(\mathbf{x}, \mathbf{y}, \mathbf{z})$ to the tetragonal unitary cell:

$$\mathbf{C} = \begin{pmatrix} \mathbf{X} = & \frac{1}{2}\mathbf{x} + \frac{1}{2}\mathbf{y} \\ \mathbf{Y} = & -\frac{1}{2}\mathbf{x} + \frac{1}{2}\mathbf{y} \\ \mathbf{Z} = & \mathbf{z} \end{pmatrix} \tag{7.1}$$

where $\mathbf{z}$ depends on the Si and Ge thicknesses. For odd-periodicity instead I have used both the tetragonal cell and the triclinic one. The first one is non-primitive, indeed two unitary cells of the Si/Ge slabs are required in order to recover the periodicity along $\mathbf{z}$. However, it reveals useful for ground state, band structure and GW calculations to take advantage of its symmetries. The triclinic cell $\mathbf{C}'$ is instead unitary, and reduce the computational cost of the optical calculations when looking for independent or random $\mathbf{k}$-points grid to better sample the Brillouin zone: symmetries here are less important. The triclinic cell has the same basis $(\mathbf{x}, \mathbf{y})$ but different third vector (that for simplicity I will call $\mathbf{Z}'$ although it is no more perpendicular to the basis), so $\mathbf{C}'$ becomes:

$$\mathbf{C} = \begin{pmatrix} \mathbf{X}' = & \frac{1}{2}\mathbf{x} + \frac{1}{2}\mathbf{y} \\ \mathbf{Y}' = & -\frac{1}{2}\mathbf{x} + \frac{1}{2}\mathbf{y} \\ \mathbf{Z}' = & \frac{1}{2}\mathbf{y} + \mathbf{z} \end{pmatrix} \tag{7.2}$$

The in-plane lattice parameter as been taken equal to 5.389 Å i.e., the one of silicon being the systems I want to compare with [92] grown on top of a Si(001) substrate. This is the lattice constant found for the pseudopotential used already in the simulation of the Si(111)/CaF$_2$. For germanium instead, I have adopted the pseudopotential of [183] that has already been tested with success for linear optics in Si/Ge nanowires. The perpendicular parameter instead has been fitted with a Murnhaghan curve for each system, looking at the value that minimizes the total energy. Their values are reported in Tab. (7.1). The studied structures are reported in Figs. (7.3-7.4). I have relaxed the systems with n =3,4,5,7. The thresholds values of the DFT calculation are the same of the previous Si/CaF$_2$ systems, while the energy cutoff varies from 30 Ha for the smallest ones, up to 50 Ha for the Si$_7$/Ge$_7$. The band structure of the Si$_5$/Ge$_5$ system is shown as an example in Fig. (7.5).

The SHG measurement is performed using afig:cellaDefA Ti:sapphire laser with 100 fs pulses at the wavelength of 800 nm (1.55 eV) corresponding to

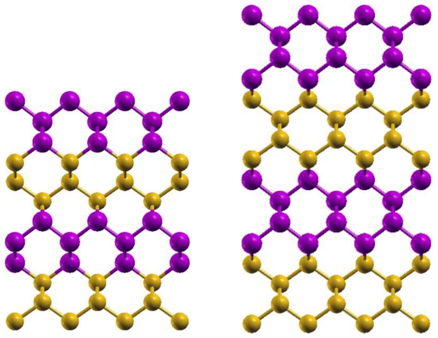

Figure 7.3: Ball and stick representation of the Si_3/Ge_3 (left) and Si_4/Ge_4 system (right), silicon is represented by yellow-balls and Ge by violet ones.

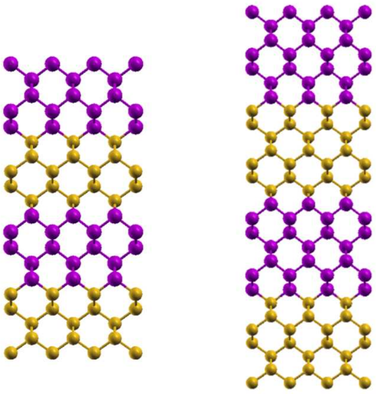

Figure 7.4: Ball and stick representation of the Si_5/Ge_5 (left) and Si_7/Ge_7 system (right), silicon is represented by yellow-balls and Ge by violet ones.

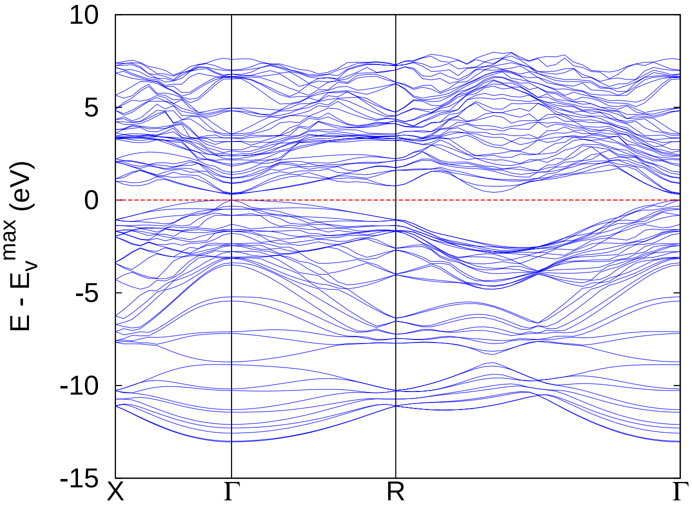

Figure 7.5: Band structure of the $\mathrm{Si}_5/\mathrm{Ge}_5$ superlattice along the $X-\Gamma-R-\Gamma$ path. The zero has been taken as the valence maximum.

the peak of the SHG response. The incident light is s-polarized and the observed SH radiation is p-polarized As observed for the Si(111)/CaF_2 system, it is important to apply a correction to the underestimation of the DFT-LDA band gap, otherwise the calculated spectra will be red-shifted with respect to the experiment, with missing peak due to the calculation of a different zone of the SHG spectrum. These corrections have been evaluated with a one-shot G_0W_0 calculation at the Γ point. The convergence parameters and the values of the quasi-particle energy gap are reported in Tab. (7.2). I have then studied the SHG signal of the defect-free superlattice structures (Figs. (7.3-7.4)). Local fields in this particular case revealed to be negligible and all the presented data are calculated in the IPA. I evaluated the tensor component $\chi^{(2)}_{xyz}$ in the tetragonal symmetry. It is given by:[1]

$$\begin{aligned}\chi^{(2)}_{zxy} = -\frac{i}{2}\epsilon^{LL}_{M}\left(\frac{\mathbf{x}+\mathbf{y}}{\sqrt{2}}, 2\omega\right)\epsilon^{LL}_{M}(\mathbf{x},\omega)\epsilon^{LL}_{M}(\mathbf{z},\omega)\\ \cdot\chi^{(2)}_{\rho\rho\rho}\left(\frac{\mathbf{x}+\mathbf{y}}{\sqrt{2}}+\mathbf{z}, \frac{\mathbf{x}+\mathbf{y}}{\sqrt{2}}, \mathbf{z}, \omega, \omega\right).\end{aligned} \tag{7.3}$$

The converged spectra have been evaluated up to 6.0 eV (Fig. 7.6). The measured intensity is almost the same for all the spectra, as observed in Ref. [92, 195, 197]. Hence the increase of the SHG signal at $n \geq 7$ does not originate from the higher different periodicity or the increasing of the separation between the Si/Ge interfaces, but is characteristic of the creation of large planar defects inside the material as suggested by [92].

---

[1] In the following I do not take into account the real formula for the reflected SHG intensity that is proportional to $\chi^{(2)}_{xyz}$ apart for some factors deriving from the Fresnel coefficients. This tensor component does not correspond directly to the one of Ref. [92] (i.e., $\chi^{(2)}_{zxy}$), but the latter cannot be accessed directly and it is necessary this intermediate step. Calculation of $\chi^{(2)}_{zxy}$ are still in progress.

	Si_3/Ge_3	Si_4/Ge_4	Si_5/Ge_5	Si_7/Ge_7
k-grid	3x3x2	3x3x2	3x3x2	3x3x1
pwwfn	3000	2000	2000	4000
pwx	4000	1500	3000	2000
bands	850	512	800	1152
pweps	1250	1000	1500	2250
bands	300	480	500	512
pwwfn	5000	4000	6000	9000
QP-gap	1.01 eV	0.97	0.852	0.71

Table 7.2: Abinit convergence parameters of the GW calculation for the Si/Ge superlattice structures (refer to [121] for a complete description). The upper values are the ones used for the screening and the lower are the ones for the self-energy calculation. *QP-gap* shows the final result for the quasi-particle gap at Γ.

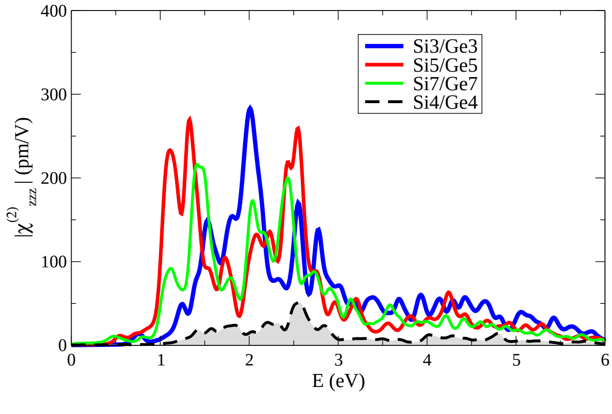

Figure 7.6: Second-harmonics generation spectra $(\chi^{(2)}_{zxy})$ calculated in the independent particle approximation for the defect free $(\mathrm{Si})_n/(\mathrm{Ge})_n$ superlattices. Odd values of n i.e., 3 (blue line), 5 (red line) and 7 (green line) shows an intense signal with respect to the even superlattice $n = 4$ (black dashed line).

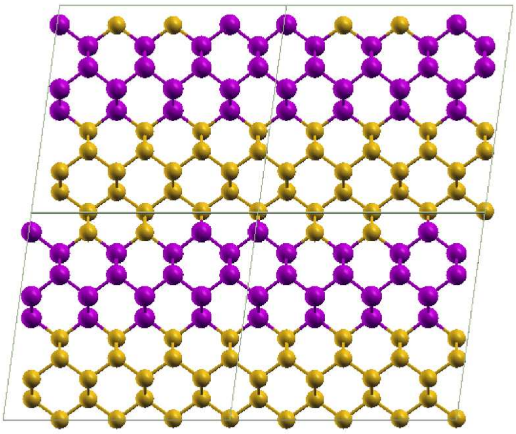

Figure 7.7: Ball and stick representation of the type-A defect: Si_5/Ge_5 with two silicon atoms (yellow) substituting germanium atoms (violet) at the interface (the simulation cell is reported).

Defect Systems

I would like to compare with two experiments, the one of Bottomley *et al.* [195, 197] where they found a non-vanishing signal for the Si_4/Ge_4 structure, although being centrosymmetric, and the experiment of Ref. [92] were *V-shape* misfit stacking fault defects have been observed for Ge_n slabs with $n \geq 7$.

Up to now only three defects have been studied, and are reported in Figs. (7.7-7.9). In the first (type A) case I have considered four crystal cells of Si_5/Ge_5 where I have substituted two interface Ge atoms with Si ones. In the others cases I have substituted four Si atoms with Ge (as shown in Fig. (7.8) and (7.9)) in the Si_4/Ge_4 structure, whose unitary cell has been considered four times.[2] The latter two substitutional defects are able to reproduce the experimental findings of [195, 197], increasing the response of the Si_4/Ge_4 superlattice. This is an evidence that the non-perfect superlattices, where the broaden interface is a mixture of odd and even periodicities, gives almost the same intensity. The relative spectra are reported in Fig. (7.10). The first defect (the one of Si_5/Ge_5) recovers the same trend and intensity. It is then interesting to notice that the signal is characteristic of the whole superlattice structure and not of the symmetry breaking at the interface. Indeed, introducing the defect, the system is more inhomogeneous and one expects a larger intensity if compared with the even or odd systems. Instead, the total signal is almost one half of the perfect[3] Si_5/Ge_5 superlattice. This confirm that the SHG signal originating at the Si/Ge interfaces is enhanced by their constructive interference and once small defects are introduced, this effect is diminished.

In the future I will try to treat the misfit stacking fault defect observed by

---

[2] I have applied the same scissor operator of the corresponding defect-free structures.

[3] I am performing ab initio simulations in order to understand the role of LF effects once these inhomogeneities are introduced. This work is still in progress.

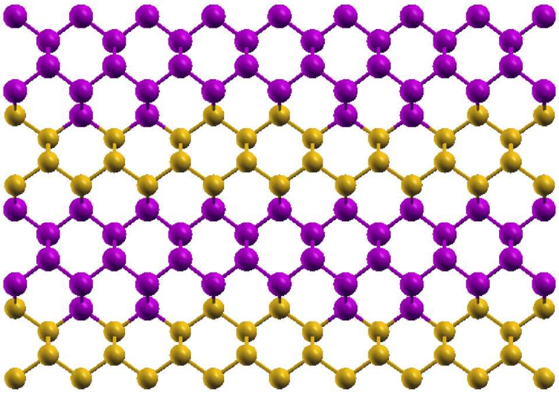

Figure 7.8: Ball and stick representation of the type-B defect: Si_4/Ge_4 with four silicon atoms (yellow) substituted by germanium ones (violet) at the interface.

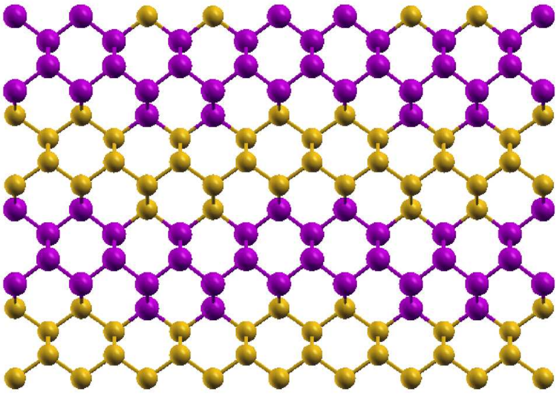

Figure 7.9: Ball and stick representation of the type-C defect: Si_4/Ge_4. Alternatively, the silicon slabs (yellow) has been shifted by one layers with respect to the Ge slabs (violet).

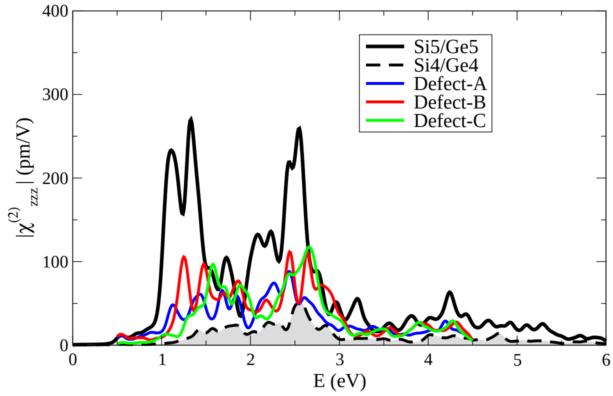

Figure 7.10: Second-harmonics generation spectra ($\chi^{(2)}_{zxy}$) calculated in the independent particle approximation for the substitutional defects of Figs. (7.7-7.9). The Si_5/Ge_5 (black continuous line) and the Si_4/Ge_4 (black dashed line) systems have been reported for comparison. The defects stay in-between the two perfect systems.

[92]. Contrary to the previous substitutional defects, this is a big mismatch plane that propagates through the superlattice and is not localized into a single slab. This higher breaking of the symmetry can be regarded as an additional interface that cross the Si/Ge ones and can following cause an enhancement of the total response.

Chapter 8

Conclusions

In this thesis I have dealt with the description of the nonlinear optical properties of materials, with a particular interest in quantum confined, silicon-based systems. The state of the art of first principle calculations of second harmonic generation is represented, nowadays, by the inclusion of many-body effects as crystal local fields and electron-hole interaction. However, due to the theoretical difficulties and the great computational effort required by nonlinear calculations, so far this accuracy has been reserved to small-size bulk systems only, while independent particle approximation is today the most used approach and the only one that has made feasible calculations of complex structures such as surfaces and interfaces. While IPA can be a good approximation for bulk materials (in GaAs it is able to get the correct shape of the SHG spectrum and fails only the quantitative agreement if excitons are neglected) in confined and discontinuous ones, other effects may be predominant. Hence their description is of great relevance although the lack of studies. My thesis fits into this context trying to give a first analysis of the SHG process in more complex systems as the interfaces and the Si-confined systems, infering new insights on the physical mechanism and its link with the nature of the system.

Here, I have presented an efficient formalism for the ab initio study of second harmonic generation, based on the Time Dependent Density Functional Theory. It is a density-based approach and, therefore, could lead to simpler calculations with respect to the previous approaches based on Many-Body Perturbation Theory present in literature. In this framework many-body effects can be included via a more sophisticated choice of the kernel. In this thesis the formalism and the code 2LIGHT based on it have been developed in order to study more complex materials at the desired accurate levels of description. New questions and difficulties, that arose from the particular nature of the studied systems, have been addressed both through theory and in the code developing new tools as the normalization of the SHG signal when comparing with the experiment, or new methods of analysis of the response. Indeed, once the direct link between the peaks position and the transition energies (characteristic of IPA) is lost in the second order Dyson equation because local fields introduction, different approaches had to be tested.

The research has been focused on a case study, the Si(111)/CaF$_2$ interface. However, its complexity allowed me to extend the study to a large variety of systems as the multilayers and the silicon confined slabs, comparing the results and hence obtaining information on the SHG signal and its dependence on the nature of the materials. Actually, new features and behavior have been observed, thanks to this formalism and code, with respect to second-order nonlinear optical processes on strained silicon, GaAs or SiC showing in particular the importance of crystal local-field effects with respect of both the independent particle approximation and the excitons. The results here presented on Si-based interfaces show a good agreement with the experiment. This underlines the efficiency and accuracy of our formalism, the possibility of improving our knowledge on these complex materials going beyond the standard approaches, and validates the particular choice of the interface structure adopted. The latter confirm the possibility of SHG ab initio simulations to be employed as a predictive technique, supporting and guiding experiments and technological developments.

More in detail, after the theoretical framework presented in chapters 2-4, and the code together with the implemented developments in chapter 5,

- in chapter 6 I have introduced the Si(111)/CaF$_2$ interface case study, discussing both the experiment and the corresponding simulation cell structure.

- I have presented the unphysical features of the SHG spectra that arise from its dependence on the vacuum volume. This is due to the particular nature of the signal, characteristic of the interface region and not of the whole cell volume as for bulk systems. I have then presented a physical interpretation of the experimental environment, choosing an equal amount of silicon and insulating material and demonstrating the same transparent nature the insulating slab shares with the vacuum in the SHG process. I have then derived a normalization procedure.

- I have performed convergence tests on the vacuum, the insulator and the semiconductor thicknesses, showing their differences and their contribution to the final outgoing signal. In particular CaF$_2$ behaves as the vacuum on top of it and already the first two layers can correctly reproduce the interface SHG process. Silicon instead, contribute to the second harmonic signal far below the interface discontinuity, demonstrating to be characteristic of small variations of the electronic density whereas the ionic structure recovers soon the bulk configuration.

- The different nature of the peaks present in the spectrum has been investigated, identifying the structure at low energy as originated by the silicon-hydrogenated surface. A comparison with different systems as the silicon-confined slabs passivated with As and P has been provided.

- I have shown that an independent particle picture can give a qualitative description of the SHG process in the Si(111)/CaF$_2$ interface, recovering the main features (in terms of energy peak position) originated from the anisotropies of the system. However, the results does not match the spectral line shape of the experiment.

- Contrary to bulk systems, LF effects become essential and are the key quantity that allow to recover the experimental data. In fact, LFs strongly influence the second-order nonlinear response close to the discontinuity region inducing a significant redistribution of the intensity. I demonstrated that this redistribution is largely more dramatic in nonlinear optical response than in the linear response. Indeed for SHG the lowering of the intensities is selective and not homogeneous while for absorption the shape of the spectrum is almost unchanged.

- As for linear optics, also second harmonic generation is really sensitive to the homogeneity of the system. In particular I have shown that along the in-plane direction the inclusion of LF effects is negligible whereas it becomes important perpendicularly to the interface.
- The presented results have far-reaching consequences beyond the specific interface I have studied. The microscopic induced polarization can have large and unpredictable effects on the SHG process, becoming essential for complex systems. In this case the major modifications are included in the variation of the second-order density response $\chi^{(2)}_{\rho\rho\rho}$ with respect to the dielectric function.
- As observed in previous studies, excitonic effects do not change the form of the SHG spectrum but increase its intensity. Opposite to the bulk systems, here the electron-hole interaction is negligible while the LF effects describes the physics of the second harmonic generation at the interface. This underlines how the process is related to the different nature of the systems where the nonlinear signal originates.

This thesis made progresses in the description of the nonlinear optical properties of materials. However, one of the major results is represented by the development of the 2LIGHT code. The use of an efficient formalism based on the well established TDDFT, and the improvements of the numerical tools open the field of investigation to a large variety of new materials, making feasible ab initio calculations. This is a great advancement that will allow a deeper knowledge of the second harmonic process applying its study to technologically interesting systems where other effects could arise as the nanowires of Si/Ge superlattices [93].

Appendix A

TDDFT formulas Derivation

A.1 Derivation of $\chi^{(2)}(1,2,3)$

Equation (3.31) can be obtained from Eq. (3.29):

$$\begin{aligned}\chi^{(2)}(1,2,3) =&\chi_0^{(2)}(1,2,3) + \chi_0^{(2)}(1,4,3)f_{vxc}(4,5)\chi^{(1)}(5,2)+\\ &\chi_0^{(2)}(1,2,4)f_{vxc}(4,5)\chi^{(1)}(5,3)+\\ &\chi_0^{(2)}(1,5,4)f_{vxc}(5,6)\chi^{(1)}(6,2)f_{vxc}(4,7)\chi^{(1)}(7,3)+\\ &\chi_0^{(1)}(1,4)g_{xc}(4,5,6)\chi^{(1)}(6,3)\chi^{(1)}(5,2)+\\ &\chi_0^{(1)}(1,4)f_{vxc}(4,5)\chi^{(2)}(5,2,3).\end{aligned} \tag{A.1}$$

where I have adopted a shorter notation, avoiding an explicit representation of the integrals which are implied when an index variable appears twice inside a product e.g., $\int d3\ A(1,3)B(3,2) = A(1,3)B(3,2)$. Using the chain rules

$$\frac{\delta A}{\delta v_{ext}} = \frac{\delta A}{\delta v_S}\frac{\delta v_S}{\delta v_{ext}}, \tag{A.2}$$

Eq. (A.1) reads:

$$\begin{aligned}\chi^{(2)}(1,2,3) =&\frac{\delta\chi_0^{(1)}(1,2)}{\delta v_S(4)}\frac{\delta v_S(4)}{\delta v_{ext}(3)}+\\ &\frac{\delta\chi_0^{(1)}(1,4)}{\delta v_S(6)}\frac{\delta v_S(6)}{\delta v_{ext}(3)}f_{vxc}(4,5)\chi^{(1)}(5,2)+\\ &\chi_0^{(1)}(1,4)\frac{\delta f_{xc}(4,5)}{\delta v_{ext}(3)}\chi^{(1)}(5,2)+\\ &\chi_0^{(1)}(1,4)f_{vxc}(4,5)\frac{\delta\chi^{(1)}(5,2)}{\delta v_{ext}(3)}.\end{aligned} \tag{A.3}$$

Remembering that from Eq. (3.23):

$$\frac{\delta v_S(1)}{\delta v_{ext}(2)} = \delta(1,2) + [v(1,3) + f_{xc}(1,3)]\chi^{(1)}(3,2), \tag{A.4}$$

and defining

$$\frac{\delta f_{xc}(4,5)}{\delta v_{ext}(3)} = g_{xc}(4,5,6)\chi^{(1)}(6,3), \tag{A.5}$$

Eq. (A.3) becomes:

$$\begin{aligned}\chi^{(2)}(1,2,3) =&\chi_0^{(2)}(1,2,4)\frac{\delta v_S(4)}{\delta v_{ext}(3)}+\\ &\chi_0^{(2)}(1,4,6)\frac{\delta v_S(6)}{\delta v_{ext}(3)}f_{vxc}(4,5)\chi^{(1)}(5,2)+\\ &\chi_0^{(1)}(1,4)g_{xc}(4,5,6)\chi^{(1)}(6,3)\chi^{(1)}(5,2)+\\ &\chi_0^{(1)}(1,4)f_{vxc}(4,5)\chi^{(2)}(5,2,6),\end{aligned} \tag{A.6}$$

$$\begin{aligned}\chi^{(2)}(1,2,3) =&\chi_0^{(2)}(1,2,4)\left[\delta(4,3)+f_{vxc}(4,5)\chi^{(1)}(5,3)\right]+\\ &\chi_0^{(2)}(1,4,6)\left[\delta(6,3)+f_{vxc}(6,7)\chi^{(1)}(7,3)\right]f_{vxc}(4,5)\chi^{(1)}(5,2)+\\ &\chi_0^{(1)}(1,4)g_{xc}(4,5,6)\chi^{(1)}(6,3)\chi^{(1)}(5,2)+\\ &\chi_0^{(1)}(1,4)f_{vxc}(4,5)\chi^{(2)}(5,2,6),\end{aligned} \tag{A.7}$$

$$\begin{aligned}\chi^{(2)}(1,2,3) =&\chi_0^{(2)}(1,2,3)+\chi_0^{(2)}(1,2,4)f_{vxc}(4,5)\chi^{(1)}(5,3)+\\ &\chi_0^{(2)}(1,4,3)f_{vxc}(4,5)\chi^{(1)}(5,2)+\\ &\chi_0^{(2)}(1,4,6)f_{vxc}(6,7)\chi^{(1)}(7,3)f_{vxc}(4,5)\chi^{(1)}(5,2)+\\ &\chi_0^{(1)}(1,4)g_{xc}(4,5,6)\chi^{(1)}(6,3)\chi^{(1)}(5,2)+\\ &\chi_0^{(1)}(1,4)f_{vxc}(4,5)\chi^{(2)}(5,2,6).\end{aligned} \tag{A.8}$$

That is exactly Eq. (3.31).

Appendix B

Fourier Tansform

B.1 Frequency-space

In this thesis, for time-frequency Fourier Transform I have adopted the following conventions:

$$f(\omega) = \frac{1}{2\pi} \int e^{i\omega t} f(t) dt \tag{B.1}$$

$$f(t) = \int e^{-i\omega t} f(\omega) d\omega \tag{B.2}$$

while for the response function I have used

$$\chi(x, ..., t - t') = \frac{1}{2\pi} \int e^{-i\omega(t-t')} \chi(x, ..., \omega) d\omega \tag{B.3}$$

B.2 Impulses space

B.2.1 One Variable Function

In the case of the reciprocal-real space transformations, the periodicity of the lattice impose $\mathbf{k}$ to be discrete and function in real space are described by a Fourier Series.

$$f(\mathbf{r}) = \sum_{\mathbf{qG}} f(\mathbf{q} + \mathbf{G}) e^{i(\mathbf{q}+\mathbf{G})\mathbf{r}} \tag{B.4}$$

and

$$f(\mathbf{q} + \mathbf{G}) = \frac{1}{V} \int d\mathbf{r} f(\mathbf{r}) e^{-i(\mathbf{q}+\mathbf{G})\mathbf{r}} \tag{B.5}$$

where $\mathbf{q}$ is a point of the 1^{st} Brillouin Zone and $\mathbf{G}$ is a vector of the reciprocal lattice. $\mathbf{r}$ and $\mathbf{k} = \mathbf{q} + \mathbf{G}$ do not share the same behavior once integrated: $\mathbf{r}$ is a continue variable whereas $\mathbf{k} = \mathbf{q} + \mathbf{G}$ is discrete. This yelds:

$$\delta(\mathbf{r} - \mathbf{r}') = \frac{1}{V} \sum_{\mathbf{k}} e^{i\mathbf{k}\cdot(\mathbf{r}-\mathbf{r}')} \tag{B.6}$$

and

$$\delta_{\mathbf{kk}'} = \frac{1}{V} \int d\mathbf{r} e^{i(\mathbf{k}-\mathbf{k}')\cdot\mathbf{r}} \tag{B.7}$$

B.2.2 Two Variables Function

$$f(\mathbf{r}_1,\mathbf{r}_2)=\frac{1}{V}\sum_{\mathbf{q}_1\mathbf{q}_2}\sum_{\mathbf{G}_1\mathbf{G}_2}e^{i(\mathbf{q}_1+\mathbf{G}_1)\mathbf{r}_1}f(\mathbf{q}_1+\mathbf{G}_1,\mathbf{q}_2+\mathbf{G}_2)e^{-i(\mathbf{q}_2+\mathbf{G}_2)\mathbf{r}_2} \tag{B.8}$$

and

$$f(\mathbf{q}_1+\mathbf{G}_1,\mathbf{q}_2+\mathbf{G}_2)=\frac{1}{V}\int d\mathbf{r}_1 d\mathbf{r}_2 e^{-i(\mathbf{q}_1+\mathbf{G}_1)\mathbf{r}_1}f(\mathbf{r}_1,\mathbf{r}_2)e^{i(\mathbf{q}_2+\mathbf{G}_2)\mathbf{r}_2} \tag{B.9}$$

As an exaple one can consider the polarization at the first and second order:

$$P^{(1)}_{ind}(\mathbf{x},\omega)=\int dx'\tilde{\alpha}^{(1)}(\mathbf{x},\mathbf{x}',\omega)E^{ext}(\mathbf{x}',\omega) \tag{B.10}$$

In the reciprocal space one has:

$$P^{(1)}(\mathbf{q}+\mathbf{G},\omega)=\frac{1}{V}\int d\mathbf{x}P^{(1)}(\mathbf{x},\omega)e^{-i(\mathbf{q}+\mathbf{G})\mathbf{x}} \tag{B.11}$$

with

$$\begin{aligned}P^{(1)}(\mathbf{q}+\mathbf{G},\omega)&=\frac{1}{V}\int d\mathbf{x}e^{-i(\mathbf{q}+\mathbf{G})\mathbf{x}}\int d\mathbf{x}'E^{ext}(\mathbf{x}',\omega)\\ \frac{1}{V}\sum_{\mathbf{q}_1\mathbf{q}_2}\sum_{\mathbf{G}_1\mathbf{G}_2}&e^{i(\mathbf{q}_1+\mathbf{G}_1)\mathbf{x}}\tilde{\alpha}^{(1)}(\mathbf{q}_1+\mathbf{G}_1,\mathbf{q}_2+\mathbf{G}_2,\omega)e^{-i(\mathbf{q}_2+\mathbf{G}_2)\mathbf{x}'}\end{aligned} \tag{B.12}$$

last equation gives:

$$\begin{aligned}P^{(1)}(\mathbf{q}+\mathbf{G},\omega)=\sum_{\mathbf{q}_1\mathbf{q}_2}\sum_{\mathbf{G}_1\mathbf{G}_2}\delta_{\mathbf{q}+\mathbf{G},\mathbf{q}_1+\mathbf{G}_1}\tilde{\alpha}^{(1)}(\mathbf{q}_1+\mathbf{G}_1,\mathbf{q}_2+\mathbf{G}_2,\omega)\\ E^{ext}(\mathbf{q}_2+\mathbf{G}_2,\omega)\end{aligned} \tag{B.13}$$

and one finally obtains

$$P^{(1)}(\mathbf{q}+\mathbf{G},\omega)=\sum_{\mathbf{q}'}\sum_{\mathbf{G}'}\tilde{\alpha}^{(1)}(\mathbf{q}+\mathbf{G},\mathbf{q}'+\mathbf{G}',\omega)E^{ext}(\mathbf{q}'+\mathbf{G}',\omega). \tag{B.14}$$

Let's consider a function $f(\mathbf{r}_1,\mathbf{r}_2)=f(\mathbf{r}_1+\mathbf{R},\mathbf{r}_2+\mathbf{R})$ where $\mathbf{R}$ is a lattice vector. It follows that

$$f(\mathbf{q}_1+\mathbf{G}_1,\mathbf{q}_2+\mathbf{G}_2)=f(\mathbf{q}_1+\mathbf{G}_1,\mathbf{q}_1+\mathbf{G}_2)\delta_{\mathbf{q}_1,\mathbf{q}_2} \tag{B.15}$$

that gives:

$$f(\mathbf{r}_1,\mathbf{r}_2)=\frac{1}{V}\sum_{\mathbf{q}}\sum_{\mathbf{G}_1\mathbf{G}_2}e^{i(\mathbf{q}+\mathbf{G}_1)\mathbf{r}_1}f(\mathbf{q}+\mathbf{G}_1,\mathbf{q}+\mathbf{G}_2)e^{-i(\mathbf{q}+\mathbf{G}_2)\mathbf{r}_2} \tag{B.16}$$

and

$$P^{(1)}(\mathbf{q}+\mathbf{G},\omega)=\sum_{\mathbf{G}'}\tilde{\alpha}^{(1)}(\mathbf{q}+\mathbf{G},\mathbf{q}+\mathbf{G}',\omega)E^{ext}(\mathbf{q}+\mathbf{G}',\omega) \tag{B.17}$$

B.2.3 Three Variables Function

$$\begin{aligned} f(\mathbf{r}_1,\mathbf{r}_2,\mathbf{r}_3) = \frac{1}{V^2}\sum_{\mathbf{q}_1\mathbf{q}_2\mathbf{q}_3}\sum_{\mathbf{G}_1\mathbf{G}_2\mathbf{G}_3} & e^{i(\mathbf{q}_1+\mathbf{G}_1)\mathbf{r}_1} e^{-i(\mathbf{q}_2+\mathbf{G}_2)\mathbf{r}_2} e^{-i(\mathbf{q}3+\mathbf{G}_3)\mathbf{r}_3} \\ & f(\mathbf{q}_1+\mathbf{G}_1,\mathbf{q}_2+\mathbf{G}_2,\mathbf{q}_3+\mathbf{G}_3) \end{aligned} \tag{B.18}$$

and

$$\begin{aligned} f(\mathbf{q}_1+\mathbf{G}_1,\mathbf{q}_2+\mathbf{G}_2,\mathbf{q}_3+\mathbf{G}_3) = \frac{1}{V}\int & d\mathbf{r}_1 d\mathbf{r}_2 d\mathbf{r}_3 e^{-i(\mathbf{q}_1+\mathbf{G}_1)\mathbf{r}_1} \\ & e^{i(\mathbf{q}_2+\mathbf{G}_2)\mathbf{r}_2} e^{i(\mathbf{q}_3+\mathbf{G}_3)\mathbf{r}_3} f(\mathbf{r}_1,\mathbf{r}_2,\mathbf{r}_3). \end{aligned} \tag{B.19}$$

Let's consider agin the polarization, the second-order term reads

$$P^{(2)}(\mathbf{x}) = \int d\mathbf{x}' \int d\mathbf{x}'' \tilde{\alpha}^{(2)}(\mathbf{x},\mathbf{x}',\mathbf{x}'') E^{ext}(\mathbf{x}') E^{ext}(\mathbf{x}'') \tag{B.20}$$

Here I omit the ω dependece to keep formulas short. In the impulse space one has:

$$P^{(2)}(\mathbf{q}+\mathbf{G}) = \frac{1}{V}\int d\mathbf{x} P^{(2)}(\mathbf{x}) e^{-i(\mathbf{q}+\mathbf{G})\mathbf{x}} \tag{B.21}$$

$$\begin{aligned} P^{(2)}(\mathbf{q}+\mathbf{G}) = \frac{1}{V}\int d\mathbf{x} e^{-i(\mathbf{q}+\mathbf{G})\mathbf{x}} \int d\mathbf{x}' \int d\mathbf{x}'' E^{ext}(\mathbf{x}') E^{ext}(\mathbf{x}'') \\ \frac{1}{V^2}\sum_{\mathbf{q}_1\mathbf{q}_2\mathbf{q}_3}\sum_{\mathbf{G}_1\mathbf{G}_2\mathbf{G}_3} e^{i(\mathbf{q}_1+\mathbf{G}_1)\mathbf{x}} e^{-i(\mathbf{q}_2+\mathbf{G}_2)\mathbf{x}'} e^{-i(\mathbf{q}3+\mathbf{G}_3)\mathbf{x}''} \\ \tilde{\alpha}^{(2)}(\mathbf{q}_1+\mathbf{G}_1,\mathbf{q}_2+\mathbf{G}_2,\mathbf{q}_3+\mathbf{G}_3) \end{aligned} \tag{B.22}$$

that gives:

$$\begin{aligned} P^{(2)}(\mathbf{q}+\mathbf{G}) = \sum_{\mathbf{q}_1\mathbf{q}_2\mathbf{q}_3}\sum_{\mathbf{G}_1\mathbf{G}_2\mathbf{G}_3} & \delta_{\mathbf{q}+\mathbf{G},\mathbf{q}_1+\mathbf{G}_1} E^{ext}(\mathbf{q}_2+\mathbf{G}_2) E^{ext}(\mathbf{q}3+\mathbf{G}_3) \\ & \tilde{\alpha}^{(2)}(\mathbf{q}_1+\mathbf{G}_1,\mathbf{q}_2+\mathbf{G}_2,\mathbf{q}_3+\mathbf{G}_3) \end{aligned} \tag{B.23}$$

and one has the final form

$$\begin{aligned} P^{(2)}(\mathbf{q}+\mathbf{G}) = \sum_{\mathbf{q}'\mathbf{q}''}\sum_{\mathbf{G}'\mathbf{G}''} & \tilde{\alpha}^{(2)}(\mathbf{q}+\mathbf{G},\mathbf{q}'+\mathbf{G}',\mathbf{q}''+\mathbf{G}'') \\ & E^{ext}(\mathbf{q}'+\mathbf{G}') E^{ext}(\mathbf{q}''+\mathbf{G}'') \end{aligned} \tag{B.24}$$

Considering a three-variables function $f(\mathbf{r}_1,\mathbf{r}_2,\mathbf{r}_3) = f(\mathbf{r}_1+\mathbf{R},\mathbf{r}_2+\mathbf{R},\mathbf{r}_3+\mathbf{R})$ où $\mathbf{R}$ one has:

$$f(\mathbf{q}+\mathbf{G},\mathbf{q}'+\mathbf{G}',\mathbf{q}''+\mathbf{G}'') = f(\mathbf{q}'+\mathbf{q}''+\mathbf{G},\mathbf{q}'+\mathbf{G}',\mathbf{q}''+\mathbf{G}'')\delta_{\mathbf{q},\mathbf{q}'+\mathbf{q}''} \tag{B.25}$$

that gives

$$\begin{aligned} f(\mathbf{r}_1,\mathbf{r}_2,\mathbf{r}_3) = \frac{1}{V^2}\sum_{\mathbf{q}_2\mathbf{q}_3}\sum_{\mathbf{G}_1\mathbf{G}_2\mathbf{G}_3} & e^{i(\mathbf{q}_2+\mathbf{q}_3+\mathbf{G}_1)\mathbf{r}_1} e^{-i(\mathbf{q}_2+\mathbf{G}_2)\mathbf{r}_2} e^{-i(\mathbf{q}3+\mathbf{G}_3)\mathbf{r}_3} \\ & f(\mathbf{q}_2+\mathbf{q}_3+\mathbf{G}_1,\mathbf{q}_2+\mathbf{G}_2,\mathbf{q}_3+\mathbf{G}_3) \end{aligned} \tag{B.26}$$

et

$$\begin{aligned} P^{(2)}(\mathbf{q}'+\mathbf{q}''+\mathbf{G}) = \sum_{\mathbf{q}'\mathbf{q}''}\sum_{\mathbf{G}'\mathbf{G}''} & \tilde{\alpha}^{(2)}(\mathbf{q}'+\mathbf{q}''+\mathbf{G},\mathbf{q}'+\mathbf{G}',\mathbf{q}''+\mathbf{G}'') \\ & E^{ext}(\mathbf{q}'+\mathbf{G}') E^{ext}(\mathbf{q}''+\mathbf{G}'') \end{aligned} \tag{B.27}$$

B.2.4 Response Function

An other example is provided by the first-orders response function:

$$\chi^{(0)}_{\rho\rho}(\mathbf{r},\mathbf{r}',\omega) = \sum_{i,\mathbf{k}_i,j,\mathbf{k}_j} (f_{\mathbf{i},k_i} - f_{j,\mathbf{k}_j}) \frac{\phi^*_{i,\mathbf{k}_i}(\mathbf{r})\phi_{j,\mathbf{k}_j}(\mathbf{r})\phi^*_{j,\mathbf{k}_j}(\mathbf{r}')\phi_{i,\mathbf{k}_i}(\mathbf{r}')}{(E_{i,\mathbf{k}_i} - E_{j,\mathbf{k}_j} + \omega + i\eta)} \tag{B.28}$$

Considering the periodicity of the crystal lattice (or the simulation cell once the supercell-technique is adopted)

$$\chi^{(0)}_{\rho\rho}(\mathbf{q}+\mathbf{G},\mathbf{q}+\mathbf{G}',\omega) = \frac{1}{V}\int d\mathbf{r}d\mathbf{r}' e^{-i(\mathbf{q}+\mathbf{G})\mathbf{r}} \chi^{(0)}_{\rho\rho}(\mathbf{r},\mathbf{r}',\omega) e^{i(\mathbf{q}+\mathbf{G}')\mathbf{r}'} \tag{B.29}$$

gives

$$\begin{gathered} \chi^{(0)}_{\rho\rho}(\mathbf{q}+\mathbf{G},\mathbf{q}+\mathbf{G}',\omega) = \frac{1}{V}\sum_{i,j,\mathbf{k}} (f_{\mathbf{i},k} - f_{j,\mathbf{k}+\mathbf{q}}) \\ \frac{< i,\mathbf{k}|e^{-i(\mathbf{q}+\mathbf{G})\mathbf{r}})|j,\mathbf{k}+\mathbf{q} >< j,\mathbf{k}+\mathbf{q}|e^{i(\mathbf{q}+\mathbf{G}')\mathbf{r}'}|i,\mathbf{k} >}{(E_{i,\mathbf{k}} - E_{j,\mathbf{k}+\mathbf{q}} + \omega + i\eta)} \end{gathered} \tag{B.30}$$

and the equivalent can be obtained for the second order term.

Appendix C

Explicit Formulas for the SHG Derivation

C.1 Time Ordering Operator

The time-ordering operator can be identified as:

$$\begin{aligned}
&\int_{t_0}^{t_1} dt_2 \int_{t_0}^{t_2} dt_3 f(t_2,t_3) = \int_{t_0}^{t_1} dt_2 \int_{t_0}^{t_1} \theta(t_2-t_3) dt_3 f(t_2,t_3) \\
=&\tfrac{1}{2}\int_{t_0}^{t_1} dt_2 \int_{t_0}^{t_1} dt_3\ \theta(t_2-t_3) dt_3 f(t_2,t_3) + \tfrac{1}{2}\int_{t_0}^{t_1} dt_2 \int_{t_0}^{t_1} dt_3\ \theta(t_2-t_3) dt_3 f(t_2,t_3) \\
=&\tfrac{1}{2}\int_{t_0}^{t_1} dt_2 \int_{t_0}^{t_1} dt_3\ \theta(t_2-t_3) dt_3 f(t_2,t_3) + \tfrac{1}{2}\int_{t_0}^{t_1} dt_3 \int_{t_0}^{t_1} dt_2\ \theta(t_3-t_2) dt_2 f(t_3,t_2) \\
&\text{obtained switching the index names} \\
=&\tfrac{1}{2}\int_{t_0}^{t_1} dt_2 \int_{t_0}^{t_1} dt_3\ T[f(t_2,t_3)],
\end{aligned} \tag{C.1}$$

where I have swapped the indexes t_2 and t_3 in the third line.

C.2 Microscopic Average

Given a function $f(\mathbf{r},\omega)$ that is periodic because of crystal periodicity (otherwise imposing Born von Karaman conditions) one can identify its Bravais' lattice basis with the spatial coordinate $\mathbf{R}$. They define a reciprocal basis $\mathbf{G}$ over which the function can be expressed through a Fourier series:

$$f(\mathbf{r},\omega) = \sum_{\mathbf{q},\mathbf{G}} f(\mathbf{q}+\mathbf{G}) e^{i(\mathbf{q}+\mathbf{G})\mathbf{r}}, \tag{C.2}$$

where vectors $\mathbf{q}$ belong to the first Brillouin Zone (BZ). This expression can be divided in two parts, as for the Bloch's states: the first one that has the periodicity of the crystal cell and the second one (described by $e^{i(\mathbf{qr})}$) that varies over a larger distance:

$$f(\mathbf{r},\omega) = \sum_{\mathbf{q}} e^{i\mathbf{qr}} \sum_{\mathbf{G}} f(\mathbf{q}+\mathbf{G}) e^{i\mathbf{Gr}}. \tag{C.3}$$

The macroscopic average is then obtained integrating the function over a space volume that is (i) big with respect to the microscopic variation inside the cell volume Ω_c containing to the electronic fluctuations, and (ii) small if compared with the external perturbation, so that the dipole approximation (i.e., the long wavelength limit) holds.

The latter assumption consists in supposing that variation of $e^{i(\mathbf{qr})}$ inside the cell at $\mathbf{R}$ are negligible and well approximated by $e^{i(\mathbf{qR})}$. Furthermore, it permits to consider $\mathbf{R}$ as the continuous coordinate appearing in the Maxwell's equations from a macroscopic point of view. The first one instead allows to obtain the fluctuations' contribution at $\mathbf{R}$ as an average (over a unit cell) around that point. The differences between the microscopic fields and the averaged (macroscopic) fields are called the *crystal local fields.* The microscopic function has the form

$$\begin{aligned} f(\mathbf{r},\omega) &= \sum_{\mathbf{q}} e^{i\mathbf{qr}} \sum_{\mathbf{G}} f(\mathbf{q}+\mathbf{G}) e^{i\mathbf{Gr}} \\ &= \sum_{\mathbf{q}} e^{i\mathbf{qr}} f'(\mathbf{r};\mathbf{q},\omega) \end{aligned} \tag{C.4}$$

where with $f'(\mathbf{r};\mathbf{q},\omega) = \sum_{\mathbf{G}} f(\mathbf{q}+\mathbf{G}) e^{i\mathbf{Gr}}$ it has been identified its periodic part.[1] In the hypothesis of a monochromatic external field with wave-vector $\mathbf{q}$ (so that summation over $\mathbf{q}$ disappears), the average over a unit cell positioned in $\mathbf{R}$ is given by:

$$\begin{aligned} f(\mathbf{R},\omega) &= e^{i\mathbf{qR}} \langle f'(\mathbf{r};\mathbf{q},\omega)\rangle_{\Omega_c(\mathbf{R})} \\ &= e^{i\mathbf{qR}} \frac{1}{\Omega_c} \int_{\Omega_c} d\mathbf{r} \ \sum_{\mathbf{G}} f(\mathbf{q}+\mathbf{G}) e^{i\mathbf{Gr}} \end{aligned} \tag{C.5}$$

and recognizing the delta function $\frac{1}{\Omega_c}\int d\mathbf{r}\ e^{i\mathbf{Gr}} = \delta\mathbf{G},0$ one obtains the final result:

$$f(\mathbf{R},\omega) = e^{i\mathbf{qR}} f(\mathbf{q},\omega). \tag{C.6}$$

---

[1] Because it can be expressed as a Fourier series over $\mathbf{G}$ it is periodic in reciprocal space with the periodicity $\mathbf{R}$ of the Bravais lattice.

Appendix D

Gauge Invariance Relations

D.1 First Order Relations

D.1.1 Induced current and induced density

The general expression for the first-order induced current-density (cfr. Eq. (4.38)) is:

$$\begin{aligned}\mathbf{j}^{(1)}_{ind}(\mathbf{r},\omega) = &-\frac{1}{c}\langle\hat{\rho}(\mathbf{r})\rangle\mathbf{A}^P(\mathbf{r},\omega) - \frac{1}{c}\int d\mathbf{r}'\chi_{\mathbf{jj}}(\mathbf{r},\mathbf{r}',\omega)\mathbf{A}^P(\mathbf{r}',\omega)\\ &+\int d\mathbf{r}'\chi_{\mathbf{j}\rho}(\mathbf{r},\mathbf{r}',\omega)\phi^P(\mathbf{r}',\omega)\end{aligned} \tag{D.1}$$

whereas the density reads:

$$\rho^{(1)}_{ind}(\mathbf{r},\omega) = -\frac{1}{c}\int d\mathbf{r}'\chi_{\rho\mathbf{j}}(\mathbf{r},\mathbf{r}',\omega)\mathbf{A}^P(\mathbf{r}',\omega) + \int d\mathbf{r}'\chi_{\rho\rho}(\mathbf{r},\mathbf{r}',\omega)\phi^P(\mathbf{r}',\omega) \tag{D.2}$$

Thanks to the gauge invariance of the scalar- and vector-potentials $(\phi^P, \mathbf{A}^P)$ that defines the perturbing electric field $\mathbf{E}^P$ through

$$\mathbf{E}^P(\mathbf{r},\omega) = \frac{i\omega}{c}\mathbf{A}^P(\mathbf{r},\omega) - \nabla_{\mathbf{r}}\phi^P(\mathbf{r},\omega), \tag{D.3}$$

one can write the previous equations Eqs. (D.1), (D.2) in a general form as:

$$\mathbf{j}^{(1)}_{ind}(\mathbf{r},\omega) = \frac{i}{\omega}\langle\hat{\rho}(\mathbf{r})\rangle\mathbf{E}^P(\mathbf{r},\omega) + \frac{i}{\omega}\int d\mathbf{r}'\chi_{\mathbf{jj}}(\mathbf{r},\mathbf{r}',\omega)\mathbf{E}^P(\mathbf{r}',\omega) \tag{D.4}$$

$$\rho^{(1)}_{ind}(\mathbf{r},\omega) = \frac{i}{\omega}\int d\mathbf{r}'\chi_{\rho\mathbf{j}}(\mathbf{r},\mathbf{r}',\omega)\mathbf{E}^P(\mathbf{r}',\omega). \tag{D.5}$$

D.1.2 Relation among the First-Order Response Functions

Let's now transform Eqs. (D.1), (D.2) in the reciprocal space. Fourier-transforming the equations one obtains:

$$\begin{aligned}\mathbf{j}^{(1)}_{ind}(\mathbf{k},\omega) = &-\frac{1}{c}\sum_{k'}\langle\hat{\rho}(\mathbf{k}-\mathbf{k}')\rangle\mathbf{A}^P(\mathbf{k}',\omega) - \frac{1}{c}\sum_{k'}\chi_{\mathbf{jj}}(\mathbf{k},\mathbf{k}',\omega)\mathbf{A}^P(\mathbf{k}',\omega)\\ &+\sum_{k'}\chi_{\mathbf{j}\rho}(\mathbf{k},\mathbf{k}',\omega)\phi^P(\mathbf{k}',\omega)\end{aligned} \tag{D.6}$$

and

$$\rho^{(1)}_{ind}(\mathbf{k},\omega) = -\frac{1}{c}\sum_{k'}\chi_{\rho\mathbf{j}}(\mathbf{k},\mathbf{k}',\omega)\mathbf{A}^P(\mathbf{k}',\omega) + \sum_{k'}\chi_{\rho\rho}(\mathbf{k},\mathbf{k}',\omega)\phi^P(\mathbf{k}',\omega). \quad \text{(D.7)}$$

The gradient of the scalar potential $\nabla_{\mathbf{r}}\phi^P(\mathbf{r},\omega)$ once ϕ^P is written in the reciprocal space becomes a simple product and the electric field in the Fourier space $\mathbf{E}^P$ reads:

$$\mathbf{E}^P(\mathbf{k},\omega) = \frac{i\omega}{c}\mathbf{A}^P(\mathbf{k},\omega) - i\mathbf{k}\phi^P(\mathbf{k},\omega) \quad \text{(D.8)}$$

Because of the arbitraryness in defining the electromagnetic field through the electromagnetic potentials, it is always possible to *gauge transform* the latter according to:

$$\begin{aligned}\bar{\mathbf{A}}^P(\mathbf{k},\omega) &= \mathbf{A}^P(\mathbf{k},\omega) + i\mathbf{k}\Lambda(\mathbf{k},\omega)\\ \bar{\phi}^P(\mathbf{k},\omega) &= \phi^P(\mathbf{k},\omega) + \frac{i\omega}{c}\Lambda(\mathbf{k},\omega),\end{aligned} \quad \text{(D.9)}$$

(with $\Lambda(\mathbf{k},\omega)$ a scalar potential) without modifying the physical observables. In particular the field $\mathbf{E}^P$ and all the induced densities and currents. This property takes the name of *gauge-invariance*.

As a consequence, substituting the new potentials of Eq. (D.9) to $(\phi^P, \mathbf{A}^P)$ into the induced current-density definition $\mathbf{j}_{ind}$ (Eq. (D.1)), one has:

$$\begin{aligned}\mathbf{j}^{(1)}_{ind}(\mathbf{k},\omega) = &-\frac{1}{c}\sum_{k'}\langle\hat{\rho}(\mathbf{k}-\mathbf{k}')\rangle\left[\mathbf{A}^P(\mathbf{k}',\omega) + i\mathbf{k}'\Lambda(\mathbf{k}',\omega)\right]\\ &-\frac{1}{c}\sum_{k'}\chi_{\mathbf{jj}}(\mathbf{k},\mathbf{k}',\omega)\left[\mathbf{A}^P(\mathbf{k}',\omega) + i\mathbf{k}'\Lambda(\mathbf{k}',\omega)\right]\\ &+\sum_{k'}\chi_{\mathbf{j}\rho}(\mathbf{k},\mathbf{k}',\omega)\left[\phi^P(\mathbf{k}',\omega) + \frac{i\omega}{c}\Lambda(\mathbf{k}',\omega)\right].\end{aligned} \quad \text{(D.10)}$$

Because of gauge invariance, Eq. (D.1) and Eq. (D.10) must be equal. Imposing their equivalency one obtains:

$$\sum_{k'}\left[-\frac{1}{c}\langle\hat{\rho}(\mathbf{k}-\mathbf{k}')\rangle\mathbf{k}' - \frac{1}{c}\chi_{\mathbf{jj}}(\mathbf{k},\mathbf{k}',\omega)\mathbf{k}' + \chi_{\mathbf{j}\rho}(\mathbf{k},\mathbf{k}',\omega)\frac{\omega}{c}\right]\Lambda(\mathbf{k}',\omega) = 0. \quad \text{(D.11)}$$

that is independent of the particular choice of Λ. This implies

$$\chi_{\mathbf{j}\rho}(\mathbf{k},\mathbf{k}',\omega) = \frac{1}{\omega}\left[\langle\hat{\rho}(\mathbf{k}-\mathbf{k}')\rangle + \chi_{\mathbf{jj}}(\mathbf{k},\mathbf{k}',\omega)\right]\mathbf{k}'. \quad \text{(D.12)}$$

In a similar way the induced density permits to obtain the relation:

$$\chi_{\rho\rho}(\mathbf{k},\mathbf{k}',\omega) = \frac{1}{\omega}\chi_{\rho\mathbf{j}}(\mathbf{k},\mathbf{k}',\omega)\mathbf{k}'. \quad \text{(D.13)}$$

Substituting the relation among $\chi_{\mathbf{j}\rho}$ and $\langle\hat{\rho}\rangle, \chi_{\mathbf{jj}}$ Eq. (D.12) into Eq. (D.1) and identifying the perturbing field $\mathbf{E}^P$ of Eq. (D.8), one achieves the final form

$$\mathbf{j}^{(1)}_{ind}(\mathbf{k},\omega) = -i\omega\sum_{k'} -\frac{1}{\omega^2}\left\{\langle\hat{\rho}(\mathbf{k}-\mathbf{k}')\rangle + \chi_{\mathbf{jj}}(\mathbf{k},\mathbf{k}',\omega)\right\}\mathbf{E}^P(\mathbf{k}',\omega). \quad \text{(D.14)}$$

Alternatively, defining the *quasi-susceptibility* or *quasi-polarizability* $\tilde{\alpha}^{(1)}$ as:

$$\tilde{\alpha}^{(1)}(\mathbf{k},\mathbf{k}',\omega) = -\frac{1}{\omega^2}\left\{\langle\hat{\rho}(\mathbf{k}-\mathbf{k}')\rangle + \chi_{\mathbf{jj}}(\mathbf{k},\mathbf{k}',\omega)\right\}, \tag{D.15}$$

equation Eq. (D.14) can be rewritten as

$$\mathbf{j}^{(1)}_{ind}(\mathbf{k},\omega) = -i\omega\sum_{k'}\tilde{\alpha}^{(1)}(\mathbf{k},\mathbf{k}',\omega)\mathbf{E}^P(\mathbf{k}',\omega). \tag{D.16}$$

or, Fourier transforming in the direct space

$$\tilde{\alpha}^{(1)}(\mathbf{r},\mathbf{r}',\omega) = \frac{1}{\omega^2}\left\{-\chi_{\mathbf{jj}}(\mathbf{r},\mathbf{r}',\omega) - \langle\hat{\rho}(\mathbf{r})\rangle\delta(\mathbf{r}-\mathbf{r}')\right\} \tag{D.17}$$

$$\mathbf{j}^{(1)}_{ind}(\mathbf{r},\omega) = -i\omega\int d\mathbf{r}'\tilde{\alpha}^{(1)}(\mathbf{r},\mathbf{r}',\omega)\mathbf{E}^P(\mathbf{r}',\omega) \tag{D.18}$$

that is exactly the results of Eq. (D.4).

Similary for $\rho^{(1)}_{ind}$, once substituting the realtion Eq. (D.13) to the first-order induced density Eq. (D.2) one obtains:

$$\rho^{(1)}_{ind}(\mathbf{k},\omega) = -\frac{1}{i\omega}\sum_{k'}\mathbf{E}^P(\mathbf{k}',\omega)\chi_{\rho\mathbf{j}}(\mathbf{k},\mathbf{k}',\omega). \tag{D.19}$$

The continuity equation holds at each perturbative order. In particular, for the first order in reciprocal space it reads

$$\mathbf{k}\cdot\mathbf{j}^{(1)}_{ind}(\mathbf{k},\omega) = \omega\rho^{(1)}_{ind}(\mathbf{k},\omega), \tag{D.20}$$

and considering the last expression for $\mathbf{j}^{(1)}_{ind}$, $\rho^{(1)}_{ind}$ one has

$$-\mathbf{k}\cdot\left\{\langle\hat{\rho}(\mathbf{k}-\mathbf{k}')\rangle + \chi_{\mathbf{jj}}(\mathbf{k},\mathbf{k}',\omega)\right\} + \omega\chi_{\rho\mathbf{j}}(\mathbf{k},\mathbf{k}',\omega) = 0 \tag{D.21}$$

that finally gives:

$$\mathbf{k}\left\{\langle\hat{\rho}(\mathbf{k}-\mathbf{k}')\rangle + \chi_{\mathbf{jj}}(\mathbf{k},\mathbf{k}',\omega)\right\}\mathbf{k}' = \omega^2\chi_{\rho\rho}(\mathbf{k},\mathbf{k}',\omega) \tag{D.22}$$

D.2 Second Order Relations

D.2.1 Induced current and induced density

The second-order perturbing terms in $(\phi^P, \mathbf{A}^P)$, once the perturbing field couples with the system are Eq. (4.15):

$$\hat{H}^{(1)}(t) = -\frac{1}{c}\int d\mathbf{r}\hat{\mathbf{j}}(\mathbf{r})\mathbf{A}^P(\mathbf{r},t) + \int d\mathbf{r}\hat{\rho}(\mathbf{r})\phi^P(\mathbf{r},t) \tag{D.23}$$

$$\hat{H}^{(2)}(t) = \frac{1}{2c^2}\int d\mathbf{r}\hat{\rho}(\mathbf{r})\left[\mathbf{A}^P(\mathbf{r},t)\right]^2 \tag{D.24}$$

The second-order induced current can then be written (cfr Eq. (4.30)) as:

$$
\begin{aligned}
\mathbf{j}^{(2)}_{ind}(\mathbf{k},\omega) = & \sum_{k'k''}\int d\omega' \int d\omega''\ \delta(\omega-\omega'-\omega'') \\
& \Big[\frac{1}{2c^2}\chi_{\mathbf{j}\rho}(\mathbf{k},\mathbf{k}'+\mathbf{k}'',\omega)\mathbf{A}^P(\mathbf{k}',\omega')\mathbf{A}^P(\mathbf{k}'',\omega'') \\
& +\frac{1}{c^2}\chi_{\rho\mathbf{j}}(\mathbf{k}-\mathbf{k}',\mathbf{k}'',\omega'')\mathbf{A}^P(\mathbf{k}',\omega')\mathbf{A}^P(\mathbf{k}'',\omega'') \\
& -\frac{1}{c}\chi_{\rho\rho}(\mathbf{k}-\mathbf{k}',\mathbf{k}'',\omega'')\mathbf{A}^P(\mathbf{k}',\omega')\phi^P(\mathbf{k}'',\omega'') \\
& +\frac{1}{2c^2}\chi_{\mathbf{jjj}}(\mathbf{k},\mathbf{k}',\mathbf{k}'',\omega',\omega'')\mathbf{A}^P(\mathbf{k}',\omega')\mathbf{A}^P(\mathbf{k}'',\omega'') \\
& -\frac{1}{2c}\chi_{\mathbf{jj}\rho}(\mathbf{k},\mathbf{k}',\mathbf{k}'',\omega',\omega'')\mathbf{A}^P(\mathbf{k}',\omega')\phi^P(\mathbf{k}'',\omega'') \\
& -\frac{1}{2c}\chi_{\mathbf{j}\rho\mathbf{j}}(\mathbf{k},\mathbf{k}',\mathbf{k}'',\omega',\omega'')\phi^P(\mathbf{k}',\omega')\mathbf{A}^P(\mathbf{k}'',\omega'') \\
& +\frac{1}{2}\chi_{\mathbf{j}\rho\rho}(\mathbf{k},\mathbf{k}',\mathbf{k}'',\omega',\omega'')\phi^P(\mathbf{k}',\omega')\phi^P(\mathbf{k}'',\omega'')\Big].
\end{aligned}
\tag{D.25}
$$

The second-order density instead reads (cfr. Eq. (4.42):

$$
\begin{aligned}
\rho^{(2)}_{ind}(\mathbf{k},\omega) = & \frac{1}{2c^2}\sum_{k'k''}\int d\omega'\chi_{\rho\rho}(\mathbf{k},\mathbf{k}'+\mathbf{k}'',\omega)\mathbf{A}^P(\mathbf{k}',\omega')\mathbf{A}^P(\mathbf{k}'',\omega-\omega') \\
& +\frac{1}{2c^2}\sum_{k'k''}\int d\omega'\int d\omega''\chi_{\rho\mathbf{jj}}(\mathbf{k},\mathbf{k}',\mathbf{k}'',\omega',\omega'')\mathbf{A}^P(\mathbf{k}',\omega')\mathbf{A}^P(\mathbf{k}'',\omega'') \\
& -\frac{1}{2c}\sum_{k'k''}\int d\omega'\int d\omega''\chi_{\rho\mathbf{j}\rho}(\mathbf{k},\mathbf{k}',\mathbf{k}'',\omega',\omega'')\mathbf{A}^P(\mathbf{k}',\omega')\phi^P(\mathbf{k}'',\omega') \\
& -\frac{1}{2c}\sum_{k'k''}\int d\omega'\int d\omega''\chi_{\rho\rho\mathbf{j}}(\mathbf{k},\mathbf{k}',\mathbf{k}'',\omega',\omega'')\phi^P(\mathbf{k}',\omega')\mathbf{A}^P(\mathbf{k}'',\omega'') \\
& +\frac{1}{2}\sum_{k'k''}\int d\omega'\int d\omega''\chi_{\rho\rho\rho}(\mathbf{k},\mathbf{k}',\mathbf{k}'',\omega',\omega'')\phi^P(\mathbf{k}',\omega')\phi^P(\mathbf{k}'',\omega'')
\end{aligned}
$$

D.2.2 Relation among the Second-Order Response Functions

Imposing the gauge-invariance while applying the trasformation Eq. (D.9) to $\mathbf{j}^{(2)}_{ind}$ in equation Eq. (D.25)

$$
\mathbf{j}^{(2)}_{ind}(\phi^P,\mathbf{A}^P) = \mathbf{j}^{(2)}_{ind}(\phi^P + \frac{i\omega}{c}\Lambda, \mathbf{A}^P + i\mathbf{k}\Lambda)
\tag{D.26}
$$

it is possible to derive a relation among the second order response functions (the explicit formula is rather long and I do not report it). The relation holds in general, for each value of the gauge-transformation potential Λ. In particular, imposing the transformations arising from Λ and $-\Lambda$ to be equal, the previous terms that are linear in Λ cancels each others and only terms that are quadratic in Λ remains:

$$\begin{aligned}0 = {} & \chi_{\mathbf{j}\rho}(\mathbf{k},\mathbf{k}'+\mathbf{k}'',\omega)\mathbf{k}'\mathbf{k}'' + \chi_{\mathbf{jjj}}(\mathbf{k},\mathbf{k}',\mathbf{k}'',\omega',\omega'')\mathbf{k}'\mathbf{k}'' \\ & - \chi_{\mathbf{jj}\rho}(\mathbf{k},\mathbf{k}',\mathbf{k}'',\omega',\omega'')\mathbf{k}'\omega'' - \chi_{\mathbf{j}\rho\mathbf{j}}(\mathbf{k},\mathbf{k}',\mathbf{k}'',\omega',\omega'')\omega'\mathbf{k}'' \\ & + \chi_{\mathbf{j}\rho\rho}(\mathbf{k},\mathbf{k}',\mathbf{k}'',\omega',\omega'')\omega'\omega''\end{aligned} \tag{D.27}$$

(where it has been considered that the sum should be zero for every choice of Λ). This means, that second-order terms in Λ vanish, indipendently from the linear ones.[1] Therefore, the remaining linear terms of Eq. (D.26) have to be zero:

$$\begin{aligned}\mathbf{0} = {} & \frac{1}{2c^2}\sum_{k'}\int d\omega' \chi_{\mathbf{j}\rho}(\mathbf{k},\mathbf{k}'+\mathbf{k}'',\omega)\mathbf{A}^P(\mathbf{k}',\omega')i\mathbf{k}'' \\ & + \frac{1}{2c^2}\sum_{k'}\int d\omega' \chi_{\mathbf{j}\rho}(\mathbf{k},\mathbf{k}'+\mathbf{k}'',\omega)i\mathbf{k}''\mathbf{A}^P(\mathbf{k}',\omega') \\ & + \frac{1}{c^2}\sum_{k'}\int d\omega' \chi_{\rho\mathbf{j}}(\mathbf{k}-\mathbf{k}',\mathbf{k}'',\omega'')\mathbf{A}^P(\mathbf{k}',\omega')i\mathbf{k}'' \\ & + \frac{1}{c^2}\sum_{k'}\int d\omega' \chi_{\rho\mathbf{j}}(\mathbf{k}-\mathbf{k}'',\mathbf{k}',\omega')i\mathbf{k}''\mathbf{A}^P(\mathbf{k}',\omega') \\ & - \frac{1}{c}\sum_{k'}\int d\omega' \chi_{\rho\rho}(\mathbf{k}-\mathbf{k}'',\mathbf{k}',\omega')i\mathbf{k}''\phi^P(\mathbf{k}',\omega') \\ & - \frac{1}{c}\sum_{k'}\int d\omega' \chi_{\rho\rho}(\mathbf{k}-\mathbf{k}',\mathbf{k}'',\omega'')\mathbf{A}^P(\mathbf{k}',\omega')\frac{i\omega''}{c} \\ & + \frac{1}{2c^2}\sum_{k'}\int d\omega' \chi_{\mathbf{jjj}}(\mathbf{k},\mathbf{k}',\mathbf{k}'',\omega',\omega'')\mathbf{A}^P(\mathbf{k}',\omega')i\mathbf{k}'' \\ & + \frac{1}{2c^2}\sum_{k'}\int d\omega' \chi_{\mathbf{jjj}}(\mathbf{k},\mathbf{k}'',\mathbf{k}',\omega'',\omega')i\mathbf{k}''\mathbf{A}^P(\mathbf{k}',\omega') \\ & - \frac{1}{2c}\sum_{k'}\int d\omega' \chi_{\mathbf{jj}\rho}(\mathbf{k},\mathbf{k}',\mathbf{k}'',\omega',\omega'')\mathbf{A}^P(\mathbf{k}',\omega')\frac{i\omega''}{c} \\ & - \frac{1}{2c}\sum_{k'}\int d\omega' \chi_{\mathbf{jj}\rho}(\mathbf{k},\mathbf{k}'',\mathbf{k}',\omega'',\omega')i\mathbf{k}''\phi^P(\mathbf{k}',\omega') \\ & - \frac{1}{2c}\sum_{k'}\int d\omega' \chi_{\mathbf{j}\rho\mathbf{j}}(\mathbf{k},\mathbf{k}',\mathbf{k}'',\omega',\omega'')\phi^P(\mathbf{k}',\omega')i\mathbf{k}'' \\ & - \frac{1}{2c}\sum_{k'}\int d\omega' \chi_{\mathbf{j}\rho\mathbf{j}}(\mathbf{k},\mathbf{k}'',\mathbf{k}',\omega'',\omega')\frac{i\omega''}{c}\mathbf{A}^P(\mathbf{k}',\omega') \\ & + \frac{1}{2}\sum_{k'}\int d\omega' \chi_{\mathbf{j}\rho\rho}(\mathbf{k},\mathbf{k}',\mathbf{k}'',\omega',\omega'')\phi^P(\mathbf{k}',\omega')\frac{i\omega''}{c} \\ & + \frac{1}{2}\sum_{k'}\int d\omega' \chi_{\mathbf{j}\rho\rho}(\mathbf{k},\mathbf{k}'',\mathbf{k}',\omega'',\omega')\frac{i\omega''}{c}\phi^P(\mathbf{k}',\omega').\end{aligned} \tag{D.28}$$

---

[1] The relation is more general and establishes that the sum of all the odd-order terms in Λ have to be zero independently from the sum of all the even-order terms, that vanish too.

Considering Eq. (D.27) and Eq. (D.13) the last equation can be rewritten as:

$$\begin{aligned}
\mathbf{0} = &\frac{1}{c}\sum_{k'}\int d\omega' \chi_{\mathbf{j}\rho}(\mathbf{k},\mathbf{k}'+\mathbf{k}'',\omega)\left[\frac{i}{c}\mathbf{A}^P(\mathbf{k}',\omega') - \frac{i}{\omega'}\mathbf{k}'\phi^P(\mathbf{k}',\omega')\right]\mathbf{k}'' \\
&+\frac{1}{c}\sum_{k'}\int d\omega' \chi_{\rho\mathbf{j}}(\mathbf{k}-\mathbf{k}'',\mathbf{k}',\omega')\left[\frac{i}{c}\mathbf{A}^P(\mathbf{k}',\omega') - \frac{i}{\omega'}\mathbf{k}'\phi^P(\mathbf{k}',\omega')\right]\mathbf{k}'' \\
&+\frac{1}{2c}\sum_{k'}\int d\omega' \chi_{\mathbf{jjj}}(\mathbf{k},\mathbf{k}',\mathbf{k}'',\omega',\omega'')\left[\frac{i}{c}\mathbf{A}^P(\mathbf{k}',\omega') - \frac{i}{\omega'}\mathbf{k}'\phi^P(\mathbf{k}',\omega')\right]\mathbf{k}'' \\
&+\frac{1}{2c}\sum_{k'}\int d\omega' \chi_{\mathbf{jjj}}(\mathbf{k},\mathbf{k}'',\mathbf{k}',\omega'',\omega')\mathbf{k}''\left[\frac{i}{c}\mathbf{A}^P(\mathbf{k}',\omega') - \frac{i}{\omega'}\mathbf{k}'\phi^P(\mathbf{k}',\omega')\right] \\
&-\frac{1}{2c}\sum_{k'}\int d\omega' \chi_{\mathbf{jj}\rho}(\mathbf{k},\mathbf{k}',\mathbf{k}'',\omega',\omega'')\left[\frac{i}{c}\mathbf{A}^P(\mathbf{k}',\omega') - \frac{i}{\omega'}\mathbf{k}'\phi^P(\mathbf{k}',\omega')\right]\omega'' \\
&-\frac{1}{2c}\sum_{k'}\int d\omega' \chi_{\mathbf{j}\rho\mathbf{j}}(\mathbf{k},\mathbf{k}'',\mathbf{k}',\omega'',\omega')\left[\frac{i}{c}\mathbf{A}^P(\mathbf{k}',\omega') - \frac{i}{\omega'}\mathbf{k}'\phi^P(\mathbf{k}',\omega')\right]\omega''
\end{aligned} \tag{D.29}$$

that, being independent of the particular choice of $(\phi^P, \mathbf{A}^P)$ or equivalently $\mathbf{E}^P$,[2] gives:

$$\begin{aligned}
\mathbf{0} = &\chi_{\mathbf{j}\rho}(\mathbf{k},\mathbf{k}'+\mathbf{k}'',\omega)\mathbf{k}'' + \chi_{\rho\mathbf{j}}(\mathbf{k}-\mathbf{k}'',\mathbf{k}',\omega')\mathbf{k}'' \\
&+\frac{1}{2}\chi_{\mathbf{jjj}}(\mathbf{k},\mathbf{k}',\mathbf{k}'',\omega',\omega'')\mathbf{k}'' + \frac{1}{2}\chi_{\mathbf{jjj}}(\mathbf{k},\mathbf{k}'',\mathbf{k}',\omega'',\omega')\mathbf{k}'' \\
&-\frac{1}{2}\chi_{\mathbf{jj}\rho}(\mathbf{k},\mathbf{k}',\mathbf{k}'',\omega',\omega'')\omega'' - \frac{1}{2}\chi_{\mathbf{j}\rho\mathbf{j}}(\mathbf{k},\mathbf{k}'',\mathbf{k}',\omega'',\omega')\omega''.
\end{aligned} \tag{D.30}$$

Combining the two relations Eqs. (D.27), (D.30) together one obtains a third one

$$\begin{aligned}
&\chi_{\mathbf{j}\rho\rho}(\mathbf{k},\mathbf{k}',\mathbf{k}'',\omega',\omega'') = \frac{1}{\omega'\omega''}\chi_{\rho\mathbf{j}}(\mathbf{k}-\mathbf{k}'',\mathbf{k}',\omega')\mathbf{k}'\mathbf{k}'' \\
&-\frac{1}{2}\frac{1}{\omega'\omega''}\chi_{\mathbf{jjj}}(\mathbf{k},\mathbf{k}',\mathbf{k}'',\omega',\omega'')\mathbf{k}'\mathbf{k}'' + \frac{1}{2}\frac{1}{\omega'\omega''}\chi_{\mathbf{jjj}}(\mathbf{k},\mathbf{k}'',\mathbf{k}',\omega'',\omega')\mathbf{k}'\mathbf{k}'' \\
&+\frac{1}{2}\frac{1}{\omega'\omega''}\chi_{\mathbf{jj}\rho}(\mathbf{k},\mathbf{k}',\mathbf{k}'',\omega',\omega'')\mathbf{k}'\omega'' - \frac{1}{2}\frac{1}{\omega'\omega''}\chi_{\mathbf{j}\rho\mathbf{j}}(\mathbf{k},\mathbf{k}'',\mathbf{k}',\omega'',\omega')\mathbf{k}'\omega'' \\
&+\frac{1}{\omega'\omega''}\chi_{\mathbf{j}\rho\mathbf{j}}(\mathbf{k},\mathbf{k}',\mathbf{k}'',\omega',\omega'')\omega'\mathbf{k}''.
\end{aligned} \tag{D.31}$$

---

[2] From its definition Eq. (D.8) one can recognize the square brackets into Eq. (D.29) as:

$$\left[\tfrac{i}{c}\mathbf{A}^P(\mathbf{k}',\omega') - \tfrac{i}{\omega'}\mathbf{k}'\phi^P(\mathbf{k}',\omega')\right] = \omega'\mathbf{E}^P(\mathbf{k}',\omega').$$

D.2.3 Expression for the second order current

Considering Eq. (D.25) and substituting $\chi_{\rho\mathbf{j}}$ to $\chi_{\rho\rho}$ through the relation Eq. (D.13),

$$\begin{aligned}
\mathbf{j}^{(2)}_{ind}(\mathbf{k},\omega) = \sum_{k'k''} \int d\omega' \int d\omega'' \delta(\omega-\omega'-\omega'')& \\
\Big[\frac{1}{2c^2}\chi_{\mathbf{j}\rho}(\mathbf{k},\mathbf{k}'+\mathbf{k}'',\omega)\mathbf{A}^P(\mathbf{k}',\omega')\mathbf{A}^P(\mathbf{k}'',\omega'')& \\
-i\frac{1}{c}\chi_{\rho\mathbf{j}}(\mathbf{k}-\mathbf{k}',\mathbf{k}'',\omega'')\mathbf{A}^P(\mathbf{k}',\omega')\frac{1}{\omega''}\mathbf{E}^P(\mathbf{k}'',\omega'')& \\
+\frac{1}{2c^2}\chi_{\mathbf{jjj}}(\mathbf{k},\mathbf{k}',\mathbf{k}'',\omega',\omega'')\mathbf{A}^P(\mathbf{k}',\omega')\mathbf{A}^P(\mathbf{k}'',\omega'')& \\
-\frac{1}{2c}\chi_{\mathbf{jj}\rho}(\mathbf{k},\mathbf{k}',\mathbf{k}'',\omega',\omega'')\mathbf{A}^P(\mathbf{k}',\omega')\phi^P(\mathbf{k}'',\omega'')& \\
-\frac{1}{2c}\chi_{\mathbf{j}\rho\mathbf{j}}(\mathbf{k},\mathbf{k}',\mathbf{k}'',\omega',\omega'')\phi^P(\mathbf{k}',\omega')\mathbf{A}^P(\mathbf{k}'',\omega'')& \\
+\frac{1}{2}\chi_{\mathbf{j}\rho\rho}(\mathbf{k},\mathbf{k}',\mathbf{k}'',\omega',\omega'')\phi^P(\mathbf{k}',\omega')\phi^P(\mathbf{k}'',\omega'')\Big]&.
\end{aligned} \tag{D.32}$$

Substituting $\chi_{\mathbf{j}\rho\rho}$ as obtained from Eq. (D.31)

$$\begin{aligned}
&\mathbf{j}^{(2)}_{ind}(\mathbf{k},\omega) = \sum_{k'k''} \int d\omega' \int d\omega'' \delta(\omega-\omega'-\omega'') \\
&\Big[\frac{1}{2c^2}\chi_{\mathbf{j}\rho}(\mathbf{k},\mathbf{k}'+\mathbf{k}'',\omega)\mathbf{A}^P(\mathbf{k}',\omega')\mathbf{A}^P(\mathbf{k}'',\omega'') \\
&-i\frac{1}{c}\chi_{\rho\mathbf{j}}(\mathbf{k}-\mathbf{k}',\mathbf{k}'',\omega'')\mathbf{A}^P(\mathbf{k}',\omega')\frac{1}{\omega''}\mathbf{E}^P(\mathbf{k}'',\omega'') \\
&+\frac{1}{2}\frac{1}{\omega'\omega''}\chi_{\rho\mathbf{j}}(\mathbf{k}-\mathbf{k}'',\mathbf{k}',\omega')\mathbf{k}'\mathbf{k}''\phi^P(\mathbf{k}',\omega')\phi^P(\mathbf{k}'',\omega'') \\
&+\frac{1}{2c^2}\chi_{\mathbf{jjj}}(\mathbf{k},\mathbf{k}',\mathbf{k}'',\omega',\omega'')\mathbf{A}^P(\mathbf{k}',\omega')\mathbf{A}^P(\mathbf{k}'',\omega'') \\
&-\frac{1}{2c}\left[\chi_{\mathbf{jj}\rho}(\mathbf{k},\mathbf{k}',\mathbf{k}'',\omega',\omega'')+\chi_{\mathbf{j}\rho\mathbf{j}}(\mathbf{k},\mathbf{k}'',\mathbf{k}',\omega'',\omega')\right] \\
&\cdot\mathbf{A}^P(\mathbf{k}',\omega')\phi^P(\mathbf{k}'',\omega'') \\
&+\frac{1}{2}\frac{1}{2}\frac{1}{\omega'\omega''}\left[\chi_{\mathbf{jj}\rho}(\mathbf{k},\mathbf{k}',\mathbf{k}'',\omega',\omega'')+\chi_{\mathbf{j}\rho\mathbf{j}}(\mathbf{k},\mathbf{k}'',\mathbf{k}',\omega'',\omega')\right] \\
&\cdot\mathbf{k}'\omega''\phi^P(\mathbf{k}',\omega')\phi^P(\mathbf{k}'',\omega'')\Big].
\end{aligned} \tag{D.33}$$

and using the following relation

$$\begin{aligned}
2\chi_{\mathbf{j}\rho}(\mathbf{k},\mathbf{k}'+\mathbf{k}'',\omega)\mathbf{k}''+2\chi_{\rho\mathbf{j}}(\mathbf{k}-\mathbf{k}'',\mathbf{k}',\omega')\mathbf{k}''& \\
+\chi_{\mathbf{jjj}}(\mathbf{k},\mathbf{k}',\mathbf{k}'',\omega',\omega'')\mathbf{k}''+\chi_{\mathbf{jjj}}(\mathbf{k},\mathbf{k}'',\mathbf{k}',\omega'',\omega')\mathbf{k}''& \\
=\chi_{\mathbf{jj}\rho}(\mathbf{k},\mathbf{k}',\mathbf{k}'',\omega',\omega'')\omega''+\chi_{\mathbf{j}\rho\mathbf{j}}(\mathbf{k},\mathbf{k}'',\mathbf{k}',\omega'',\omega')\omega''&
\end{aligned} \tag{D.34}$$

derived from the linear combination of Eq. (D.27) and Eq. (D.30), one has:

$$
\begin{aligned}
&\mathbf{j}^{(2)}_{ind}(\mathbf{k},\omega) = \frac{1}{2c^2}\sum_{k'k''}\int d\omega'\int d\omega''\chi_{\mathbf{j}\rho}(\mathbf{k},\mathbf{k}'+\mathbf{k}'',\omega)\mathbf{A}^P(\mathbf{k}',\omega')\mathbf{A}^P(\mathbf{k}'',\omega'')\delta(\omega-\omega'-\omega'')\\
&-i\frac{1}{c}\sum_{k'k''}\int d\omega'\int d\omega''\chi_{\rho\mathbf{j}}(\mathbf{k}-\mathbf{k}',\mathbf{k}'',\omega'')\mathbf{A}^P(\mathbf{k}',\omega')\frac{1}{\omega''}\mathbf{E}^P(\mathbf{k}'',\omega'')\delta(\omega-\omega'-\omega'')\\
&+\frac{1}{2}\sum_{k'k''}\int d\omega'\int d\omega''\frac{1}{\omega'\omega''}\chi_{\rho\mathbf{j}}(\mathbf{k}-\mathbf{k}'',\mathbf{k}',\omega')\mathbf{k}'\mathbf{k}''\phi^P(\mathbf{k}',\omega')\phi^P(\mathbf{k}'',\omega'')\delta(\omega-\omega'-\omega'')\\
&+\frac{1}{2c^2}\sum_{k'k''}\int d\omega'\int d\omega''\chi_{\mathbf{jjj}}(\mathbf{k},\mathbf{k}',\mathbf{k}'',\omega',\omega'')\mathbf{A}^P(\mathbf{k}',\omega')\mathbf{A}^P(\mathbf{k}'',\omega'')\delta(\omega-\omega'-\omega'')\\
&-\frac{1}{2c}\sum_{k'k''}\int d\omega'\int d\omega''\frac{1}{\omega'}\chi_{\mathbf{jjj}}(\mathbf{k},\mathbf{k}',\mathbf{k}'',\omega',\omega'')\mathbf{k}''\mathbf{A}^P(\mathbf{k}',\omega')\phi^P(\mathbf{k}'',\omega'')\delta(\omega-\omega'-\omega'')\\
&-\frac{1}{2c}\sum_{k'k''}\int d\omega'\int d\omega''\frac{1}{\omega''}\chi_{\mathbf{jjj}}(\mathbf{k},\mathbf{k}',\mathbf{k}'',\omega',\omega'')\mathbf{k}'\mathbf{A}^P(\mathbf{k}'',\omega'')\phi^P(\mathbf{k}',\omega')\delta(\omega-\omega'-\omega'')\\
&+\frac{1}{2}\sum_{k'k''}\int d\omega'\int d\omega''\frac{1}{\omega'\omega''}\chi_{\mathbf{jjj}}(\mathbf{k},\mathbf{k}',\mathbf{k}'',\omega',\omega'')\mathbf{k}'\mathbf{k}''\phi^P(\mathbf{k}',\omega')\phi^P(\mathbf{k}'',\omega'')\delta(\omega-\omega'-\omega'')\\
&-\frac{1}{2c}\sum_{k'k''}\int d\omega'\int d\omega''\frac{1}{\omega''}\left[2\chi_{\mathbf{j}\rho}(\mathbf{k},\mathbf{k}'+\mathbf{k}'',\omega)\mathbf{k}''+2\chi_{\rho\mathbf{j}}(\mathbf{k}-\mathbf{k}'',\mathbf{k}',\omega')\mathbf{k}''\right]\\
&\cdot\mathbf{A}^P(\mathbf{k}',\omega')\phi^P(\mathbf{k}'',\omega'')\delta(\omega-\omega'-\omega'')\\
&+\frac{1}{2}\sum_{k'k''}\int d\omega'\int d\omega''\frac{1}{2}\frac{1}{\omega'\omega''}\left[2\chi_{\mathbf{j}\rho}(\mathbf{k},\mathbf{k}'+\mathbf{k}'',\omega)+2\chi_{\rho\mathbf{j}}(\mathbf{k}-\mathbf{k}'',\mathbf{k}',\omega')\right]\\
&\cdot\mathbf{k}'\mathbf{k}''\phi^P(\mathbf{k}',\omega')\phi^P(\mathbf{k}'',\omega'')\delta(\omega-\omega'-\omega'').
\end{aligned}
\tag{D.35}
$$

$$
\begin{aligned}
&\mathbf{j}^{(2)}_{ind}(\mathbf{k},\omega) = \sum_{k'k''} \int d\omega' \int d\omega'' \delta(\omega-\omega'-\omega'') \\
&\Bigg[\frac{1}{2c^2}\chi_{\mathbf{j}\rho}(\mathbf{k},\mathbf{k}'+\mathbf{k}'',\omega)\mathbf{A}^P(\mathbf{k}',\omega')\mathbf{A}^P(\mathbf{k}'',\omega'') \\
&- i\frac{1}{c}\chi_{\rho\mathbf{j}}(\mathbf{k}-\mathbf{k}',\mathbf{k}'',\omega'')\mathbf{A}^P(\mathbf{k}',\omega')\frac{1}{\omega''}\mathbf{E}^P(\mathbf{k}'',\omega'') \\
&+ \frac{1}{2}\frac{1}{\omega'\omega''}\chi_{\rho\mathbf{j}}(\mathbf{k}-\mathbf{k}'',\mathbf{k}',\omega')\mathbf{k}'\mathbf{k}''\phi^P(\mathbf{k}',\omega')\phi^P(\mathbf{k}'',\omega'') \\
&+ \frac{1}{2c^2}\chi_{\mathbf{jjj}}(\mathbf{k},\mathbf{k}',\mathbf{k}'',\omega',\omega'')\mathbf{A}^P(\mathbf{k}',\omega')\mathbf{A}^P(\mathbf{k}'',\omega'') \\
&- \frac{1}{2c}\frac{1}{\omega'}\chi_{\mathbf{jjj}}(\mathbf{k},\mathbf{k}',\mathbf{k}'',\omega',\omega'')\mathbf{k}''\mathbf{A}^P(\mathbf{k}',\omega')\phi^P(\mathbf{k}'',\omega'') \qquad \text{(D.36)} \\
&- \frac{1}{2c}\frac{1}{\omega''}\chi_{\mathbf{jjj}}(\mathbf{k},\mathbf{k}',\mathbf{k}'',\omega',\omega'')\mathbf{k}'\mathbf{A}^P(\mathbf{k}'',\omega'')\phi^P(\mathbf{k}',\omega') \\
&+ \frac{1}{2}\frac{1}{\omega'\omega''}\chi_{\mathbf{jjj}}(\mathbf{k},\mathbf{k}',\mathbf{k}'',\omega',\omega'')\mathbf{k}'\mathbf{k}''\phi^P(\mathbf{k}',\omega')\phi^P(\mathbf{k}'',\omega'') \\
&- \frac{1}{2c}\frac{1}{\omega''}\left[2\chi_{\mathbf{j}\rho}(\mathbf{k},\mathbf{k}'+\mathbf{k}'',\omega)\mathbf{k}''+2\chi_{\rho\mathbf{j}}(\mathbf{k}-\mathbf{k}'',\mathbf{k}',\omega')\mathbf{k}''\right] \\
&\cdot\,\mathbf{A}^P(\mathbf{k}',\omega')\phi^P(\mathbf{k}'',\omega'') \\
&+ \frac{1}{2}\frac{1}{2}\frac{1}{\omega'\omega''}\left[2\chi_{\mathbf{j}\rho}(\mathbf{k},\mathbf{k}'+\mathbf{k}'',\omega)+2\chi_{\rho\mathbf{j}}(\mathbf{k}-\mathbf{k}'',\mathbf{k}',\omega')\right] \\
&\cdot\mathbf{k}'\mathbf{k}''\phi^P(\mathbf{k}',\omega')\phi^P(\mathbf{k}'',\omega'')\Bigg]\,.
\end{aligned}
$$

Collecting the terms as function of the perturbing field $\mathbf{E}^P$ given by Eq. (D.8) one achieves the final *gauge-invariant* result for the second-order induced current-density $\mathbf{j}^{(2)}_{ind}$ (cfr. Eq. (4.31)):

$$
\begin{aligned}
\mathbf{j}^{(2)}_{ind}(\mathbf{k},\omega) = \sum_{k'k''}\int d\omega' \int d\omega'' \frac{1}{\omega'\omega''}&\Bigg[-\frac{1}{2}\chi_{\mathbf{j}\rho}(\mathbf{k},\mathbf{k}'+\mathbf{k}'',\omega) \\
&-\chi_{\rho\mathbf{j}}(\mathbf{k}-\mathbf{k}'',\mathbf{k}',\omega') - \frac{1}{2}\chi_{\mathbf{jjj}}(\mathbf{k},\mathbf{k}',\mathbf{k}'',\omega',\omega'')\Bigg] \qquad \text{(D.37)} \\
&\mathbf{E}^P(\mathbf{k}',\omega')\mathbf{E}^P(\mathbf{k}'',\omega'')\delta(\omega-\omega'-\omega'').
\end{aligned}
$$

A similar relation can be obtained for the second-order density correction $\rho^{(2)}_{ind}$:

$$
\begin{aligned}
&\hat{\rho}_{ind}(1)^{(2)} \\
&= \frac{1}{2}\int d\omega' \int d\omega'' \chi_{\rho\rho\rho}(\mathbf{k}'+\mathbf{k}'',\mathbf{k}',\mathbf{k}'',\omega',\omega'')\frac{i\mathbf{k}'\cdot\mathbf{E}^P(\mathbf{k}',\omega')}{\mathbf{k}'\cdot\mathbf{k}'}\frac{i\mathbf{k}''\cdot\mathbf{E}^P(\mathbf{k}'',\omega'')}{\mathbf{k}''\cdot\mathbf{k}''} \\
&= \frac{1}{2}\int d\omega' \int d\omega'' \chi_{\rho\rho\rho}(\mathbf{k}'+\mathbf{k}'',\mathbf{k}',\mathbf{k}'',\omega',\omega'')\frac{i}{|\mathbf{k}'|}|\mathbf{E}^P|(\mathbf{k}',\omega')\frac{i}{|\mathbf{k}''|}|\mathbf{E}^P|(\mathbf{k}'',\omega'') \\
&= \frac{1}{2}\int d\omega' \int d\omega'' \chi_{\rho\rho\rho}(\mathbf{k}'+\mathbf{k}'',\mathbf{k}',\mathbf{k}'',\omega',\omega'')\frac{i}{k'}E^P(\mathbf{k}',\omega')\frac{i}{k''}E^P(\mathbf{k}'',\omega''), \\
&\qquad \text{(D.38)}
\end{aligned}
$$

cfr. Eq. (4.43).

D.3 Relation between second-order density and current-density

Starting from the continuity equation Eq. (4.36), that should hold for each perturbative order:

$$\mathbf{q}\cdot\delta\langle\hat{\mathbf{j}}(\mathbf{q},\omega)\rangle^{(i)} = i\omega\delta\langle\hat{\rho}(\mathbf{q},\omega)\rangle^{(i)}, \tag{D.39}$$

it is possible to find relations among the density and current-density response functions.

At the second order in the long wavelength limit Eq. (4.30) reduces to:

$$\begin{aligned}\delta\langle\hat{\mathbf{j}}_{tot}(\mathbf{q}_1,\omega_1)\rangle^{(2)} &= \delta\langle\hat{\mathbf{j}}_{tot}(\mathbf{q}_2+\mathbf{q}_3,\omega_2+\omega_3)\rangle^{(2)}\\ &= \frac{1}{2}\frac{1}{\omega_2\omega_3}\chi^{(2)}_{\mathbf{jjj}}(\mathbf{q}_1,\mathbf{q}_2,\mathbf{q}_3,\omega_2,\omega_3)\cdot\mathbf{E}^P(\mathbf{q}_2,\omega_2)\cdot\mathbf{E}^P(\mathbf{q}_3,\omega_3)\end{aligned} \tag{D.40}$$

While the density can be rewritten thanks to gauge invariance as (cfr. Eq. (D.38)):

$$\begin{aligned}\delta\langle\hat{\rho}_{tot}(\mathbf{q}_1,\omega_1)\rangle^{(2)} &= \delta\langle\hat{\rho}_{tot}(\mathbf{q}_2+\mathbf{q}_3,\omega_2+\omega_3)\rangle^{(2)}\\ &= \frac{1}{2}\chi^{(2)}_{\rho\rho\rho}(\mathbf{q}_1,\mathbf{q}_2,\mathbf{q}_3,\omega_2,\omega_3)\frac{i}{q_2}E^P(\mathbf{q}_2,\omega_2)\frac{i}{q_3}E^P(\mathbf{q}_3,\omega_3).\end{aligned} \tag{D.41}$$

With $q_i = |\mathbf{q}_i|$ and $E^P = |\mathbf{E}^P|$, where the perturbing electric field has been substituted through its general definition Eq. (4.25) that in reciprocal space reads

$$\mathbf{E}^P(\mathbf{q},\omega) = -i\mathbf{q}\phi^P(\mathbf{q},\omega) + \frac{i\omega}{c}\mathbf{A}^P(\mathbf{q},\omega). \tag{D.42}$$

These equations substituted into Eq. (D.39) for the second perturbative order give:

$$\begin{aligned}&\mathbf{q}_1\cdot\delta\langle\hat{\mathbf{j}}_{tot}(\mathbf{q}_1,\omega_1)\rangle^{(2)} = i\omega_1\delta\langle\hat{\rho}(\mathbf{q}_1,\omega_1)\rangle^{(2)}\\ &\quad\frac{1}{2}\frac{1}{\omega_2\omega_3}\mathbf{q}_1\cdot\chi^{(2)}_{\mathbf{jjj}}(\mathbf{q}_1,\mathbf{q}_2,\mathbf{q}_3,\omega_2,\omega_3)\cdot\mathbf{E}^P(\mathbf{q}_2,\omega_2)\cdot\mathbf{E}^P(\mathbf{q}_3,\omega_3) =\\ &\qquad\qquad i\omega_1\frac{1}{2}\chi^{(2)}_{\rho\rho\rho}(\mathbf{q}_1,\mathbf{q}_2,\mathbf{q}_3,\omega_2,\omega_3)\frac{i}{q_2}E^P(\mathbf{q}_2,\omega_2)\frac{i}{q_3}E^P(\mathbf{q}_3,\omega_3)\\ &\quad\frac{1}{\omega_2\omega_3}\mathbf{q}_1\cdot\chi^{(2)}_{\mathbf{jjj}}(\mathbf{q}_1,\mathbf{q}_2,\mathbf{q}_3,\omega_2,\omega_3)\cdot\hat{\mathbf{q}}_2E^P(\mathbf{q}_2,\omega_2)\cdot\hat{\mathbf{q}}_3E^P(\mathbf{q}_3,\omega_3) =\\ &\qquad\qquad i\omega_1\chi^{(2)}_{\rho\rho\rho}(\mathbf{q}_1,\mathbf{q}_2,\mathbf{q}_3,\omega_2,\omega_3)\frac{i}{q_2}E^P(\mathbf{q}_2,\omega_2)\frac{i}{q_3}E^P(\mathbf{q}_3,\omega_3),\end{aligned} \tag{D.43}$$

where $\hat{\mathbf{q}}$ represents the polarization versor $\frac{\mathbf{q}}{q}$. Simplifying E^P and dividing by q_1 to both sides one obtains the final relation Eq. (4.46):

$$\begin{aligned}\hat{\mathbf{q}}_1\cdot\chi^{(2)}_{\mathbf{jjj}}(\mathbf{q}_1,\mathbf{q}_2,\mathbf{q}_3,\omega_2,\omega_3)\cdot\hat{\mathbf{q}}_2\cdot\hat{\mathbf{q}}_3 &= -i\frac{\omega_1\omega_2\omega_3}{q_1q_2q_3}\chi^{(2)}_{\rho\rho\rho}(\mathbf{q}_1,\mathbf{q}_2,\mathbf{q}_3,\omega_2,\omega_3)\\ \chi^{(2)LLL}_{\mathbf{jjj}}(\mathbf{q}_1,\mathbf{q}_2,\mathbf{q}_3,\omega_2,\omega_3) &= -i\frac{\omega_1\omega_2\omega_3}{q_1q_2q_3}\chi^{(1)}_{\rho\rho\rho}(\mathbf{q}_1,\mathbf{q}_2,\mathbf{q}_3,\omega_2,\omega_3).\end{aligned} \tag{D.44}$$

A similar derivation can be obtained also for the first order responses.

D.4 Length and Velocity gauges

In section 4.3.2 I have provided the general expression for the second-order density response function developed on Bloch's states when $\mathbf{q} \to 0$. It has been obtained in the *length gauge* that express the second-order response in terms of $\chi^{(2)}_{\rho\rho\rho}$, the only quantity that can be derived through TDDFT. However, it finds a correspondence to the *velocity gauge* thanks to the continuity equations that links $\chi^{(2)}_{\rho\rho\rho}$ and $\chi^{(2)LLL}_{\mathbf{jjj}}$ (descending directly from the gauge invariance that is independent of the gauge where $\varphi^P, \mathbf{A}^P$ are expressed). They are reconnected via the relation:

$$\langle \psi_{n\mathbf{k}} | i\mathbf{r} | \psi_{m\mathbf{k}} \rangle = \frac{\langle \psi_{n\mathbf{k}} | \mathbf{v} | \psi_{m\mathbf{k}} \rangle}{\epsilon_{n\mathbf{k}} - \epsilon_{m\mathbf{k}}}. \tag{D.45}$$

For practical purpose it is convenient to evaluate all the matrix elements in the *velocity gauge*, because of the simple expression they takes, then passing through Eq. (D.45) to the correspective *length gauge* where $\chi^{(2)}_{\rho\rho\rho}$ is expressed. Indeed the velocity is related to the operator $-i\nabla$ that simply gives a factor $\mathbf{q}$ in front of the Bloch's state $\langle \psi_{n\mathbf{k}} | \mathbf{v} | \psi_{m\mathbf{k}} \rangle = -i\mathbf{q} \langle \psi_{n\mathbf{k}} | \psi_{m\mathbf{k}} \rangle$. This avoids the evaluation of the more complex $\langle \psi_{n\mathbf{k}} | i\mathbf{r} | \psi_{m\mathbf{k}} \rangle$ integral.

The results is equivalent to the one developed by Hughes and Sipe [50] for the *length gauge* that has been largely used also by other authors [22, 53, 54] for SHG calculation within the independent particle approximation.

Appendix E

2light Approximations Derivation

Equation (5.17) is easily obtained considering the results of appendix D.4. Being

$$\langle \psi_{n\mathbf{k}} | i\mathbf{r} | \psi_{m\mathbf{k}} \rangle = \frac{\langle \psi_{n\mathbf{k}} | \mathbf{v} | \psi_{m\mathbf{k}} \rangle}{\epsilon_{n\mathbf{k}} - \epsilon_{m\mathbf{k}}} \tag{E.1}$$

for $H_{\mathbf{k}}$, the same holds also for H_{SO}:

$$\langle \psi_{n\mathbf{k}} | i\mathbf{r} | \psi_{m\mathbf{k}} \rangle = \frac{\langle \psi_{n\mathbf{k}} | \mathbf{v}_{SO} | \psi_{m\mathbf{k}} \rangle}{\epsilon^{SO}_{n\mathbf{k}} - \epsilon^{SO}_{m\mathbf{k}}} \tag{E.2}$$

because the position matrix elements $\langle \psi_{n\mathbf{k}} | i\mathbf{r} | \psi_{m\mathbf{k}} \rangle$ depends only on the eigenstates $|\psi_{n\mathbf{k}}\rangle$ that are the same for both the system. As a consequence

$$\begin{aligned} \frac{\langle \psi_{n\mathbf{k}} | \mathbf{v} | \psi_{m\mathbf{k}} \rangle}{\epsilon_{n\mathbf{k}} - \epsilon_{m\mathbf{k}}} &= \frac{\langle \psi_{n\mathbf{k}} | \mathbf{v}_{SO} | \psi_{m\mathbf{k}} \rangle}{\epsilon^{SO}_{n\mathbf{k}} - \epsilon^{SO}_{m\mathbf{k}}} \\ \langle \psi_n | \mathbf{v}_{SO} | \psi_m \rangle &= \langle \psi_n | \mathbf{v} | \psi_m \rangle \frac{\epsilon^{SO}_{n\mathbf{k}} - \epsilon^{SO}_{m\mathbf{k}}}{\epsilon_{n\mathbf{k}} - \epsilon_{m\mathbf{k}}}. \end{aligned} \tag{E.3}$$

Appendix F

System

F.1 Hexagonal System, $\chi^{(2)}_{zzz}$ Component

For the hexagonal symmetry, the non-vanishing elements of the second-order dielectric susceptibility $\chi^{(2)}_M$ have the form [Shenbook]: $\chi^{(2)}_{xzx} = \chi^{(2)}_{yzy}, \chi^{(2)}_{xxz} = \chi^{(2)}_{yyz}, \chi^{(2)}_{zxx} = \chi^{(2)}_{zyy}, \chi^{(2)}_{zzz}$. The macroscopic second-order polarization then reads:

$$P^{(2)}_M = \begin{pmatrix} \chi^{(2)}_{xzx}(\omega)E_{1z}E_{2x} \\ \chi^{(2)}_{yzy}(\omega)E_{1z}E_{2y} \\ \chi^{(2)}_{zxx}(\omega)E_{1x}E_{2x} + \chi^{(2)}_{zyy}(\omega)E_{1y}E_{2y} + \chi^{(2)}_{zzz}(\omega)E_{1z}E_{2z} \end{pmatrix} \tag{F.1}$$

where the electric fields have been decomposed in their coordinates $\mathbf{E}_i = (E_{ix}, E_{iy}E_{iz})$. The longitudinal polarization $P^{(2)L}_M$ is:

$$\begin{aligned} P^{(2)L}_M &= \frac{\mathbf{u}_1 + \mathbf{u}_2}{|\mathbf{u}_1 + \mathbf{u}_2|} P^{(2)}_M \\ &= \frac{1}{|\mathbf{u}_1 + \mathbf{u}_2|} \Big\{ (u_{1x} + u_{2x}) \chi^{(2)}_{xzx}(\omega) E_{1z}E_{2x} + (u_{1y} + u_{2y}) \chi^{(2)}_{yzy}(\omega) E_{1z}E_{2y} \\ &\quad + (u_{1z} + u_{2z}) \left[\chi^{(2)}_{zxx}(\omega)E_{1x}E_{2x} + \chi^{(2)}_{zyy}(\omega)E_{1y}E_{2y} + \chi^{(2)}_{zzz}(\omega)E_{1z}E_{2z} \right] \Big\} . \end{aligned} \tag{F.2}$$

The last equation has a general validity. Once looking at the second harmonic generation (i.e., $\omega_1 = \omega_2 = \omega$) $\mathbf{q}_1$ and $\mathbf{q}_2$ have the same modulus q: $q = \omega/c$. Considering longitudinal perturbing fields, the polarization vector are: $\mathbf{u}_i = \frac{\mathbf{E}_i}{E_i} = \frac{\mathbf{q}_i}{q}$ (where $E_i = |\mathbf{E}_i|$).

According to Eq. (4.114) (here $\mathbf{q} = \mathbf{q}_1 + \mathbf{q}_2,\ \mathbf{q}' = \mathbf{q}_1$ and $\omega = 2\omega,\ \omega' = \omega$), the macroscopic polarization is related to the microscopic one through:

$$\begin{aligned} & P^{(2)}_M(\mathbf{q}_1 + \mathbf{q}_2, 2\omega) = \\ & \quad \left[1 + 4\pi \frac{\tilde{\alpha}^{(1)}(\mathbf{q}_1 + \mathbf{q}_2, \mathbf{q}_1 + \mathbf{q}_2, 2\omega)}{1 - 4\pi\tilde{\alpha}^{(1),LL}(\mathbf{q}_1 + \mathbf{q}_2, \mathbf{q}_1 + \mathbf{q}_2, 2\omega)} \frac{\mathbf{q}_1 + \mathbf{q}_2}{|\mathbf{q}_1 + \mathbf{q}_2|} \frac{\mathbf{q}_1 + \mathbf{q}_2}{|\mathbf{q}_1 + \mathbf{q}_2|} \right] \\ & \quad \tilde{\alpha}^{(2)}(\mathbf{q}_1 + \mathbf{q}_2, \mathbf{q}_1, \mathbf{q}_2, \omega, \omega) \left[1 + 4\pi \frac{\mathbf{q}_1}{q_1} \frac{\mathbf{q}_1}{q_1} \frac{\tilde{\alpha}^{(1)}(\mathbf{q}_1, \mathbf{q}_1, \omega)}{1 - 4\pi\tilde{\alpha}^{(1),LL}(\mathbf{q}_1\mathbf{q}_1, \omega)} \right] \\ & \quad \left[1 + 4\pi \frac{\mathbf{q}_2}{q_2} \frac{\mathbf{q}_2}{q_2} \frac{\tilde{\alpha}^{(1)}(\mathbf{q}_2, \mathbf{q}_2, \omega)}{1 - 4\pi\tilde{\alpha}^{(1),LL}(\mathbf{q}_2, \mathbf{q}_2, \omega)} \right] \mathbf{E}(\mathbf{q}_1, \omega)\mathbf{E}(\mathbf{q}_2, \omega). \end{aligned} \tag{F.3}$$

In the particular case of a longitudinal field, Eq. (4.120) holds for the longitudinal-longitudinal component of the dielectric function:

$$\left[1+4\pi\frac{\mathbf{q}}{|\mathbf{q}|}\frac{\mathbf{q}}{|\mathbf{q}|}\frac{\tilde{\alpha}^{(1)}}{1-4\pi\tilde{\alpha}^{(1),LL}}\right]\mathbf{E}(\mathbf{q},\omega)=\epsilon_M^{LL}(\mathbf{q},\omega)\mathbf{E}(\mathbf{q},\omega) \tag{F.4}$$

Consequently one has

$$\begin{aligned} P_M^{(2)L}(\mathbf{q}_1+\mathbf{q}_2,2\omega) = {} & E_1E_2\epsilon_M^{LL}(\mathbf{u}_1+\mathbf{u}_2,2\omega)\epsilon_M^{LL}(\mathbf{u}_1,\omega)\epsilon_M^{LL}(\mathbf{u}_2,\omega) \\ & \frac{\mathbf{u}_1+\mathbf{u}_2}{|\mathbf{u}_1+\mathbf{u}_2|} \\ & \tilde{\alpha}^{(2)}(\mathbf{q}_1+\mathbf{q}_2,\mathbf{q}_1,\mathbf{q}_2,\omega,\omega)\mathbf{u}_1\mathbf{u}_2 \end{aligned} \tag{F.5}$$

Going back to the definition of the longitudinal polarization as function of the perturbing field, if $\mathbf{E}^P$ is longitudinal too

$$P^{(2)L}(\mathbf{q}_1+\mathbf{q}_2,2\omega)=\frac{\mathbf{u}_1+\mathbf{u}_2}{|\mathbf{u}_1+\mathbf{u}_2|}\tilde{\alpha}^{(2)}(\mathbf{q}_1+\mathbf{q}_2,\mathbf{q}_1,\mathbf{q}_2,\omega,\omega)\mathbf{u}_1\mathbf{u}_2E_1^PE_2^P \tag{F.6}$$

The longitudinal polarization is linked to the induced density through the continuity equation

$$P^{(2)L}(\mathbf{q}_1+\mathbf{q}_2,2\omega)=\frac{i}{|\mathbf{q}_1+\mathbf{q}_2|}\rho_{ind}^{(2)}(\mathbf{q}_1+\mathbf{q}_2,2\omega) \tag{F.7}$$

that gives (cfr. Eq. (4.125)):

$$\begin{aligned} & \frac{\mathbf{q}_1+\mathbf{q}_2}{|\mathbf{q}_1+\mathbf{q}_2|}\tilde{\alpha}^{(2)}(\mathbf{q}_1+\mathbf{q}_2,\mathbf{q}_1,\mathbf{q}_2,\omega,\omega)\frac{\mathbf{q}_1}{q_1}\frac{\mathbf{q}_2}{q_2} = \\ & \frac{-i}{2q_1q_2|\mathbf{q}_1+\mathbf{q}_2|}\chi_{\rho\rho\rho}(\mathbf{q}_1+\mathbf{q}_2,\mathbf{q}_1,\mathbf{q}_2,\omega,\omega). \end{aligned} \tag{F.8}$$

Substituting Eq. (F.8) into Eq. (F.8) one finally obtains for the secon-harmonic generation in an hexagonal symmetry

$$\begin{aligned} & \frac{1}{|\mathbf{u}_1+\mathbf{u}_2|}\Big\{(u_{1x}+u_{2x})\chi_{xzx}^{(2)}(\omega)E_{1z}E_{2x}+(u_{1y}+u_{2y})\chi_{yzy}^{(2)}(\omega)E_{1z}E_{2y} \\ & +(u_{1z}+u_{2z})\left[\chi_{zxx}^{(2)}(\omega)E_{1x}E_{2x}+\chi_{zyy}^{(2)}(\omega)E_{1y}E_{2y}+\chi_{zzz}^{(2)}(\omega)E_{1z}E_{2z}\right]\Big\} = \\ & \frac{-i\ E_1E_2}{2q_1q_2|\mathbf{q}_1+\mathbf{q}_2|}\epsilon_M^{LL}(\mathbf{u}_1+\mathbf{u}_2,2\omega)\epsilon_M^{LL}(\mathbf{u}_1,\omega)\epsilon_M^{LL}(\mathbf{u}_2,\omega)\chi_{\rho\rho\rho}(\mathbf{q}_1+\mathbf{q}_2,\mathbf{q}_1,\mathbf{q}_2,\omega,\omega). \end{aligned} \tag{F.9}$$

If the two fields has the same amplitude $E_1=E_2=E$ then Eq. (F.9) reduces to

$$\begin{aligned} & \Big\{(u_{1x}+u_{2x})\chi_{xzx}^{(2)}u_{1z}u_{2x}+(u_{1y}+u_{2y})\chi_{yzy}^{(2)}u_{1z}u_{2y} \\ & +(u_{1z}+u_{2z})\left[\chi_{zxx}^{(2)}(u_{1x}u_{2x}+u_{1y}u_{2y})+\chi_{zzz}^{(2)}u_{1z}u_{2z}\right]\Big\} \\ & =\epsilon_M^{LL}(\mathbf{u}_1+\mathbf{u}_2,2\omega)\epsilon_M^{LL}(\mathbf{u}_1,\omega)\epsilon_M^{LL}(\mathbf{u}_2,\omega)\frac{-i}{2q^3}\chi_{\rho\rho\rho}(\mathbf{q}_1+\mathbf{q}_2,\mathbf{q}_1,\mathbf{q}_2,\omega,\omega). \end{aligned} \tag{F.10}$$

In the particular case I am interested $\chi^{(2)}_{zzz}$ can be obtained from the last equation with the appropriate choice of the polarization directions: $\mathbf{u}_1 = \mathbf{u}_2 = \mathbf{z}$:[1]

$$\chi^{(2)}_{zzz} = \frac{-i}{4}\epsilon^{LL}_M(\mathbf{z}, 2\omega)\epsilon^{LL}_M(\mathbf{z}, \omega)\epsilon^{LL}_M(\mathbf{z}, \omega)\chi_{\rho\rho\rho}(2\mathbf{z}, \mathbf{z}, \mathbf{z}, \omega, \omega). \tag{F.11}$$

F.2 Dielectric Function Derivation

The dielectric function ϵ^{LL}_M is given by Eq. (5.10):

$$\epsilon_M(\omega) = lim_{\mathbf{q}\to 0}\frac{1}{\epsilon^{-1}_{\mathbf{GG}'}(\mathbf{q}, \omega)|_{\mathbf{G}=\mathbf{G}'=0}} \tag{F.12}$$

The inverse of the dielectric function ϵ^{LL}_M is given by:

$$\left[\epsilon^{LL}_M\right]^{-1} = 1 + v\chi^{(1)}. \tag{F.13}$$

These are function of the reciprocal lattice vectors $\mathbf{G}$, and can be represented by matrices of (**npwmat**×**npwmat**) dimension once the $\mathbf{G}$-basis has been truncated to **npwmat**. In the Independent Particle Approximation one keeps the only terms $\mathbf{G} = 0$ corresponding to **npwmat**$= 1$ and all these matrices reduce to scalar quantities. Consequently, their inverse corresponds to their reciprocal and one has:

$$\begin{aligned}\epsilon^{IPA}_M =& \frac{1}{\epsilon^{IPA}_M}\\ =& \frac{1}{1 + v\chi^{(1)}}\\ =& \frac{1 + v\chi^{(1)} - v\chi^{(1)}}{1 + v\chi^{(1)}}\\ =& 1 - \frac{v\chi^{(1)}}{1 + v\chi^{(1)}}.\end{aligned} \tag{F.14}$$

Remembering the Dyson equation for the linear density susceptibility Eq. (5.5), it holds the following relation:

$$\begin{aligned}\chi^{(1)} &= \chi^{(1)}_0 + \chi^{(1)}_0 v\chi^{(1)}\\ &= \chi^{(1)}_0\left(1 + v\chi^{(1)}\right)\end{aligned} \tag{F.15}$$

$$\left(1 + v\chi^{(1)}\right) = \left[\chi^{(1)}_0\right]^{-1}\chi^{(1)} \tag{F.16}$$

---

[1] In this case $u_{ix} = u_{iy} = 0$.

that substituted in Eq. (F.14) gives:[2]

$$
\begin{aligned}
\epsilon_M^{IPA} =& 1 - \frac{v\chi^{(1)}}{\left[\chi_0^{(1)}\right]^{-1}\chi^{(1)}} \\
=& 1 - \frac{v}{\left[\chi_0^{(1)}\right]^{-1}} \\
=& 1 - v\chi_0^{(1)} \\
=& 1 - 4\pi\chi_0^{(1)}
\end{aligned}
\tag{F.17}
$$

While introducing Local Fields in the Random Phase Approximation i.e., **npwmat**>1, the solution is more complicated. From Eqs. (F.12) and (F.13) one has:

$$
\begin{aligned}
\epsilon_M^{RPA} =& \frac{1}{(1+v\chi^{(1)})|_{\mathbf{G}=\mathbf{G}'=0}}. \\
=& \frac{1}{1+4\pi\chi^{(1)}|_{\mathbf{G}=\mathbf{G}'=0}}.
\end{aligned}
\tag{F.18}
$$

---

[2] In reciprocal space $v(\mathbf{G}) = -\frac{4\pi}{|\mathbf{q}+\mathbf{G}|^2}$. In principle the term $\mathbf{G}=0$ diverges in the long wavelength limit. However, in formulas it is always multiplied by $\chi^{(i)}$, that removes the divergence and the dependence on $|\mathbf{q}|$ once it is expanded in powers of $\mathbf{q}$ (see section 4.3.2). Therefore, in the limit $\mathbf{q}\to 0$ after the $\mathbf{q}$-expansion of $\chi^{(i)}$, the product $v\chi^{(1)}$ reads $4\pi\chi^{(1)}|_{\mathbf{G}=0}$.

Appendix G

Renormalization Problem

G.1 Simulation Cell Response

It is immediate to notice that for a given system, different thicknesses of the surrounding vacuum will give different responses. The volume of the cell enters as a multiplicative factor in front of the linear and nonlinear response (cfr. Eq. (4.56)) that I will call $\tilde{\chi}^{(i)}_{sys}$.[1] The first-order density response $\chi^{(1)}_0$ can then be written as:

$$\chi^{(1)}_0 = \frac{1}{V_{cell}} \tilde{\chi}^{(1)}_{sys}. \tag{G.1}$$

$\tilde{\chi}^{(1)}_{sys}$ is characteristic of the material, it comes only from the volume of the cell occupied by the material (V_{sys}) where all the electronic states are localized. The total volume of Eq. (G.1) is given by the cell and the vacuum (V_{vac}):

$$V_{cell} = V_{sys} + V_{vac}. \tag{G.2}$$

Varing the vacuum will therefore change V_{sys} without modifying $\tilde{\chi}^{(1)}_{sys}$. The difference between two response functions arising from the same system in two simulation cell of different vacuum-height, is therefore a constant factor that depends on the ratio $\frac{V_{vac}}{V_{sys}}$.

G.1.1 Bulk Response

Let's now consider as an example the Si surface. The simulation cell is composed of a silicon slab, with the upper surface reconstructed in a (2×1) structure and the bottom one made of cutted bulk silicon passivated by hydrogen atoms, and a vacuum slab on top of it.

Signals that are proportional to the bulk part i.e., that arise from bulk states inside the Si, are proportional to the volume of the slab V_{sys}. Indeed, adding new bulk layers will increase the number of bulk states and consequently the

---

[1] As an example, in Eq. (4.56) $\tilde{\chi}^{(2)}_{sys}$ coincides with the summation over the possible transitions between the electronic states.

response $\tilde{\chi}^{(1)}_{sys}$: $\tilde{\chi}^{(1)}_{sys} \propto V_{sys}$. The ratio $\frac{\tilde{\chi}^{(1)}_{sys}}{V_{sys}}$ is therefore constant[2] and the linear response $\chi^{(1)}_0$ becomes:

$$\begin{aligned}\chi^{(1)}_0 &= \frac{1}{V_{sys}+V_{vac}}\tilde{\chi}_{sys} \\ &= \frac{V_{sys}}{V_{sys}+V_{vac}}\frac{\tilde{\chi}_{sys}}{V_{sys}} \\ &= \frac{1}{1+\dfrac{V_{vac}}{V_{sys}}}\frac{\tilde{\chi}_{sys}}{V_{sys}}.\end{aligned} \tag{G.3}$$

Hence, systems with different silicon thickness will give the same response if the ratio $\frac{V_{vac}}{V_{sys}}$ is constant, being all the others terms constant. From Eqs. (F.17) and (F.18), also the dielectric functions in the independent particle or the random phase approximations are unchanged if $\frac{V_{vac}}{V_{sys}}$ is the same (see Figs. (G.1), (G.2)). Keeping this ratio fixed is then the requirement to make comparison between the bulk-response of different size systems.

For a defined slab V_{sys}, it is also possible to pass from the response obtained within a certain value of the vacuum V_a to the one of another value V_b:

$$\chi^{(1)}_a = \frac{1}{V_{sys}+V_a}\tilde{\chi}^{(1)}_{sys} \tag{G.4}$$

$$\chi^{(1)}_b = \frac{1}{V_{sys}+V_b}\tilde{\chi}^{(1)}_{sys} \tag{G.5}$$

$$\chi^{(1)}_b = \frac{V_{sys}+V_a}{V_{sys}+V_b}\chi^{(1)}_a. \tag{G.6}$$

This renormalization factor $\frac{V_{sys}+V_a}{V_{sys}+V_b}$ has to be applied to $\chi^{(1)}$ IPA (RPA) to obtain the corresponding IPA (RPA) dielectric function (see Figs. (G.3-G.6)). It is even possible to *renormalize* to the volume of the system only, posing $V_b = 0$ hence neglecting the vacuum. However, the choice of the appropriate amount of vacuum represents a nontrivial task for absolute comparison with the experiments, as discussed in chapter 6.3.

G.1.2 Surface and Interface Response

While considering responses that arise from a two-dimensional region such as the surface or the interface, the previous considerations are no more valid. In particular $\tilde{\chi}^{(1)}_{sys}$ arise from a confined region close to the surface/interface and is no more proportional to V_{int}.

The optical signal changes until all the active region (where it is originated from) is included into the simulation cell. Once it has been achieved, $\tilde{\chi}^{(1)}_{sys}$ does not change anymore and the surface spectra will present a well defined shape. Further increasing the thickness of the underlying silicon slab adds electronic states that are characteristic of the volume only. As a consequence, the signal

---

[2] One can figure it imaging a bulk system ($V_{vac} = 0$). Changing the cell thickness e.g., doubling its height, does not modify the response, since both $\tilde{\chi}_{sys}$ and V_{sys} are doubled and $\chi^{(1)}_0 = \frac{\tilde{\chi}_{sys}}{V_{sys}}$ remains unchanged.

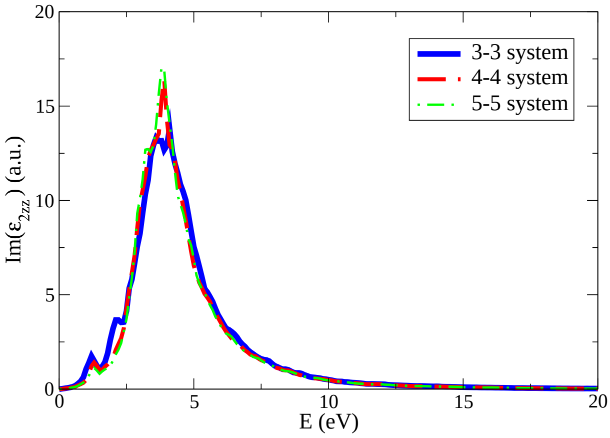

Figure G.1: Imaginary part of the dielectric function ϵ_{zz}. The silicon surface systems are composed of an equal amount of Si and vacuum ($n - n$ system). Here are reported the IPA spectra of the surface composed by three (3-3 system, blue straight line), four (4-4 system, red dashed line) and and five silicon cells (5-5 system, green dotted-dashed line). The intensity is almost the same. Small differences in the main peak arise from the non complete convergence of the bulk in the 3-3 system. Convergence is achieved with four cells of bulk silicon. The small peak at about 2.5 eV decreases while increasing the bulk thickness and is characteristic of the Si surface.

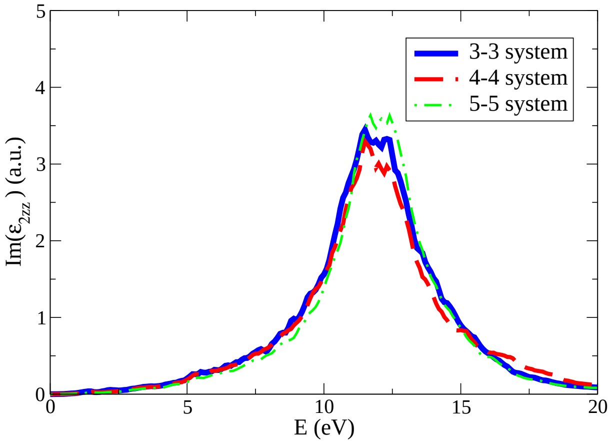

Figure G.2: Imaginary part of the dielectric function ϵ_{zz}. The silicon surface systems are composed of an equal amount of Si and vacuum (n-n system). Here are reported the RPA spectra of the surface composed of three silicon cells (3-3 system, blue straight line), four (4-4 system, red dashed line) and and five silicon cells (5-5 system, green dotted-dashed line). The peak of Fig. (G.1) is blue shifted an the intensity is decreased according to the f-sum rule. The spectra of the three systems and their intensities coincide within good agreement.

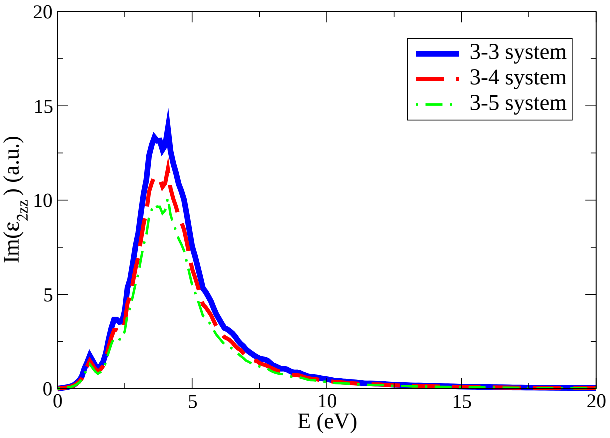

Figure G.3: Imaginary part of the dielectric function ϵ_{zz}. The silicon surface systems are composed of 3 silicon cells and a varying amount of vacuum (3-n system). Here are reported the IPA spectra of the 3-3 system (blue straight line), 3-4 system (red dashed line) and 3-5 system (green dotted-dashed line). The intensity is different depending on the vacuum thickness but the peaks share the same shape and position.

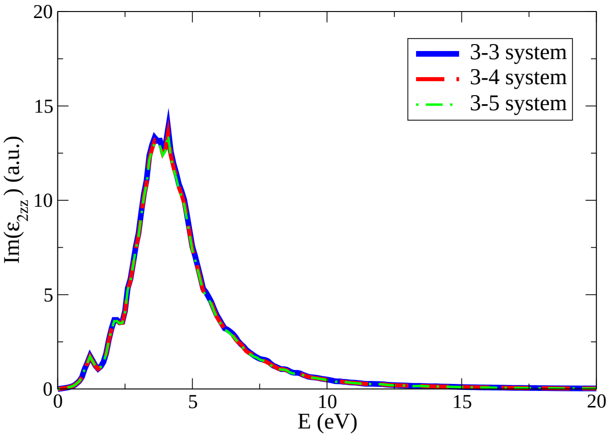

Figure G.4: Imaginary part of the dielectric function ϵ_{zz}. The IPA spectra of the silicon surface systems of Fig. (G.3) have been renormalized to vacuum thickness of the 3-3 system. After the renormalization procedure (Eq. (G.6)) the spectra of the 3-3 system (blue straight line), 3-4 system (red dashed line) and 3-5 system (green dotted-dashed line) are identical.

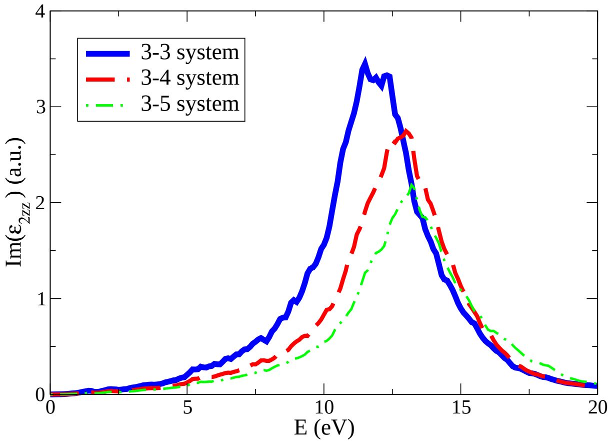

Figure G.5: Imaginary part of the dielectric function ϵ_{zz}. The silicon surface systems are composed of 3 silicon cells and a varying amount of vacuum (3-n system). Here are reported the RPA spectra of the 3-3 system (blue straight line), 3-4 system (red dashed line) and 3-5 system (green dotted-dashed line). Once LF effects are introduced, contrary to IPA (Fig. (G.3)) the peak position and height depend on the vacuum thickness.

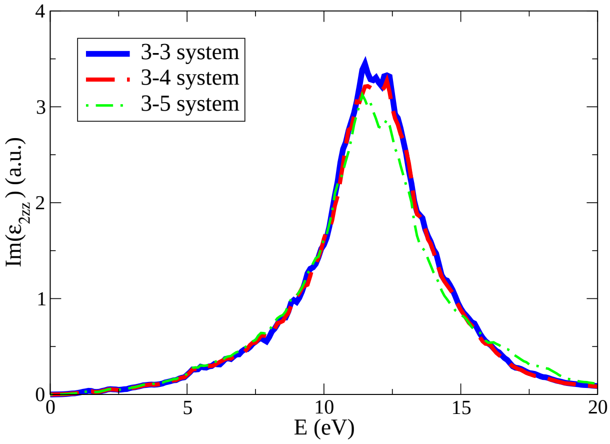

Figure G.6: Imaginary part of the dielectric function ϵ_{zz}. The RPA spectra of the silicon surface systems of Fig. (G.5) have been renormalized to vacuum thickness of the 3-3 system according to Eq. (G.6). After the renormalization procedure the spectra of the 3-3 system (blue straight line), 3-4 system (red dashed line) and 3-5 system (green dotted-dashed line) are identical, both the intensity and the position of the peak.

will start to decrease proportionally to $\frac{1}{V}$ (see the small peak at about 2.5 eV in Fig. (G.1)).

The signal becomes soon very small compared to the bulk one (e.g., in a linear optics absorption spectra Fig. (G.1)). In DFT/TDDFT ab initio calculations it is not clear how to establish the absolute intensity of the spectrum, that decreases proportionally to the chosen volume of the simulation cell. In my simulation I assume it as the one of the system where convergence in the surface/interface peaks position and shape is reached i.e., when all the active optical region is included.

Even experimentally the magnitude of the nonlinear coefficient is not easy to determine because of technical difficulties. Therefore, often only relative comparison can be performed with the theoretical results. An example is provided by the experiment of Heinz *et al.* [82]. The output is the reflected SHG signal, measured as the ratio of the SHG intensity I_{SHG} and the laser I_L that pass through the interface: $\frac{I_{SHG}}{I_L}$. However, the latter does not coincide with the total laser intensity I[3] used to normalize I_{SHG} in the experiment: $\frac{I_{SHG}}{I}$. Therefore, the total intensity of the signal Fig. (6.2) is reported in arbitrary units.

G.1.3 Renormalization of the SHG response

The same conclusions holds also for the second harmonic generation process. As a consequence, whereas for bulk systems one can compare also quantitatively the SHG signal [72], for interfaces such as the Si/CaF$_2$ [82] this is not trivial. Ab initio calculations demonstrate hence useful for SHG intensity predictions or in comparison with experiments where, due to technical difficulties, accurate intensity measurements are not available.

For practical uses, in simulation cell containing the vacuum it is always possible to renormalize the SHG signal passing from different vacuum thickness according to the renormalization procedure of Eq. (G.6):

$$\chi_a^{(2)} = \frac{1}{V_{sys}+V_a}\tilde{\chi}_{sys}^{(2)} \tag{G.7}$$

$$\chi_b^{(2)} = \frac{1}{V_{sys}+V_b}\tilde{\chi}_{sys}^{(2)} \tag{G.8}$$

$$\chi_b^{(2)} = \frac{V_{sys}+V_a}{V_{sys}+V_b}\chi_a^{(2)} \tag{G.9}$$

see Figs. (G.7) and (G.8).

---

[3] E.g., part of it is reflected at the sample surface and part cross the material without passing through the interface region because of the almost planar incidence and the great dimension of the laser spot (about 1 mm).

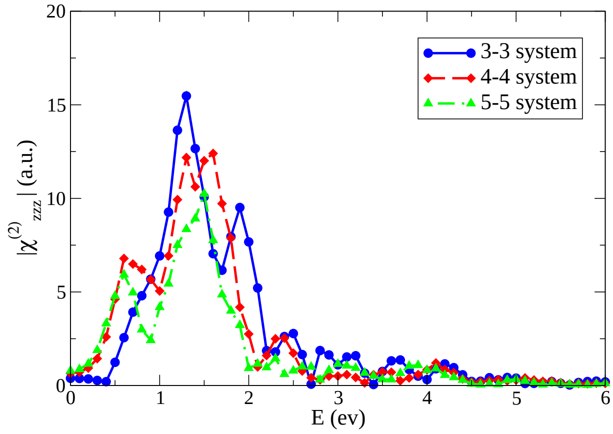

Figure G.7: Second-harmonic generation spectra of the Si surface composed of an equal amount of Si and vacuum ($n-n$ system). The IPA $\chi^{(2)}_{zzz}$ component has been reported for the 3-3 (blue straight line), 4-4 (red dashed line) and and 5-5 (green dotted-dashed line) systems. Contrary to the bulk response, the intensity decreases proportionally to the cell volume although the ratio $\frac{V_{vac}}{V_{sys}}$ is constant, being characteristic of the surface. The spectrum converges in the 5-5 system, showing the larger amount of underlying Si required by the nonlinear optical process with respect to the linear one.

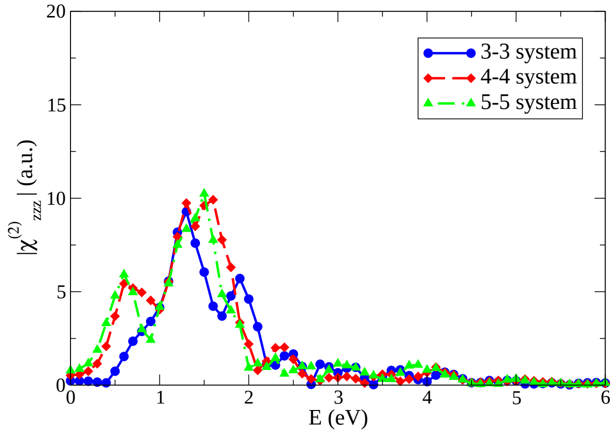

Figure G.8: Renormalized second-harmonic generation spectra of the Si(2x1) surface composed of an equal amount of Si and vacuum (n-n system). The IPA $\chi^{(2)}_{zzz}$ component of the three (3-3 system, blue straight line), four (4-4 system, red dashed line) and and five (5-5 system, green dotted-dashed line) silicon cells systems has been renormalized to the volume of the 5-5 system according to Eq. (G.9). The intensity of the signal is recovered, although differences among the spectral shapes arise from the non complete convergence of the bulk-silicon in the 3-3 and 4-4 systems.

Bibliography

[1] N. Bloembergen, *Nonlinear Optics*, (Benjamin Press, New York, 1965).

[2] Y. R. Shen, *The Principles of Nonlinear Optics* (Wiley-Interscience, New York, 1984).

[3] M. Göppert-Mayer, Annalen der Physik **401** (1931).

[4] P. A. Franken, A. E. Hill, C. W. Peters, and G. Weinreich, Phys. Rev. Lett. **7**, 118 (1961).

[5] H. Ehrenreich, *The Optical Properties of solids*, (Academic, New York,1965, p. 106.).

[6] R. Paschotta, K. Fiedler, P. Kürz, and J. Mlynek, Appl. Phys. B **58**, 117 (1994).

[7] R. Paschotta, P. Kürz, R. Henking, S. Schiller, and J. Mlynek, Opt. Lett. **19**, 1325 (1994).

[8] J.-P. Meyn and M. M. Fejer, Opt. Lett. **22**, 1214 (1997).

[9] Q. H. Xue, Q. Zheng, Y. K. Bu, F. Q. Jia, and L. S. Qian, Opt. Lett. **31**, 1070 (2006).

[10] C. Chen, Z. Lin, and Z. Wang, Appl. Phys. B **80**, 1 (2005).

[11] D. A. Hammons *et al.*, Opt. Commun.. **156**.

[12] A. Lupei *et al.*, Phys. Rev. B **65**, 224518 (2002).

[13] M. Cazzanelli, F. Bianco, E. Borga, G. Pucker, M. Ghulinyan, E. Degoli, E. Luppi, V. Véniard, S. Ossicini, D. Modotto, S. Wabnitz, R. Pierobon, and L. Pavesi, Nature Mat. **11**, 148 (2012).

[14] U. Höfer, Appl. Phys. A **63**, 533 (1996).

[15] W. A. Tisdale, K. J. Williams, B. A. Timp, D. J. Norris, E. S. Aydil, and X.-Y. Zhu, Science **328**, 1543 (2010).

[16] R. M. Corn and D. A. Higgins, Chem. Rev. **94**, 107 (1994).

[17] G. Lüpke, Surf. Sci. Rep. **35**, 75 (1999).

[18] M. Kauranen, T. Verbiest, J. J. Maki, and A. Persoons, J. Chem. Phys. **101**, 8193 (1994).

[19] B. Fluegel, A. Mascarenhas, J. F. Geisz, and J. M. Olson, Phys. Rev. B **57**, R6787 (1998).

[20] C. Zhang *et al.*, Appl. Phys. Lett. **72**, 2072 (1998).

[21] E. Ghahramani, D. J. Moss, and J. E. Sipe, Phys. Rev. B **43**, 8990 (1991).

[22] V. I. Gavrilenko, Phys. Rev. B **77**, 155311 (2008).

[23] A. Savoia, D. Paparo, P. Perna, Z. Ristic, M. Salluzzo, F. M. Granozio, U. S. di Uccio, C. Richter, S. Thiel, J. Mannhart, and L. Marrucci, Phys. Rev. B **80**, 075110 (2009).

[24] P. J. Campagnola, H. A. Clark, W. A. Mohler, A. Lewis, and L. M. Loew, Nature Biotech. **21**, 1356 (2003).

[25] B. E. Cohen, Nature (London) **467**, 407 (2010).

[26] H. M. Su, J. T. Ye, Z. K. Tang, and K. S. Wong, Phys. Rev. B **77**, 125428 (2008).

[27] J. Mejía, B. S. Mendoza, and K. Pedersen, Surface Science **605**, 941 (2011).

[28] E. J. Adles and D. E. Aspnes, Phys. Rev. B **77**, 165102 (2008).

[29] Y. Zeng, W. Hoyer, J. Liu, S. W. Koch, and J. V. Moloney, Phys. Rev. B **79**, 235109 (2009).

[30] S. Abe and K. Kajikawa, Phys. Rev. B **74**, 035416 (2006).

[31] S. A. Yang, X. Li, A. D. Bristow, and J. E. Sipe, Phys. Rev. B **80**, 165306 (2009).

[32] F. X. Wang, F. J. Rodríguez, W. M. Albers, R. Ahorinta, J. E. Sipe, and M. Kauranen, Phys. Rev. B **80**, 233402 (2009).

[33] Z. H. Levine and D. C. Allan, Phys. Rev. B **48**, 7783 (1993).

[34] J. Chen, L. Jönsson, J. W. Wilkins, and Z. H. Levine, Phys. Rev. B **56**, 1787 (1997).

[35] J. A. Armstrong, N. Bloembergen, J. Ducuing, and P. S. Pershan, Phys. Rev. **127**, 1918 (1962).

[36] R. Loudon, Proceedings of the Physical Society **80**, 952 (1962).

[37] P. N. Butcher and T. P. McLean, Proceedings of the Physical Society **81**, 219 (1963).

[38] P. N. Butcher and T. P. McLean, Proceedings of the Physical Society **83**, 579 (1964).

[39] D. E. Aspnes, Phys. Rev. B **6**, 4648 (1972).

[40] C. Y. Fong and Y. R. Shen, Phys. Rev. B **12**, 2325 (1975).

[41] D. J. Moss, J. E. Sipe, and H. M. van Driel, Phys. Rev. B **36**, 9708 (1987).

[42] E. Ghahramani, D. J. Moss, and J. E. Sipe, Phys. Rev. B **43**, 9269 (1991).

[43] Z. H. Levine and D. C. Allan, Phys. Rev. B **44**, 12781 (1991).

[44] Z. H. Levine and D. C. Allan, Phys. Rev. B **43**, 4187 (1991).

[45] Z. H. Levine and D. C. Allan, Phys. Rev. Lett. **66**, 41 (1991).

[46] Z. H. Levine, Phys. Rev. B **42**, 3567 (1990).

[47] J. E. Sipe and E. Ghahramani, Phys. Rev. B **48**, 11705 (1993).

[48] J. E. Sipe and A. I. Shkrebtii, Phys. Rev. B **61**, 5337 (2000).

[49] C. Aversa and J. E. Sipe, Phys. Rev. B **52**, 14636 (1995).

[50] J. L. P. Hughes and J. E. Sipe, Phys. Rev. B **53**, 10751 (1996).

[51] J. L. P. Hughes and J. E. Sipe, Phys. Rev. B **58**, 7761 (1998).

[52] S. N. Rashkeev and W. R. L. Lambrecht, Phys. Rev. B **63**, 165212 (2001).

[53] T. R. Paudel and W. R. L. Lambrecht, Phys. Rev. B **79**, 245205 (2009).

[54] S. Sharma, J. K. Dewhurst, and C. Ambrosch-Draxl, Phys. Rev. B **67**, 165332 (2003).

[55] S. Sharma and C. Ambrosch-Draxl, Phys. Scr. **2004**.

[56] V. I. Gavrilenko and R. Q. Wu, Phys. Rev. B **65**, 035405 (2001).

[57] J. L. Cabellos, B. S. Mendoza, M. A. Escobar, F. Nastos, and J. E. Sipe, Phys. Rev. B **80**, 155205 (2009).

[58] H. Sano, G. Mizutani, W. Wolf, and R. Podloucky, Phys. Rev. B **66**, 195338 (2002).

[59] H. Sano, G. Mizutani, W. Wolf, and R. Podloucky, Phys. Rev. B **70**, 125411 (2004).

[60] S. Yu and J. Guo, J. Chem. Phys. **129**, 194704 (2008).

[61] G. Y. Guo, K. C. Chu, D.-S. Wang, and G.-G. Duan, Phys. Rev. B **69**, 205416 (2004).

[62] I. J. Wu and G. Y. Guo, Phys. Rev. B **78**, 035447 (2008).

[63] V. A. Margulis, E. A. E. E. Muryumin, and Gaiduk, Phys. Rev. B **82**, 235426 (2010).

[64] A. D. Corso, F. Mauri, and A. Rubio, Phys. Rev. B **53**, 15638 (1996).

[65] B. Adolph and F. Bechstedt, Phys. Rev. B **57**, 6519 (1998).

[66] E. C. Chang, E. L. Shirley, and Z. H. Levine, Phys. Rev. B **65**, 035205 (2001).

[67] R. Leitsmann, W. G. Schmidt, P. H. Hahn, and F. Bechstedt, Phys. Rev. B **71**, 195209 (2005).

[68] R. Del Sole and E. Fiorino, Phys. Rev. B **29**, 4631 (1984).

[69] N. H. R. Kubo, J. Phys. Soc. Jpn. **12**, 570 (1957).

[70] J. E. Mejía, B. S. Mendoza, M. Palummo, G. Onida, R. Del Sole, S. Bergfeld, and W. Daum, Phys. Rev. B **66**, 195329 (2002).

[71] B. S. Mendoza, M. Palummo, G. Onida, and R. D. Sole, Phys. Rev. B **63**, 205406 (2001).

[72] E. Luppi, H. Hübener, and V. Véniard, Phys. Rev. B **82**, 235201 (2010).

[73] E. Luppi, H. Hübener, and V. Véniard, J. Chem. Phys. **132**, 241104 (2010).

[74] H. Hübener, E. Luppi, and V. Véniard, Phys. Rev. B **83**, 115205 (2011).

[75] E. Luppi, H. Hübener, M. Bertocchi, E. Degoli, S. Ossicini and V. Véniard (2011). Second-Harmonic Generation Spectroscopy from Time-Dependent Density-Functional Theory. MRS Proceedings, **1370**, mrss11-1370-yy02-08 doi:10.1557/opl.2011.789.

[76] C. A. Lucas, D. Loretto, and G. C. L. Wong, Phys. Rev. B **50**, 14340 (1994).

[77] J. Harada, I. Takahashi, Y. Itoh, N. S. Sokolov, N. L. Yakovlev, Y. Shusterman, and J. C. Alvarez, J. Cryst. Growth **163**, 31 (1996).

[78] F. J. Himpsel, U. O. Karlsson, J. F. Morar, D. Rieger, and J. A. Yarmoff, Phys. Rev. Lett. **56**, 1497 (1986).

[79] D. Rieger, F. J. Himpsel, U. O. Karlsson, F. R. McFeely, J. F. Morar, and J. A. Yarmoff, Phys. Rev. B **34**, 7295 (1986).

[80] J. L. Batstone, J. M. Phillips, and E. C. Hunke, Phys. Rev. Lett. **60**, 1394 (1988).

[81] A. B. McLean and F. J. Himpsel, Phys. Rev. B **39**, 1457 (1989).

[82] T. F. Heinz, F. J. Himpsel, E. Palange, and E. Burstein, Phys. Rev. Lett. **63**, 644 (1989).

[83] F. J. Himpsel, T. F. Heinz, A. B. McLean, E. Palange, and E. Burstein, J. Vac. Sci. Technol. B **7**, 879 (1986).

[84] S. Satpathy and R. M. Martin, Phys. Rev. B **39**, 8494 (1989).

[85] H. Fujitani and S. Asano, Surf. Sci. **268**, 265 (1992).

[86] S. Ossicini, A. Fasolino, and F. Bernardini, Phys. Rev. Lett. **72**, 1044 (1994).

[87] E. Degoli and S. Ossicini, Phys. Rev. B **57**, 14776 (1998).

[88] R. M. Tromp and M. C. Reuter, Phys. Rev. Lett. **61**, 1756 (1988).

[89] J. Zegenhagen and J. P. Patel, Phys. Rev. B **41**, 5315 (1990).

[90] G. C. L. Wong, D. Loretto, E. Rotenberg, M. A. Olmstead, and C. A. Lucas, Phys. Rev. B **48**, 5716 (1993).

[91] T. P. Pearsall *et al.*, Phys. Rev. Lett. **58**, 729 (1987).

[92] C. Zhang *et al.*, Appl. Phys. Lett. **72**, 2072 (1998).

[93] N. Geyer *et al.*, Nano Lett. **9**, 3106 (2009).

[94] M. Born and J. M. Oppenheimer, Ann. Phys. **84**, 457 (1927).

[95] P. Hohenberg and W. Kohn, Phys. Rev. **136**, B864 (1964).

[96] L. H. Thomas, Proc. Cambridge Philos. **23**, 542 (1927).

[97] E. Fermi, Z. Phys. **48**, 73 (1928).

[98] P. A. M. Dirac, Proc. Cambridge Philos. **26**, 376 (1930).

[99] W. Kohn and L. J. Sham, Phys. Rev. **140**, A1133 (1965).

[100] R. P. Feynman, *Statistical Mechanics* (Benjamin Publishing Company, Reading, 1972).

[101] R. M. Dreizler and E. K. U. Gross, *Density Functional Theory: an approach to the quantum many-body problem* (Springer, 1990).

[102] D. M. Ceperley and B. J. Alder, Phys. Rev. Lett. **45**, 566 (1980).

[103] J. P. Perdew and A. Zunger, Phys. Rev. B **23**, 5048 (1981).

[104] J. P. Perdew, K. Burke, and M. Ernzerhof, Phys. Rev. Lett. **77**, 3865 (1996).

[105] C. A. Ullrich, U. J. Gossmann, and E. K. U. Gross, Phys. Rev. Lett. **74**, 872 (1995).

[106] S. Kummel and J. P. Perdew, Phys. Rev. Lett. **90**, 043004 (2003).

[107] A. D. Becke, J. Chem. Phys. **98**, 1372 (1993).

[108] J. P. Perdew, M. Ernzerhof, and K. Burke, J. Chem. Phys. **105**, 9982 (1996).

[109] J. F. Janak, Phys. Rev. B **18**, 7165 (1978).

[110] J. F. Koopmans, Physica **1**, 104 (1934).

[111] P. E. Trevisanutto, C. Giorgetti, L. Reining, M. Ladisa, and V. Olevano, Phys. Rev. Lett. **101**, 226405 (2008).

[112] J. P. Perdew, R. G. Parr, M. Levy, and J. L. Balduz, Phys. Rev. Lett. **49**, 1691 (1982).

[113] J. P. Perdew and M. Levy, Phys. Rev. Lett. **51**, 1884 (1983).

[114] L. J. Sham and M. Schlüter, Phys. Rev. Lett. **51**, 1888 (1983).

[115] L. J. Sham and M. Schlüter, Phys. Rev. B **32**, 3883 (1985).

[116] M. Grüning, A. Marini, and A. Rubio, J. Chem. Phys. **124**, 154108 (2006).

[117] P. P. Ewald, Ann. Phys. **64**, 253 (1921).

[118] H. Hellmann, *Einführung in die Quantenchemie* (Fran Deuticke, Leipzig, 1937).

[119] R. P. Feynman, Phys. Rev. **56**, 340 (1939).

[120] J. C. Slater, J. Chem. Phys. **57**, 2389 (1972).

[121] X. Gonze *et al.* ABINIT:First-principles approach to material and nanosystem properties. *Computer Phys. Commun.* **180**, 2582 (2009). X. Gonze *et al.* A brief introduction to the ABINIT software package. *Zeit. Kristallogr.* **220**, 558 (2005).

[122] H. J. Monkhorst and J. D. Pack, Phys. Rev. B **13**, 5188 (1976).

[123] J. Moreno and J. M. Sole, Phys. Rev. B **45**, 13891 (1992).

[124] W. E. Pickett, Comp. Phys. Rep. **9**, 115 (1989).

[125] M. C. Payne, M. P. Teter, D. C. Allan, T. A. Arias, and J. D. Joannopoulos, Rev. Mod. Phys. **64**, 1045 (1992).

[126] N. Troullier and J. L. Martins, Phys. Rev. B **43**, 1993 (1991).

[127] F. Sottile, V. Olevano, and L. Reining, Phys. Rev. Lett. **91**, 056402 (2003).

[128] G. Adragna, R. Del Sole, and A. Marini, Phys. Rev. B **68**, 165108 (2003).

[129] F. Bruneval, F. Sottile, V. Olevano, R. Del Sole, and L. Reining, Phys. Rev. Lett. **94**, 186402 (2005).

[130] S. Botti, A. Schindlmayr, R. Del Sole, and L. Reining, Reports on Progress in Physics **70**, 357 (2007).

[131] V. Peuckert, J. Phys. Chem. **11**, 4945 (1978).

[132] A. Zangwill and P. Soven, Phys. Rev. A **21**, 1561 (1980).

[133] E. Runge and E. K. U. Gross, Phys. Rev. Lett. **52**, 997 (1984).

[134] E. K. U. Gross and W. Kohn, Phys. Rev. Lett. **55**, 2850 (1985).

[135] E. Gross, J. Dobson, and M. Petersilka, in *Density-functional theory of time-dependent phenomena*, Topics in Current Chemistry, Vol. 181 (Springer, 1996) pp. 81–172.

[136] J. F. Dobson, in *Electronic Density Functional Theory : Reccent Progress and New Directions*, edited by J. F. Dobson, G. Vignale, and M. P. Das (Plenum Publishing Corporation, New York, 1997).

[137] M. A. L. Marques *et al.*, in *Time-Dependent Density Functional Theory*, Lect. Notes Phys., Vol. 706 (Springer, Berlin Heidelberg, 2006).

[138] R. v. Leeuwen, Phys. Rev. Lett. **82**, 3863 (1999).

[139] A. Zangwill and P. Soven, Phys. Rev. Lett. **45**, 204 (1980).

[140] S. Botti *et al.*, Phys. Rev. B **69**, 155112 (2004).

[141] N. H. R. Kubo, Rep. Prog. Phys. **29**, 255 (1966).

[142] N. H. R. Kubo and M. Toda, Statistical Physics II **31** (1978).

[143] R. van Leeuwen, "Introduction to time-dependent density functional theory," Http://www.tddft.org/TDDFT2006/2006tddft/docs/school/vanLeeuwen-I+II.pdf.

[144] F. Sottile *et al.*, Int. J. Quantum Chem. **102**, 684 (2005).

[145] F. Bruneval, S. Botti, and L. Reining, Phys. Rev. Lett. **94**, 219701 (2005).

[146] H. Ehrenreich, in *The Optical Properties of solids*, Proceedings of the International School of Physics Enrico Fermi, Vol. 706 (Academic, New York, 1965).

[147] J. D. Franson and M. M. Donegan, Phys. Rev. A **65**, 052107 (2002).

[148] D. Pines and P. Nozieres, *The Theory of Quantum Liquids*, (Vol.I, Addison-Wesley,New York,1989).

[149] P. M. Platzmann and P. A. Wolff, *Waves and Interactions in Solid State Plasma*, (Academic Press, New York, 1973).

[150] O. V. Dolgov and E. G. Maksimov, in *The Dielectric Function of Condensed Systems*, Modern Problems in Condensed Matter Sciences (North-Holland, Amsterdam, 1989).

[151] N.W.Ashcroft and N.D.Mermin, *Solid State Physics*, (Saunders College, New York,1976).

[152] F. Nastos, B. Olejnik, K. Schwarz, and J. E. Sipe, Phys. Rev. B **72**, 045223 (2005).

[153] A. F. Starace, Phys. Rev. A **3**, 1242 (1971).

[154] V. Olevano unpublished, http://www.dp-code.org.

[155] S. L. Adler, Phys. Rev. **126**, 413 (1962).

[156] S. Datta, C. T. Chan, K. M. Ho, and C. M. Soukoulis, Phys. Rev. B **48**, 14936 (1993).

[157] S. Scandolo and F. Bassani, Phys. Rev. B **51**, 6928 (1995).

[158] K. Sturm, Phys. Rev. B **52**, 8028 (1995).

[159] G. Onida, L. Reining, and A. Rubio.

[160] X. Gonze, P. Ghosez, and R. W. Godby, Phys. Rev. Lett. **74**, 4035 (1995).

[161] V. Olevano and L. Reining, Phys. Rev. Lett. **86**, 5962 (2001).

[162] L. Hedin, Phys. Rev. **139**, A796 (1965).

[163] G. Strinati, Rivista del Nuovo Cimento **11**, 1 (1988).

[164] R. W. Godby, M. Schlüter, and L. J. Sham, Phys. Rev. B **35**, 4170 (1987).

[165] M. S. Hybertsen and S. G. Louie, Phys. Rev. Lett. **55**, 1418 (1985).

[166] F. Aryasetiawan and O. Gunnarsson, Rep. Prog. Phys. **61**, 237 (1998).

[167] S. G. Louie and A. Rubio, "Quasiparticle and optical properties of solids and nanostructures: The gw-bse approach," in *Handbook of Materials Modeling*, Vol. 1 (Springer, 2005) pp. 1–26.

[168] S. Sharma and C. Ambrosch-Draxl, Physica Scripta T109, **128**, (2004).

[169] B. Adolph and F. Bechstedt, Phys. Rev. B **62**, 1706 (2000).

[170] R. Del Sole and R. Girlanda, Phys. Rev. B **48**, 11789 (1993).

[171] L. Reining, V. Olevano, A. Rubio, and G. Onida, Phys. Rev. Lett. **88**, 066404 (2002).

[172] A. Marini, R. Del Sole, and A. Rubio., Phys. Rev. Lett. **91**, 256402 (2003).

[173] D. Hsieh, J. W. McIver, D. H. Torchinsky, D. R. Gardner, Y. S. Lee, and N. Gedik, Phys. Rev. Lett. **106**, 057401 (2011).

[174] J. R. Power, J. D. O'Mahony, S. Chandola, and J. F. McGilp, Phys. Rev. Lett. **75**, 1138 (1995).

[175] J. E. Mejía *et al.*, Phys. Rev. B **66**, 195329 (2002).

[176] M. W. Klein, C. Enkrich, M. Wegener, and S. Linden, Science **313**, 502 (2006).

[177] F. A. d'Avitaya, L. Vervoort, F. Bassani, S. Ossicini, A. Fasolino, and F. Bernardini, Europhys. Lett. **31**, 25 (1995).

[178] F. A. d'Avitaya, L. Vervoort, F. Bassani, S. Ossicini, A. Fasolino, and F. Bernardini, Phys. Status Solidi B **190**, 123 (1995).

[179] F. Bassani, I. Mihalcescu, J. C. Vial, and F. A. d'Avitaya, Appl. Surf. Sci. **117-118**, 670 (1997).

[180] J. Wollschläger, C. Deiter, M. Bierkandt, A. Gerdes, M. Bäumer, C. Wang, B. Müller, and K. Hofmann, Surf. Sci. **600**, 3637 (2006).

[181] E. Degoli and S. Ossicini, The Journal of Luminescence **80**, 411 (1999).

[182] S. Ossicini, C. Arcangeli, and O. Bisi, Phys. Rev. B **43**, 9823 (1991).

[183] M. Amato, M. Palummo, and S. Ossicini, Materials Science and Engineering: B **177**, 705 (2012).

[184] E. Degoli, 1999 Ph.D. thesis, Univeristà di Modena e Reggio Emilia, Italy.

[185] D. N. Batchelder and R. O. Simmons, J. Chem. Phys. **41**, 2324 (1964).

[186] M. Bertocchi, Master thesis, Università degli Studi di Modena e Reggio Emilia, Italy, 2009.

[187] R. Guerra *et al.*, Phys. Rev. B **79**, 075342 (2009).

[188] R. Guerra, M. Marsili, O. Pulci, and S. Ossicini, Phys. Rev. B **84**, 075342 (2011).

[189] L. Caramella, G. Onida, F. Finocchi, L. Reining, and F. Sottile, Phys. Rev. B **75**, 205405 (2007).

[190] M. A. U. Schmid, N. E. Christensen and M. Cardona, Phys. Rev. B **43**, 14597 (1991).

[191] G. T. H. M. Polatoglou and C. Tserbak, Phys. Rev. B **49**, 8132 (1994).

[192] E. A. Montie, G. F. A. van de Walle, D. j. Gravesteijn, A. A. Gorkum, and C. W. T. Bulle-Lieuwma, Appl. Phys. Lett. **56**, 340 (1990).

[193] M. Virgilio, G. Pizzi, and G. Grosso, Appl. Phys. Lett. **110**, 083105 (2011).

[194] X. Xiao, C. Zhang, A. B. Fedotov, Z. Chen, and M. M. T. Loy, J. Vac. Sci. Technol. B **15**, 1112 (1997).

[195] D. J. Bottomley, J.-M. Baribeau, and H. M. van Driel, Phys. Rev. B **50**, 8564 (1994).

[196] X. Zhang, Z. Chen, L. Xuan, S. Pan, and G. Yang, Phys. Rev. B **56**, 15842 (1997).

[197] D. J. Bottomley, G. Lüpke, M. L. Ledgerwood, X. Q. Zhou, and H. M. van Direl, Appl. Phys. Lett. **63**, 2324 (1993).

[198] X. Zhang *et al.*, Appl. Phys. Lett. **71**, 3359 (1997).

[199] W. G. Aulbur, Z. H. Levine, J. W. Wilkins, and D. C. Allan, Phys. Rev. B **51**, 10691 (1995).

[200] E. Ghahramani, D. J. Moss, and J. E. Sipe, Phys. Rev. Lett. **64**, 2815 (1990).

Acknowledgements

Un grazie di cuore a tutti coloro che mi sono stati vicini in questi tre importanti anni della mia vita. In particolare a Stefano Ossicini, che ha creduto in me ed ha fatto molto per la mia crescita personale e professionale. Se sono arrivato fin qui, il merito di avermi convinto a percorrere questa strada è suo.

Je remercie également Valerié Véniard pour l'aide précieuse et irremplaçable quand tout semblait impossible. Seulement sa grande expérience et sa connaissance m'ont permis de accomplir ce travail, en m'apprenant au même temps à faire face à chaque problème avec compétence.

Un ringraziamento particolare ad Elena ed Eleonora, senza le quali non avrei saputo superare le molte difficoltà incontrate. Grazie alla loro spinta a puntare sempre in alto ed a fare di più posso dire di essere soddisfatto del mio lavoro e dei risultati raggiunti.

In questi tre anni, assieme a tutti i membri dei gruppi di Modena e Parigi, hanno contribuito a creare un ambiente di lavoro stimolante, collaborativo ed accogliente. Con la libertà concessami ho potuto gestire autonomamente gran parte del mio lavoro, imparando a pormi delle domande, a cercare le risposte e ad assumermi delle responsabilità. Ho potuto sempre contare sul loro supporto e la loro esperienza che mi hanno trasmesso attraverso un confronto stimolante ed educativo. Per questo ringrazio in particolar modo Lucia Reining.

Più di tutto mi preme ringraziare queste persone per l'affetto dimostratomi, l'amicizia, la disponibiltà e l'avermi accompagnato per un po' sulla strada della vita. Questo non lo dimenticherò mai.

Ringrazio infine Feffe, che mi ha aiutato a superare le prime difficoltá e mi ha introdotto alla vita parigina. Un abbraccio di cuore invece a chi mi è sempre stato accanto: Daniela, i miei amici ed i miei genitori. Perché, dopotutto, non c'è solo la fisica a questo mondo.

Summary

In this thesis I have dealt with the ab initio description of the second-harmonic generation (SHG) process, a nonlinear optical property of materials, focusing in particular on quantum confined, silicon-based systems. In the last decades, the accuracy and possibilities of ab initio studies have demonstrated a great relevance in both the interpretation and prediction of the materials properties. It is then mandatory to improve the knowledge of the nonlinear optical processes as well as the SHG first-principle description.

Nowadays, due to nontrivial difficulties, nonlinear optics has not yet reached the accuracy and development of linear phenomena. In particular, the state of the art of ab initio SHG calculations is represented by the inclusion of many-body effects as crystal local fields (LF) and electron-hole interaction, but today, the mostly used approach is the independent particle approximation (IPA), the only one able to approach calculations of complex structures such as surfaces and interfaces. Whereas IPA can be a good approximation for bulk systems, in discontinuous materials other effects may be predominant. Hence their description is of great relevance although the lack of studies. My thesis tries to give a first analysis of the SHG process in more complex systems as the interfaces and the Si-confined systems, inferring new insights on the physical mechanism and its link with the nature of the system. I use an efficient formalism based on the Time Dependent Density Functional Theory (TDDFT) where many-body effects are included via an appropriate choice of the TDDFT kernels. Both the formalism and the code have been developed during the thesis work permitting the study complex materials.

The research has been focused on the Si(111)/CaF$_2$ (T_4 B-type) interface case study. Convergence studies show the importance of the semiconductor material with respect to the insulator. The response is characteristic of a deep region beyond the Si interface whereas the CaF$_2$ converges soon after the first interface layers. Moreover, the signal demonstrates to be sensitive to the electronic-states modifications that are induced far below the interface, and not to the Si ionic structure that recovers soon the bulk configuration. A normalization procedure to compare with the experiment has been proposed. The SHG spectra have been calculated in the IPA, introducing LF and excitonic interactions. New behaviors have been observed with respect to the SHG processes on strained silicon, GaAs or SiC showing in particular the importance of crystal local-field effects with respect to both the IPA and the excitons. Whereas IPA can describe the position of the SHG main peaks and the excitonic effects slightly modify the total intensity, only LF are able to correctly reproduce the spectral shape and the relative intensities of the peaks. This underlines how SHG and the different involved effects depends on the nature of the materials.

New methods of analysis of the response have been proposed; actually, the direct link between the peaks position and the transition energies is lost in SHG calculations (i.e. the signal comes from a second order Dyson equation where linear and nonlinear response functions at different frequencies are mixed together). Furthermore, the complexity of the system allowed me to extend the study to a large variety of materials as the multilayers and the silicon confined slabs. The results show a good agreement with the experiment confirming the proposed T_4 B-type interface structure. This underlines the accuracy of the formalism, the possibility of improving our knowledge on these complex materials going beyond the standard approaches, and confirms the possibility of SHG ab-initio simulations to be employed as a predictive technique, supporting and guiding experiments and technological developments.

Preliminary results on Si/Ge superlattice are presented.

Résumé

Dans cette thèse, je me suis interessé à la description ab initio du processus de génération de seconde harmonique (SHG), qui est une propriété optique non-linéaire des matériaux, et je me suis concentré sur les systèmes quantiques confinés, à base de silicium. Ces dernières années, les études ab initio ont suscité un grand intérêt pour l'interprétation et la prévision des propriétés des matériaux. Il est indispensable d'améliorer la connaissance des processus non-linéaires et de proposer une description de SHG, à partir des premiers principes.

En raison de difficultés importantes, la description de l'optique non linéaire n'a pas encore atteint la précision des phénomènes linéaires. L'état de l'art des calculs ab initio SHG est représenté par l'inclusion des effets à plusieurs corps comme les champs locaux (LF) et l'interaction électron-trou, mais aujourd'hui, l'approche la plus utilisée est l'approximation de particules indépendantes (IPA), la seule en mesure d'aborder les calculs de structures complexes, tels que des surfaces et des interfaces. Alors que IPA peut être une bonne approximation pour les systèmes massifs, dans des matériaux discontinus d'autres effets peuvent être prédominants.

L'objectif de ma thèse est de donner une analyse du processus de SHG dans des systèmes complexes comme les interfaces et les systèmes confinés à base de silicium, d'inférer de nouvelles connaissances sur le mécanisme physique mis en jeu et son lien avec la nature du système. J'utilise un formalisme fondé sur la théorie de la fonctionnelle de la densité dépendant du temps (TDDFT) où les effets à plusieurs corps sont inclus par un choix approprié des noyaux de la TDDFT. Le formalisme et le code ont été développés au cours de mon travail, permettant l'étude de matériaux complexes.

Mes recherches ont porté sur l'étude de l'interface Si (111)/CaF2 (de type B,T4). Des études de convergence montrent l'importance du matériau semi-conducteur par rapport à l'isolant. La réponse est caractéristique d'une région profonde au-delà de l'interface Si, alors que CaF2 converge rapidement juste après l'interface. La réponse montre une sensibilité aux modifications électroniques, induites dans des états bien en-dessous de l'interface, et non à la structure ionique du silicium, qui retrouve rapidement la configuration du matériau massif. Une procédure de normalisation pour comparer avec l'expérience a été proposée. Les spectres de SHG ont été calculés en IPA, et en introduisant les interactions de champs locaux et excitoniques. De nouveaux comportements ont été observés par rapport aux processus SHG dans GaAs ou SiC, montrant l'importance des effets de champ locaux cristallins. Alors que IPA décrit la position des pics principaux de SHG et que les effets excitoniques modifient légèrement l'intensité totale, seuls les champs locaux reproduisent la forme spectrale et les intensités relatives des pics. Cela souligne combien les effets des différents acteurs dans le processus dépendent de la nature des matériaux.

De nouvelles méthodes d'analyse de la réponse ont été proposées: en effet, le lien direct entre la position des pics et les énergies de transition est perdu dans les calculs de SHG : le signal provient d'une équation de Dyson du second ordre où les fonctions de réponse linéaires et non-linéaire pour des fréquences différentes sont mélangées. En outre, la complexité du matériau m'a permis d'obtenir des informations sur une grande variété de systèmes comme les multicouches et les couches de silicium confinées. Les résultats montrent un bon accord avec l'expérience, confirmant la structure de l'interface proposée. Cela souligne la précision du formalisme, la possibilité d'améliorer nos connaissances sur ces matériaux complexes. Les simulations ab-initio de SHG peuvent être utilisées comme une technique prédictive, pour soutenir et guider les expériences et les développements technologiques.

Les résultats préliminaires sur les structures Si/Ge sont présentés.

Riassunto

In questa tesi ho trattato la descrizione ab initio del processo di generazione di seconda armonica (SHG), un fenomeno di ottica non lineare dei materiali, concentrandomi in particolare sui sistemi confinati a base di silicio. Negli ultimi decenni, l'accuratezza e le potenzialità degli studi ab initio hanno dimostrato una grande rilevanza sia nell'interpretazione che nella predizione delle proprietà dei materiali. Diviene quindi essenziale migliorare la descrizione da principi primi dei processi nonlineari come la SHG.

Oggi, l'ottica nonlineare non ha ancora raggiunto il livello di accuratezza e sviluppo dei fenomeni di ottica lineare a causa delle notevoli difficoltà che la descrizione comporta. In particolare, lo stato dell'arte dei conti ab initio di SHG è rappresentato dall'inclusione degli effetti many-body come i campi locali (LF) e l'interazione elettrone-lacuna. Ad oggi l'approccio più utilizzato rimane l'approssimazione di particelle indipendenti (IPA), l'unico capace di affrontare calcoli di strutture complesse come le superfici e le interfacce. Mentre l'IPA può essere una buona approssimazione per i sistemi di volume, nei materiali discontinui altri effetti possono essere predominanti. La loro descrizione diviene quindi di grande importanza nonostante la mancanza di studi. La mia tesi cerca di fornire una prima analisi del processo di SHG in sistemi complessi come le interfacce ed i sistemi confinati di Si, ottenendo una più approfondita comprensione del fenomeno e della sua relazione con la natura del materiale. Ho utilizzato un efficiente formalismo basato sulla Time Dependent Density Functional Theory (TDDFT) in cui è possible descrivere gli effetti many-body attraverso l'appropriata scelta dei kernels TDDFT. In questa tesi sia il formalismo che il codice sono stati sviluppati per rendere possibile lo studio di materiali complessi.

La ricerca è stata focalizzata sul sistema prototipo dell'interfaccia Si(111)/CaF$_2$ (T_4 B-type). Gli studi di convergenza evidenziano l'importanza del materiale semiconduttore rispetto all'isolante. La risposta è infatti caratteristica di una profonda regione di Si sotto l'interfaccia mentre il CaF$_2$ converge già dopo i primi layers. Inoltre, il segnale si dimostra sensibile alle variazioni degli stati elettronici molto al di sotto l'interfaccia, e non alla struttura del Si che raggiunge velocemente la configurazione di volume. Si è proposta una procedura di normalizzazione per il confronto con l'esperimento. Gli spettri di SHG sono stati calcolati in IPA, introducendo i LF e l'interazione eccitonica. Sono stati osservati nuovi comportamenti rispetto al processo di SHG nei sistemi di volume (GaAs o SiC) che evidenziano l'importanza dei campi locali rispetto all'IPA e agli eccitoni. Infatti, mentre l'IPA riesce a descrivere la posizione dei picchi principali del segnale SHG e gli effetti eccitonici ne modificano lievemente l'intensità totale, solo i LF riproducono correttamente la forma spettrale e le intensità relative dei picchi. Ciò mostra come la SHG ed i differenti effetti coinvolti dipendano dalla natura del materiale.

Nuovi metodi di analisi del segnale sono stati proposti; infatti, il legame tra la posizione del picco e le energie di transizione tra gli stati elettronici è perso nel calcolo della SHG (il segnale è ottenuto tramite un'equazione di Dyson di secondo ordine dove le funzioni di risposta lineari e nonlineari a frequenze differenti sono mescolate tra di loro). In aggiunta, la complessità del sistema mi ha permesso di estendere lo studio a materiali quali i multistrati e gli strati confinati di Si. I risultati mostrano un buon accordo con l'esperimento confermando inoltre la struttura T_4 B-type proposta. Ciò avvalora l'accuratezza del formalismo, la possibilità di migliorare la nostra conoscenza del processo in materiali complessi e conferma la possibilità di utilizzare le simulazioni ab initio come tecnica predittiva per la SHG, supportando e guidando gli esperimenti e gli sviluppi tecnologici.

Sono infine presentati i risultati preliminari sui supercristalli di Si/Ge.